Human Middle Ear: Material Characterization, Analysis of Effects of Uncertainties, and Investigation of Impacts of Medical-Device Attachment

by

Arash Ebrahimian

A thesis

presented to the University of Waterloo

in fulfillment of the

thesis requirement for the degree of

Doctor of Philosophy

in

Systems Design Engineering

Waterloo, Ontario, Canada, 2022

© Arash Ebrahimian 2022

Examining Committee Membership

The following served on the Examining Committee for this thesis. The decision of the Examining Committee is by majority vote.

External Examiner	Elizabeth S. Olson Professor, Departments of Biomedical Engineering and Otolaryngology/Head and Neck Surgery, Columbia University
Supervisor	Nima Maftoon Assistant Professor, Department of Systems Design Engineering, University of Waterloo
Internal Member	John McPhee Professor, Department of Systems Design Engineering, University of Waterloo
Internal Member	Jonathan Kofman Associate Professor, Department of Systems Design Engineering, University of Waterloo
Internal-external Member	Armaghan Salehian Associate Professor, Department of Mechanical and Mechatronics Engineering, University of Waterloo

Author's Declaration

This thesis consists of material all of which I authored or co-authored: see Statement of Contributions included in the thesis. This is a true copy of the thesis, including any required final revisions, as accepted by my examiners.

I understand that my thesis may be made electronically available to the public.

Statement of Contributions

Chapter 2:

Inaccuracies of deterministic finite-element models of human middle ear revealed by stochastic modelling

First author: Arash Ebrahimian

Methodology; Created the Mesh and Model; Created FE model; Validation; Investigation; Writing (original draft)

Second author: Hossein Mohammadi

Provided comments and suggestions; Writing (review and editing)

Third author: John J. Rosowski

Provided comments and suggestions; Writing (review and editing)

Fourth author: Jeffrey Tao Cheng

Provided comments and suggestions; Writing (review and editing); Funding acquisition

Fifth author: Nima Maftoon

Conceptualization; Methodology; Writing (review and editing); Funding acquisition; Supervision

Chapter 3:

Relative importance and interactions of parameters of finite-element models of human middle ear

First author: Arash Ebrahimian

Methodology; Created the Mesh and Model; Created FE model; Validation; Analysis; Writing (original draft)

Second author: Hossein Mohammadi

Provided comments and suggestions; Writing (review and editing)

Third author: Nima Maftoon

Conceptualization; Methodology; Writing (review and editing); Funding acquisition; Supervision

Chapter 4:

Material characterization of thin planar structures using full-field harmonic vibration response measured with stroboscopic holography, Published in the International Journal of Mechanical Sciences, 15 May 2021, Volume 198, 106390.

First author: Arash Ebrahimian

Methodology; Software (all codes and simulations); Validation; Investigation; Writing (original draft)

Second author: Haimi Tang

Investigation; Software (related to experimental data).

Third author: Cosme Furlong

Resources; Writing (review and editing); Funding acquisition

Fourth author: Jeffrey Tao Cheng

Methodology; Writing (review and editing); Funding acquisition

Fifth author: Nima Maftoon

Conceptualization; Methodology; Writing (review and editing); Funding acquisition; Supervision

Chapters 5&6:

Material characterization of human middle ear using machine-learning-based surrogate models (Chapter 5)

Mechanical effects of medical device attachment to human tympanic membrane: A finite-element analysis (Chapter 6)

First author: Arash Ebrahimian

Methodology; Created the Mesh and Model; Created FE model; Validation; Analysis; Writing (original draft)

Second author: Hossein Mohammadi

Provided comments and suggestions; Writing (review and editing)

Third author: Nima Maftoon

Conceptualization; Methodology; Writing (review and editing); Funding acquisition; Supervision

Chapter 7:

Acoustical effects of medical device attachment to human tympanic membrane: A finite-element analysis

First author: Arash Ebrahimian

Methodology; Created the Mesh and Model; Created FE model; Validation; Analysis; Writing (original draft)

Second author: Hamid Motallebzadeh

Provided comments and suggestions

Third author: Nima Maftoon

Conceptualization; Methodology; Writing (review and editing); Funding acquisition; Supervision

Abstract

The middle ear is a complex organ that plays a vital role in the hearing process. This thesis attempts to investigate different aspects of the biomechanics of the middle ear for diagnosis and treatment. This thesis can be divided into three broad categories which are, analysis of the effects of uncertainties of the middle-ear model parameters and finding the most influential parameters on the vibrations of middle-ear structures, estimation of the material properties of the structures in the middle ear for diagnostic purposes, and investigation of the effects of attachment of medical devices to the tympanic membrane on the middle-ear vibrations.

The inter-individual variabilities in the material properties and geometrical features of the middle ear lead to uncertainties in the middle-ear responses and the models of the middle ear. To be able to develop realistic models of the middle ear, we need to have a clear understanding of the effects of these uncertainties on the middle ear vibrations. However, these effects and especially the interactions of uncertainties with one another have not been well addressed in the literature. We used stochastic finite-element method to study the effects of these uncertainties on the sound conduction in the middle ear. Our results suggest that the uncertainties in the model parameters can be magnified by up to more than three times in the umbo and stapes footplate responses. Additionally, we used our stochastic finite-element model results to perform a global sensitivity analysis of middle-ear parameters. For this aim, we used the Sobol′ sensitivity analysis method that can evaluate the global impact of model parameters as well as the interactions among them. To reduce the computational cost of evaluating Sobol′ indices, we first created surrogate models of the middle ear using the polynomial chaos expansion method. We then estimated the values of Sobol′ indices from these surrogate models. Our results suggest that Young's modulus and thickness of the tympanic membrane, Young's modulus and damping of the stapedial annular ligament, and the Young's modulus of the ossicles are the parameters with the greatest impacts on the amplitudes of the umbo and stapes footplate and the phase of the stapes footplate. The greatest interactions in the parameters were observed between the thickness and Young's modulus of the tympanic membrane.

In this thesis, we also proposed a novel method for material characterization of the middle ear. In the first step, the method was used to estimate the Young's modulus of 2D thin planar structures using single frequency full-field harmonic vibration data of the structure. Our proposed method uses Bayesian optimization for parameter estimation and we found that the estimated values of the Young's modulus had errors of less than 5% even with very low values of signal-to-noise ratio. In the next step, we made some changes to the method to make it suitable to apply to the tympanic membrane. In order to increase the speed of the parameter estimation of the middle-ear structures and make the proposed estimation method suitable for future real-time applications, we combined our parameter estimation method with machine-learning-based surrogate models created using the eXtreme gradient boosting (XGBoost) method. The results show that the created surrogate models can fairly represent the behaviours of the middle ear. Also, the proposed machine-learning-based parameter estimation method can estimate the Young's modulus of the tympanic membrane and the Young's modulus of the stapedial annular ligament (with mean absolute percentage errors of less than 7%) which are among the most influential mechanical parameters in the middle ear as was demonstrated using our global sensitivity analysis.

Another objective of this study was to identify the mechanical and acoustical effects of medical devices attached to the tympanic membrane on middle-ear vibrations. The outcomes of this section can lead to optimizing current and future medical devices that are designed to be attached to the tympanic membrane. We used finite-element modelling to systematically study the effects of changes of middle-ear responses as a result of the attachment of the device. We first investigated the mechanical effects of the attachment of the device (due to changes in the mass and stiffness of the middle ear) on the sound conduction in the middle ear. We found that variations of the material properties of the device have significant effects on the umbo and stapes footplate motions at frequencies below 5 kHz. We also observed that the variations of geometrical properties of the device and its location on the tympanic membrane can have significant effects on the middle-ear vibrations at several frequencies in the frequency range of 100 Hz to 10 kHz. In the next step, we studied the acoustical effects of the medical device

and its combination with the mechanical effects of the device. The acoustical effects of the device are significant if the desired treatment method requires perforating the tympanic membrane in addition to attaching a medical device to it. We observed that when both the mechanical effects (due to the mass and stiffness of the device) and the acoustical effects (due to perforations of the tympanic membrane) are present, the acoustical effects are dominant at low frequencies (below about 1 kHz) while the mechanical effects are dominant at frequencies above 1 kHz.

Acknowledgments

I would like to express my gratitude to my supervisor Dr. Nima Maftoon for his dedication, invaluable insights and comments, continuous support, and patience during my Ph.D. journey. His immense knowledge and plentiful experience steered me through this research and I will always cherish the valuable lessons I learned from him. I am indebted to him for all his support and scholarly guidance. I gratefully acknowledge my Ph.D. committee members Dr. Elizabeth S. Olson, Dr. Armaghan Salehian, Dr. John McPhee, and Dr. Jonathan Kofman for the time they spent for reviewing my thesis and for participating in my Ph.D. defense. I would also like to thank Dr. John J. Rosowski, Dr. Hamid Motallebzadeh, Dr. Jeffrey Tao Cheng, Dr. Haimi Tang, and Dr. Cosme Furlong for all their contributions and supports. Special thanks to my lab mate and my dear friend Hossein Mohammadi for all his helps, all the stimulating discussions, and all the great times we had together.

My heartfelt gratitude goes to my parents Ahmad and Soghra for bestowing their unconditional love and affection. I wouldn't have accomplished a thing if it wasn't for them. I owe them my endless gratitude that I would never be able to pay back. I would also like to thank my brother Arman for being a great brother and for all his helps.

I owe my deepest gratitude to my wife and my best friend Maedeh for her understanding, encouragement, and patience, which made this research possible. She has been extraordinarily supportive and has made countless sacrifices throughout the entire process.

This work was supported by the Natural Sciences and Engineering Research Council of Canada (RGPIN-2020-05522) and the Canada Foundation for Innovation and the Ontario Research Fund-Research Innovation (38964). Furthermore, the infrastructures of the Digital Research Alliance of Canada[1] were used for several simulations presented in this thesis.

[1] www.alliancecan.ca

Dedication

I dedicate this thesis to my wife and my parents for their continuous encouragement and love.

Table of Contents

Author's Declaration iii

Statement of Contributions iv

Abstract vii

Acknowledgments x

Dedication xi

List of Figures xviii

List of Tables xxiii

Chapter 1 Introduction 1

1.1 Motivation 1

1.2 Objectives 3

1.3 Summary of thesis 4

1.4 Anatomy 4

1.4.1 Outer ear 5

1.4.2 Middle ear 5

1.4.3 Inner ear 6

1.5 Literature review 7

1.5.1 Modelling of middle-ear mechanics 7

1.5.2 Experimental measurements of vibrations of middle ear 14

Chapter 2 Inaccuracies of deterministic finite-element models of human middle ear revealed by stochastic modelling 16

Preface 16

Overview 17

2.1 Introduction 18

2.2 Materials and methods 19
2.2.1 Geometry, model components, and mesh 19
2.2.2 Deterministic FE modelling 20
2.2.3 Mesh Dependency 22
2.2.4 Time-step and time-span dependency 23
2.2.5 Uncertainty propagation 23
2.3 Results 26
2.3.1 Middle-ear model can magnify parameter uncertainties up to more than three times in the output 26
2.3.2 At low frequencies, middle-ear models attenuate uncertainties and approximate a robust simple lever 31
2.3.3 The Middle-ear model is biased 31
2.3.4 Uncertainties in the vibration patterns of the TM are spread in space with increased frequency 33
2.4 Discussions 36
Chapter 3 Relative importance and interactions of parameters of finite-element models of human middle ear 39
Preface 39
Overview 40
3.1 Introduction 41
3.2 Materials and methods 43
3.2.1 Mesh and deterministic finite-element model 43
3.2.2 Uncertainty propagation and stochastic finite-element model 45
3.2.3 Global sensitivity analysis 45
3.2.4 Creation of surrogate models using polynomial chaos expansion 47

3.3 Results 49
3.3.1 Evaluation of the quality of the surrogate models 49
3.3.2 Global sensitivity analysis 54
3.3.2.1 Umbo displacement amplitude at low frequency 54
3.3.2.2 Stapes footplate displacement amplitude at low frequency 55
3.3.2.3 Stapes footplate displacement phase at low frequency 55
3.3.2.4 Umbo displacement amplitude at mid-frequency 57
3.3.2.5 Stapes footplate displacement amplitude at mid-frequency 57
3.3.2.6 Stapes footplate displacement phase at mid-frequency 57
3.3.2.7 Umbo displacement amplitude at high frequency 59
3.3.2.8 Stapes footplate displacement amplitude at high frequency 59
3.3.2.9 Stapes footplate displacement phase at high frequency 61
3.3.2.10 Maximum parameter interactions at all frequencies 61
3.3.2.11 Parameter importance as a function of continuous frequency 62
3.4 Discussions 65
Chapter 4 Material characterization of thin planar structures using full-field harmonic vibration response measured with stroboscopic holography 72
Preface 72
Overview 73
4.1 Introduction 74
4.2 Materials and Methods 76
4.2.1 Governing equation 77
4.2.2 Finite-difference formulations 79
4.2.3 Inverse problem 80

4.2.4 Optimization process 82
4.3 Results 85
4.3.1 Validation using analytical data 85
4.3.1.1 Simply-supported thin square plate 86
4.3.1.2 Clamped thin square plate 89
4.3.2 Validation using finite-element data 90
4.3.2.1 Elliptical and triangular plates 90
4.3.2.2 Non-Gaussian noise 93
4.3.2.3 Effect of uncertainty in thickness, Poisson's ratio, and boundary conditions 94
4.3.2.4 Non-uniform thickness 98
4.3.2.5 Thick plates 99
4.3.2.6 Effects of uncertainty in boundary conditions 99
4.3.2.7 Mesh size and runtime 100
4.3.2.8 Effects of camera angle 103
4.3.3 Validation using experimental data 104
4.4 Discussions 106
Chapter 5 Material characterization of human middle ear using machine-learning-based surrogate models 109
Preface 109
Overview 110
5.1 Introduction 111
5.2 Methods 113
5.2.1 Finite-element model 113
5.2.2 Uncertain model parameters and design of experiments 115

5.2.3 Machine-learning model 116
5.2.4 Parameter estimation 119
5.3 Results 123
5.3.1 Predictions of machine-learning models 123
5.3.2 Parameter estimation using combination of machine-learning models and Bayesian optimization 128
5.4 Discussions 135
Chapter 6 Mechanical effects of medical device attachment to human tympanic membrane: A finite-element analysis 140
Preface 140
Overview 141
6.1 Introduction 142
6.2 Methods 145
6.2.1 Baseline model 145
6.2.2 Medical-device model 146
6.3 Results 149
6.3.1 Baseline model results and comparison with experimental data 149
6.3.2 Effects of material properties of attached device 151
6.3.3 Effects of geometrical properties of attached device 159
6.3.4 Effects of location of device 164
6.3.5 Effects of device attachment on vibration patterns of TM 167
6.4 Discussions 168
Chapter 7 Acoustical effects of medical device attachment to human tympanic membrane: A finite-element analysis 175
Preface 175

Overview 176
7.1 Introduction 177
7.2 Methods 179
7.2.1 Geometry and mesh 179
7.2.1.1 Perforations in the model 182
7.2.1.2 Model of the medical device 183
7.2.2 Finite-element model 184
7.3 Results 186
7.3.1 Baseline model results 186
7.3.2 Effects of varying the size of perforations 191
7.3.3 Effects of varying the location of perforations 195
7.3.4 Vibrations patterns of the TM 196
7.3.5 Simultaneous mechanical and acoustical effects of medical devices 198
7.4 Discussions 202
Chapter 8 Conclusions and future work 206
8.1 Summary 206
8.2 Original contributions 206
8.3 Future work 209
References 212
Appendices 230
Appendix A Range of model parameters for Chapter 2 230
Appendix B Comparison of the stochastic FE model results with several experimental results in the literature for Chapter 2 232
Appendix C Range of model parameters for Chapter 3 233

List of Figures

Figure 1-1 – Overview of the human-ear anatomy (Source: Blausen.com staff [13]; the figure is available under the Creative Commons Attribution License (CC-BY)). 5

Figure 2-1 – 3D model of the middle ear. Constructed geometry from two different viewing angles (left and center) and mesh of the human middle-ear model (right).. 20

Figure 2-2 – Distribution of some of the uncertain model parameters and workflow of the stochastic FE analysis.. 26

Figure 2-3 – Stochastic frequency response function of the umbo displacement. 28

Figure 2-4 – Stochastic frequency response function of the stapes footplate displacement and the stochastic middle-ear transfer function. 30

Figure 2-5 – Violin plots and circular histograms for the amplitude and phase of the umbo and stapes footplate. 32

Figure 2-6 – Stochastic full-field vibration patterns of the TM. 35

Figure 2-7 – Stochastic full-field vibration phase of the TM. 36

Figure 3-1 – Workflow of the stochastic FE modelling and global sensitivity analysis. 50

Figure 3-2 – Quality (in terms of Q^2) of the surrogate models to represent the stochastic finite-element model of the middle ear. 51

Figure 3-3 – Percentage of the leave-one-out (LOO) error of the created PCEs with respect to the number of FE calculations used in the training set of PCEs at three frequencies F_{low} =708 Hz, F_{mid} =6.52 kHz, and F_{high} =9.74 kHz for the three quantities of interest (displacement amplitude of the umbo and stapes footplate and phase of the stapes footplate). 52

Figure 3-4 – Validation of PCE calculations against ground truth frequency responses obtained using the deterministic FE model. 53

Figure 3-5 – Sobol′ indices for the displacement amplitudes of the umbo and stapes footplate and displacement phase of the stapes footplate at F_{low} =708 Hz. 56

Figure 3-6 – First and total order Sobol′ indices for all three quantities of interest at F_{mid} =6.52 kHz. 58

Figure 3-7 – Sobol′ indices for all three quantities of interest at F_{high} =9.74 kHz. 60

Figure 3-8 – Column (a): maximum value of the total-order Sobol′ indices for the three quantities of interest among all frequencies in the range of 100 Hz to 10 kHz for which the value of Q^2 of the created PCE is greater than 0.9. The thin red lines show the total-order Sobol′ index of 0.02. Column (b):

maximum values of the second-order Sobol′ indices among the same frequencies in (a) (only the second-order Sobol′ indices greater than 0.005 are shown). 63
Figure 3-9 – Total-order Sobol′ indices for the displacement amplitude of the umbo. 64
Figure 3-10 – Total-order Sobol′ indices for the displacement amplitude of the stapes footplate.. 66
Figure 3-11 – Total-order Sobol′ indices for the stapes footplate displacement phase.. 67
Figure 3-12 – Displacement amplitude of the ossicles in the direction of the stapes footplate piston-like motion at the excitation frequency of 10 kHz. 68
Figure 4-1 – Flowchart of the proposed material characterization method. 77
Figure 4-2 – (a) Schematic diagram of the numerical grid used in the finite-difference method. The classical plate equation is applied to the yellow nodes that are located in the vibrating region indicated in blue, the green nodes are considered to be the boundaries of the moving plate and the red nodes are auxiliary nodes. (b) Visual explanation of the progression of the Bayesian optimization process represented by the value of the objective function for iterations 5, 20, 60, and 80 for estimation of the Young's modulus of a simply-supported square plate (discussed in section 4.3.1.1) using the measured displacement field..... 80
Figure 4-3 – (a) The analytically calculated harmonic response of a simply-supported square plate with known material properties (given in Table 4-1) excited with a harmonic pressure with a magnitude of 10 kPa and frequency of Ω=7.95 kHz. This displacement field was used as the input to our material characterization method and the error of the estimated Young's modulus was 0.01%. (b) The same analytically calculated harmonic response as in Panel (a) after application of white Gaussian noise with a signal to noise ratio of 10 dB. This noisy displacement field was also used as the input to the proposed material characterization method to study the estimation error in presence of the noise. The error of the estimated Young's modulus was 0.68%. (c) The minimum value of the objective function with respect to the number of evaluations of the objective function for material characterization of the simply-supported square plate: using noiseless data shown in panel (a) (blue line) and using noisy data shown in panel (b) (red line). 88
Figure 4-4 – The analytically calculated harmonic response of a clamped plate with known material properties (given in Table 4-1) excited with a harmonic pressure with a magnitude of 10 kPa. 91
Figure 4-5 – White Gaussian noise with a signal to noise ratio of 10 dB applied to the analytically calculated harmonic response of a clamped plate (Figure 4-4) with known material properties (given in Table 4-1) excited with a harmonic pressure with a magnitude of P=10 kPa.. 92

Figure 4-6 – Finite-element calculated harmonic displacement magnitude response of an elliptical plate inside a 10 cm × 10 cm square field of view (top: 3D and bottom: 2D projections)..... 94
Figure 4-7 – Finite-element calculated harmonic displacement magnitude response of a triangular domain inside a 10 cm × 10 cm square field of view (top: 3D and bottom: 2D projections)..... 95
Figure 4-8 – White Gaussian noise with a signal to noise ratio of 10 dB applied to the finite-element calculated harmonic displacement magnitude responses of the elliptical plate of Figure 4-6 and triangular plate of Figure 4-7..... 97
Figure 4-9 – Errors in the assumed value of thickness and Poisson's ratio used in the proposed material characterization method..... 101
Figure 4-10 – (a) Effect of grid resolution on the estimated Young's modulus for the elliptical plate of Figure 4-6. This study was performed to find the sensitivity of the estimation error to the mesh size. It can be observed that the estimation error is large for coarse meshes (for instance for a mesh with a size of 2.5×2.5 per cm, the estimation error is larger than 70%). However, the error rapidly drops by refining the mesh. (b) Runtime with respect to total number of nodes for the elliptical plate shown in Figure 4-6. Increasing the number of nodes results in an approximately linear increase in the runtime. (c) Error of the estimated Young's modulus with respect to the error in the viewing angle of the camera (α) for the elliptical plate of Figure 4-6.. 105
Figure 4-11 – (a) The digital holography system used in this work. The experimental setup consists of a speaker, a microphone, and an otoscope head which includes a camera and an object illumination component. (b) Experimental displacement magnitude normalized by the stimulus sound pressure at 4350 Hz of a thin copper plate obtained using the holography setup..... 106
Figure 5-1 – Workflow of the creation of ML models and parameter estimation..... 122
Figure 5-2 – Results of predictions of created ML models for the amplitude and phase of umbo.... 124
Figure 5-3 – Results of predictions of created ML models for the amplitude and phase of the stapes footplate..... 125
Figure 5-4 – Values of R^2 (for the amplitude) and MCD (for the phase) of the umbo and stapes footplate in the frequency range of 100 Hz to 10 kHz. 126
Figure 5-5 – The values of R^2 with respect to the size of the training dataset at three different frequencies: 100 Hz (low), 5 kHz (middle), and 10 kHz (high)..... 127
Figure 5-6 – ML model prediction results of the TM amplitude vibration pattern.. 129
Figure 5-7 – ML model prediction results of the TM phase vibration pattern.. 130

Figure 5-8 – Left: all sample nodes on the TM with the nodes that have values of feature importance of greater than 0.5 for the Young's modulus of SAL at 100 Hz shown in red (187 nodes). Right: all sample nodes on the TM with the nodes that have values of feature importance of greater than 0.5 for the Young's modulus of TM at 5 kHz shown in red (173 nodes) 133
Figure 5-9 – Best observed values of objective functions for the estimation the Young's modulus of the TM, Young's modulus of the SAL, and simultaneous estimation of the Young's modulus of TM and SAL with respect to the iteration number in the Bayesian optimization process. 137
Figure 6-1 – (a) Schematic of the baseline model (the middle-ear model without any medical devices attached to the TM). (b) Steps of creating the mesh of the medical device. In the first step, we chose the location of the base of the device on the mesh of the TM. 148
Figure 6-2 – The displacement amplitude and phase of the umbo and stapes footplate from the baseline model (the middle-ear model without any medical devices attached to the TM)..... 151
Figure 6-3 – Umbo displacement frequency response function of the model with medical devices attached to the TM. 153
Figure 6-4 – Stapes footplate displacement frequency response function of the model with medical devices attached to the TM. 155
Figure 6-5 – Comparison of the stapes footplate displacement results of the models with the rigid medical devices with the results of the models with deformable medical devices..... 158
Figure 6-6 – Comparison of the stapes footplate displacement results of the model with the full medical device attached to the anterior inferior quadrant of the TM with the results of the model in which the medical device is represented as a point mass..... 158
Figure 6-7 – Effects of changing the diameter of the device on the stapes footplate displacement amplitude and phase. 160
Figure 6-8 – Effects of changing the height of the device on the stapes footplate displacement amplitude and phase. 161
Figure 6-9 – Comparison of the results of the stapes footplate displacement of two devices with the same volume but different aspect ratios. 163
Figure 6-10 – Effects of variations of the location of the medical device on the stapes footplate displacement amplitude and phase.. 164

Figure 6-11 – Vibration patterns of the TM displacement amplitude without any medical devices attached to it (baseline) and with medical devices with different material properties attached to the anterior inferior quadrant.....168
Figure 6-12 – Phase patterns of the TM displacement without any medical devices attached to it (baseline) and with medical devices with different material properties attached to the anterior inferior quadrant......169
Figure 7-1 – (a) Reconstructed 3D models of the malleus, incus, and stapes from the "Theta" dataset in OpenEar library (left) and from our dataset (right). The size and morphological features obtained using both datasets are very similar to each other. The models of structures in the middle ear were created from segmentation of our dataset and the middle-ear cavity model was created by segmentations provided in the "Theta" dataset of OpenEar library. (b) The created meshes of the middle-ear structures and middle-ear cavity......180
Figure 7-2 – Frequency response curve of the umbo displacement normalized with respect to P_{TM}.. 187
Figure 7-3 – Frequency response curve of the stapes footplate displacement normalized with respect to P_{TM}.....189
Figure 7-4 – The pressure distribution inside the middle-ear cavity.. 191
Figure 7-5 – Effects of variations of perforation size on the stapes footplate responses.....193
Figure 7-6 – Pressure ratio P_{cav}/P_{TM} of the baseline model (intact TM) and models with perforations of different sizes (Hole 1, Hole 2, Hole 3, and Hole 4). 194
Figure 7-7 – Effects of variations of the location of the perforations on the stapes footplate responses. 196
Figure 7-8 – Effects of TM perforations on the full-field vibration amplitude pattern of the TM.....198
Figure 7-9 – Effects of TM perforations on the full-field vibration phase pattern of the TM.....199
Figure 7-10 – Amplitude ratio of the stapes footplate in the presence of the medical device and perforations.....200
Figure B – Comparison of the stochastic FE model results of the stapes footplate with several experimental results in the literature. ……..…..……..232

List of Tables

Table 2-1 – Material properties of the baseline model. 21
Table 2-2 – Values of skewness and kurtosis for the output distributions shown in Figure 2-5. 33
Table 4-1 – Material properties used in analytical and some of the FEM simulations to validate the proposed holography-based material characterizing method. 89
Table 4-2 – Results of the proposed material characterization method estimated from noiseless (Figure 4-4) and noisy data (SNR=10 dB, Figure 4-5) of a clamped square plate with the true Young's modulus of 200 GPa. 93
Table 4-3 – Estimated Young's modulus for elliptical and triangular plates with the true Young's moduli of 200 GPa using the noiseless displacement fields shown in Figure 4-6 and Figure 4-7. 96
Table 4-4 – Estimated Young's modulus for elliptical and triangular plates with the true Young's moduli of 200 GPa using displacement fields obtained by applying non-Gaussian noise to the displacement fields shown in Figure 4-6 and Figure 4-7. 98
Table 4-5 – Estimated Young's modulus for the triangular plate after increasing the original thickness (0.1 mm) of the plate of Figure 4-7 to study the errors of the proposed material characterization method for two thick plates with thicknesses of 5 and 10 mm. 102
Table 4-6 – Effects of errors in boundary conditions of the input displacement field on the estimated Young's modulus for the triangular plate. 102
Table 5-1 – Range of parameters considered in creating ML models. 116
Table 5-2 – Ture and estimated values and estimation error of E_{SAL} 132
Table 5-3 – True and estimated values and estimation error of E_{TM}. 134
Table 5-4 – True and estimated values and estimation error of the E_{TM} and E_{SAL} 136
Table 6-1 – Material properties of PDMS, Teflon, and stainless steel. 149
Table 6-2 – Base area and volume of the medical devices used for results reported in Figure 6-10. 165
Table 6-3 – Mean of the absolute values of the amplitude ratio among all frequencies in the range of 100 Hz to 10 kHz 166
Table 7-1 – Surface area of the holes on the TM. PS, AS, AI, and PI stand for posterior-superior, anterior-superior, anterior-inferior, and posterior-inferior quadrants of the TM, respectively. 184
Table A – Range of the uncertain parameters used in stochastic FE model. 230
Table C – Range of variation of model parameters and the values used for generating results in column (b) of Figure 3-4 233

Chapter 1
Introduction

1.1 Motivation

The middle ear plays a vital role in the hearing process by conducting sound energy, which enters through the ear canal, to the inner ear. In fact, the middle ear facilitates the effective transfer of acoustic energy from the low-impedance air to the high-impedance inner ear fluid by acting like an impedance transformer [1]. Investigating the biomechanics of the middle ear helps us to improve our fundamental knowledge of the hearing process and can provide new insights for developing new diagnostic and treatment methods for middle ear pathologies. The core motivation of the current study has been to explore untouched research areas, related to the biomechanics of the middle ear, that can assist future researchers in the development of diagnostic and treatment methods for middle-ear pathologies. In what follows, we introduce these research areas and our specific motivation for each one of them.

One of the common procedures for the treatment of several middle-ear pathologies is using implantable medical devices. Implantable medical devices can be used for a variety of applications. For instance, a common treatment method for otitis media, a group of inflammatory diseases that can happen in the middle ear and is very common in children [2], is placing a specific medical device called “tympanostomy tube”. Other examples of implantable middle-ear medical devices include different types of transducers that are used to compensate for the loss of functionality of a particular structure in the middle ear [3]. Studying the mechanical and acoustical effects of these medical devices on sound conduction in the middle ear enables the optimization of similar devices in the future. Although currently there are some studies on the effects of attachment of some types of middle-ear implants on middle-ear vibrations [4]–[6], there are very few studies that have focused on the attachment of medical devices to the tympanic membrane (TM). Analyzing the mechanical and acoustical effects of implantable hearing devices attached to the TM was one of the motivations for this study. Such a study can facilitate the optimal design of future medical devices so that their attachment results in the least adverse effect on sound conduction in the middle ear.

Finite-element (FE) models of the middle ear are powerful tools that can be employed in diagnostic methods and in the design of implantable medical devices. Although in the last forty years, models of middle-ear have been widely used for simulating the biomechanics of middle-ear, still these models are not reliable enough to be employed in diagnostic and therapeutic approaches [7]. One reason for this is that most of these models are deterministic and do not consider the effects of intrinsic inter-individual variabilities, which are inseparable parts of biological structures. These variabilities can be seen for example in the measurements of umbo and stapes footplate motions in the populations of middle ears (e.g., Aibara et al. and Whittemore et al. [8], [9]). These inter-individual variabilities lead to uncertainties in the values of mechanical and geometrical parameters of the middle-ear models. In order to be able to use middle-ear models reliably, it is vital to have a clear understanding of the effects of these uncertainties in the parameters of middle-ear models on the uncertainty in the vibrations of middle-ear structures. Providing a systematic analysis of the effects of these uncertainties on the middle ear vibration outputs was another motivation for the current study.

Additionally, the middle ear includes several structures and even if we consider the simplest linear elastic assumption for all these structures, we end up having tens of model parameters. The global impact of the mechanical and geometrical properties of most structures of the middle ear on its vibrations and also the interactions among these parameters are still unknown. Understanding the effects of each parameter on the sound conduction in the middle ear can ease the interpretation of diagnostic results [10], and can significantly reduce the time required for tuning future patient-specific models of the middle ear. Studying the effects of variations of parameters in the middle ear to provide a clear-cut understanding of the importance of each of the parameters was another motivation for this study.

Along with the previously mentioned items, another motivation for the current thesis was to propose and develop novel non-invasive diagnostic methods that can be eventually used for detecting middle-ear pathologies based on the estimations of the mechanical properties of middle-ear structures. The mechanical properties of tissues undergo changes when the tissue is diseased [11], and thus can be used as a diagnostic index for different diseases. In the area

of middle-ear mechanics, there is a growing need for such non-invasive diagnostic methods that can be eventually used in clinical applications upon further development.

1.2 Objectives

This thesis covers three board categories. In this section, we list these categories and the specific objectives for each of them.

The first part of this study is an investigation on the effects of uncertainties in the middle ear (Chapters 2 and 3). The specific objectives for this part are:

1. To Study the effects of uncertainties in the values of mechanical and geometrical parameters of different structures in the middle-ear models on sound conduction in the middle ear.

2. To analyze the global impact of mechanical and geometrical parameters of different structures in the middle-ear models on their vibrations in order to find the most impactful parameters in the middle ear. Also, to study and find the interactions among different parameters in the middle ear.

The second part of this study aims to propose a novel method for material characterization of the middle-ear structures (Chapters 4 and 5). The specific objectives of this part are:

3. To propose and develop a novel method that uses full-field harmonic vibration patterns of 2D thin planar structures to estimate their material properties.

4. To propose and develop a method for fast estimation of the most influential mechanical parameters of the middle ear using full-field harmonic vibration pattern of the TM.

The third part of this study is dedicated to analyzing the mechanical and acoustical effects of medical devices attached to the TM on middle-ear vibrations (Chapters 6 and 7). The specific objectives for this part are as follows:

5. To investigate the effects of changes in the mechanical characteristics of the middle ear as a result of the attachment of medical devices to the TM in silico.

6. To investigate the effects of changes in the acoustical characteristics of the middle ear as a result of the attachment of medical devices to the TM in silico.

1.3 Summary of thesis

In the next sections of this chapter, a brief introduction to the anatomy of the ear as well as a brief literature review of the modeling and experimental works on the biomechanics of the middle ear are presented. In Chapter 2, stochastic modelling techniques are employed to investigate the effects of uncertainties on middle-ear vibrations. In Chapter 3, a part of the simulation results of Chapter 2 is used to perform a global sensitivity analysis of the middle ear parameters. Chapter 4, presents a method for estimation of the Young's modulus of thin planar structures using full-field vibration data. In Chapter 5, a method similar to one proposed in Chapter 4 is implemented for fast estimation of mechanical properties of middle-ear structures using full-field harmonic vibration of the TM. Chapter 6, investigates the mechanical effects of medical devices attached to the TM, and Chapter 7 presents the study on the acoustical effects of medical devices attached to the TM. In Chapter 8, conclusions and suggestions for future works are presented.

1.4 Anatomy

The human auditory system consists of different complicated organs that work together to convert sound waves into nerve signals. The whole process makes us able to hear sounds and distinguish them in a wide frequency range. The structures in our auditory system can be grouped into three main parts: the outer ear, middle ear, and inner ear. In this section, we present a brief introduction to the anatomy of the ear. A more detailed explanation of the anatomy and physiology of the ear can be found in [12]. Figure 1-1 presents the anatomy of the human ear [13].

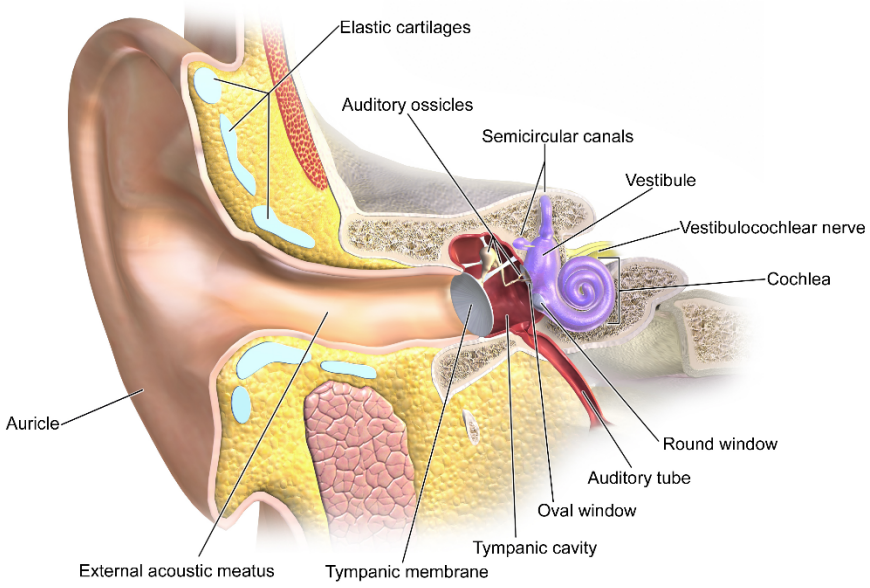


Figure 1-1 – Overview of the human-ear anatomy (Source: Blausen.com staff [13]*; the figure is available under the Creative Commons Attribution License (CC-BY)[2]). The sound pressure enters the ear canal and vibrates the TM. The vibrations of the TM are transmitted to the oval window which is located at the base of the cochlea through three ossicles. The sound waves are then transformed into electric signals in the cochlea.*

1.4.1 Outer ear

The external part of the ear is called the outer ear that includes the pinna (Auricle), which is the visible part of the ear, and the ear canal. Pinna acts as a funnel that directs the sound waves into the ear canal. The sound waves are transmitted to the eardrum through the ear canal.

1.4.2 Middle ear

The middle-ear consists of five main parts: the eardrum or tympanic membrane, the middle-ear cavity, and three tiny ossicles which are called: the malleus, incus, and stapes. The main

[2] Creative Commons Attribution 3.0 Unported (CC BY 3.0), https://creativecommons.org/licenses/by/3.0/deed.en

purpose of the middle-ear is to transmit sound pressure, which enters through the ear canal, to the inner-ear. The tympanic membrane and three ossicles are shown in Figure 1-1.

TM is a thin layer of tissue and is usually divided into two areas: the pars flaccida and pars tensa. The pars flaccida is located in the superior section of the TM and is smaller than pars tensa. TM is situated with a fibrocartilaginous ring which is called the tympanic ring. The central part of the pars tensa is connected to malleus through umbo which is the part of the TM that is drawn inward and has a tent shape. The part of the malleus connected to the TM is called the manubrium.

The sound pressure is transmitted to the malleus from the tympanic membrane. It then makes the incus and stapes move and this movement conveys the sound energy to the cochlea. The stapes footplate is connected to the inner ear through the oval window.

The ossicles are placed in an air-filled area called the middle-ear cavity which is separated from the external ear by the TM and from the internal ear by the lateral wall of the inner ear which is called the medial wall. Also, there is a canal called the eustachian tube that connects the middle ear to the upper part of the throat behind the nose (nasopharynx). The eustachian tube is responsible for equalizing the pressure between the outside air and the air inside the middle-ear cavity.

1.4.3 Inner ear

The inner ear is comprised of two main parts which are the cochlea and vestibular system. The cochlea is a snail-shaped structure that consists of three fluid-filled canals. These canals are called scala vestibuli, scala media, and scala tympani. The excitations of the oval window make waves in the fluids in the cochlea canals. These mechanical waves are transmitted into the electrical signals in an organ called the organ of Corti.

As mentioned before, the cochlea is connected to the stapes through the oval window which is a membrane covering the entrance of the cochlea. The round window is also located below the oval window. The round window moves in the opposite direction of the oval window and makes it possible for the fluid inside the cochlea to move.

The vestibular system has a different application and is responsible for the sense of balance. The details of the mechanisms of the cochlea and vestibular system are not of interest of the current thesis.

1.5 Literature review

In this section, we present a brief literature review in both areas of modelling and experimental measurements of the middle ear. The introductory sections of Chapter 2 to Chapter 7 include a more detailed literature review related to the specific subjects of those chapters.

1.5.1 Modelling of middle-ear mechanics

Early models of the middle ear were lumped-parameter models. In these models, the variables are only functions of time and not spatial coordinates. Onchi was among the first researchers who put an effort to create a circuit model of the middle ear in 1949 [14]. In 1962, Zwislocki used experimental measurements to present a lumped electrical circuit model of the middle ear [15]. One of the aims of the study was to quantitatively express the acoustic behaviours of the middle ear using circuit elements instead of using complicated algebraic equations. Some other researchers also used more complicated lumped-parameter models of the middle ear in their studies. Hudde and Weistenhöfer provided a 3D circuit model for the middle ear [16]. They were searching for a method that could provide the simplicity and speed of circuit models and be more accurate than them.

Most of the studies with lumped-parameter models of the middle ear are based on the frequency domain. However, some researchers investigated these models in the time domain as well. Parent and Allen provided a time-domain model of the cat TM and ossicular chain [17]. Their main interest was to capture the spreading of the waves on the TM surface.

Although the lumped-parameter models can be simple and fast, they do not result in good accuracy in many cases as they are not able to consider the complex morphological features and material properties [18]. Thus, many researchers tried to consider the models based on continuum mechanics to simulate the behaviours of middle-ear structures.

One of the most prominent continuum mechanics-based techniques used in the study of middle-ear mechanics is the finite-element method. In this method, the continuous boundary is discretized and the response distribution is evaluated on the whole domain of interest. One of the benefits of FE method is that it is capable to deal with sophisticated geometries and different material behaviours and boundary conditions. More details about FE method can be found in related FE textbooks (e.g., [19], [20]).

The first FE model of the middle ear was presented by Funnel and Laszlo in 1978 [21]. One of their aims was to present a model that includes the effects of the 3D conical shape of the TM and they presented a model that was validated at low frequencies (below 2 kHz). They applied linear vibrations assumptions and validated their model with experimental laser holography data of the cat TM. In 1983, Funnell calculated undamped natural frequencies and mode shapes of the cat eardrum with their FE model [22]. In the same work, they also studied the effects of changing several material and geometrical parameters of their model on the natural frequencies. In both of these works, the geometry of the cat TM was approximated by circular arcs. Funnel et al. added the effects of damping to their model of the cat eardrum later in 1987 [23]. They represented the damping by both mass and stiffness proportional terms and simulated the dynamic damped forced response of the TM. By comparing the model results and experimental measurement results, they concluded that the mass proportional damping can fairly represent the experimental data. In 1990, Williams and Lesser presented an FE model of decoupled human tympanic membrane to study its natural frequencies [24]. Later in 1991, Lesser et al. presented a 2D FE model of the human middle-ear joints to study displacement and stress levels in the reconstructed ossicular chain [25]. However, previous studies had shown that the 3D shapes of the ossicles can have some major effects on the FE model results [26]. In 1992, Wada et al. presented a 3D model of the human middle ear that included the ossicles and TM [27]. They used this FE model and compared its results with experimental measurement results to determine the boundary conditions and material properties of the middle ear. In their model, the cochlear load was modelled as some lumped stiffness attached to the stapes. Ladak and Funnell developed 3D FE models of the cat middle ear to study both

normal and surgically repaired ears [28]. They modelled the stapes footplate as a thin plate with a thickened rim and the cochlear load as springs attached to the stapes footplate. They studied the effects of adding prostheses to repair the discontinuity in the ossicular chain.

When it comes to FE modelling, one of the main aspects is how to generate an accurate geometry and mesh of the middle ear. Due to the complicated morphological features of the structures of the middle ear, reconstruction of the geometry and creating a high-quality mesh can be challenging. Different techniques have been implemented by researchers for this aim. In 1996, Funnel et al. utilized moiré shape measurements [29] to increase the accuracy of their finite-element TM model [30]. They employed this measurement technique to find the shape of the TM with higher accuracy than what existed in the literature at that time. They used this method for the reconstruction of four different cat eardrums and compared their FE model results with each other. The results of these simulations and previous studies revealed that the 3D shape of the TM has considerable effects on the accuracy of middle-ear models [31]. The moiré technique can be used for the reconstruction of the TM, but it is not useful for creating models of other parts of the middle ear including ossicles. This is due to the fact that this method does not have the ability to measure the volumetric geometry of objects [18]. In the work of Daniel et al., the moiré shape measurement was used to precisely define the shape of TM, while histological serial sections and high-resolution magnetic resonance microscopy were employed to reconstruct the other parts of the middle ear for creating the FE model of the human middle-ear [32]. Another useful technique for shape reconstruction of the middle ear is by using micro-computed tomography (μCT) imaging data [33]. Kelly et al. used μCT and nuclear magnetic resonance imaging to reconstruct the geometries of the TM and ossicles [34]. They used their FE model to study the effects of total and partial ossicular replacement prostheses. Mikhael et al. scanned the human temporal bone using x-ray μCT and segmented the detailed middle-ear structures [35]. They used their segmented geometries to create an FE model and compared the static results of their model with low-frequency laser Doppler vibrometry (LDV) measurements performed on the same temporal bone. Elkhouri et al. used μCT, magnetic resonance, and histological sections to create an FE model of the gerbil middle

ear at frequencies below 1 kHz [36]. They also performed a sensitivity analysis to find the effects of various parameters on the FE model results. They assumed linear, isotropic, and elastic material properties for all structures in their model and used experimental data to validate their model. Maftoon et al. used a 3D geometry that was reconstructed using a combination of μCT and histological sections in their FE model of the gerbil middle ear [37].

One of the main aspects of modelling any biological structure is whether to consider nonlinearities in the model or not. It is known that the middle ear behaves linearly in regular hearing tasks [31]. Having that said, the response of the middle ear to very loud sounds (such as explosions) is nonlinear. Ladak et al. studied the effects of geometric nonlinearity in their FE model of the cat TM [38]. They provided a model for pressures in the ranges of the pressure values used in clinical tympanometry (up to ±2.2 kPa). They found that the largest pars tensa strains were about 2% which means that the linearized material model is a reasonable approximation. However, they stated that for pressures higher than what they studied, considering material nonlinearity may be necessary. Also, they observed that strain variations are larger for the pars flaccida. Some other researchers tried to implement a combination of geometrical and material nonlinearities. Wang et al. provided an FE model of the human ear to study the static and dynamic behaviour of the middle ear [39]. They combined geometric nonlinearity with the hyperelastic Mooney-Rivlin material model. In another study, Qi et al. presented a 3D FE model of a 22-day-old newborn ear canal [40]. They used hyperplastic constitutive law and used a generalization of neo-Hookean and Mooney-Rivlin methods which is called the polynomial method. They evaluated the effects of different material parameters on their model. Ihrle et al. presented a nonlinear elastic multibody system model of the human middle ear that can describe it based on a low number of nonlinear equations [41]. They compared the results of the reduced model with FE model results. Motallebzadeh et al. considered both viscoelasticity and nonlinearity of the TM and presented a finite-element model that included both of these features [42]. They used one of the approaches they had suggested in an earlier study by Charlebois et al. [43].

Oftentimes, TM and middle-ear structures are assumed to be isotropic, however, some researchers modelled some of these structures as orthotropic materials. Gan et al. provided a 3D finite-element model of the middle ear and considered the TM as an orthotropic material while considering the ossicles as isotropic materials [44]. They considered the Rayleigh damping for all materials in their model as well. Fay et al. considered both isotropic and orthotropic models of human TM in their work [45]. Tuck-Lee et al. presented a finite-element model that included a layered composite model of the cat eardrum [46]. They generated their model from cadaver anatomy via μCT imaging to investigate the role of collagen fiber sublayers of the TM. O'Connor et al. presented the results of models with both isotropic and orthotropic material properties for the TM [10]. They observed that for some combinations of model parameters, isotropic model responses are very similar to orthotropic model responses. Their results suggest that even when the isotropic models are used for simplicity, accurate results comparable to experimental measurements can be generated if the value of the Young's modulus of the TM is chosen correctly.

One of the aspects that should be considered in the modelling of the middle ear is the effects of the cochlea. Many middle-ear FE models in the literature do not contain the detailed model of the cochlea and the effects of the cochlea are represented in other ways. In the early FE models (e.g., [22]), there was no explicit model representing the cochlea and the effects of the cochlea were distributed in other model parameters such as the stiffness of the TM. As mentioned earlier, in 1992, Wada et al. represented the cochlear load by attaching springs to the stapes footplate [27]. Some other researchers used dampers to model cochlear load as the cochlea damps the middle-ear vibrations. In 2002, Koike et al. proposed using dampers instead of springs to model the cochlear load and to reproduce complex ossicular chain movements [47]. They validated their model by comparing the vibrations of the TM and ossicles with the experimental data. Gan et al. added the effects of the cochlea to their model by considering dashpots with a specific mass that was calculated from values reported values for the impedance and volume of the cochlear fluid [48]. However, some of middle-ear models in the literature also included the cochlea. Gan et al. provided a 3D finite-element model of the human

ear that consists of the external ear, middle ear, and cochlea [49]. They implemented an acoustic-mechanical analysis in their model which included the ear canal, the TM, the ossicles, the middle-ear cavity, the liquid inside the cochlea, and the cochlea structure itself.

The acoustic effects of the middle-ear cavity and ear canal are also studied in some of the models in the literature. Prendergast et al. included the ear canal in their model [50]. They considered cases with and without an ossicular prosthesis and studied the translational and rotational motions of the stapes footplate. The FE model of Koike et al. also consisted of the external auditory meatus as well as the middle-ear cavity [47]. They compared the vibration modes of open and closed cavity models and observed that the inclusion middle-ear cavity does not have significant effects on the vibration mode of the TM. The model of Gan et al. also included the middle-ear cavity and ear canal [48]. Motallebzadeh et al. presented a model of the human newborn middle ear that included both the middle-ear cavity and ear canal [51].

Middle-ear models have also been used for the purpose of characterization of the mechanical properties of the middle ear. Aernouts and Dirckx estimated linear and nonlinear elastic properties of the gerbil pars flaccida by inverse analysis of the *in situ* static pressure inflation experiment [52]. They used the Veronda-Westmann hyperelastic model for the nonlinear part of their work and found the parameters with their FE model. In another work, Aernouts et al. estimated the viscoelastic and elastic properties of the human TM using the indentation test *in situ* [53]. For this aim, they optimized their FE model parameters to be able to provide results close to experimental measurement results. In another study, Greef et al. used FE modelling along with experimental measurements to estimate the viscous damping of the TM [54].

Some researchers used FE models to run sensitivity analyses to identify the most influential parameters in the middle ear. Most of the works in this area used local sensitivity analysis methods that are able to show the importance of different parameters using a one-at-a-time technique. One-at-a-time sensitivity analysis methods are not able to show the interactions of the model parameters with one another. Maftoon et al. performed a one-at-a-time sensitivity analysis on the gerbil middle-ear model [37]. O'Connor et al. used their FE model of the human middle ear to study the effects of material properties of the TM on sound conduction in the

middle ear [10]. Motallebzadeh et al. also employed both one-at-a-time and Morris sensitivity analysis methods to investigate the effects of varying different parameters in their human newborn FE model [55].

Some researchers have also used FE models to simulate diseased and post-procedure middle-ear conditions and some of these works (such as studies on the effects of adding a prosthesis) were introduced in the previous sections. Huber et al. studied the effects of partial mallear fixation and the conductive hearing loss resulting from it [56]. They used both FE results and experimental data measured using laser Doppler interferometry in their work. In another study, Dai et al. studied fixation and detachment of both superior mallear ligament and anterior mallear ligament in the human middle ear [57]. They used two laser Doppler vibrometers to measure the motions of the TM and stapes footplate in their experiments. They also used a 3D FE model in which ligament fixations and detachments were considered. They discussed the effects of fixation and detachment of the ligaments on the motions of the TM and stapes footplate. Gan and Wang used FE modelling to simulate the otitis media with effusion [58]. In their work, they studied the effects of fluid accumulation in the middle ear on vibrations of middle-ear structures by considering various fluid levels in the middle ear. In another work, Lee et al. used their FE model to study the effects of TM reconstruction for three different sizes of TM perforations [59]. Their main purpose was to find the optimal graft thickness for cartilage myringoplasty. In another work, Gan et al. presented a 3D finite-element model of the human ear canal, middle ear, and cochlea to study the effects of TM perforations on hearing and sound conduction inside the middle ear [60]. In their FE model, they created two perforations in the inferior site of the TM and calculated the vibrations of the TM and stapes in the presence of these perforations. They also created similar perforations in the TMs of human temporal bones in order to measure the same parameters using LDV and compare the results. Recently, Sackmann et al. used FE modelling to simulate and predict several pathologies such as malleus fixation and otosclerosis [61].

More detailed reviews on the modelling studies in the areas of the biomechanics of the middle ear and TM can be found in [31], [62].

1.5.2 Experimental measurements of vibrations of middle ear

In 1940s, Békésy used a capacitive probe to measure the motion of multiple points on the TM and study the vibration pattern on the TM [63]. He concluded that at least at frequencies below 2 kHz, the TM motion can be described as a hinged plated movement [53], [64]. In 1972, Khanna and Tonndorf used time-averaged holography to measure TM vibration patterns in cadaveric human and cat ears [64]. They stated that the small size of the TM, its low stiffness, and its transparency cause technical difficulties in these measurements. They captured time-averaged holograms at different frequencies in the range of 600-6000 Hz. They found the iso-amplitude regions using their measurement technique and observed that even at low frequencies, the motion of the TM cannot be described as a stiff surface as Békésy suggested. In 1980, Løkberg et al.used the time-averaged holography method to study the vibration patterns of human TM [65]. One of the drawbacks of the time-average holograms is that they cannot provide any information about the phase [18].

Alongside the time-averaged holography technique, many researchers also used laser Doppler vibrometry to study the motions in the middle ear. LDV can provide more accurate measurements of the amplitude and phase in comparison to time-averaged holographic techniques [26]. In 1981, Buunen and Vlaming used LDV method to measure malleus vibrations in cat ears [66]. Later in 1999, Rosowski et al. used LDV to measure the stapes vibrations in the gerbil middle ear [67]. In 2000, Voss et al. used LDV to measure stapes footplate velocity to study the acoustic and mechanical responses of human cadaver ears [68]. Rosowski and Lee measured the effects of static pressure on the sensitivity of gerbil malleus and pars tensa to sound using LDV [69]. They performed their measurements before and after immobilizing the pars flaccida. Maftoon et al. used the LDV to measure the closed cavity vibration responses of the gerbil TM to audio frequency sine sweeps [70]. In another work, Maftoon et al. studied the effects of opening the middle-ear cavity on the motions of the gerbil TM using LDV measurements [71].

LDV can give us the vibration data at specific points on the vibrating structure. However, usually, it is not possible to capture the high-spatial-resolution vibration response of the whole

domain using this technique. Recently, researchers developed optoelectronic stroboscopic holography vibrometry to be able to capture vibration responses (including both amplitude and phase) of the TM with a high spatial resolution. Flores-Moreno et al. used the advanced stroboscopic holography method to capture nano-displacements of the tympanic membrane [72]. Khaleghi et al. developed an optoelectronic holographic system to capture the 3D vibration patterns of human TM [73]. Cheng et al. used the stroboscopic holography measurement to study the vibrations of the human TM surface excited by forward and reverse stimulation [74].

Chapter 2

Inaccuracies of deterministic finite-element models of human middle ear revealed by stochastic modelling

Preface

In this chapter, we present the details of generating mesh and creating our FE model of middle ear (with an open cavity) and compare the model results with experimental measurement results in the literature. We then use stochastic modelling techniques to study the effects of uncertainties and inter-individual variabilities in all mechanical parameters of the middle ear and in the thickness of the TM on middle-ear vibrations. Parts of the stochastic FE model results presented in this chapter are used to generate surrogate models for the purpose of global sensitivity analysis in Chapter 3.

Overview

For over forty years finite-element models of the mechanics of the middle ear have been mostly deterministic in nature. Deterministic models do not take into account the effects of inter-individual variabilities on middle-ear parameters. We present a stochastic finite-element model of the human middle ear that uses variability in the model parameters to investigate the uncertainty in the model outputs (umbo, stapes, and tympanic-membrane displacements). We demonstrate: (1) uncertainties in the model parameters can be magnified by more than three times in the umbo and stapes footplate responses at frequencies above 2 kHz; (2) middle-ear models are biased and they distort the output distributions; and (3) with increased frequency, the highly-uncertain regions spatially spread out on the tympanic membrane surface. Our results assert that we should be mindful when using deterministic finite-element middle-ear models for critical tasks such as novel device developments and diagnosis.

2.1 Introduction

The middle ear plays a vital role in our hearing process by converting acoustic energy from the environment to mechanical vibrations and conducting them to the inner ear. Many studies have used different methods to model middle-ear mechanics in order to improve our fundamental understanding of the hearing process [37], [48], [68], [75]–[77]. Middle-ear models can be helpful for other purposes such as predicting the hearing loss from middle ear pathologies and injuries, simulating surgeries, and developing and advancing diagnostic and treatment methods.

Different approaches for modelling middle-ear mechanics were reviewed elsewhere [31]. The finite-element method is a powerful continuum-mechanics-based method that has been extensively used to model middle-ear mechanics starting with the pioneering work of Funnell and Laszlo [21]. The FE method can deal with complex geometries and different material properties and boundary conditions.

In order to obtain reliable results from an FE model, realistic mechanical properties of different structures of the middle ear should be known. Several studies attempted to identify the mechanical properties of some of the structures in the middle ear [54], [78]–[83]. For instance, laser Doppler vibrometry, stroboscopic holography, and FE modelling were used to estimate the viscoelastic properties of the human TM [54]. Also, indentation measurements and inverse FE method were used to estimate the quasi-static Young's modulus of the human TM [78]. Recently, a Bayesian inverse method was proposed that can be used to find the material properties of thin structures including the TM [79]. A review of the material characterization of the TM can be found elsewhere [62].

The mechanical/geometrical properties of middle-ear structures have intrinsic inter-individual variability that can be taken into account with stochastic uncertainties [84]. Indeed, differences observed in physiological data from different individuals (e.g., the normative study by Whittemore et al. [8]) can be attributed to the probabilistic distribution of the morphological features and mechanical properties of the middle-ear structures among individuals. Since the

first FE model of the middle ear in 1978 [21], most FE middle-ear models in the literature were deterministic and few systematically considered the effects of these uncertainties in the model parameters on its predictions. In the present chapter, we developed a stochastic FE model of the human middle ear to investigate the effects of different levels of natural variability in the model parameters on its outputs.

2.2 Materials and methods

2.2.1 Geometry, model components, and mesh

The 3D geometry was created based on the segmentation of μCT image datasets of a 73-year-old male cadaver temporal bone that included 1024×1012×1014 cubic voxels with a voxel size of 18.0828 μm. The scan was done with Xradia MicroXCT-200 at 90 kV and 8W. The segmentation process and meshing were done in 3D Slicer (www.slicer.org) software (version 4.11.20200930) [85]. After finalizing segmenting all parts, we used the Segment Mesher toolbox of Slicer for creating the mesh. We used Cleaver2 (www.sci.utah.edu/cibc-software/cleaver.html) meshing library for creating a conformal volumetric mesh for all parts of the model. A sizing field was created manually and was modified several times in order to create the desired mesh that consists of coarse elements in the regions where no considerable deformations are expected (i.e., bones) and fine elements in other regions. For the TM only, the generated volumetric mesh was converted to a surface mesh and only the medial section of the mesh (which is connected to manubrium) was used in the FE model. Thus, our model had volumetric mesh for all components in the middle ear except the TM for which we had surface mesh. The details about the number of elements will be provided later in this section.

The model included the TM, ossicles, anterior mallear ligament (AML), lateral mallear ligament (LML), incudostapedial and incudomallear joints (IMJ and ISJ), superior mallear ligament (SML), stapedial annular ligament (SAL), posterior incudal ligament (PIL), and manubrial fold. Tensor tympani tendon and stapedial tendon were not included in the model as the model was validated using ex vivo human data. Also, our model does not include the

middle ear cavity. The geometry and mesh of the middle-ear model are shown in Figure 2-1. In the following, we discuss the motions of the anatomical landmarks highlighted in this figure.

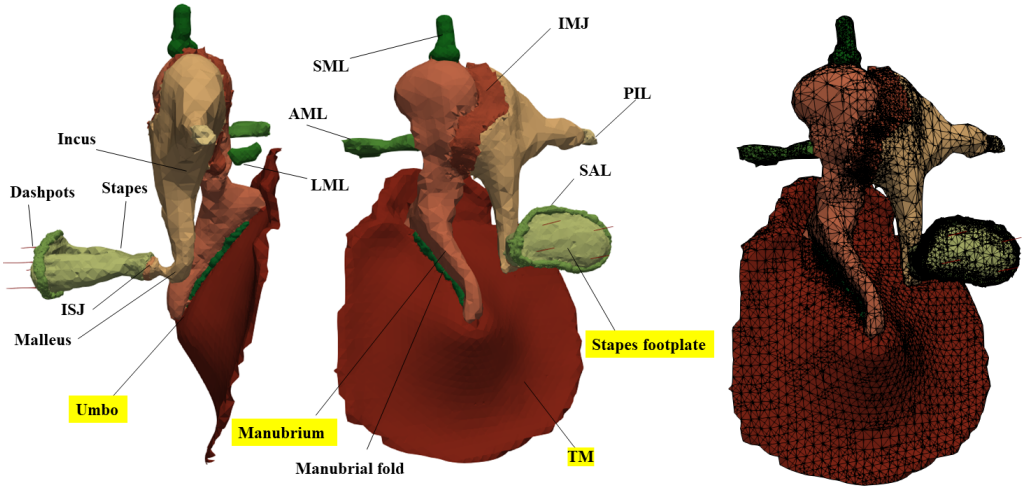


Figure 2-1 – 3D model of the middle ear. Constructed geometry from two different viewing angles (left and center) and mesh of the human middle-ear model (right). This model was used in our stochastic FE analysis and the motions of the highlighted structures are discussed in this study.

2.2.2 Deterministic FE modelling

The material properties of the baseline model are presented in the Table 2-1. We assumed all materials to be isotropic and elastic [37]. Besides, we considered nearly incompressible material properties (Poisson's ratio of 0.49) for all soft tissues [37]. For the ossicles, the value of Poisson's ratio was set to be 0.3 [48]. Moreover, the values of the Young's modulus of the TM and SAL reported in Table 2-1 were chosen to be in the range of the values reported in the literature [62], [80]. We used Rayleigh damping considering stiffness-proportional damping for all structures except for the TM, and manubrial fold [47], [54]. In Table 2-1, α_1 and α_2 are the Rayleigh-damping coefficients of mass and stiffness matrices, respectively.

Table 2-1 – Material properties of the baseline model.

Structure	**E (MPa)**	**density (kg/ m^3)**	**Poisson's ratio**	**α_1 (1/s)**	**α_2 (s)**
TM	12	1200 [54]	0.49	700	4×10^{-6}
Malleus	14000 [10]	2390 [10]	0.3	0	4×10^{-7}
Incus	14000 [10]	2150 [10]	0.3	0	4×10^{-7}
Stapes	14000 [10]	2200 [10]	0.3	0	4×10^{-7}
IMJ	30 [10]	1100 [10]	0.49	0	13×10^{-5}
ISJ	30 [10]	1100 [10]	0.49	0	13×10^{-5}
SAL	1.4	1200 [10]	0.49	0	13×10^{-5}
PIL	2 [10]	1200 [10]	0.49	0	13×10^{-5}
LML	2 [10]	1200 [10]	0.49	0	13×10^{-5}
Manubrial fold	1.2 [54]	1200 [54]	0.49	700	4×10^{-6}
SML	4.9 [48]	1200 [86]	0.49	0	13×10^{-5}
AML	2 [10]	1200 [10]	0.49	0	13×10^{-5}

For modelling the cochlear load, we considered a cochlear impedance of 20 GΩ which is the same value used by Gan et al. [48]. In our model, the surface area of the stapes footplate was measured to be 3.6 mm^2 which is also in the range reported by Motallebzadeh et al. [55]. From these values, we calculated a viscous damping coefficient of 0.26 Ns/m that we uniformly distributed to four dashpots attached to the stapes footplate and in the direction parallel to the piston-like motion [37]. Using dashpots to model the cochlear load is a common approach in the literature of FE modelling of the middle ear [37], [47], [48]. The thickness of the TM was assumed to be uniform and it was considered to be 74 μm which is the same as the value used by Gan et al. [48]. The average TM thickness values used in most models in the literature are also close to this value (74 μm) [87]. The references for the values of the Young's modulus and density of the model components are listed in Table 2-1. In addition to these a priori

material properties, we determined the Rayleigh damping coefficients of all the middle-ear structures by manually adjusting them to closely replicate the experimental measurements of Voss et al. [68].

To excite the model, we applied uniform pressure (with the amplitude of 1 Pa) to the entire TM area laterally. The TM annulus was considered to be fully clamped [53]. Also, the ligaments (AML, LML, SML, PIL, and SAL) were considered to be fixed at their distal ends where they normally connect to the wall of the middle-ear cavity. For all simulations except the full-field vibration patterns, we performed a transient dynamic analysis with a uniform pressure step function as the input [37] and used the implicit Newmark-β scheme [88]. In order to have an unconditionally stable solution, we chose values of β and γ in the Newmark-β scheme to be 0.25 and 0.5, respectively [37]. To obtain the displacement frequency response function, we found the impulse response by differentiating the step response (with respect to time) and then used the fast Fourier transform to construct the frequency response function. The full-field vibration patterns were obtained using harmonic vibration analysis. The Code_Aster (www.code-aster.org) open-source FE code (version 14.4.0) was used for the computations. We modelled the TM using seven-node second-order TRIA7 COQUE_3D shell elements [37], while all other structures (ossicles, joints, and ligaments) were modelled using ten-node second-order TETRA10 3D solid tetrahedral elements in Code_Aster.

2.2.3 Mesh Dependency

The original mesh of our model consisted of 205,322 tetrahedral elements (TETRA10 3D) for all parts of the model except the TM that was composed of 7,778 shell elements (TRIA7 COQUE_3D). In order to check the mesh convergence, we used the Homard [89] utility of Code_Aster to refine the original mesh. We divided each triangle into four coplanar triangles and as a result, the numbers of tetrahedral elements and triangular elements were increased by factors of eight and four, respectively. It was observed that the refined mesh does not result in substantial changes in the trend and the values of the vibration responses of the umbo and stapes footplate in the frequency range of 100 Hz to 10 kHz. We compared the results at 405 equally spaced frequencies in this frequency range for the displacement amplitude of the umbo

and stapes footplate. For the umbo amplitude, the differences between the results obtained from the original and refined meshes were less than 1 dB at 354 frequencies, with a maximum difference of 1.40 dB at 1.24 kHz. Additionally, for the displacement amplitude of the stapes footplate, the difference between the results obtained from the original mesh and refined mesh was less than 1 dB at 321 frequencies, with a maximum difference of 2.11 dB at 1.17 kHz. As a trade-off between the accuracy and computational cost, we chose to perform all calculations with the original mesh.

2.2.4 Time-step and time-span dependency

We chose the time span of 25 ms (which provides a frequency resolution of 24 Hz). For checking whether the response is affected by increasing this time span, we increased it to 50 ms (which provides a frequency resolution of 12 Hz) and observed less than 0.001 dB difference for both amplitudes of displacement of the umbo and stapes footplate and for all frequencies in the range of 100 Hz to 10 kHz.

We chose the time step of 10 μs (the maximum frequency of 50 kHz) and decreased it to 5 μs (the maximum frequency of 100 kHz). We observed that in the frequency range of 100 Hz to 10 kHz, decreasing the time step caused maximum changes of 0.36 dB (at 7.59 kHz) and 0.44 dB (at 7.59 kHz) in the displacement amplitudes of the umbo and stapes footplate, respectively. Therefore, we used the original time step (10 μs) and time span (25 ms) for all our calculations.

2.2.5 Uncertainty propagation

We made a baseline conventional deterministic FE model with a priori material parameters from the literature and validated this model against existing experimental data. We then considered the probability distribution of the model parameters, sampled the N-dimensional parameter space and propagated the uncertainties to the model outputs. We considered having uncertainties in the material properties (Young's modulus, Poisson's ratio, and stiffness-proportional damping coefficient) for all of the components of the model as well as in the thickness of the TM and in the cochlear load. All these uncertainties existed at the same time in our simulations.

We quantified uncertainties using two indices: the coefficient of variation (CV):

$$\mathrm{CV} = \left|\frac{\text{standard deviation}}{\text{mean}}\right| \times 100, \qquad \text{if} \quad \text{mean} \neq 0 \tag{2-1}$$

and uncertainty amplification (UA) which quantifies the amplification of the uncertainties of the outputs with respect to the uncertainties in the model parameters [90]:

$$\mathrm{UA} = \frac{\mathrm{CV}_{\mathrm{Output}}}{\frac{1}{\mathrm{n}}\sum_{\mathrm{i}=1}^{\mathrm{n}} \mathrm{CV}_{\mathrm{Inputs}}} \tag{2-2}$$

where n is the number of uncertain model parameters. A UA value of greater than one indicates amplification.

The stochastic sets of model parameters were created by the Latin Hypercube Sampling method for each scenario (each combination of random parameters sampled from the N-dimensional parameter space) with the mean values equal to values for the baseline model (Table 2-1 for material properties, TM thickness of 74 μm, and cochlear load viscous damping coefficient of 0.26 Ns/m) and CV of 20% and 10%. The ranges of variation of each model parameter for both CV values are reported in Appendix A. We used UQLab [91] (version 1.3.0) for creating stochastic sets of model parameters. In the absence of reported probability distributions for most parameters of the model, we assumed normal distribution, which is advocated to be a suitable choice for many biological variables [92]. However, because the value of the Poisson's ratio was set to 0.49 for soft tissues in the baseline model, we considered a half-normal distribution for soft tissues with the mean of 0.49 that only resulted in values less than or equal to the mean. Also, in order to reduce the number of parameters, we considered all three ossicles to have the same Young's modulus, Poisson's ratio, and damping in our stochastic modelling. Visualization of the sampled N-dimensional parameter space is not directly possible but Figure 2-2-a shows the distribution of parameters on the planes of some pairs of parameters of the space with CV of 20%. The planes in this figure show normal and half-normal distributions as described above.

The uncertainty in the model parameter space was propagated to the output by performing FE analysis for each set of the stochastic model parameters described above. We evaluated the FE model with 1992 parameter scenarios to cover the N-dimensional parameter space. All of the FE calculations were performed on the Niagara cluster of Digital Research Alliance of Canada (www.alliancecan.ca) with Intel Skylake (2.4 GHz, AVX512) processors running under the CentOs 7 distribution of Linux. Each single simulation of the model with the original mesh and original time step and time span (Section 2.3) was performed on one core using 18 GB memory. Each node of the cluster has 40 cores and 188 GiB of memory, allowing 10 parallel simulations on one node and a total number of 100 model evaluations on one node took about 14 hours to complete.

After propagating the uncertainties to the outputs, statistical analyses were done on the outputs. For the output phases, we implemented circular statistics to find values of the mean, standard deviation, skewness, and kurtosis using the Circular Statistics Toolbox of Matlab [93]. Using circular statistics, we consider the circular nature of all of these parameters, which is important for phase values. For instance, the circular standard deviation is analogous to linear standard deviation but it considers the cyclic nature of phase values when evaluating their variabilities. More details about these parameters can be found in the documentation of the Circular Statistics Toolbox [93]. To calculate the skewness and kurtosis of the output phase, we employed the methods described by Pewsey [94] and Fisher [95], respectively.

Figure 2-2-b provides a summary of the workflow of the stochastic FE analysis that we used in the current chapter.

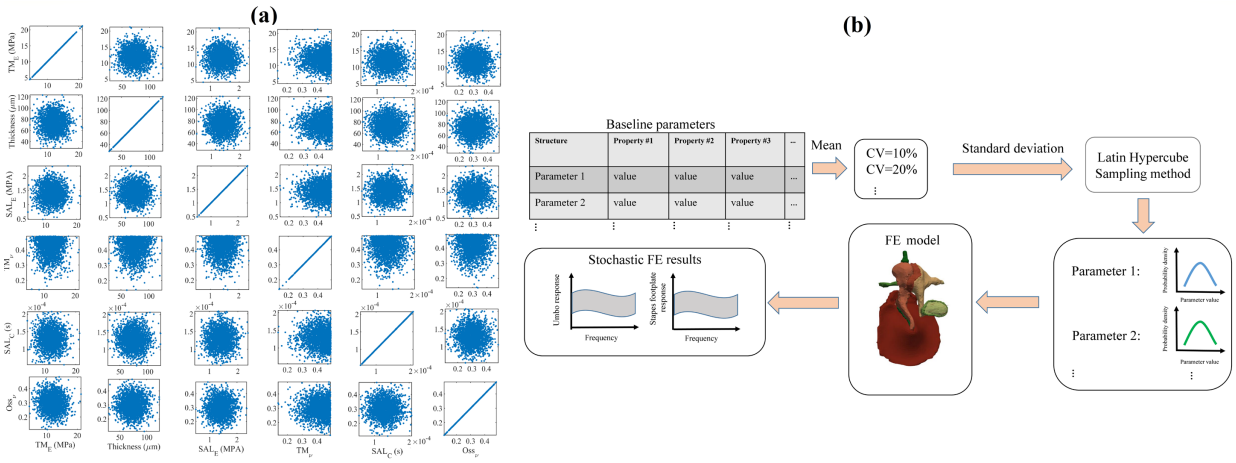


Figure 2-2 – Distribution of some of the uncertain model parameters and workflow of the stochastic FE analysis. Panel (a): Some of the 2D views of the N-dimensional parameter space sampled using the Latin Hypercube method with the coefficient of variation (standard deviation/mean) of 20%. Depending on the nature of the parameter, the sampled space shows normal and half-normal distributions. We used 1992 sets of stochastic model parameters in our stochastic FE analysis. Panel (b): Workflow of the stochastic FE analysis process used to study the effects of uncertainty in the middle-ear model. In the first step, we used the values of the baseline model (reported in Table 2-1) as the mean values of our stochastic sets of model parameters. We then specified the amount of coefficient of variation (standard deviation/mean) of the uncertain parameters. We considered the coefficient of variation to be 10% and 20% in the current chapter and used the Latin Hypercube Sampling method to create stochastic sets of model parameters with normal and half-normal distributions. The next step was to solve the FE model for all of these stochastic sets of model parameters, and from here, we found the stochastic outputs of the system. We used these stochastic outputs to study the amplification of the uncertainties in the system outputs and determine the output distributions.

2.3 Results

2.3.1 Middle-ear model can magnify parameter uncertainties up to more than three times in the output

Figure 2-3-a and Figure 2-3-c, respectively, present the stochastic normalized amplitude and phase of the umbo displacement for model parameters with the CV of 10%. The middle-ear resonance frequency, identified by the peak in the umbo amplitude response, was about 1.5 kHz in the deterministic baseline response and had a UA of about 0.77 in the stochastic model. At low frequencies (below the middle-ear resonance frequency), the uncertainty of the

umbo displacement amplitude was not amplified (UA of about 0.6). Also, the value of the circular standard deviation of the phase remained close to zero at low frequencies. Above the middle-ear resonance frequency, the uncertainties were amplified in the umbo displacement output with the highest UA of 4.38 near 2.5 kHz for the amplitude and maximum values of the circular standard deviation in the phase (0.06 cycles) happened near frequencies of 1.9 kHz and 3.5 kHz.

Increasing the uncertainty in the model parameters to the CV of 20% (Figure 2-3-b and Figure 2-3-d) did not lead to uncertainty amplification at low frequencies: the UA of the amplitude remained about 0.6 and the circular standard deviation values of the phase remained close to zero. Also, the UA of the middle-ear resonance frequency experienced a negligible increase (0.83 vs 0.77). At frequencies higher than the middle-ear resonance, the increased uncertainty in the model parameters caused more dispersed umbo displacement responses with an average CV of about 32% for amplitude. (was about 17% when CV of inputs were 10%) and an average standard deviation of 0.05 cycles in phase (was 0.02 cycles for CV of 10%). Near 1.8 kHz, the circular standard deviation of the phase shows its maximum (0.09 cycles). Also, the greatest UA peak (3.19) of the umbo displacement amplitude was in the vicinity of 2.5 kHz. In this frequency neighborhood, for some sets of model parameters, an anti-resonance occurred as can be seen in Figure 2-3-b and Figure 2-3-d. These anti-resonances did not exist in Figure 2-3-a and Figure 2-3-c where the CV of uncertain model parameters was 10%.

The stapes displacement describes the output of the complete middle ear. Figure 2-4-a and Figure 2-4-c show the frequency response of the stapes footplate with the CV of 10% for all uncertain model parameters. Similar to the umbo response, at low frequencies (below the middle-ear resonance at 1.5 kHz), uncertainty amplification did not occur: the UA was about 1 for the amplitude and the values of the circular standard deviation were close to zero. For frequencies above the middle-ear resonance frequency, the model amplified the uncertainty in the stapes response (average amplitude UA: 1.72 and average phase circular standard deviation: 0.02 cycles). The maximum UA of 3.12 happened at about 2.2 kHz for the stapes

displacement amplitude. Also, for the phase, the maximum circular standard deviation of 0.05 cycles happened near frequencies of 1.9 and 3.6 kHz.

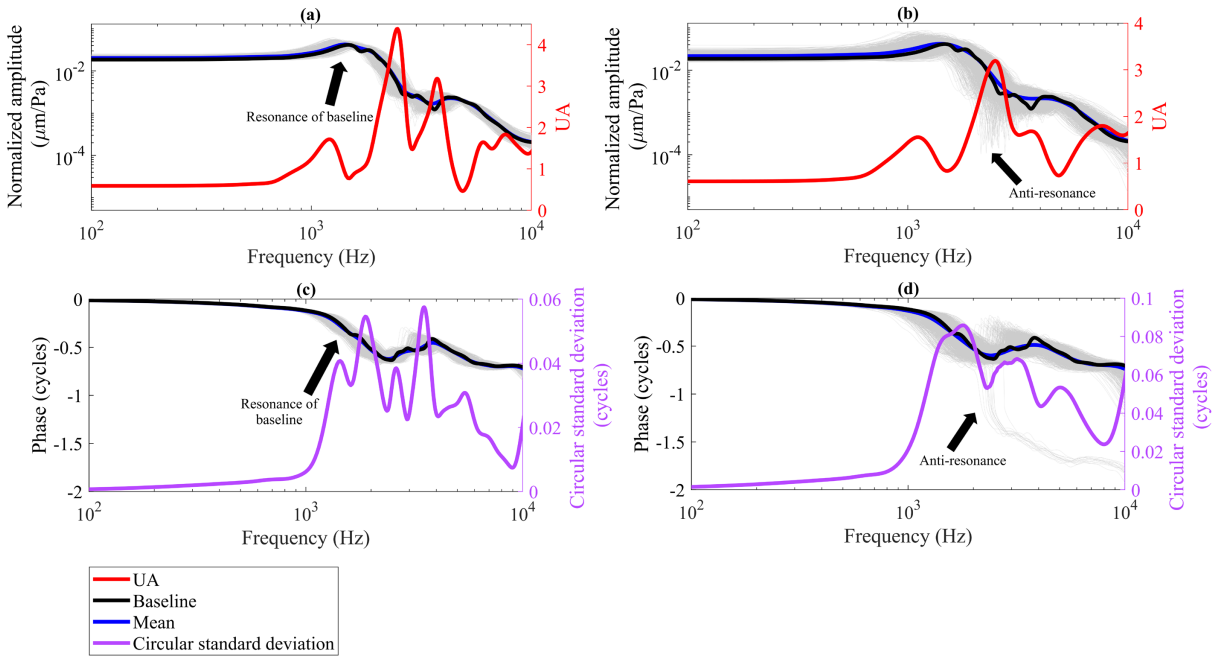


Figure 2-3 – Stochastic frequency response function of the umbo displacement. Amplitude and phase of the umbo (normalized with respect to excitation pressure) are presented in this figure. The motion of the umbo is reported in the direction normal to the manubrium at the umbo. The results of individual simulations (n=1992) are plotted with gray thin lines and because they are all close to each other, the whole response region looks like a gray shaded area. Panels (a) and (c): The CV of all uncertain model parameters was set to be 10%. The UA (Equation (2-2)) is about 0.6 for the umbo displacement amplitude below the middle-ear resonance frequency (at ~1.5 kHz). The maximum UA of about 4.38 happens near 2.5 kHz for the umbo displacement amplitude. For the phase, the values of circular standard deviation are close to zero at low frequencies and the maximum circular standard deviation happens near frequencies of 1.9 kHz and 3.5 kHz. Panels (b) and (d): The CV of all uncertain model parameters was set to be 20%. The UA (Equation (2-2)) is about 0.6 for the umbo displacement amplitude at frequencies below the middle-ear resonance frequency (at ~1.5 kHz). For the amplitude, the maximum UA (3.19) happens near about 2.5 kHz and for the phase, the maximum circular standard deviation (0.09 cycles) happens at about 1.8 kHz.

Also, the open-cavity stapes footplate velocity data of Voss et al. are presented in Figure 2-4 [68]. We compared the stapes displacement amplitude of the baseline model with these experimental results and found that the maximum difference was less than 1.6 dB for all frequencies below the middle-ear resonance frequency (1.5 kHz). Also, as Figure 2-4 displays, the middle-ear resonance frequency and the maximum stapes footplate displacement amplitude obtained from the model match well with the experimental data.

Figure 2-4-b and Figure 2-4-d present the frequency response of the stapes footplate for the CV of 20% for all uncertain model parameters. At low frequencies, the UA was about 1.10 for the amplitude and the circular standard deviation values of the phase were close to zero. At 2.3 kHz, the amplitude response was most uncertain and the uncertainty in the model parameters was magnified by a factor of 2.41 while the circular standard deviation of the phase response drastically decreased at this frequency to 0.02 cycles (from 0.07 cycles at 1.8 kHz) and went up to 0.07 again near the frequency of 10 kHz. Here the anti-resonances, observed in the umbo response (Figure 2-3-b and Figure 2-3-d), are not present. Compared to panels (a) and (b) of Figure 2-4, the increased uncertainty (CV of 20%) in the model parameters, caused an approximately similar average amplitude UA (1.58 vs 1.72) and a higher average phase standard deviation (0.04 cycles vs 0.02 cycles) and the stapes response was in a better agreement with the experimental results. A comparison of the stochastic model results of the stapes footplate (with CV of 20%) with several experimental measurement results in the literature is also provided in Appendix B.

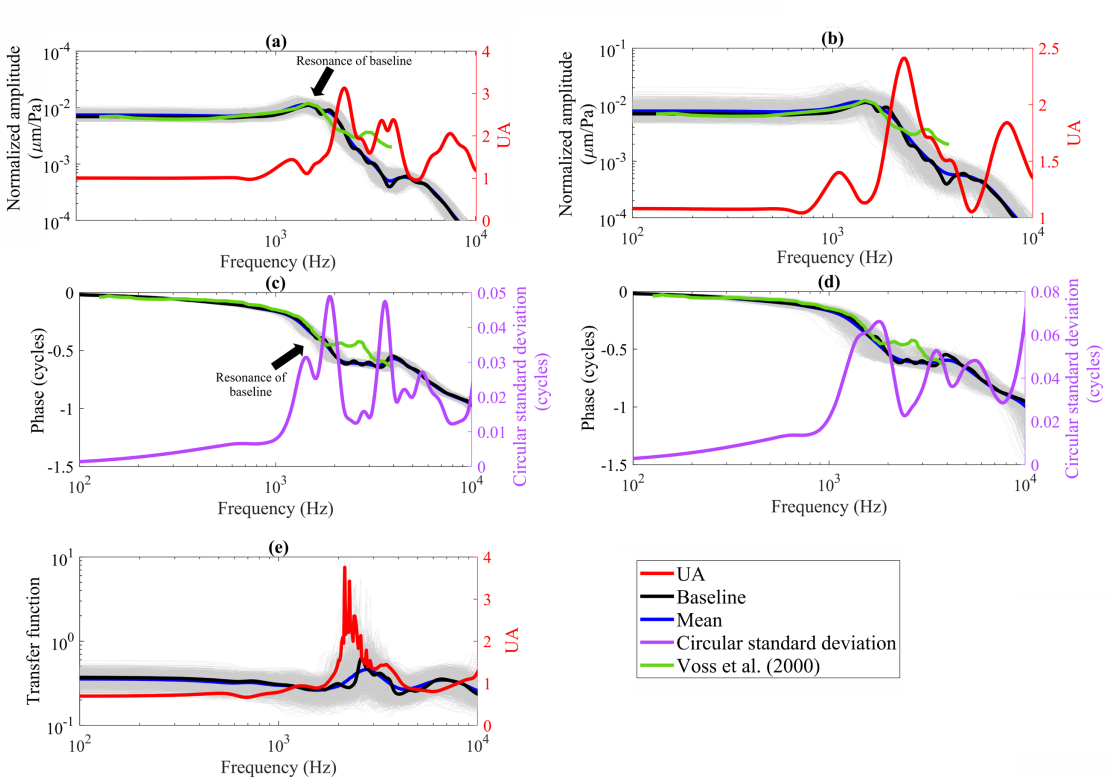


Figure 2-4 – Stochastic frequency response function of the stapes footplate displacement and the stochastic middle-ear transfer function. The results of individual simulations are plotted with gray thin lines and because they are all close to each other, the whole response region looks like a gray shaded area. The stapes footplate motion is reported in the piston-like direction. Also, the green line presents the experimental results of Voss et al. [68] *(Bone 25) converted to displacement and corrected for the viewing angle of 35°; the mean of their reported viewing angle range of 20°−50° degrees. Panels (a) and (c): Amplitude and phase of the stapes footplate (normalized with respect to excitation pressure) with the CV of 10% for all uncertain model parameters. At frequencies below the middle-ear resonance frequency (at ~1.5 kHz), the UA (Equation (2-2)) is about 1 for the stapes displacement amplitude. The maximum UA (3.12) happens near 2.2 kHz for amplitude and the maximum circular standard deviation (0.05 cycles) happens near the frequencies of 1.9 kHz and 3.6 kHz for the phase. Panels (b) and (d): Amplitude and phase of the stapes footplate (normalized with respect to excitation pressure) with the CV of 20% for all uncertain model parameters. The UA (Equation (2-2)) is about 1.1 for amplitude at frequencies below the middle-ear resonance frequency (at ~1.5 kHz). The maximum UA (2.41) happens near 2.3 kHz for the stapes displacement amplitude and the greatest circular standard deviation happens (0.07 cycles) near frequencies of 1.8 kHz and 10 kHz for the phase. Panel (e): Stochastic middle-ear transfer function calculated using the stochastic model with CV of 20% in model parameters (Figure 2-3-b and Figure 2-4-b). The maximum UA of the lever ratio (3.75) happens at about 2.1 kHz.*

2.3.2 At low frequencies, middle-ear models attenuate uncertainties and approximate a robust simple lever

Figure 2-4-e presents the stochastic ossicular transfer function of the model with the CV of 20% for the uncertain model parameters. This ossicular transfer function is defined as the ratio of the stapes footplate displacement amplitude (in the piston-like direction) to the umbo displacement amplitude (in the direction normal to the manubrium at the umbo). At low frequencies (below the middle-ear resonance), the transfer function can be thought as the lever ratio (at low frequencies, the mean value of the lever ratio is less than 0.4 and the UA of the lever ratio is about 0.7). However, UA increases up to a maximum of about 3.75 near 2.1 kHz. The uncertainties in the model parameters make the transfer function highly uncertain at most frequencies between 2 kHz and 4 kHz. At the frequencies below 1 kHz, the model robustly attenuates uncertainties and portrays the middle ear as a highly certain simple lever. The same trend of attenuating uncertainty at low frequencies is evident in all results of Figure 2-3 and Figure 2-4 as discussed earlier.

2.3.3 The Middle-ear model is biased

To study the probability distributions of stochastic responses at low, mid, and high frequencies, we focused on three frequencies (F_{low} =708 Hz, F_{mid} =2.51 kHz, and F_{high} =9.74 kHz). Figure 2-5 presents violin plots [96] of the amplitude and circular histograms of the phase of both umbo and stapes footplate displacement at these frequencies (for CV of 20% for uncertain model parameters). The horizontal axes in the violin plots show kernel density estimations for each distribution. We used Kuiper's normality test to check whether the distributions shown in Figure 2-5 are normal (von Mises for circular distributions [97]). We found that for all outputs, the null hypothesis was rejected at 5% significance level except for the phase of the stapes footplate at F_{low}. This means that although most of the uncertain model parameters were considered to have normal distributions, the output distributions may be distorted with non-normal distributions.

The values of skewness and kurtosis reported in Table 2-2 also confirm that most of the distributions presented in Figure 2-5 are non-normal as their skewness and kurtosis values are far from the respective values for the normal distribution (skewness of zero and kurtosis of three for the amplitude [98], [99] and skewness and kurtosis of zero for the phase [93]). For the amplitude of the umbo displacement, the absolute value of skewness is greater than 0.90 at all three frequencies with a maximum absolute value of 1.59 at F_{low}. Also, the values of kurtosis for the amplitude of the umbo displacement are greater than 4.12 at all three frequencies with the maximum value of 7.88 at F_{low}. For the phase of the umbo displacement, the value of skewness is very close to zero at all three frequencies. Additionally, the values of kurtosis of the phase of the umbo displacement are about 1.94, 12.70, and 19.72 at frequencies F_{low}, F_{mid}, and F_{high}, respectively. These findings are consistent with the results of the normality test above.

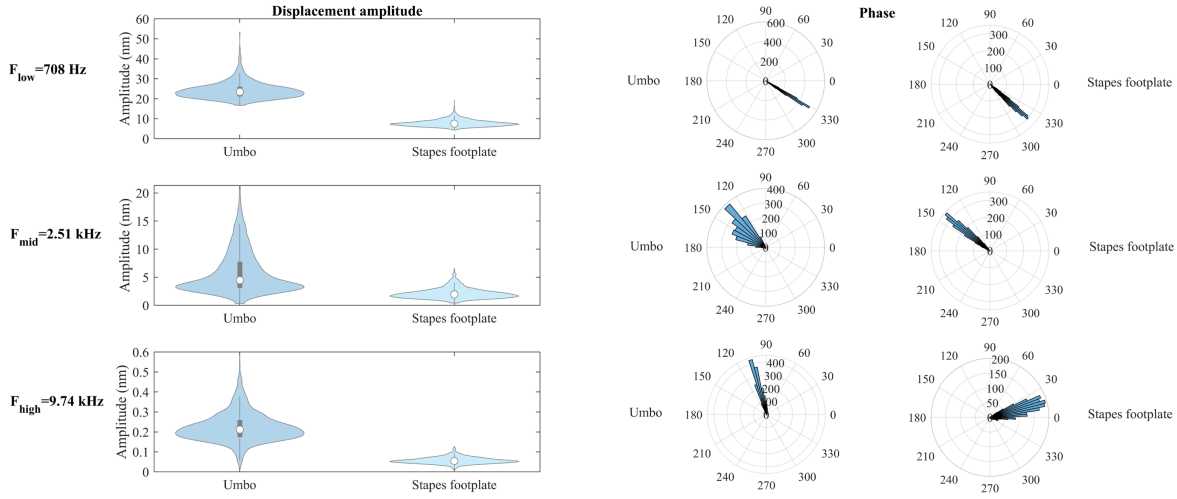


Figure 2-5 – Violin plots and circular histograms for the amplitude and phase of the umbo and stapes footplate. The results are presented at frequencies F_{low}, F_{mid}, and F_{high}. The CV of uncertain model parameters was set to be 20%. The horizontal axes in the violin plots show kernel density estimations for each distribution. The values of skewness and kurtosis of the distributions shown in this figure are presented in Table 2-2. We used Kuiper's normality test to check whether the distributions shown in Figure 2-5 are normal (von Mises for circular distributions [97]*). Based on Kuiper test results presented in Section 2.3, the null hypothesis was rejected at 5% significance level except for the phase of the stapes footplate at F_{low}.*

For the displacement amplitude of the stapes footplate, the value of skewness is greater than 1.17 at all three frequencies with a maximum value of 1.27 at F_{mid}. Furthermore, the values of kurtosis for the amplitude of stapes displacement are greater than 4.22 at all three frequencies with a maximum of 5.80 at F_{low}. Table 2-2 also shows that, like the umbo response, the values of skewness for the phase of the displacement of the stapes footplate are very close to zero at all three frequencies. Besides, the values of kurtosis for the phase of the displacement of the stapes footplate are greater than 0.88 at all three frequencies with the maximum value of 17.48 at F_{mid}.

Table 2-2 – Values of skewness and kurtosis for the output distributions shown in Figure 2-5.

Frequency	**F_{low} (708 Hz)**		**F_{mid} (2.51 kHz)**		**F_{high} (9.74 kHz)**	
Statistical information	**Skewness**	**Kurtosis**	**Skewness**	**Kurtosis**	**Skewness**	**Kurtosis**
Umbo amplitude	1.59	7.88	1.25	4.12	0.90	4.63
Umbo phase	0.00	1.94	-0.06	12.70	0.05	19.72
Stapes footplate amplitude	1.17	5.80	1.27	5.15	0.69	4.22
Stapes footplate phase	0.00	0.88	-0.01	17.48	0.07	14.27

2.3.4 Uncertainties in the vibration patterns of the TM are spread in space with increased frequency

The previous results showed the propagated uncertainties only for the umbo and stapes footplate. To provide a more complete view about the stochastic motions in the model, Figure 2-6 presents the vibration amplitude of the TM at the same three frequencies. This figure

considers the displacement of the baseline and stochastic FE model with CV of 20% for the model parameters. For the 15,728 nodes of the TM model, we calculated the displacement amplitude and phase in the baseline model as well as their mean and standard deviation in the stochastic model. The results of the amplitude are presented in the three left columns of Figure 2-6 and the results for the phase are provided in the Figure 2-7. The rightmost column of Figure 2-6 presents the values of CV of the displacement amplitude. We should note that only the CV of the nodes of the TM that have mean displacement values of greater than 0.1 nm are plotted in this column. The patterns obtained from the baseline model have similarities to the mean stochastic results shown in the "mean" column. At all three frequencies, the manubrium (outlined in black at F_{low}) has the smallest motion in the baseline and has the smallest values of the mean and standard deviation. At F_{low}, the maximum deformation of about 0.25 μm occurred in the posterior side of the TM (left to the manubrium in Figure 2-6), as expected [70]. Besides, at this low frequency, the standard deviation plot shows that posterior to the TM, the standard deviation of the motion can be as large as the mean or baseline displacement (also evident from the CV of about 110%). At F_{mid} and F_{high}, some features in the baseline pattern (one example is marked with the white circle) are not present in the mean pattern because they were smoothed out due to averaging and due to the high variations in the results at these locations. At the middle frequency (F_{mid}), the major area of the TM shows standard deviations of more than 0.02 μm except in the superior region of the TM where standard deviations of down to 0.001 μm dominate the region. Consistently, the CV plot at F_{mid} shows that regions with high CV (≥50%) are apparent in all regions of the TM. Increasing the frequency to F_{high} leads to nearly even distribution of regions with high standard deviations and high CV on the entire TM, especially in comparison to the vibration patterns at F_{low}. The mean values of CV of the TM nodes (Figure 2-6) are about 46%, 56%, and 38% for the F_{low}, F_{mid}, and F_{high}, respectively. This shows that although by increasing the frequency the regions with high CV are spatially spread out on the TM, the mean value of the CV does not follow any specific trends.

The stochastic phases of vibration patterns of the TM are presented in Figure 2-7. Compared to the displacement amplitude, the displacement phase has a more evenly distributed standard deviation at F_{low}. Also, at F_{low}, the vibration phase is nearly constant and highly certain over the entire TM except in a small circular region in the TM anterior with concentrated uncertainty and a maximum standard deviation of about 102°. The displacement phase pattern becomes more uncertain as the frequency increases and at F_{mid} several hot spots with concentrated uncertainty are present in the standard deviation plot. As the frequency increases to F_{high} the uncertainty is dispersed in the entire TM. The average values of the circular standard deviation at F_{mid} and F_{high} (38° and 20°, respectively), are much greater than that at F_{low} (4°).

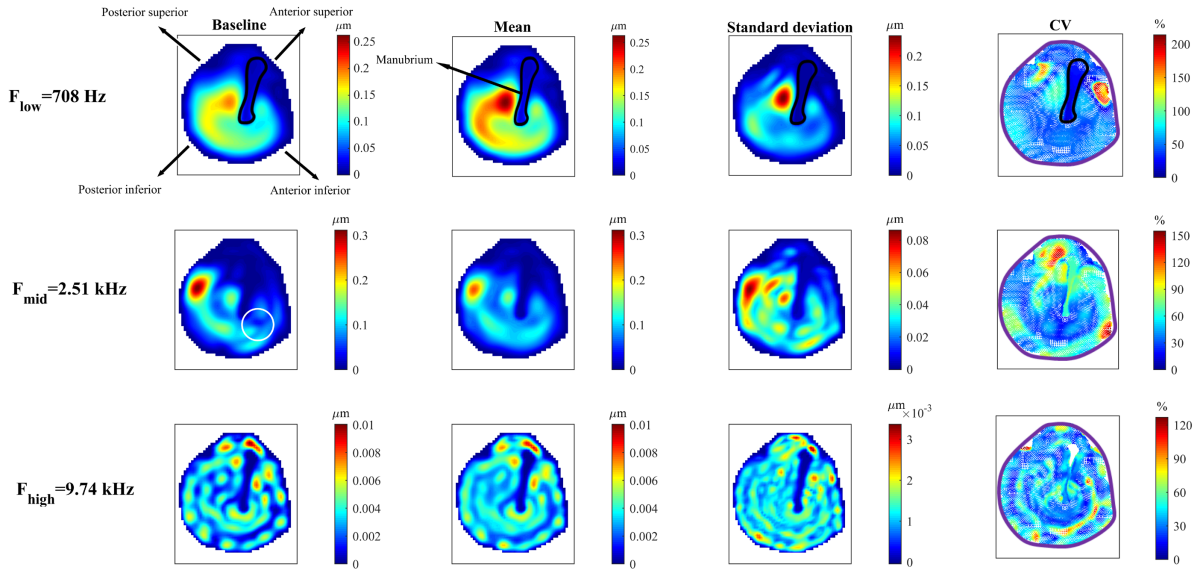


Figure 2-6 – Stochastic full-field vibration patterns of the TM. Vibration patterns of the baseline model and the spatial distribution of the mean and standard deviation of the displacement amplitude of the tympanic membrane at three frequencies F_{low}, F_{mid}, and F_{high} are presented in the three left columns. The vibration patterns are reported in the direction normal to the manubrium at the umbo. Comparing the mean and baseline patterns shows that at F_{mid} and F_{high}, some high-frequency features are not present in the mean pattern due to the averaging and high variations in the stochastic results. The white circle shows one example of such high-frequency features. The right column shows the distribution of the coefficient of variation for points where the mean values are far from zero. The manubrium is outlined in black. The purple line shows the tympanic annulus.

2.4 Discussions

In this study, we presented a stochastic FE model of the human middle ear that instead of generating deterministic vibrations and model outputs, provides a probabilistic description of middle-ear vibrations to account for the natural variabilities in the human middle ear. Current FE models do not have enough accuracy to be considered as acceptable tools for diagnosis and surgical planning [7], [100]. This study is a step toward increasing the accuracy and reliability of the predictions of FE models by considering the uncertainty in the model parameters.

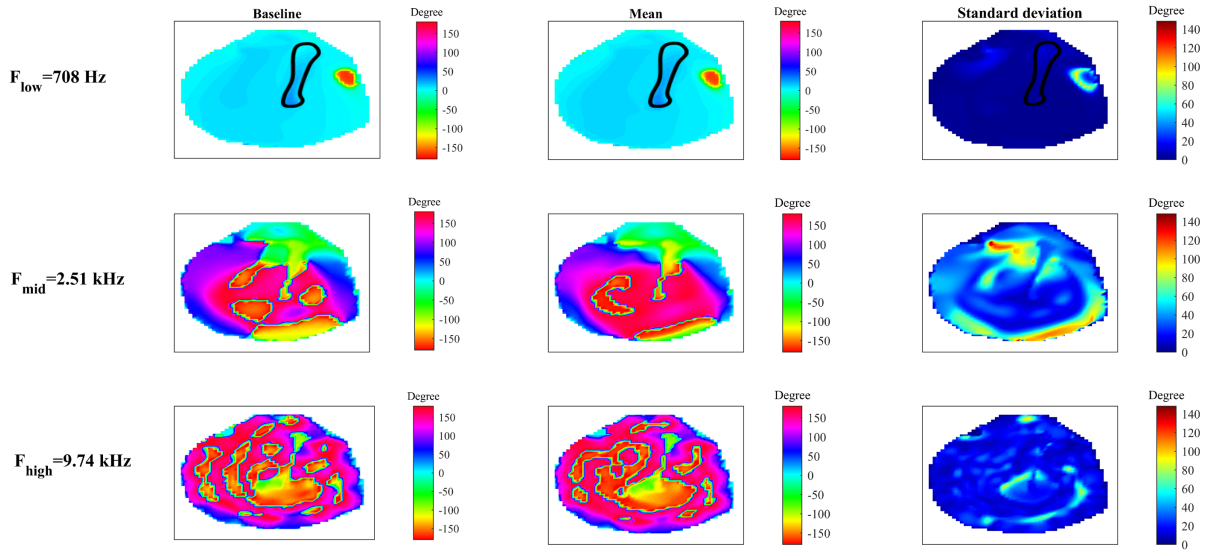


Figure 2-7 – Stochastic full-field vibration phase of the TM. Distribution of the displacement phase of the baseline model and the spatial distribution of circular mean and circular standard deviation of the phase of the tympanic membrane. The results are presented at three frequencies F_{low}, F_{mid}, and F_{high}. The manubrium is outlined in black.

To take the variability in individual ears into account, the stochastic model considered uncertainty in the mechanical parameters as well as the thickness of the TM. We demonstrated that the middle-ear model can magnify the uncertainties in the model parameters to more than 300% in the outputs. For both CV values of 10% and 20% of the model parameters, the highest

UA happened in the frequency range of 1 kHz to 5 kHz for the amplitudes of the umbo and stapes displacements. This new finding enhances our existing knowledge [37], [101] about the sensitivity of the middle ear to variability. Uncertainty amplification that we report here was also observed in models of other organs of the body (e.g., left ventricle [102]).

Also, for the model with the CV of 20%, for some sets of model parameters, we saw an additional anti-resonance in umbo displacement at frequencies around 2-3 kHz that does not exist in the baseline model. Based on our results, for the sample sets that lead to these anti-resonances in the umbo response, the values of the thickness or the Young's modulus of the TM (or both of them for most samples) are small (below mean values). However, the values of other model parameters and their interactions may also have some effects in the presence of these anti-resonances. The presence of anti-resonances for some sets of model parameters is consistent with the presence of similar antiresonances in some ears in experimental observations of populations of middle ears [8], [9]. Additionally, the noisy behaviour of the transfer function (Figure 2-4-e) can be due to these anti-resonances for some sets of model parameters.

All the observations described above have important implications for FE models of the middle ear because in addition to inter-individual variability that makes the model parameters intrinsically uncertain, most material parameters of the models were not and cannot be measured accurately in vivo, at least with the existing methods. If conventional deterministic FE models of the middle ear are to be used for developing new medical devices or for planning therapeutic interventions, the ignored error in the values of material and geometrical parameters (uncertainty) may be amplified as errors in the model results. We observed that the umbo and stapes footplate responses and the middle-ear transfer function are less uncertain at low frequencies. This suggests that if, despite uncertainties, a deterministic model is used, the model predictions at low frequencies are more reliable than those at high frequencies.

Moreover, by investigating stochastic vibration patterns of the TM, we observed that as the frequency of excitation increases, the regions with high uncertainty are spread out more evenly on the entire TM surface and the vibration pattern becomes increasingly less certain. This

suggests that similar to what we discussed for the umbo, stapes footplate and the middle-ear transfer function, if conventional deterministic FE models of the middle ear are used for developing new technologies that rely on the exact details of the vibration patterns of the TM, low-frequency vibration patterns should be preferred over the high-frequency ones.

One of the limitations of our current stochastic FE model is that we only considered normal and half-normal distributions for the model parameters. We chose these distributions based on the fact that normal distributions are suitable choices for many biological variables [92]. However, the exact distribution of each of the model parameters should be determined by performing further experiments on a large number of human ears.

In the absence of more accurate estimates of the value of the CV of most of the uncertain model parameters, we considered the CV values of 10% and 20%. However, additional experimental measurements should be carried out in order to quantify the CV of each of the model parameters. Recently, Lobato et al. tried to quantify the CV of mechanical parameters of the middle ear [103] based on the ranges reported in the literature for each value. However, their study does not include all mechanical properties of the middle ear structures. For instance, CV of damping, Poisson's ratio, and cochlear load is not reported in their work. Additionally, as Lobato et al. also mentioned in their work, even for the parameters reported in their work, the values of CV were calculated from small sample sets and therefore, those values might not be accurate enough. Furthermore, to avoid excessive sophistication of performing this study, we only considered the variability in the TM thickness among all morphological parameters of the middle ear because that was the only morphological variability that would not need creations of new 3D models. Future studies should explore the effects of morphological variability in interaction with material variability.

Chapter 3

Relative importance and interactions of parameters of finite-element models of human middle ear

Preface

In this chapter, we performed a global sensitivity analysis on the human middle ear to find the parameters that have the most remarkable global impact on sound conduction in the middle ear and also to find the interactions among model parameters. We used the stochastic FE results presented in Chapter 2 with CV of 20% of model parameters to create surrogate models that can be used instead of FE models to make the computationally massive global sensitivity analysis process manageable. We then verified the accuracy of these surrogate models with respect to the FE results and used them to perform a global sensitivity analysis on the middle ear using Sobol′ sensitivity analysis method.

Overview

In the last decades, finite-element models of the middle ear have been widely used to predict the middle-ear vibration outputs. Even with the simplest linear assumption for material properties of the structures in the middle ear, these models need tens of parameters. Due to the complexities of measurements of material properties of these structures, accurate estimations of the values of most of these parameters are not possible. In this study, we benefited from the stochastic finite-element model of the middle ear we had developed in the past, to perform global sensitivity analysis. For this aim, we implemented Sobol′ sensitivity analysis which ranks the importance of all uncertain parameters and most importantly, the interactions among them at different frequencies. In order to decrease the computational costs, we found Sobol′ indices from surrogate models that we created using stochastic finite-element results and the polynomial chaos expansion method. Our quantities of interest for the global sensitivity analysis are the displacement amplitude of the umbo and displacement amplitude and phase of the stapes footplate. Based on the results, the Young's modulus of the tympanic membrane and stapedial annular ligaments, the damping of the stapedial annular ligament, the Young's modulus of ossicles, and the thickness of the tympanic membrane are among the parameters with greatest impacts on our quantities of interest. Furthermore, the results reveal that the most significant interactions happen between the Young's modulus and thickness of the tympanic membrane.

3.1 Introduction

The human middle ear is a complex system that plays a key role in auditory processing by conducting sound waves from the ear canal to the inner ear. Models of the middle ear are valuable resources that can be used for different purposes such as obtaining a better quantified understanding of the mechanics of the middle ear, optimizing new or existing hearing devices, investigating the response of the middle ear to pathological changes, and developing diagnostic tools. Different approaches have been employed to model the mechanics of the middle ear [31]. The finite-element method is one of the most prominent and powerful methods that has been used in this area.

Specifying the values of the mechanical and geometrical properties of all structures in the model is one of the most crucial requirements for developing an accurate FE model. However, even with the linear isotropic elastic material assumption, there are tens of model parameters in the middle-ear model. This number is higher for more complicated mechanical models such as nonlinear elastic models.

Due to the small size of most middle-ear structures and the rapid changes in their mechanical properties, once they are removed from the body due to drying and other effects, it has been challenging to measure their mechanical properties. Additionally, the mechanical properties and morphological features of the middle-ear structures are affected by inter-individual variabilities. These uncertainties can have substantial effects on the predictions of the middle-ear models. Therefore identifying the influential parameters and the interactions of parameters of the middle ear is of paramount importance for providing a deeper insight into the biomechanics of the middle ear and for interpreting diagnostic measurements of the middle ear [10]. Also, the findings can help researchers to focus their measurements on the mechanical properties of the structures that have the most considerable effects on the middle ear responses to reduce uncertainty. Furthermore, modellers can use these findings to focus exclusively on the influential and interacting parameters when tuning their FE models to reproduce experimental measurements. This will significantly reduce the computational costs of creating new patient-specific middle-ear FE models for diagnostic and therapeutic purposes.

There have been some sensitivity analysis investigations in the literature to determine influential parameters of middle-ear models [10], [37], [51], [55], [101]. Maftoon et al. performed one-at-a-time sensitivity analysis on the gerbil middle-ear model [37]. They considered the Young's modulus, density, damping, and the bulk modulus of all structures in their model as well as the cochlear load and thickness of the TM. O'Connor et al. performed a sensitivity analysis to study the effects of varying the TM material properties on the responses of a human middle-ear model [10]. Motallebzadeh et al. applied both one-at-a-time and Morris sensitivity analysis methods to ear canal and middle-ear models of a human newborn [55]. For the ear canal, they studied the variations of the Young's modulus, density, Poisson's ratio, and damping ratio of the soft tissue and for the middle-ear, they studied the impacts of the variations of 12 different model parameters including the middle-ear cavity volume, cochlear load, and Young's modulus of TM, ossicles, and ligaments. Furthermore, they investigated the effects of anatomical variability by scaling the middle ear and ear canal geometries in x, y, and z directions simultaneously. In another study, Greef et al. created FE models for three different human temporal bones and used these models to perform one-at-a-time investigation of the effects of variations of different model parameters including the damping of TM, Young's modulus of TM, and cochlear impedance [101]. Most of these works have been limited to a few structures in the model and few excitation frequencies. Furthermore, most sensitivity analyses of middle-ear models have been performed using one-at-a-time approach, which does not consider the possible interactions among parameters when they are changed at the same time to cover the parameter space instead of perturbing the model in the vicinity of a single point in the parameter space. When two parameters interact, the impacts of the variations in one of the parameters on the outputs are affected by the variations in the other parameter.

In the present chapter, we employed stochastic FE model results of the human middle ear, to perform global sensitivity analysis for all mechanical parameters of the model as well as the thickness of the TM. Unlike previous one-at-a-time analyses, this enabled us to study not only the effects of each parameter on the model responses but also the interactions among parameters for the first time.

3.2 Materials and methods

3.2.1 Mesh and deterministic finite-element model

The details of segmentation and mesh generation were provided in Chapter 2. We created the 3D model of the middle ear by segmentation of a μCT image dataset of a cadaver temporal bone and generated the mesh of the middle ear from the segmented geometry. The segmentation and mesh generation were done in 3D Slicer 4.11.20200930 [85]. The FE model consisted of 7,778 seven-node second-order triangular shell elements for the TM and 205,322 ten-node second-order tetrahedral elements for all other structures in the model.

Our model included the TM, ossicles, LML, AML, IMJ, ISJ, SAL, SML, PIL, and manubrial fold. The middle ear cavity, tensor tympani tendon, and stapedial tendon were not considered in the model. In Chapter 2 we performed a mesh convergence study to test the quality of the created mesh. For this aim, we increased the number of tetrahedral elements by a factor of eight and the number of triangular elements by a factor of four. We compared the results of this refined mesh with the results obtained using the original mesh at 405 equally spaced frequencies in the frequency range of 100 Hz to 10 kHz. We found that for the stapes footplate displacement amplitude, the differences between the results of refined and original meshes were less than 1 dB at 321 frequencies and the maximum difference was 2.11 dB at 1.17 kHz. Also, for the umbo displacement amplitude, we observed that the differences between the results of models with the original mesh and the refined mesh were less than 1 dB at 354 frequencies and the maximum difference was 1.40 dB at 1.24 kHz. As a trade-off between the computational cost and accuracy, we used the original mesh for our calculations.

The material properties of the baseline deterministic model are presented in Table 2-1. Similar to Chapter 2, all materials were considered to be linear which is shown to be a valid assumption for regular hearing tasks (e.g., response sounds below the threshold of pain, 120 dB SPL) [68], [104]. Additionally, we assumed all materials to be isotropic. We considered fully clamped boundary conditions for the TM annulus. Also, the ligaments were fixed at their distal ends where they are connected to the middle-ear cavity wall. The excitation of the model was

uniform pressure (with a magnitude of 1 Pa) applied to the TM surface laterally. The thickness of the TM was considered to be 74 μm [48], [87]. The cochlear impedance was considered to be 20 GΩ which is the same value used by Gan et al. [48]. As mentioned in Chapter 2, the surface area of the stapes footplate in our model is 3.6 mm^2. From these values, we calculated viscous damping of 0.26 Ns/m for the cochlear load. In our FE model, the cochlear load was represented by four dashpots attached to the stapes footplate.

We used Code_Aster (version 14.4.0) for FE simulations. All FE computations were carried out using transient dynamic analysis unless specified otherwise. In order to find the displacement frequency response function of the umbo and stapes footplate, we first calculated the transient response of these structures to the pressure step function with the magnitude of 1 Pa (applied to the TM laterally) using Newmark-β scheme ($\beta = 0.25$ and $\gamma = 0.5$ in the Newmark-β scheme). We then differentiated the step response (with respect to time) and employed the fast Fourier transform to generate the frequency response functions. Similar to Chapter 2, we chose a time step of 10 μs and a time span of 25 ms in this chapter. In Chapter 2, we analyzed the sensitivity of the model results to the values of the time step and time span. The results revealed that, in the frequency range of 100 Hz to 10 kHz, changing the time step from 10 μs to 5 μs caused maximum differences of 0.44 dB and 0.36 dB in the displacement amplitudes of stapes footplate and umbo, respectively. Additionally, we increased the time span from 25 ms to 50 ms and observed that this change resulted in less than 0.001 dB difference in both stapes footplate and umbo displacement amplitudes in the frequency range of 100 Hz to 10 kHz. Based on these observations, we chose the time step of 10 μs and the time span of 25 ms for all simulations.

As mentioned in Chapter 2, to validate our baseline deterministic model, we compared the amplitude and phase of the stapes footplate displacement obtained from our FE model with the open cavity experimental measurements of Voss et al. (measurements of Bone 25 in their work) [68]. At frequencies below the middle-ear resonance frequency (1.5 kHz), our model outputs were in very good agreement (less than 1.6 dB difference) with the results of the experimental

measurements. Also, the minimum cosine difference[3] between the phase of our model and the phase of experiments of Voss et al. at frequencies below 1.5 kHz was 0.98. Furthermore, the values of the middle-ear resonance frequency obtained from our model and the experiments of Voss et al. were very close to each other (both at about 1.5 kHz). Between the frequency of 1.5 kHz to about 4 kHz (maximum frequency in measurements of Voss et al. [68]), the mean difference between the amplitude of the stapes footplate of our model results and the results of Voss et al. was 6.64 dB and the mean value of cosine difference between the results was 0.80.

3.2.2 Uncertainty propagation and stochastic finite-element model

We considered existence of uncertainties in the cochlear load, thickness of the TM, and mechanical properties (Young's modulus, Poisson's ratio, and stiffness-proportional damping coefficients) of all of the components of the model. Overall, we had 32 model parameters in our sensitivity analysis. We created 1992 sets of stochastic model parameters using the Latin Hypercube Sampling method [105]. The mean values of model parameters for creating stochastic sets were considered to be the same as the values of parameters of the baseline model (Table 2-1). The normal distribution was considered for all of the model parameters (except for the Poisson's ratio of soft tissues that half-normal distribution was considered). To reduce the number of parameters, we considered all three ossicles to have the same mechanical properties (Young's modulus, Poisson's ratio, and damping). In this chapter, we created the stochastic model with the coefficient of variation of 20% for model parameters. Appendix C presents the range of the values of our middle-ear model parameters. All FE computations were carried out on the Niagara cluster of the Digital Research Alliance of Canada.

3.2.3 Global sensitivity analysis

Global sensitivity analysis aims to quantify the impact of individual and combined uncertainties in the model parameters on the outputs. A review of different global sensitivity analysis methods can be found in [106]. In this study, we used Sobol′ sensitivity analysis that

[3] We define the cosine difference of angles θ and φ as $cos(\theta-\varphi)$.

is a variant-based sensitivity analysis method and does not need the model to behave linearly or monotonously [107]. Considering the middle-ear FE model f and a vector of uncertain independent variables $Z = (Z_1, Z_2, .., Z_n)^T$, quantities of interest (Y) can be written as:

$$Y = f(Z) \tag{3-1}$$

In Sobol′ sensitivity analysis, the importance of each parameter is found by decomposing the variance of the outputs into fractions that can be attributed to the inputs. The Sobol′ decomposition of a square-integrable function f can be defined as [107]:

$$f(Z) = f_0 + \sum_{s=1}^{n} \sum_{i_1<\cdots<i_S}^{n} f_{i_1 \ldots i_S}(Z_{i_1}, \ldots, Z_{i_S}), \tag{3-2}$$

where f_0 is the expected value of $f(Z)$ and is a constant. Also, it was shown that for an integrable function $f(Z)$ and independent input variables, the integrals of summands with respect to their own variables are zero [107]:

$$\int_0^1 f_{i_1,\ldots,i_S}(Z_{i_1}, Z_{i_2}, \ldots, Z_{i_S}) dZ_{i_k} = 0 \quad for\ k = 1, \ldots, s \tag{3-3}$$

Moreover, it was shown that summands can be recursively computed by integrals [107]:

$$f_0 = \int f(Z) dZ, \tag{3-4}$$

$$f_i(Z_i) = \int \ldots \int f(Z) dZ_{\sim i} - f_0, \tag{3-5}$$

$$f_{ij}(Z_i, Z_j) = \int \ldots \int f(Z) dZ_{\sim i} - f_0 - f_i(Z_i) - f_j(Z_j), \tag{3-6}$$

where Z is the set of input parameters as mentioned before and $\sim i$ shows that the variable i is excluded. The higher-order summands can be defined similarly. Squaring equation (3-2) and integrating it results in [107]:

$$\int f^2(Z) dZ - f_0^2 = \sum_{s=1}^{n} \sum_{i_1<\cdots<i_S}^{n} \int f^2{}_{i_1 \ldots i_S} \, d_{Z_{i_1},\ldots,Z_{i_S}}. \tag{3-7}$$

The total variance is defined as:

$$D = \int f^2(Z)dZ - f_0^2, \tag{3-8}$$

and partial variances are:

$$D_{i_1,\dots,i_S} = \int f^2{}_{i_1\dots i_S}\left(Z_{i_1},\dots,Z_{i_S}\right). \tag{3-9}$$

The Sobol′ sensitivity indices are defined as:

$$S_{i_1\dots i_S} = \frac{D_{i_1\dots i_S}}{D} \tag{3-10}$$

which represents the relative contribution of each group of input parameters to the total variance [108]. The Sobol′ index considering only one input parameter is called the first-order Sobol′ index and it shows the effects of that individual parameter alone. If we consider multiple terms for calculating the Sobol′ indices (high-order indices), we will be able to find the interaction among parameters as well. The total-order Sobol′ index due to the parameter *i* is the sum of all Sobol′ indices involving that specific parameter and is defined as:

$$S_i^T = 1 - S_{\sim i} \tag{3-11}$$

The total-order Sobol′ index shows the overall contribution of a parameter on the output including its interactions with other parameters. In fact, the sensitivity analysis performed by considering only the first-order Sobol′ indices is similar to one-at-a-time sensitivity analysis as it does not consider the interactions among parameters. On the other hand, for each parameter, the total-order Sobol′ indices show the direct contribution of the parameter to the output (first Sobol′ index) as well as all of its interactions with other parameters. The second-order Sobol′ indices represent the interactions between pairs of parameters of the model on the output. In this chapter, we used first, second, and total order Sobol′ indices to study the effects of each parameter as well as its interactions with other parameters on the outputs of the middle-ear model. More information about calculating Sobol′ indices can be found in [108].

3.2.4 Creation of surrogate models using polynomial chaos expansion

In practice, direct calculation of Sobol′indices needs a huge number of evaluations of the model(in the order of thousands) [108]–[110]. It is hard to achieve this number of evaluations,

specifically if the computational cost of the model is high as it is the case for FE models. Fortunately, the Sobol′ indices can be easily calculated from surrogate models created using polynomial chaos expansion (PCE) [111]. In this chapter, we created separate PCEs at each frequency and for each quantity of interest and then used these PCEs to evaluate Sobol′ indices. The quantities of interest were chosen to be the amplitude of displacement of the umbo and stapes footplate and the phase of the stapes footplate in the frequency range of 100 Hz to 10 kHz. The reason that we did not consider the phase of the umbo as a quantity of interest is that we found large errors in the created surrogate models of the phase of the umbo at mid to high frequencies which can be due to the high variance of the output. As mentioned in Chapter 2, we also observed an additional anti-resonance at those frequencies for some sets of model parameters in our stochastic FE model results that can be one of the reasons for this high variance of the outputs.

The scalar model response can be expressed as a set of multivariable orthonormal polynomials so that:

$$Y = f(Z) \approx \sum_{\alpha=1}^{P} y_\alpha \psi_\alpha(Z) \tag{3-12}$$

where $\psi_\alpha(Z)$ represents multivariable basis functions in terms of input parameters, y_α shows the coefficient of the polynomials that should be found during creating the PCE model, and P is the number of terms which is a function of the number of model parameters and the degree of polynomials. The multivariable polynomial basis functions are chosen based on the distribution of the input parameters. Here, we used multivariable Hermite polynomials for the parameters with the normal distribution [112] and arbitrary polynomials created with Stieltjes procedure [113] for parameters with the half-normal distribution.

We used degree-adaptive PCEs with a degree range of 3 to 10 and for each case, and the PCE with the highest accuracy (with respect to the FE results) in this range was chosen. Also, for calculating the unknown coefficients (y_α) in Equation (3-12), among different methods in the

literature [112], we used the least angle regression method [114], which is suitable for high-dimensional simulations [113].

It is known that in most applied science problems, only low-order interactions exist among parameters [113]. Due to this fact and to decrease the computational costs, we limited the maximum interactions in the PCEs to the order of two.

In order to evaluate the accuracy of the created PCEs with respect to the FE results, we used the leave-one-out (LOO) error [115]. The relative LOO error is defined as [113]:

$$\epsilon_{LOO} = \frac{\sum_{i=1}^{n}\left(\frac{f(Z^i) - f^{PC}(Z^i)}{1-h_i}\right)^2}{\sum_{i=1}^{n}\left(f(Z^i) - \frac{1}{N}\sum_{i=1}^{n} f(Z^i)\right)^2} \quad , \tag{3-13}$$

$$h_i = i^{th}\ component\ of\ diag(A(A^TA)^{-1}A^T)\ , A_{ij} = \psi_j(Z^{(i)})$$

In this chapter, we measured the quality of the PCEs by the Q^2 parameter which is defined as:

$$Q^2 = 1 - \epsilon_{LOO} \tag{3-14}$$

The value of Q^2 is between zero and one. The larger is Q^2, the higher is the accuracy of the PCE (with respect to the FE results). The procedures of creating stochastic sets of model parameters, creating PCEs, and calculating Sobol′ indices were performed using UQLab (version 1.3.0) [91] in MATLAB 2019a.

Figure 3-1 provides a summary of the workflow of the stochastic FE model and the global sensitivity analysis that we used in the current chapter.

3.3 Results

3.3.1 Evaluation of the quality of the surrogate models

As explained in Section 3.2.3, because finding the Sobol′ indices involves an immense number of evaluations of the computationally expensive FE model, we created a surrogate model using our stochastic FE model and the PCE method as detailed in Section 3.2.4. In this section, we

present the results related to the error of the PCEs to analyze their accuracies with respect to the FE results.

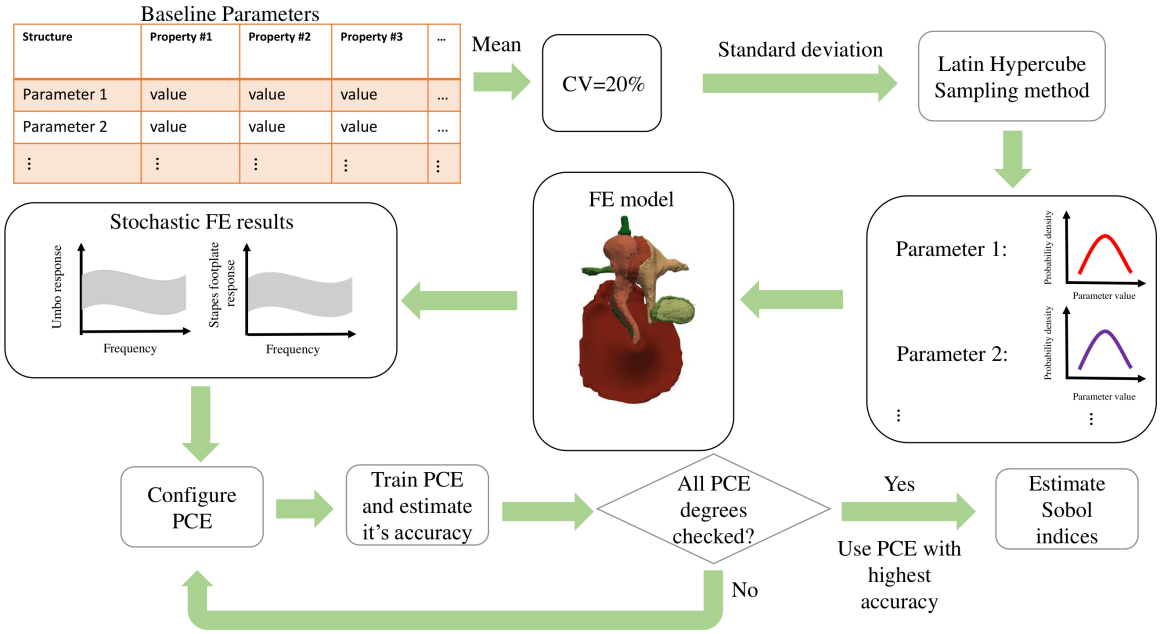


Figure 3-1 – Workflow of the stochastic FE modelling and global sensitivity analysis. We first created stochastic sets of model parameters with the mean values of the baseline model, CV of 20%, and normal distribution (half-normal for Poisson's ratio of incompressible materials). We then solved our FE model for all these sets of model parameters and found the distribution of our quantities of interest. The next step in our work was to use these stochastic sets of input and outputs to train PCEs for each quantity of interest and in each frequency. We used degree adaptive PCEs and found the degree for which, the PCEs had the highest accuracy with respect to the FE results. We then used these PCEs to estimate Sobol' indices to perform a global sensitivity analysis on the model.

Figure 3-2 presents the value of Q^2 for all three quantities of interest. A high value of Q^2 (near one) shows the high accuracy of the PCE to imitate the stochastic FE model at a lower computational cost. For all three quantities, the smallest error of PCE was attained at low-frequency responses (Q^2 of about 1). For the amplitude of the umbo and stapes footplate, the maximum error (the minimum Q^2 value of about 0.87) occurred near frequencies of 3.3 kHz

and 1.6 kHz, respectively. For the phase of the stapes footplate, the maximum error occurred near the frequency of 2.7 kHz and the minimum value of Q^2 was 0.74.

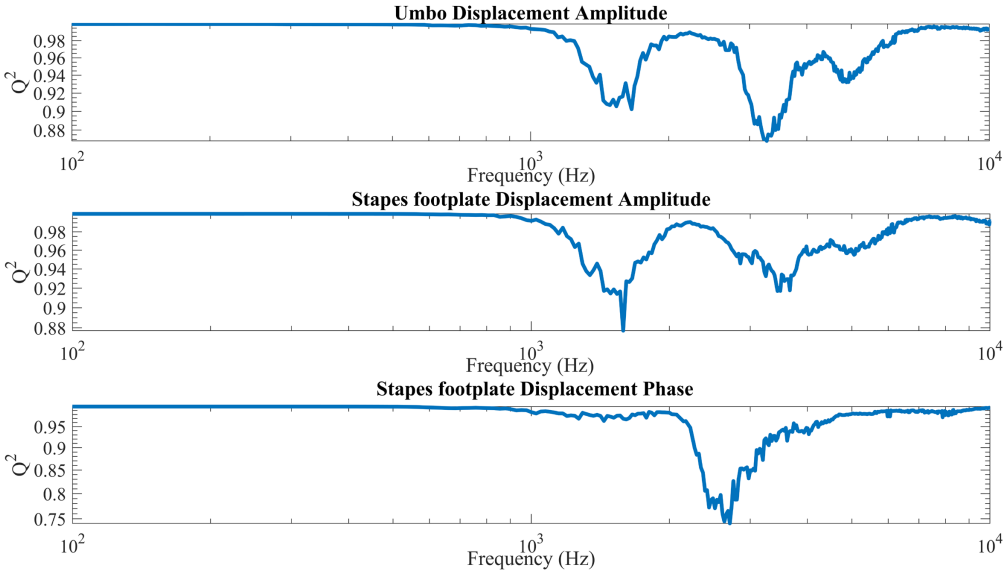


Figure 3-2 – Quality (in terms of Q^2) of the surrogate models to represent the stochastic finite-element model of the middle ear. The value of Q^2 is between zero and one and the larger is Q^2, the higher is the accuracy of the PCE with respect to the FE results. The value of Q^2 is shown for all quantities of interest (displacement amplitude of the umbo and stapes footplate and the displacement phase of the stapes footplate) at different excitation frequencies. For all three quantities of interest, the smallest error was attained at low frequencies. For displacement of the umbo and stapes footplate, the greatest error was attained at about 3.3 kHz and 1.6 kHz, respectively. Also, for the displacement phase of the stapes footplate, the greatest error was attained at about 2.7 kHz.

We also investigated how the LOO error changes with increasing the size of the training set of the PCEs at three frequencies F_{low} = 708 Hz, F_{mid} = 6.52 kHz, and F_{high} = 9.74 kHz (Figure 3-3). As expected, increasing the size of the training set resulted in decreasing the LOO error and for all three outputs of interest, the LOO error became less than 2% when 800 or more FE model evaluations were included in the training set of PCEs. Note that all results, except Figure 3, the size of the training set was 1992 as explained in Section 3.2.2.

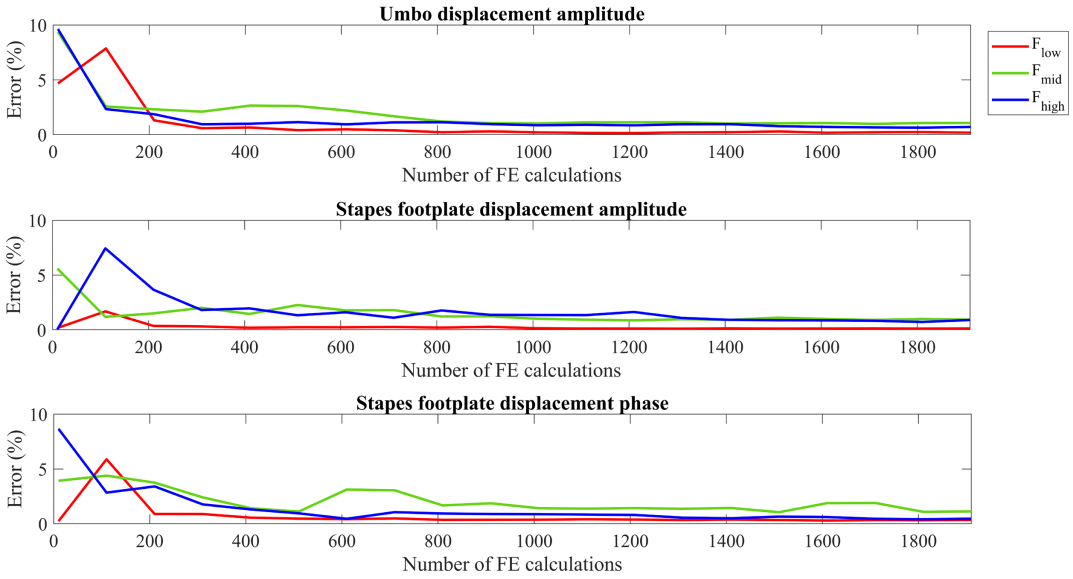


Figure 3-3 – Percentage of the leave-one-out (LOO) error of the created PCEs with respect to the number of FE calculations used in the training set of PCEs at three frequencies F_{low} =708 Hz, F_{mid} =6.52 kHz, and F_{high} =9.74 kHz for the three quantities of interest (displacement amplitude of the umbo and stapes footplate and phase of the stapes footplate). For all three frequencies and all three outputs of interest, a training set that consisted of more than 800 FE model calculation results, led to the LOO errors of less than 2%.

In order to analyze the accuracy of the created PCEs with respect to the FE results, we used them to calculate the umbo and stapes footplate frequency responses for two sets of parameters, that were not used in the training of PCEs. The PCE surrogate model calculations and the ground truth for these two parameter sets obtained using the FE model are compared in Figure 3-4. In column (a), the parameters of the baseline model (Table 2-1) were used to illustrate the accuracy of the PCEs (with respect to the FE results) when model parameters are very close to their mean values. At most frequencies, the responses obtained from PCE and FE are very close to each other (less than 1 dB in more than 90% of frequencies for the amplitude of the umbo and in 97% of frequencies for the amplitude of the stapes footplate) with maximum differences of 2.29 and 1.94 dB for the displacement amplitudes of the umbo and stapes

footplate, respectively. Moreover, the mean cosine difference between the PCE and FE phase among all frequencies in the frequency range of 100 Hz to 10 kHz is very close to one.

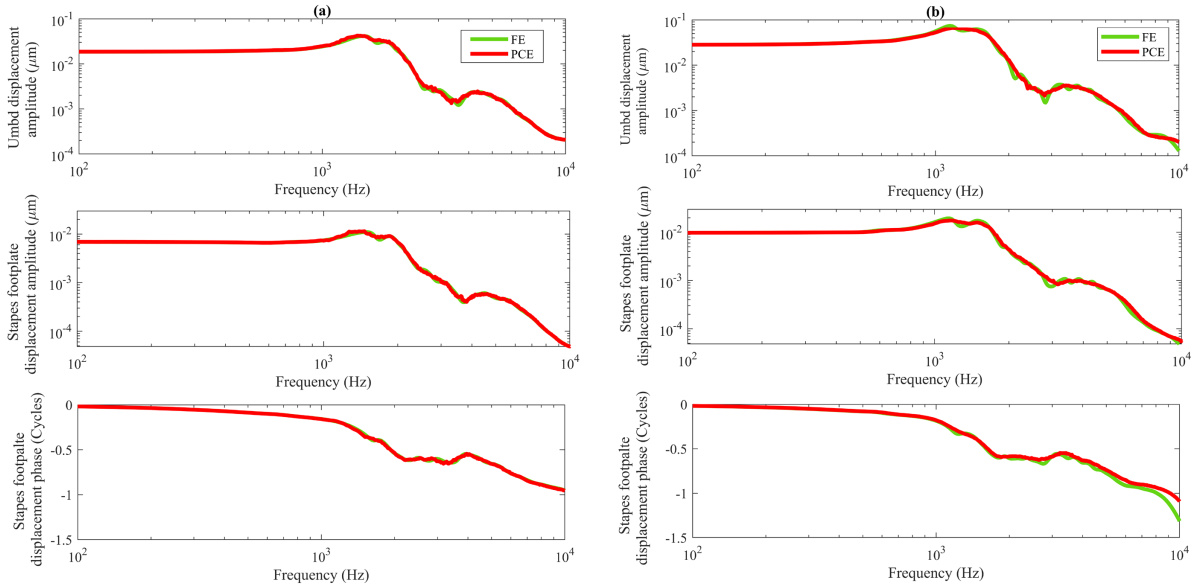


Figure 3-4 – Validation of PCE calculations against ground truth frequency responses obtained using the deterministic FE model. (a) Using the parameters of the baseline model and (b) using the parameter values obtained from the subtraction of the standard deviation of model parameters (with CV of 20%) from the values of the parameters of the baseline model. The two-parameter sets were not used in the training sets of PCEs. The results reveal that the PCEs can accurately calculate the umbo and stapes displacement responses (with respect to the FE results) even for points in the n-dimensional parameter space far from the mean of the parameter space.

To validate the PCE surrogate models for model parameters far from their mean values in the parameter space, we subtracted the standard deviation values of the model parameters (with CV of 20%) from their baseline values (Table 2-1). The results of PCE and ground truth FE calculations for this parameter set (presented in Appendix C) are shown in column (b) of Figure 3-4. Here also, the responses calculated using the PCEs are very close to the FE ground-truth ones with maximum differences of 4.00 dB and 2.90 dB for the amplitudes of the umbo and stapes footplate, respectively. Also, this difference is less than 1 dB in more than 65% and 75% of frequencies for the amplitudes of the umbo and stapes footplate, respectively. Also, the

mean cosine difference between the PCE and FE phase among all frequencies in the frequency range of 100 Hz to 10 kHz is 0.91.

These results demonstrate that the created PCEs can accurately reproduce the FE results at most frequencies even if the values of the model parameters are far from their mean values. This enabled replacing the expensive FE models with PCEs to avoid running the immense number of FE simulations (order of tens of thousands [108]–[110] for a model with the dimension of 32 parameters) required for global sensitivity analysis.

3.3.2 Global sensitivity analysis

In this section, we present the Sobol′ indices to study the effects of each of the model parameters and their interactions on the three quantities of interest mentioned in Section 3.3.1. We first focus on three specific frequencies introduced in Section 3.3.1 (F_{low} = 708 Hz, F_{mid} = 6.52 kHz, and F_{high} = 9.74 kHz) to be able to accurately assess the interactions of parameters using the first, second, and total order Sobol′ indices. These frequencies were chosen to represent three frequency ranges while based on quality results of Figure 3-2 the created PCEs have high accuracies (with respect to the FE results) at these frequencies (Q^2 of greater than 0.98).

It should be noted that in all figures in this section, the subscripts E, C and ν stand for the Young's modulus, the stiffness damping coefficient (α_2), and the Poisson's ratio, respectively. Also, "Thickness" is the thickness of the tympanic membrane, "Coc" stands for the cochlear load, and "Oss" stands for ossicles.

3.3.2.1 Umbo displacement amplitude at low frequency

Figure 3-5 shows the first, second, and total order Sobol′ indices for the three quantities of interest at F_{low} (708 Hz). Based on the values of the first-order Sobol′ index (red columns in the first row of Figure 3-5-a), the parameters that have the greatest effects on the displacement amplitude of the umbo are the thickness of the TM (0.29) and the Young's moduli of the TM (0.29), SAL (0.19), and ossicles (0.09). Also, the values of total-order Sobol′ indices in Figure 3-5-a (green stacked columns) show that the Young's modulus and thickness of the TM have

some interactions with other parameters as their total-order Sobol′ indices are greater (about 0.02) than their first-order indices. Our calculations of second-order Sobol′ indices (presented in Figure *3-5*-b) also confirm that the most significant interactions happen between the Young's modulus and thickness of the TM (second-order Sobol′ index of 0.02).

3.3.2.2 Stapes footplate displacement amplitude at low frequency

Based on the second row of Figure 3-5-a, values of the first-order Sobol′ indices (red columns), the parameter that has the highest impact on the displacement amplitude of the stapes footplate at F_{low} is the Young's modulus of the SAL (0.76). Also, the results show that the variations of the Young's modulus of the TM (0.07), damping of SAL (0.07), and thickness of the TM (0.04) have some effects on the displacement amplitude of the stapes footplate. The values of the total-order Sobol′ indices (green stacked columns in Figure 3-5-a) are very close to the values of the first-order Sobol′ indices for all parameters. This shows that the interactions among parameters are very small for the amplitude of the stapes footplate at F_{low}. The maximum values of second-order indices (presented in Figure 3-5-b) are in the order of 0.003.

3.3.2.3 Stapes footplate displacement phase at low frequency

The values of the first-order Sobol′ indices (red columns in the third row of Figure 3-5-a) show that the parameters that have the greatest impacts on the displacement phase of the stapes footplate at F_{low} are the damping of SAL (0.53) and the Young's modulus of SAL (0.24). The variations of the cochlear load (0.09), the Young's modulus of the TM (0.06), and thickness of the TM (0.04) also have some effects on the variations of the phase of the displacement of the stapes footplate at F_{low}. The values of the total-order Sobol′ indices (green stacked columns in Figure 3-5-a) are very close to the values of the first-order Sobol′ indices for all parameters. This demonstrates that the interactions among parameters are very small. This is confirmed by the small second-order Sobol′ indices (Figure 3-5-b) with the maximum value of about 0.003, suggesting poor interactions among parameters affecting the phase of the displacement of the stapes footplate at F_{low}.

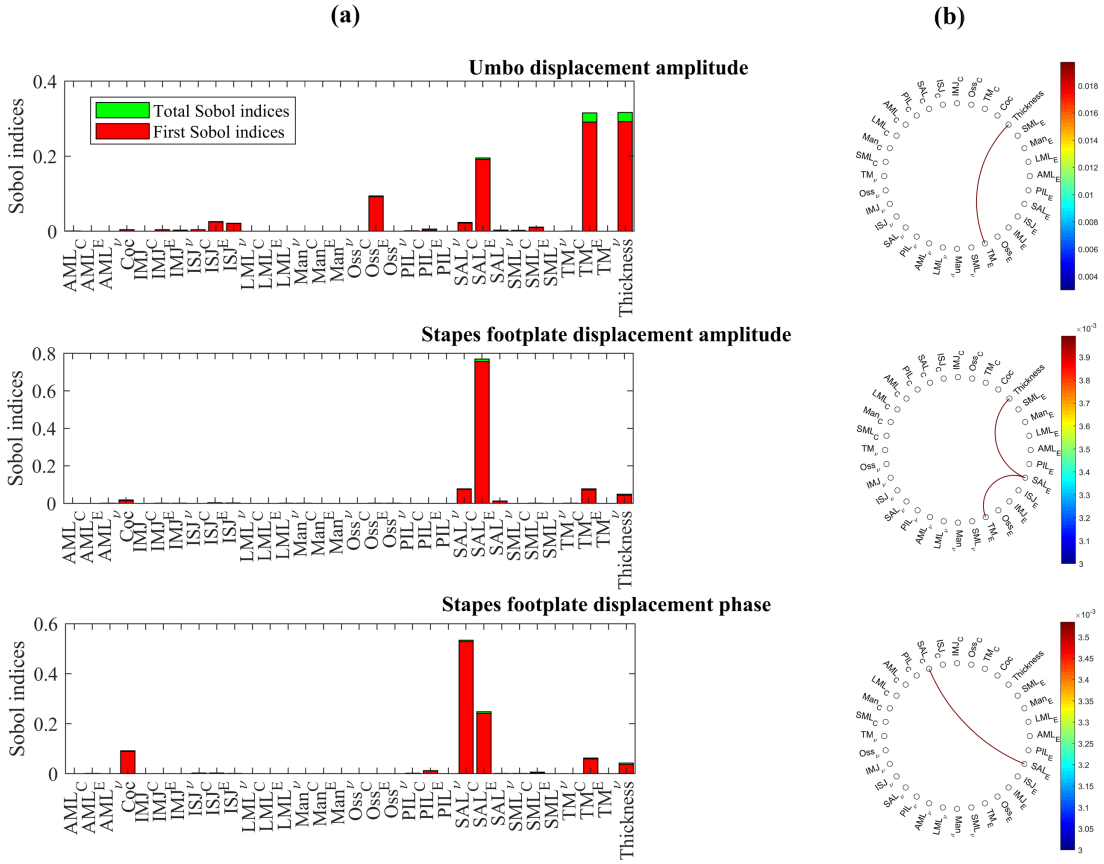


Figure 3-5 – Sobol' indices for the displacement amplitudes of the umbo and stapes footplate and displacement phase of the stapes footplate at F_{low} =708 Hz. Column (a) shows the first and total order Sobol' indices, and column (b) shows the values of second-order Sobol' indices (only second-order Sobol' indices greater than 0.003 are presented here). The values of the first-order Sobol' indices, show the direct effects of each of the input parameters on the variations of the outputs while the values of the second-order Sobol' indices represent the interactions between pairs of model parameters. Additionally, the values of the total-order Sobol' indices include the direct effect of each of the parameters as well as the effect of its interactions with other parameters on the variation of the output. The variations of the thickness of the TM and the Young's modulus of the TM, SAL, and ossicles have the greatest impact on the amplitude of the umbo. The variation of the Young's modulus of the SAL has the most significant impact on the amplitudes of the stapes footplate. Moreover, the variations of the Young's modulus and damping of the SAL have the most considerable impact on the phase of the stapes footplate. Also, the most considerable interactions among parameters happen between the Young's modulus and the thickness of the TM. The subscripts E, C and v stand for the Young's modulus, the stiffness damping coefficient (α_2), and the Poisson's ratio, respectively. Also, "Thickness" is the thickness of the TM, "Coc" stands for the cochlear load, and "Oss" stands for ossicles.

3.3.2.4 Umbo displacement amplitude at mid-frequency

Similarly, for the amplitude of the umbo displacement at F_{mid} (6.52 kHz), Figure 3-6 shows the following. The first-order Sobol′ indices (red columns) show that the Young's modulus of the TM (0.68) has the greatest impact and the thickness of the TM (0.08) and the Young's modulus of the ossicles (0.15) have some effects. Moreover, the values of the total-order Sobol′ indices (green stacked columns in Figure 3-6-a) and the second-order Sobol′ indices (Figure 3-6-b) demonstrate that the most significant interactions are among the Young's modulus and thickness of the TM (the second-order Sobol′ index of about 0.04).

3.3.2.5 Stapes footplate displacement amplitude at mid-frequency

For the amplitude of the displacement of the stapes footplate at F_{mid}, the second row of Figure 3-6 shows the following. Based on the values of first-order Sobol′ indices (red columns in Figure 3-6-a), the Young's modulus of the TM (0.65) has the highest impact followed by the Young's modulus of the SAL (0.07), damping of SAL (0.09), and the thickness of the TM (0.07). Also, the values of the total-order Sobol′ indices (green stacked columns) are greater than the values of the first-order Sobol′ indices for the thickness of the TM (difference of about 0.03) and the Young's modulus of the TM (difference of about 0.05). This suggests some interactions between these two parameters which is confirmed by the second-order Sobol′ indices of about 0.03 (Figure 3-6-b).

3.3.2.6 Stapes footplate displacement phase at mid-frequency

For the phase of the displacement of the stapes footplate at F_{mid}, the third row of Figure 3-6 shows the following. Based on the values of the first-order Sobol′ indices (red columns in Figure 3-6-a), the parameter that has the most considerable effects is the Young's modulus of the TM (0.67). Furthermore, the Young's modulus of the SAL (0.07) and the damping of and TM (0.04) have some effects. Also, there is a large difference (about 0.1) between the total-order Sobol′ indices (green stacked columns in Figure 3-6-a) and the first-order Sobol′ indices for the thickness and Young's modulus of the TM, showing considerable interaction between

these two parameters. The second-order Sobol′ indices (Figure 3-6-b) also show a high interaction between these two parameters (second-order index of about 0.1).

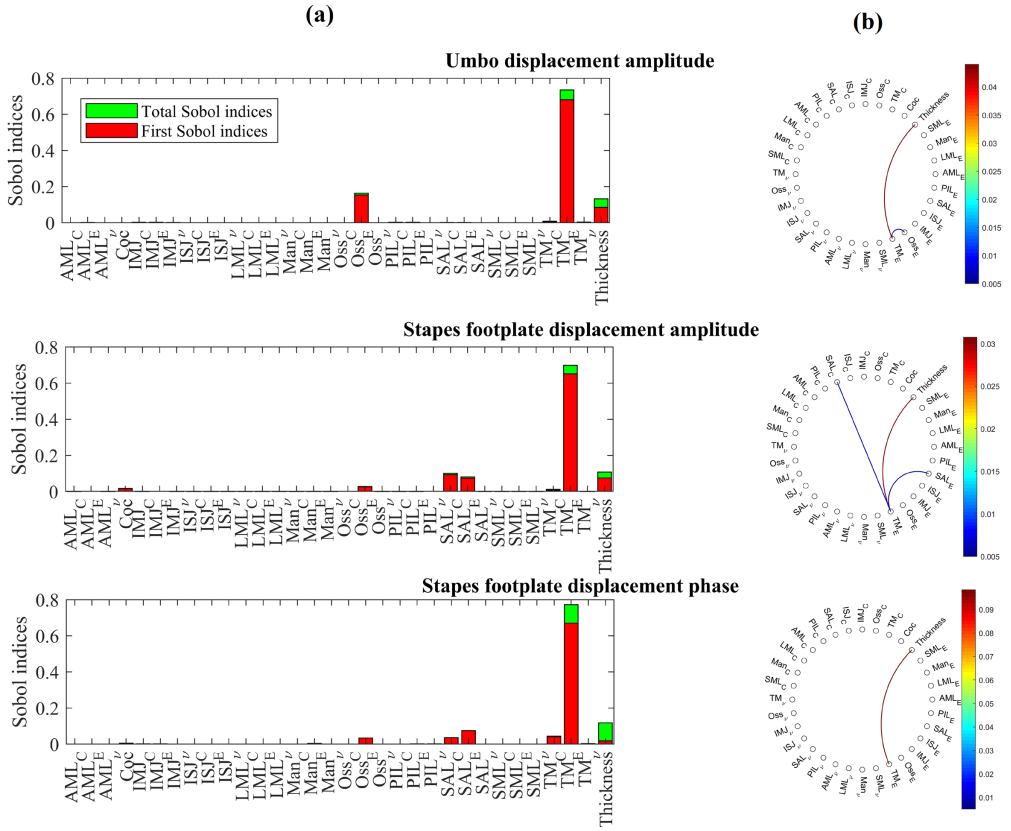


Figure 3-6 – First and total order Sobol' indices for all three quantities of interest at F_{mid} =6.52 kHz. Column (a) shows the first and total order Sobol' indices, while column (b) presents the values of second-order Sobol' indices (only second-order Sobol' indices greater than 0.005 are presented here). The values of the first-order Sobol' indices, show the direct effects of each of the input parameters on the variations of the outputs while the values of the second-order Sobol' indices represent the interactions between pairs of model parameters. Additionally, the values of the total-order Sobol' include the direct effect of each of the parameters as well as the effect of its interactions with other parameters on the variation of the output. The variations of the Young's modulus of the TM have the greatest impact on the amplitudes of the umbo and stapes footplate, and the phase of the stapes footplate at this frequency. Also, the most considerable interactions among parameters happen between the Young's modulus and the thickness of the TMThe subscripts E, C and v stand for the Young's modulus, the stiffness damping coefficient (α_2), and the Poisson's ratio, respectively. Also, "Thickness" is the thickness of the TM, "Coc" stands for the cochlear load, and "Oss" stands for ossicles.

3.3.2.7 Umbo displacement amplitude at high frequency

At F_{high} (9.74 kHz), Figure 3-7 presents the following for the umbo displacement magnitude. Based on the values of the first-order Sobol′ indices (red columns in Figure 3-7-a) the parameters that have the most significant impact are the Young's moduli of ossicles (0.59) and TM (0.26). Additionally, the values of the total-order Sobol′ indices (green stacked columns in Figure 3-7-a) are greater than the values of the first-order Sobol′ indices for some parameters such as the Young's modulus of the TM (difference of about 0.05) and ossicles (difference of about 0.03) suggesting some interactions among the model parameters. The second-order Sobol′ indices (Figure 3-7-b) help finding possible interactions. The greatest values of the second-order Sobol′ indices are related to the interactions between the Young's modulus of the TM and the Young's modulus of the ossicles (0.021), the Young's modulus and the thickness of the TM (0.012), and the Young's modulus and the damping of the TM (0.011).

3.3.2.8 Stapes footplate displacement amplitude at high frequency

The third row of Figure 3-7 shows the following at F_{high} for the displacement amplitude of the stapes footplate. Based on the values of the first-order Sobol′ indices (red columns in Figure 3-7-a) the parameters that have the greatest impacts are the Young's moduli of the TM (0.61) and ossicles (0.20). Furthermore, the differences between the values of the total-order and first-order Sobol′ indices (green stacked columns in Figure 3-7-a) for the Young's modulus of the TM (difference of about 0.07), thickness of the TM (difference of about 0.03), and damping of the TM (difference of about 0.03) indicate interactions for these parameters. Consistently, second-order Sobol′ indices (Figure 3-7-b) show that the highest value of the second-order Sobol′ indices (0.03) is related to the interaction between the Young's modulus and thickness of the TM. Additionally, interactions were observed between the Young's modulus and damping of the TM (second-order Sobol′ index: 0.022) and between the Young's modulus of the TM and ossicles (second-order Sobol′ index: 0.012).

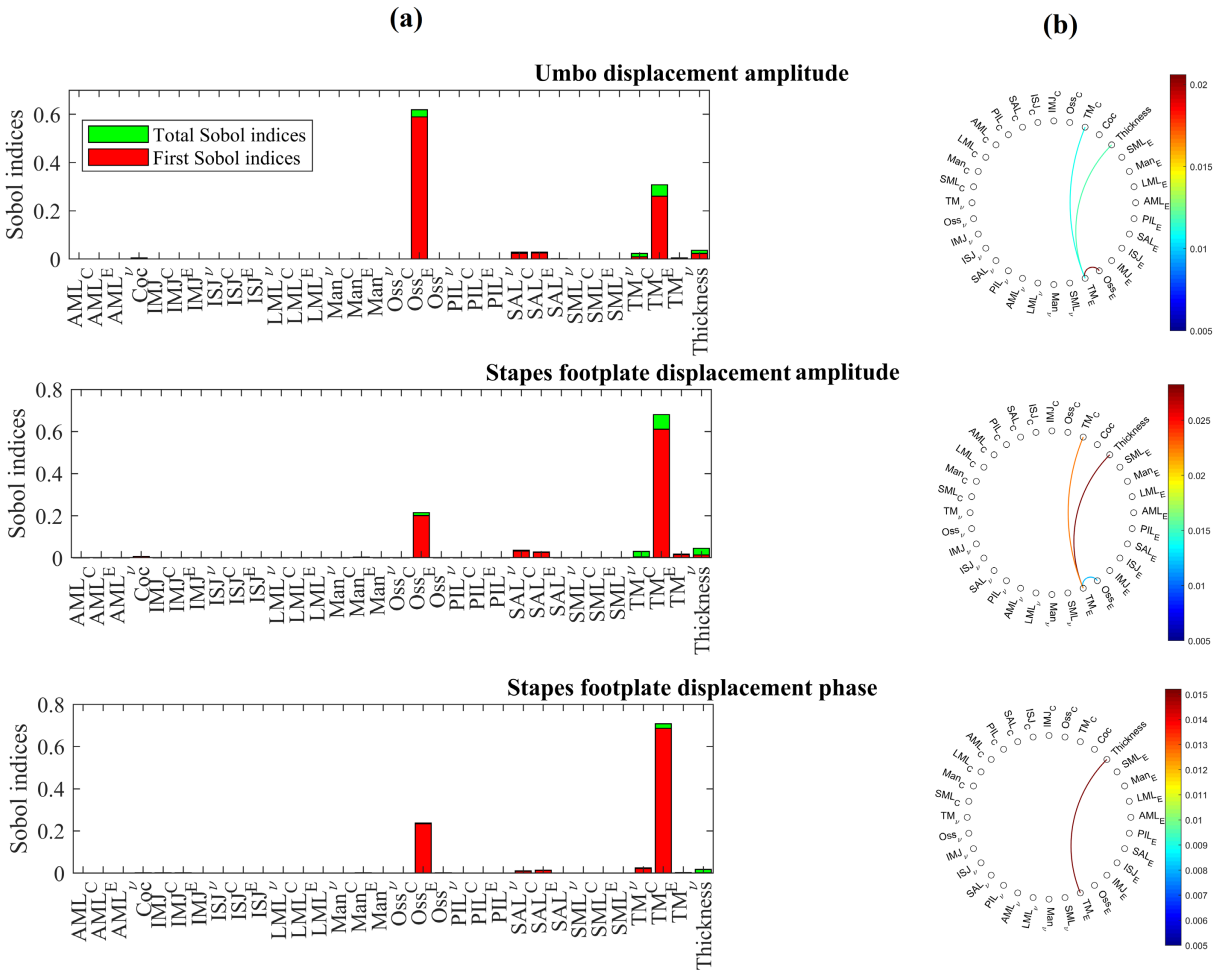


Figure 3-7 – Sobol' indices for all three quantities of interest at F_{high} =9.74 kHz. Column (a) shows the first and total order Sobol' indices, while column (b) presents the values of second-order Sobol' indices (only second-order Sobol' indices greater than 0.005 are presented here). The values of the first-order Sobol' indices, show the direct effects of each of the input parameters on the variations of the outputs while the values of the second-order Sobol' indices represent the interactions between pairs of model parameters. Additionally, the values of the total-order Sobol' include the direct effect of each of the parameters as well as the effect of its interactions with other parameters on the variation of the output. The variations of the Young's modulus of the TM and ossicles have the greatest impact on the amplitudes of the umbo and stapes footplate, and the phase of the stapes footplate at this frequency. Also, the most considerable interactions among parameters happen between the Young's modulus and the thickness of the TM. The subscripts E, C and ν stand for the Young's modulus, the stiffness damping coefficient (α_2), and the Poisson's ratio, respectively. Also, "Thickness" is the thickness of the TM, "Coc" stands for the cochlear load, and "Oss" stands for ossicles.

3.3.2.9 Stapes footplate displacement phase at high frequency

The values of the first-order Sobol′ indices (red columns in the third row of Figure 3-7-a) show that the parameters that have the most significant effects on the phase of the stapes footplate at frequency F_{high} are the Young's modulus of the TM (0.69) and ossicles (0.23). The values of the total-order Sobol′ indices (green stacked columns in Figure 3-7-a) are greater (about 0.02) than the values of the first-order Sobol′ indices for the thickness and Young's modulus of the TM. Second-order Sobol′ indices of 0.015 in the third row of Figure 3-7-b also confirm interaction between these two parameters.

3.3.2.10 Maximum parameter interactions at all frequencies

Figure 3-8 presents the maximum value of the second and total order Sobol′ indices at all frequencies in the range of 100 Hz to 10 kHz except the frequencies at which the values of Q^2 of the created PCE are less than 0.9 (Figure 3-2) for the three quantities of interest. The parameters with a total-order Sobol′ index of less than or very close to 0.02 (indicated by the thin red line in the Figure 3-8) are not investigated here. Based on the values of total-order Sobol′ indices in the first row of Figure 3-8-a, the parameters that have the greatest effects on the displacement amplitude of the umbo are the Young's moduli of the TM (0.92), ossicles (0.64), SAL (0.50), and the thickness of the TM (0.86). Also, the dampings of the TM (0.07), SAL (0.04) and ISJ (0.03), Young's moduli of PIL (0.05) and ISJ (0.06), and Poisson's ratio of ISJ (0.04). Besides, the total-order Sobol′ indices (second row of Figure 3-8-a) show that the parameters that have the highest impact on the displacement amplitude of the stapes footplate are the Young's moduli of the SAL (0.97), TM (0.80), and ossicles (0.22), the thickness of the TM (0.68) and damping of SAL (0.36). Also, the variations of the cochlear load (0.07) and the damping of the TM (0.04) have some impacts on the variations of the amplitude of the stapes footplate. Additionally, the values of the total-order Sobol′ indices shown in the third row of Figure 3-8-a demonstrate that the parameters that have the greatest impact on the phase of the stapes footplate are the damping of the SAL (0.72), the Young's moduli of the TM (0.92), ossicles (0.30), and SAL (0.29), and the thickness of the TM (0.79). Furthermore, the variations of the Young's modulus of the PIL (0.04), cochlear load (0.14),

and damping of the TM (0.13) have some impacts on this quantity of interest at different frequencies.

Besides, Figure 3-8-b illustrates that for all three outputs of interest, the maximum value of the second-order Sobol′ index related to the interactions between the Young's modulus and the thickness of the TM is considerably larger than the values of the second-order Sobol′ indices related to the other interactions among model parameters.

3.3.2.11 Parameter importance as a function of continuous frequency

Figure 3-9, Figure 3-10, and Figure 3-11 show the values of the total-order Sobol′ indices as functions of excitation frequencies in the range of 100 Hz to 10 kHz for the three outputs of interest. It should be noted that as Figure 3-2 shows, the estimation errors of the created PCEs vary by frequency and as a result, at some frequencies the values of Sobol′ indices may be less accurate.

Figure 3-9 presents the values of the frequency-dependent total-order Sobol′ indices for the displacement amplitude of the umbo. At low frequencies (below 1 kHz), the Young's modulus of SAL has the most considerable effects on the displacement amplitude of the umbo and the variations of the thickness of the TM and the Young's moduli of the TM and ossicles have some effects. At higher frequencies, the effects of the Young's modulus of SAL become smaller, but the effects of the Young's modulus of the TM and ossicles, and the thickness of the TM become considerably larger.

Figure 3-10 presents the values of frequency-dependent total-order Sobol′ indices for the amplitude of the stapes footplate. Similar to the displacement amplitude of the umbo, at low frequencies (below 1 kHz), the parameter that has the greatest impact on the displacement amplitude of the stapes footplate is the Young's modulus of SAL, while at high frequencies, the effects of variations of this parameter become smaller and the effects of the variations of the Young's modulus and thickness of the TM become considerable. Additionally, the impacts of variations of the damping of SAL are considerable around 5 kHz and the variations of the Young's modulus of the ossicles have some effects at frequencies higher than 8 kHz.

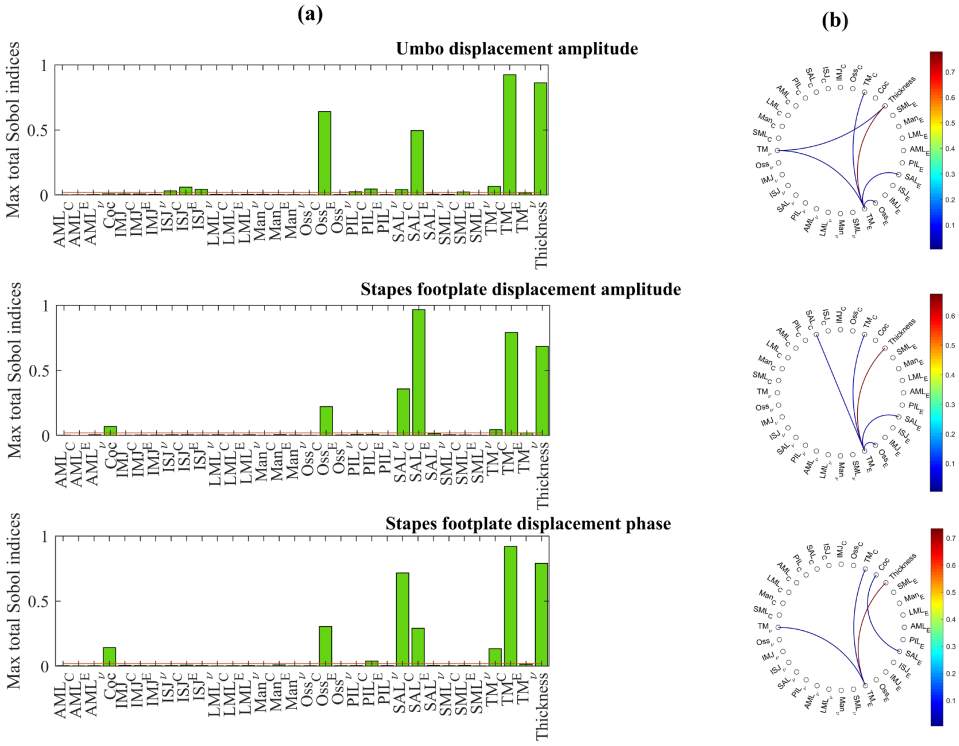


Figure 3-8 – Column (a): maximum value of the total-order Sobol' indices for the three quantities of interest among all frequencies in the range of 100 Hz to 10 kHz for which the value of Q^2 of the created PCE is greater than 0.9. The thin red lines show the total-order Sobol' index of 0.02. Column (b): maximum values of the second-order Sobol' indices among the same frequencies in (a) (only the second-order Sobol' indices greater than 0.005 are shown). The values of the first-order Sobol' indices, show the direct effects of each of the input parameters on the variations of the outputs while the values of the second-order Sobol' indices represent the interactions between pairs of model parameters. Additionally, the values of the total-order Sobol' indices include the direct effect of each of the parameters as well as the effect of its interactions with other parameters on the variation of the output. The variations of the thickness of the TM and the Young's modulus of the TM, SAL, and ossicles have the greatest impact on the amplitude of the umbo. The variation of the thickness and Young's modulus of the TM, Young's modulus and damping of the SAL, and Young's modulus of the ossicles have the most significant impact on the amplitude of the stapes footplate. Moreover, the variations of the Young's modulus and thickness of the TM, the Young's modulus and damping of the SAL, and the Young's modulus of the ossicles have the most considerable impacts on the phase of the stapes footplate. Also, the most considerable interactions among all frequencies considered here happen between the Young's modulus and the thickness of the TM. The subscripts E, C and ν stand for the Young's modulus, the stiffness damping coefficient (α_2), and the Poisson's ratio, respectively. Also, "Thickness" is the thickness of the TM, "Coc" stands for the cochlear load, and "Oss" stands for ossicles.

Figure 3-11 presents the values of frequency-dependent total-order Sobol′ indices for the displacement phase of the stapes footplate. At low frequencies (below 1 kHz), the damping of SAL and at high frequencies, the thickness and Young's modulus of the TM have the greatest effects. Additionally, the variations of the Young's moduli of the SAL and ossicles have some impacts at some frequencies while the variations of the cochlear load have some minor effects at some frequencies.

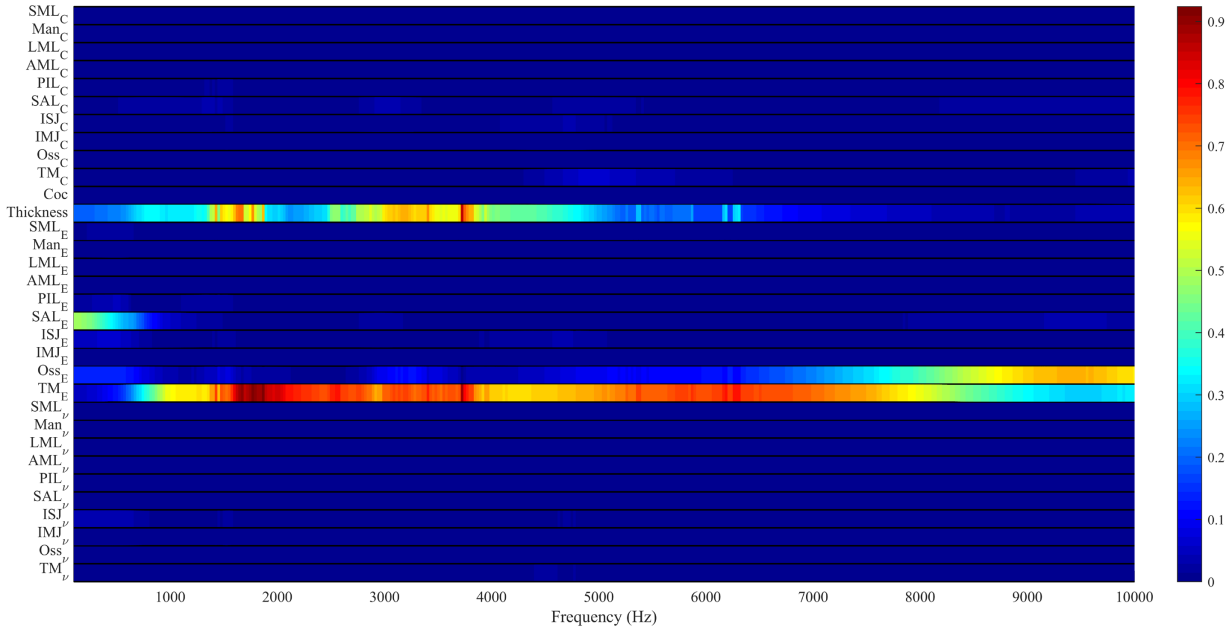


Figure 3-9 – Total-order Sobol' indices for the displacement amplitude of the umbo. The values of the total-order Sobol' indices include the direct effect of each of the parameters as well as the effect of its interactions with other parameters on the variation of the output. At low frequencies, the variations of the Young's modulus of the SAL have the highest impact on the variations of the displacement amplitude of the umbo, while at higher frequencies, the effects of this parameter become small and the impacts of variations of Young's modulus of TM and ossicles and the thickness of the TM become considerable. The subscripts E, C and ν stand for the Young's modulus, the stiffness damping coefficient (α_2), and the Poisson's ratio, respectively. Also, "Thickness" is the thickness of the TM, "Coc" stands for the cochlear load, and "Oss" stands for ossicles.

3.4 Discussions

In this study, we performed a global sensitivity analysis of the middle-ear model by calculating Sobol′ indices. The global sensitivity analysis helped us to understand the relative importance of the uncertainty of the model parameters on its predictions and how these parameter uncertainties interact with one another. To avoid the computational cost of the FE model, we created surrogate models using PCEs for the displacement amplitudes of the umbo and stapes footplate and the displacement phase of the stapes footplate in the range of 100 Hz to 10 kHz using the stochastic FE model results. We then used these PCEs for finding the first, second, and total order Sobol′ indices. The first-order Sobol′ indices show the direct impact of the variation of each of the model parameters on the variations of the outputs. The second-order Sobol′ indices show the interactions among pairs of parameters and total-order Sobol′ indices are the summation of the first-order Sobol′ index and higher-order indices.

In Section 3.3.1, we demonstrated that the number of FE simulations in this chapter (1992) was enough to have accurate PCEs (with respect to the FE results) at most frequencies. Based on the results, the created PCEs had quality values (Q^2) of greater than 0.95 at most frequencies in the range of 100 Hz to 10 kHz. Also, using two case studies with parameter values near and far from the mean of the parameter values, we demonstrated that the created PCEs were very accurate (with respect to the FE results) at most frequencies. These results show that the created PCEs can be used as reliable replacements for the FE model results at most frequencies and using them, instead of running heavy FE simulations, the response of the middle ear can be calculated in a few seconds. These surrogate models can be used in applications other than global sensitivity analysis where an instant calculation of the middle ear response is required (e.g., for developing real-time surgical simulators) [116], [117].

The results presented in Section 3.3.2 demonstrated that the greatest interactions among parameters happen between the Young's modulus and thickness of the TM. These two parameters affect the stiffness of the TM and therefore they are expected to be naturally coordinated. Furthermore, the observation of strong interactions between the Young's modulus and thickness of the TM is consistent with our previous observations of anti-

resonances in the umbo response for some sets of model parameters in Chapter 2. Our investigation showed that for most sets of model parameters that lead to those anti-resonances in the model outputs, the values of the Young's modulus and thickness of the TM were simultaneously below their mean values.

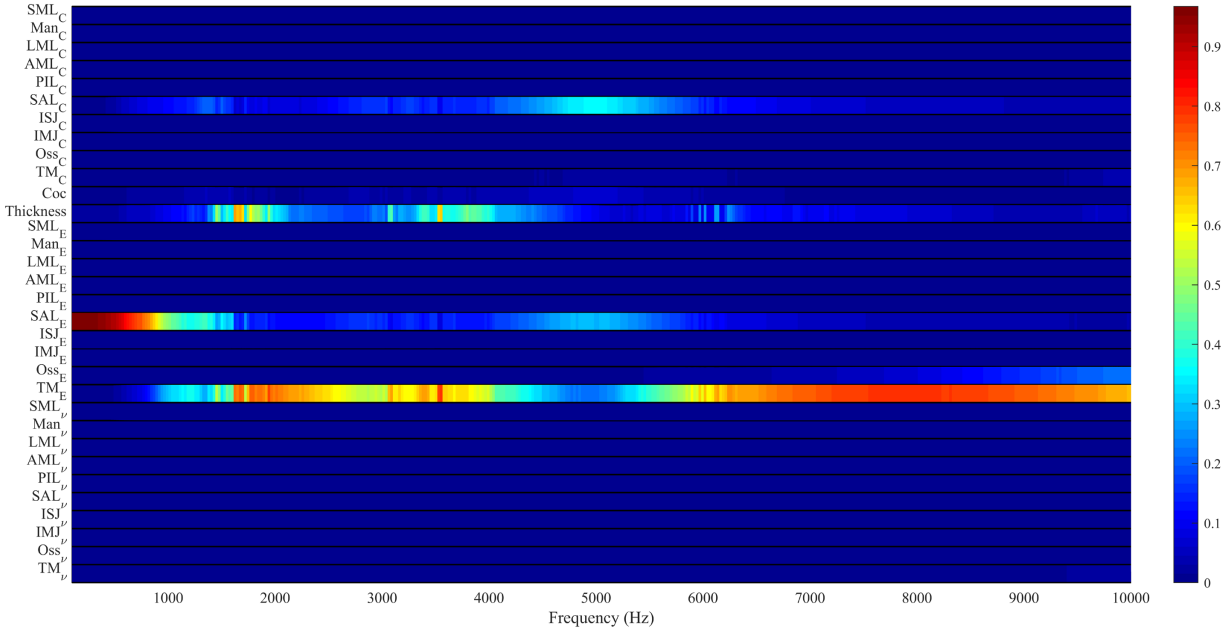


Figure 3-10 – Total-order Sobol' indices for the displacement amplitude of the stapes footplate. The values of the total-order Sobol' indices include the direct effect of each of the parameters as well as the effect of its interactions with other parameters on the variation of the output. At low frequencies, the variations of the Young's modulus of the SAL have the highest impact on the variations of the amplitude of the stapes footplate, while at higher frequencies, the parameters that have the highest impact on the variations of the output are the thickness and Young's modulus of the TM. In addition, the effects of damping of the SAL are also considerable at some frequencies. The subscripts E, C and ν stand for the Young's modulus, the stiffness damping coefficient (α_2), and the Poisson's ratio, respectively. Also, "Thickness" is the thickness of the TM, "Coc" stands for the cochlear load, and "Oss" stands for ossicles.

Other studies in the literature have also reported the significance of the Young's modulus and thickness of the TM. For instance, the sensitivity analysis results of the study performed by Maftoon et al. also concluded that the thickness and Young's modulus of TM are among the

most influential parameters in the middle ear [37]. However, due to the limitations of the one-at-a-time sensitivity analysis methods, the interactions between these two parameters were not quantitatively demonstrated in previous studies.

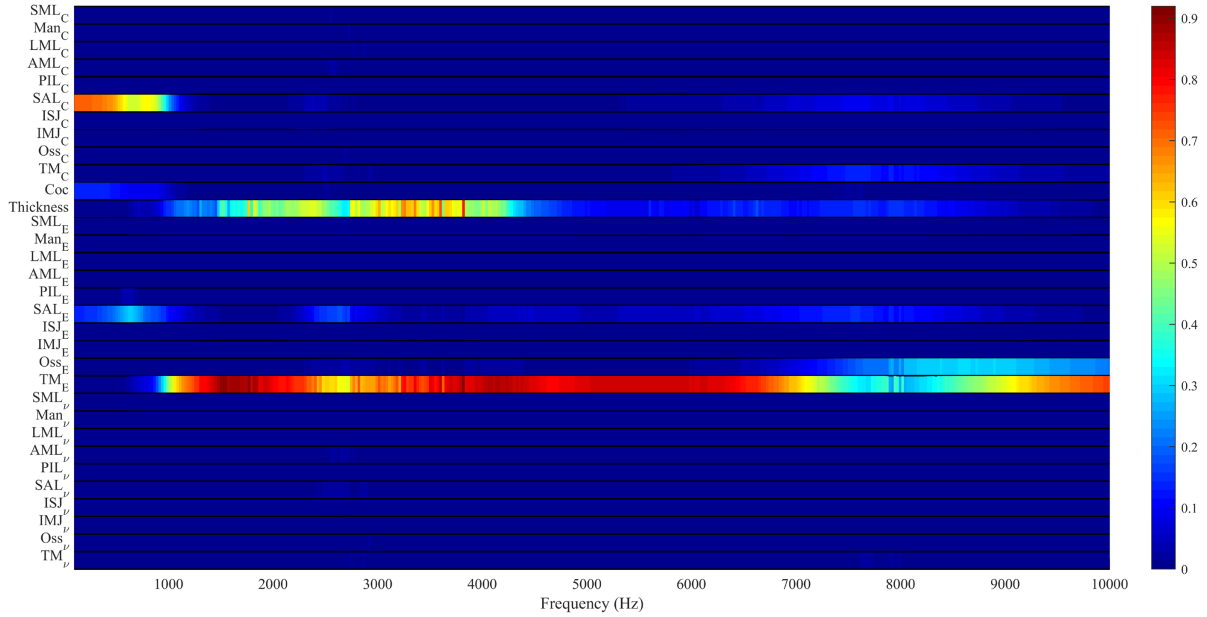


Figure 3-11 – Total-order Sobol' indices for the stapes footplate displacement phase. The values of the total-order Sobol' indices include the direct effect of each of the parameters as well as the effect of its interactions with other parameters on the variations of the output. At low frequencies, the variations of the damping of the SAL have the highest impact on the displacement phase of the stapes footplate. At higher frequencies, the effects of this parameter become small and the parameters that have a high impact at those frequencies are the thickness of the TM and the Young's modulus of the TM. The subscripts E, C and v stand for the Young's modulus, the stiffness damping coefficient (α_2), and the Poisson's ratio, respectively. Also, "Thickness" is the thickness of the TM, "Coc" stands for the cochlear load, and "Oss" stands for ossicles.

We also observed that at some frequencies, the value of the first-order Sobol′ index of some specific parameters is very small and does not show the importance of that parameter, whereas the values of the total-order Sobol′ index are remarkably larger and can represent the actual contribution of the parameter. Because the first-order Sobol′ index provides information

similar to one-at-a-time sensitivity analysis, this observation demonstrates that the global sensitivity analysis method, implemented in this study, is capable of uncovering previously unknown contributions of some model parameters. For instance, based on the results presented in Sections 3.3.2.6, 3.3.2.8, and 3.3.2.9, the first-order Sobol′ index does not show the significance of the effects of the thickness of the TM at mid to high frequencies. However, the total-order Sobol′ index reveals the real contribution of the thickness of the TM and its interaction with the Young's modulus of the TM at those frequencies.

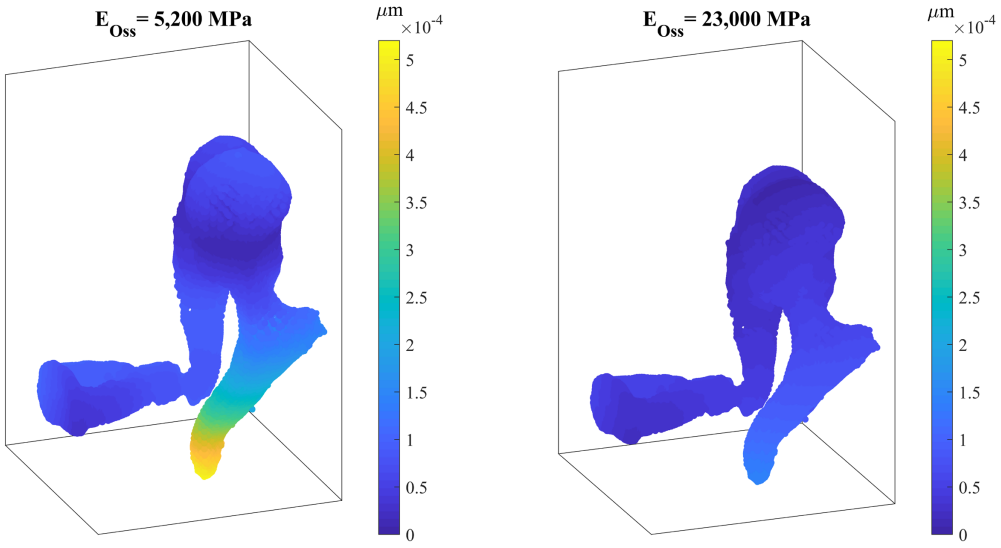


Figure 3-12 – Displacement amplitude of the ossicles in the direction of the stapes footplate piston-like motion at the excitation frequency of 10 kHz. The values of the Young's modulus of all three ossicles were 5,200 MPa for the results presented in the left panel and 23,000 MPa for the result illustrated in the right panel. The values of other parameters were the same as the values presented in Table 2-1 for both simulations. The results show that, as suggested by the values of Sobol' indices calculated in Section 3.3.2.11, at very high frequencies, the variations of the Young's modulus of ossicles can have significant effects on the motions of manubrium, and also some weaker effects on the stapes crura and pedicle of the incus. The maximum values of the displacement amplitude of the ossicles (that occur at the umbo) obtained from the models with the Young's moduli of 5,200 MPa and 23,000 Mpa are 0.52 nm and 0.15 nm, respectively.

Although our results show that the most significant interactions happen between the Young's modulus and the thickness of the TM, we observed some weaker interactions between other pairs of parameters at some specific frequencies (Section 3.3.2). It should be mentioned that the maximum values of the second-order Sobol′ indices (reported in Section 3.3.2.10) for the interaction between the thickness and Young's modulus of the TM were in the order of about 0.7. However, the maximum values of the second-order Sobol′ indices for interactions among other parameters had orders of around 0.01. This shows that those interactions are remarkably weaker than the interactions between the Young's modulus and thickness of the TM. Based on the results of Section 3.3.2.10, those interactions (second-order Sobol′ index of greater than 0.005) occur between the Young's modulus of the TM and Young's modulus of the ossicles; Young's modulus and damping of the TM; Young's modulus of the TM and Young's modulus of the SAL; Young's modulus of the TM and damping of the SAL; cochlear load and Young's modulus of the SAL; Young's modulus and Poisson's ratio of the TM; and Poisson's ratio and thickness of the TM. Some weaker interactions might also exist that have smaller values of the second-order Sobol′ index and hence are not listed here.

At the low frequency (708 Hz, Figure 3-5), the second-order Sobol′ index demonstrated interactions of the Young's modulus of the SAL with the Young's modulus and thickness of the TM. This is consistent with the notion of the middle ear as a simple one degree of freedom stiffness-dominated oscillator at low frequencies [36], [118]. In this notion, the stiffness of the TM and SAL can be thought to work in series.

Additionally, based on the results of total order Sobol′ indices for different structures of the model (Section 3.3.2.10 and Section 3.3.2.11), the Young's modulus of the TM, Young's modulus of the SAL, thickness of the TM, and Young's modulus of ossicles have remarkable effects on the displacement amplitudes of the umbo and stapes footplate and the phase of the stapes footplate. Moreover, the damping of the SAL has considerable effects on the amplitude of the stapes footplate and the damping of the SAL and cochlear load have significant effects on the phase of the stapes footplate. Many of these parameters such as the Young's modulus of the TM, Young's modulus of the SAL, and thickness of the TM have been reported in the

literature as the parameters with great impacts on the middle ear vibration outputs [37], [55], [101].

One of the intriguing findings of the current study is the impacts of the Young's modulus of the ossicles at very high frequencies (above 8 kHz) that can be interpreted from the results presented in Sections 3.3.2.7 to 3.3.2.9 and Section 3.3.2.11. To the best of the authors' knowledge, these effects have not been observed in previous studies. Based on the values of Sobol′ indices, the impacts of variations of the Young's modulus of ossicles at these frequencies are more noticeable in the motions of the umbo than the motions of the stapes footplate. To investigate the reason for the considerable effects of the Young's modulus of the ossicles at those high frequencies, we ran two simulations with two different values of the Young's modulus of ossicles far from each other (5,200 MPa and 23,000 MPa, very close to the minimum and maximum in Appendix C). All other model parameters for these two simulations were considered to be the same as the baseline values reported in Table 2-1. We performed harmonic analysis at 10 kHz and the results of the simulations are provided in Figure 3-12. The results show that, at 10 kHz, the low values of the Young's modulus of ossicles in the probability distribution function (here 5,200 MPa) allowed flexing in the manubrium, and to a lower degree in the stapes crura and pedicle of the incus. The maximum values of the displacement amplitude of the ossicles (that occur at the umbo) were 0.52 nm and 0.15 nm, obtained from the models with the Young's moduli of 5,200 MPa and 23,000 MPa, respectively. These results confirm that the variations of the Young's modulus of ossicles can have substantial effects on the motions in the middle ear. The considerable effects on the deformations observed in the manubrium area are consistent with the larger values of Sobol′ indices in the umbo responses in comparison to those associated with the stapes footplate responses (Sections 3.3.2.7 to 3.3.2.9 and Section 3.3.2.11). Consistently, Figure 3-7 shows interactions between the Youngs moduli of the TM and the ossicles in the umbo displacement at 9.74 kHz.

Moreover, our results demonstrate that for some parameters (Young's modulus of AML, IMJ, LML, and manubrial fold, Poisson's ratio of AML, IMJ, LML, manubrial fold, PIL, and SML,

and damping of AML, IMJ, LML, manubrial fold, and SML), the maximum values of total-order Sobol′ indices at all frequencies are very close to zero. This systematically establishes that the variations of these parameters do not have considerable impacts on the variations of the amplitudes of the umbo and stapes footplate and phase of the stapes footplate and also these parameters do not have significant interactions with other parameters. Thus, accurate identification of these parameters is not critical in obtaining accurate models of the middle ear, and inter-individual differences of these parameters among humans do not contribute to the statistical distribution of the middle-ear output. Some of these parameters were reported by other researchers as less-influential parameters as well. For instance, Greef et al. concluded that the variations of some model parameters such as the Young's modulus and loss factor (damping) of tympano-mallear connection (manubrial fold) and Young's modulus of IMJ did not have significant effects on their model outputs [101].

Chapter 4

Material characterization of thin planar structures using full-field harmonic vibration response measured with stroboscopic holography

Published in the International Journal of Mechanical Sciences, 15 May 2021, Volume 198, 106390 [79].

Preface

In this chapter, we present a novel method for estimating the Young's modulus of 2D thin planar structures. Our method uses harmonic full-field vibration pattern of the structure, obtained using holography, for parameter estimation. We ran different case studies obtained from analytical solutions, numerical solutions, and experimental measurements to investigate the accuracy of our proposed method. This chapter establishes the main basis for the methodology of the material characterization of the middle ear presented in Chapter 5. In Chapter 5, we benefit from the global sensitivity analysis results presented in Chapter 3 and the material characterization method presented in this chapter to propose a method for fast estimation of the most influential parameters of the middle ear.

Overview

We propose a novel material characterization method to estimate the Young's modulus of thin 2D structures using non-modal noisy single frequency harmonic vibration data measured with holography. The method uses finite-difference discretization to apply the plate equation to all measured pixels inside the boundary of the vibrating structure and then treats the problem as a Bayesian optimization process to find the value of the Young's modulus by minimizing the Euclidian distance between the measured displacement field and repeatedly calculated displacement field using the plate equation. In order to assess the accuracy of the method, ground truth harmonic displacement magnitude fields of different plates were obtained using analytical solutions and the finite-element method and were used to estimate the Young's moduli. We applied Gaussian and non-Gaussian noise with different intensities to assess the robustness and accuracy of the proposed material characterization method in the presence of noise. We demonstrated that for multiple benchmarks for signal to noise ratio of down to 0 dB, our proposed method had errors of less than 5%. We also quantified the effects of uncertainties in the geometrical and material parameters as well as boundary conditions on the estimated Young's modulus. Furthermore, we studied the effects of the mesh size on the runtime and applied the method to experimental holography vibration measurement data of a copper plate.

4.1 Introduction

Holography has been used in recent years to perform high-resolution vibrometry for different applications such as noise reduction [119], energy-flow measurements [120], measurement of ultrasonic surface wave fields [121], and piezoelectric surface vibration characterization [122]. It was also used to study the motions of the tympanic membrane with a high spatial resolution [72], [73], [123], [74].

In the present chapter, we propose a method that will be the basis for further developments for estimating the Young's modulus of the tympanic membrane as a diagnostic index for hearing pathologies. This method uses noisy 2D full-field high-spatial-resolution holographic stroboscopic measurements of the harmonic motion at a single frequency. Although recently some researchers have worked on the transient response and modal parameters of the tympanic membrane [124], [125], for material characterization in this work, we use harmonic measurements because they can provide better signal to noise ratio than transient measurements do and they are possible with less expensive hardware (e.g., no need for an expensive high-speed camera). Hence, the main novelty of the present work is to enable material characterization using only single frequency full-field noisy vibration measurements data. Because the proposed method does not require data with a high signal to noise ratio, no averaging is needed and the data can be collected quickly. This is especially important for applications such as medical applications where movement of the subject, breathing and heart beats can interfere with measurements.

Caillet et al. used the data from the nearfield acoustic holography to estimate the Young's modulus of 2D structures [126]. They used the plate equation and the finite-difference method to estimate the Young's modulus using free-vibration holography data. Alfano et al. presented a method for estimating the Poisson's ratio and Young's modulus of thin plates using two of the first four natural frequencies [127]. Labelle et al. presented a method for estimating material properties from modal data extracted from video of the vibrating object [128]. To show the accuracy of their proposed method, they used modal data obtained using different techniques (visual vibrometry, laser Doppler vibrometry, and accelerometers) for estimating the

mechanical properties of a steel cantilever and compared the results with each other. Hasheminejad et al. used scanning laser Doppler vibrometry measurements to develop a method for estimating the Young's modulus of asphalt mixtures with modal data [129]. Material characterization using vibration data can be performed using finite-element model updating but much of the literature of finite-element model updating was developed for modal data [130] and therefore cannot be used with harmonic vibration data. More detailed reviews of the different vibration-based methods for material characterization can be found in [131] and [132]. However, to the best of our knowledge, no method exists in the literature that can find the material properties of 2D structures using single frequency harmonic vibration measurements data especially for data affected by noise.

Various methods have been used to find the dynamic response of plates including some analytical methods for simple geometries [133] and numerical methods such as finite element and finite difference for more complicated geometries [134]. Because stroboscopic digital holography provides vibration data on a 2D image of the structure, the vibration field is known on an equally-spaced structured grid that is easy to implement using the finite-difference method. The finite-difference method was successfully used by some researchers to study the vibrations of plates (e.g., the free vibration of stiffened plates [135], the vibrations of a beam-plate structure in the time domain [136], and axially-moving viscoelastic plates [137]).

To find the Young's modulus, we formulated the parameter estimation as an optimization problem. Our long-term goal is to develop the material characterization method to be used for clinical hearing diagnosis and therefore to reduce the calculation time and make it relevant for real time clinical use, it is important to be able to find the global optimum using the fewest possible number of iterations. Bayesian optimization is a global optimization method which creates a surrogate model of the objective function that is cheaper to evaluate than the real objective function and is updated in each iteration. Bayesian optimization is known to be able to find the global optimum with a fewer number of iterations in comparison with many other optimization algorithms such as particle swarm, pattern search, and genetic algorithm [138]–[141]. A review of Bayesian optimization can be found in [140].

Bayesian finite-element model updating was also the subject of several studies for different applications such as parameter estimation and robust prediction of the desired outputs [142]. Yuen et al. used Bayesian model updating to find optimized values of the modal parameters as well as the uncertainties associated with them [143]. Moravej et al. used the Bayesian technique to calibrate a structural finite-element model based on modal vibration measurements for health monitoring purposes [144]. Unlike these studies that used experimental modal data, our proposed finite-difference-based method estimates material parameters using single frequency vibration measurement data and Bayesian optimization. The chapter is organized as follows: Section 4.2 is dedicated to the methodology including the details of the material characterization procedure. In Section 4.3 we present the validation of the proposed method using analytical, numerical, and experimental benchmarks, respectively. We also studied the effects of different uncertainties as well as the effects of Gaussian and non-Gaussian noise on the accuracy of the proposed parameter-estimation method. In Section 4, we discuss the performance of the Bayesian optimization and the limitations of the proposed method.

4.2 Materials and Methods

Figure 4-1 shows the flowchart of the proposed material characterization method. This method uses the holography measurements of the harmonic vibration at different stroboscopic phases to obtain the displacement magnitude and phase. It then solves the governing equation of the motion of the structure for all of the nodes inside the boundary at each frequency and eventually finds the optimum Young's modulus which yields a finite-difference solution of the plate equation with a displacement magnitude field as close as possible to the one measured using holography. Details of the proposed method are as follows:

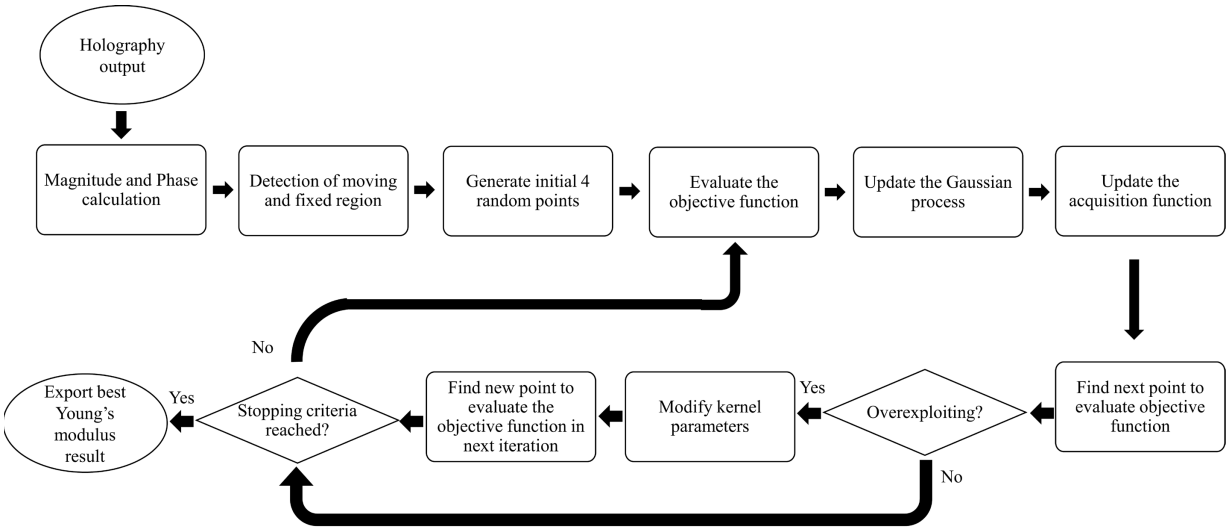


Figure 4-1 – Flowchart of the proposed material characterization method. The magnitude and phase of the displacements of the nodes inside the vibrating domain are calculated from holography data and the full-field displacement is then used to find the boundaries of the vibrating domain. Our proposed material characterization method is based on the Bayesian optimization process. It begins by considering four initial random guesses for the Young's modulus, applying the plate equation to all nodes inside the detected boundary for these random guesses and evaluating the objective function (the Euclidean distance between the measured and calculated fields). Then the Gaussian process regression model and the acquisition function are formed and updated in each step in order to find the next value of the Young's modulus for which the objective function needs to be calculated. This procedure continues until the stopping criteria (which is set to be a specific number of model evaluations in this work) is reached. Also, in each iteration, if overexploiting is detected, the kernel function is modified and a new Young's modulus point is calculated.

4.2.1 Governing equation

In the present study, we used the classical plate theory to describe the transversal linear deformation of thin elastic objects [145]. In this chapter, we use the words displacement and deformation interchangeably and both as the short forms of transversal deformation. The plate theory has the following assumptions: the thickness of the plate is relatively small in comparison to its other dimensions; the thickness of the plate does not change during deformation and straight lines normal to mid-surface remain straight and normal after deformation [133], [145]. The classical plate transversal deformation is expressed as:

$$D\left(\frac{\partial^4 w(x,y,t)}{\partial x^4}+2\frac{\partial^4 w(x,y,t)}{\partial x^2\partial y^2}+\frac{\partial^4 w(x,y,t)}{\partial y^4}\right)+\rho h\frac{\partial^2 w(x,y,t)}{\partial t^2}=p(x,y,t) \quad (4\text{-}1)$$

where t is time and x and y are lateral coordinates of the plate and w represents the transversal deformation. The plate is subject to the uniform harmonic transverse excitation pressure p of frequency Ω

$$p(x,y,\Omega,t)=P(x,y,\Omega)cos(\Omega t) \quad (4\text{-}2)$$

where the pressure amplitude is considered to be constant for all values of x and y and for all excitation frequencies. D, the flexural rigidity of the plate, is defined as:

$$D=\frac{Eh^3}{12(1-\upsilon^2)} \quad (4\text{-}3)$$

where E, h, and υ are the Young's modulus, thickness, and Poisson's ratio of the plate, respectively. Due to linearity, the frequency of the transversal deformation response is the same as the frequency of excitation:

$$w(x,y,\Omega,t)=W(x,y,\Omega)cos(\Omega t+\varphi) \quad (4\text{-}4)$$

W and φ represent the amplitude and phase of the harmonic response, respectively. By substituting Equations (4-2) and (4-4) in Equation (4-1), the time-dependent terms cancel out from both sides:

$$D\left(\frac{\partial^4 W(x,y,\Omega)}{\partial x^4}+2\frac{\partial^4 W(x,y,\Omega)}{\partial x^2\partial y^2}+\frac{\partial^4 W(x,y,\Omega)}{\partial y^4}\right)-\rho h\Omega^2 W(x,y,\Omega)=P(x,y,\Omega) \quad (4\text{-}5)$$

Because in this chapter we focus on systems with negligible damping, the discussions are concentrated on the deformation magnitude rather than the phase which is always 0 or 180 degrees for undamped structures.

4.2.2 Finite-difference formulations

In digital holography, the vibration data are obtained by post-processing the images gathered using a camera and therefore the data are available on structured equally spaced grids formed by treating the pixels of the digital images as nodes. The classical plate equation (Equation (4-5)) can be easily discretized and solved on a structured grid using the finite-difference method.

In our holographic vibration measurements, we collect data of both the moving object and some parts of the stationary boundary around it and the boundary of the moving object can be delineated in the measurement data. We used a second-order central difference scheme to discretize Equation (4-5) [146] and we had to consider auxiliary nodes out of the boundary (Figure 4-2-a) to be able to use this scheme. For each of the x and y directions, the first node out of the boundary (in the stationary surrounding structure) was considered to be fixed (green nodes in Figure 4-2-a) and the next node (red nodes in Figure 4-2-a) further away from the moving object (in the stationary surrounding structure) was considered as an auxiliary node. In Figure 4-2-a, d is the uniform grid spacing in both x and y directions. The plate equation was solved for the nodes inside the boundary (yellow nodes in Figure 4-2-a).

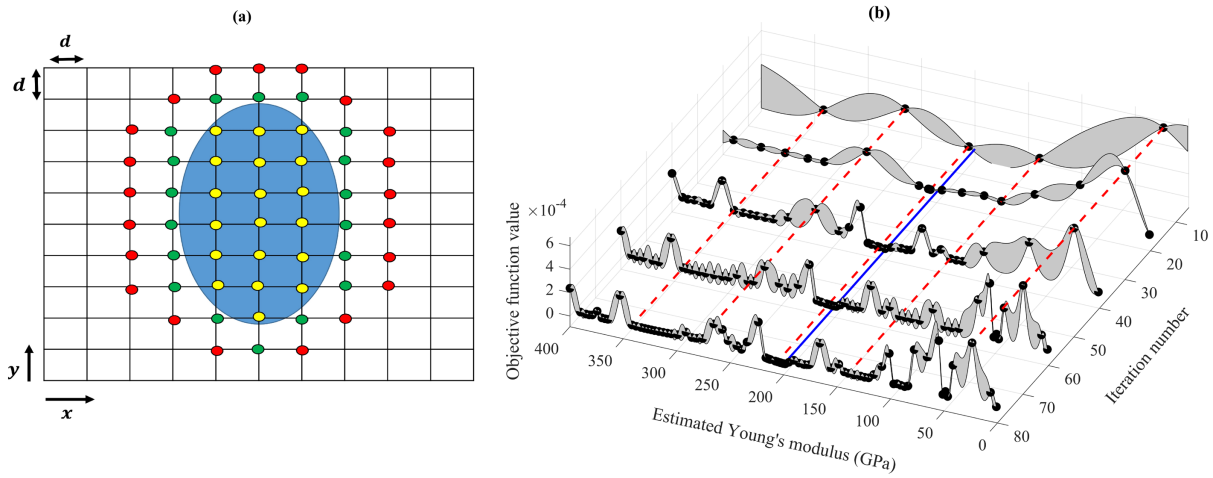


Figure 4-2 – (a) Schematic diagram of the numerical grid used in the finite-difference method. The classical plate equation is applied to the yellow nodes that are located in the vibrating region indicated in blue, the green nodes are considered to be the boundaries of the moving plate and the red nodes are auxiliary nodes. (b) Visual explanation of the progression of the Bayesian optimization process represented by the value of the objective function for iterations 5, 20, 60, and 80 for estimation of the Young's modulus of a simply-supported square plate (discussed in section 4.3.1.1) using the measured displacement field. The black dots represent the points at which the objective function was evaluated, the gray shaded areas show the confidence interval which becomes smaller by each iteration. Before the main optimization procedure starts, four initial random guesses for the Young's modulus are made, the plate equation is solved for the structure four times and the objective function is calculated for these four guesses. The main optimization process starts from iteration #5 (which is the first iteration shown). Dashed red lines trace the five points considered in iteration #5 and the blue line indicates the true value of the Young's modulus. This process eventually leads to estimating the global minimum of the objective function.

4.2.3 Inverse problem

The inverse problem can be formulated by rearranging Equation (4-5) to express the Young's modulus as a function of other mechanical properties and the spatial derivatives of the measured holographic displacement field (Equation (4-6)). The formulation presented in Equation (4-6) must be satisfied for all of the nodes inside the vibrating domain which results in an overdetermined system of equations.

$$E = \frac{12(1-\upsilon^2)}{h^3}\left(\frac{\partial^4 W(x,y,\Omega)}{\partial x^4} + 2\frac{\partial^4 W(x,y,\Omega)}{\partial x^2 \partial y^2} + \frac{\partial^4 W(x,y,\Omega)}{\partial y^4}\right)^{-1}(P(x,y,\Omega) + \rho h \Omega^2 W(x,y,\Omega)) \quad (4\text{-}6)$$

This method can provide an accurate estimate when the data are noise-free [147]. However, the presence of even a very low level of noise in the vibration measurement data will result in large errors in the estimated Young's modulus due to the noise amplification in the differentiation process of Equation (4-5) that is of order four in both spatial directions [148], [149]. We verified that in parameter estimations using noisy data, these large errors indeed occur as expected.

To avoid noise amplification due to differentiation, we proposed the method which is presented in Figure 4-1. First, some initial guesses for the Young's modulus were made, then Equation (4-5) was directly solved to calculate the displacement field. The calculated and measured displacement fields were then compared and the values of the Young's modulus were iteratively modified (Section 4.2.4) to reduce the error between the calculated and measured displacement fields. This process led to an optimization problem in which the objective function, the Euclidean distance between measured and calculated fields, described by Equation (4-7) had to be minimized.

$$obj(E_i) = \sqrt{\sum_{j=1}^{n}\left(w_j^C - w_j^m\right)^2} \quad (4\text{-}7)$$

where w_j^C and w_j^m respectively represent the calculated and measured displacements of the node *j* and *n* indicates the number of nodes in the vibrating domain. It should be noted that the calculated displacement is a function of the Young's modulus (E_i) considered in each iteration of the optimization process.

4.2.4 Optimization process

We used Bayesian optimization in our proposed material characterization method to minimize the objective function (Equation (4-7)). In our implementation, we used the BayesOpt algorithm in MATLAB[4].

The Bayesian optimization works with a Gaussian process model of the objective function as a response surface and trains this model by strategically exploring the parameter space and evaluating the objective function (Equation (4-7)). In the present work, we used the Gaussian process regression $\mathcal{GP}$ [150], [151] to define the Gaussian model $\widetilde{obj}(E_i)$ of the objective function as:

$$\widetilde{obj}(E_i) = \mathcal{GP}\left[\mu(E_i, \theta); k\left(E_i, E_j; \theta\right)\right] \tag{4-8}$$

where E_i and E_j are two Young's moduli points in the parameter space, μ is the expected value function in the Gaussian process, k is a covariance kernel function, and θ is the vector of kernel parameters that are defined based on standard deviation and characteristic length scale. Standard deviation specifies the variation of the function values from the expected value and the characteristic length scale determines the amount of smoothness of the Gaussian process regression [152], [153]. A small length scale means that the function becomes quickly uncertain when we get far from known positions. In this work, we used automatic relevance determination Matern 5/2 covariance kernel function [152], [154]:

$$k\left(E_i, E_j; \theta\right) = \sigma_f^2 \left(1 + \sqrt{5}r + \frac{5}{3}r^2\right) exp\left(-\sqrt{5}r\right) \tag{4-9}$$

where r is:

[4] https://www.mathworks.com/help/stats/bayesian-optimization-algorithm.html

$$r = \sqrt{\sum_{m=1}^{N} \frac{\left(E_i - E_j\right)^2}{\sigma_m^2}} \tag{4-10}$$

and θ is defined as:

$$\theta_m = log(\sigma_m) \ \ for \ \ m = 1,2,..,N \quad \& \quad \theta_{N+1} = log(\sigma_f) \tag{4-11}$$

where σ_m represent the characteristic length scale for each parameter and σ_f shows the standard deviation of the response surface. Kernel parameters are found by maximizing their marginal likelihood in each iteration [151], [153], [155]. Also, N is the number of parameters that we want to estimate (here *N=1*) [152].

In fact, Equation (4-8) uses the Gaussian process regression to create a posterior distribution based on our prior knowledge, and this posterior distribution can be later used to find the expected value and standard deviation of the objective function for each unexplored value of the Young's modulus. The standard deviation of $\widetilde{obj}(E_i)$ then shows how likely it is for the expected value of the Gaussian objective function *($\widetilde{obj}(E_i)$)* to be close to its actual value *(Obj(E_i))* at each E_i point [152].

Before the main optimization process starts, the objective function (Equation (4-7)) is evaluated at four random Young's moduli points and a Gaussian process regression (Equation (4-8)) is created from them (Figure 4-1). The method then updates the Gaussian process regression in each iteration step through evaluating the objective function and learning more about it. In fact, in each iteration step we calculate the value of the objective function for a specific point in the Young's modulus space and we use this knowledge to update the Gaussian process regression for the current step, we then proceed to the next iteration and calculate the value of the objective function for a new Young's modulus point and update the Gaussian process again and this process continues until we reach the stopping criterion.

Deciding the next Young's modulus point to evaluate the objective function (Equation (4-7)), is critical. In order to strategically choose the next Young's modulus to evaluate the objective function (Equation (4-7)) for each iteration step, we found the Young's modulus point that maximized an acquisition function [156]. The acquisition function was evaluated using the Gaussian process regression (Equation (4-8)) of the objective function rather than the objective function itself (Equation (4-7)), so its extrema can be found cheaply and quickly at each iteration step [157].

The most commonly used acquisition function is the expected improvement function defined as [158]:

$$EI = \mathbb{E}[max\ (0, \widetilde{obJ}(E^*) - \widetilde{obJ}(E))] \tag{4-12}$$

where $\mathbb{E}$, E^* and $\widetilde{obJ}(E^*)$ are the expected value, best Young's modulus and best observed value of the objective function so far, respectively. For the acquisition function, we used a modified version of the expected improvement function, known as expected improvement plus, that escapes local extrema and therefore helps better estimate the global extrema of the objective function. The expected improvement plus is similar to the typical expected improvement function (Equation (4-12)) but it benefits from a method to stop the optimization from overexploiting a specific region by defining an exploration ratio: for each step if the algorithm finds that overexploiting is happening, it multiplies the vector of kernel parameters (θ) by the number of iterations [159]. It then generates a new point based on the new kernel function. We set the exploration ratio to be 0.5 and our verifications, which will be presented in the following sections, show that this value results in finding the global optimum for all cases considered in the current chapter. The same value of exploration ratio was also used in several works in the literature [160], [161].

In the Bayesian optimization, it is common to consider a large enough number of evaluations of the objective function as the stopping criterion [162]–[164]. This is due to the complexity of defining convergence of errors in the Bayesian optimization [162]. For all of the parameter

estimations in this chapter, therefore, the number of iterations was fixed to 180 evaluations of the objective function (as will be discussed in Section 4.3.1.1). This value may need to be changed for other applications or if higher accuracies than what is targeted in this chapter are desired. Moreover, the range of the solution space for the Young's modulus was chosen to be from 1 GPa to 400 GPa for the benchmarks investigated in the present study.

For providing a visual explanation of the optimization process, Figure 4-2-b demonstrates a few iterations (iterations 5, 20, 60, and 80) of the evolution of our Bayesian parameter estimation procedure for the simply-supported plate which will be discussed in Section 4.3.1.1. At first 4 random initial guesses for the Young's modulus were made and the objective function was evaluated and then at each step, the Young's modulus points with the highest expected improvement were chosen to be searched as potential minimizers of the objective function. In fact, from the fifth iteration (the first curve shown in Figure 4-2-b), the real process begins and in each step, the next evaluation point is identified based on the acquisition function. Figure 4-2-b shows the values of the objective function evaluated at the candidate points as well as the confidence interval region (shaded gray). For better visualization, the dashed red lines trace the five points identified in the fifth iteration while the new guesses are added in each iteration step of the optimization and the solid blue line shows the true value of Young's modulus. In each iteration, the new evaluation points are chosen to be near the local and global minima of the function and after several iterations, the error regions become smaller. This process eventually estimates the global minimum after several iterations. It should be noted that in this figure the results of iterations 5, 20, 60, and 80 are presented while the optimization procedure continues up to iteration 180.

4.3 Results

4.3.1 Validation using analytical data

We analytically calculated the forced harmonic response of a square plate with two types of boundary conditions (simply-supported and clamped) via mode superposition. We then found

the optimum Young's modulus that could best replicate the analytically calculated harmonic vibration patterns using our proposed material characterization method.

4.3.1.1 Simply-supported thin square plate

The natural frequencies ω_{mn} and mode shapes W_{mn} of a simply-supported thin rectangular plate can be expressed as [165]:

$$\omega_{mn} = \pi^2 \sqrt{\frac{D}{\rho h}} \left[\left(\frac{m}{a}\right)^2 + \left(\frac{n}{b}\right)^2 \right] \tag{4-13}$$

$$W_{mn}(x,y) = A_{mn} sin\frac{m\pi x}{a} sin\frac{n\pi y}{b} \tag{4-14}$$

where both *m* and *n* are integers and the subscript mn represents the mode number *mn* of the plate. Additionally, *a* and *b* are the length and width of the rectangular plate and *h* is the thickness of the plate, respectively. Also, A_{mn} represents the amplitude coefficient.

The response of the plate to a harmonic pressure with the frequency of Ω and amplitude of $f(x,y)$ can be written as [166]:

$$w\,(x,y,\Omega,t) = \int_0^a \int_0^b f(\overline{x},\overline{y}) W(x,y,\overline{x},\overline{y},\Omega) d\overline{x} d\overline{y}\, cos\,(\Omega t) \tag{4-15}$$

where:

$$W(x,y,\overline{x},\overline{y},\Omega) = \sum_{m,n=1}^{\infty} \frac{W_{mn}(\overline{x},\overline{y})}{(\omega_{mn}^2 - \Omega^2) \int_0^a \int_0^b \rho h {W_{mn}}^2 dxdy} W_{mn}(x,y) \tag{4-16}$$

In Equations (4-15) and (4-16), $\overline{x}, \overline{y}$ represent the coordinates at which the pressure is applied. In this section, it was assumed that the pressure was uniformly applied all over the plate.

We used Equations (4-13) to (4-16), with mode superposition over the first 20 modes, to calculate the harmonic responses of a thin square plate as inputs to our material characterization

method. Figure 4-3-a, shows the analytically calculated harmonic response of a plate with geometrical and material parameters listed in Table 4-1, excited at 7.9 kHz which is close to the 13^{th} natural frequency (8.1 kHz) of the plate. The magnitude of the applied uniform harmonic pressure was 10 kPa and the plate was discretized on a 1000×1000 grid. The value of the Young's modulus was estimated to be 200.03 GPa (error of 0.01%).

As mentioned in Section 4.2, we used the Euclidian distance for our objective function in Equation (4-7) and the above estimation was based on that distance. We studied the effect of the distance definition in the objective function (Equation (4-7)). When we replaced the Euclidian distance with Manhattan and Chebyshev distances, the estimated Young's moduli were 200.75 GPa (error of 0.37%) and 199.35 GPa (error of 0.32%), respectively. Because the definition of distance did not have substantial effects on the estimated Young's modulus, in the current chapter, we chose Euclidian distance for all our calculations as explained for Equation (4-7).

In order to assess the robustness and accuracy of the proposed material characterization method when the measured displacement magnitude field is affected by experimental noise, we applied white Gaussian noise to the magnitude of the analytical displacement field of Figure 4-3-a. Figure 4-3-b shows the magnitude of the noisy displacement field (1000×1000) with a signal to noise ratio (SNR) of 10 dB. The value of the estimated Young's modulus using these noisy data was 201.37 GPa (error of 0.68%).

The convergence of the minimum value of the objective function with respect to the number of iterations is presented in Figure 4-3-c for both displacement fields shown in Figure 4-3. After almost 20 evaluations, the error remained almost constant. This demonstrates that 180 iterations of the objective function are enough for the studies reported in this chapter.

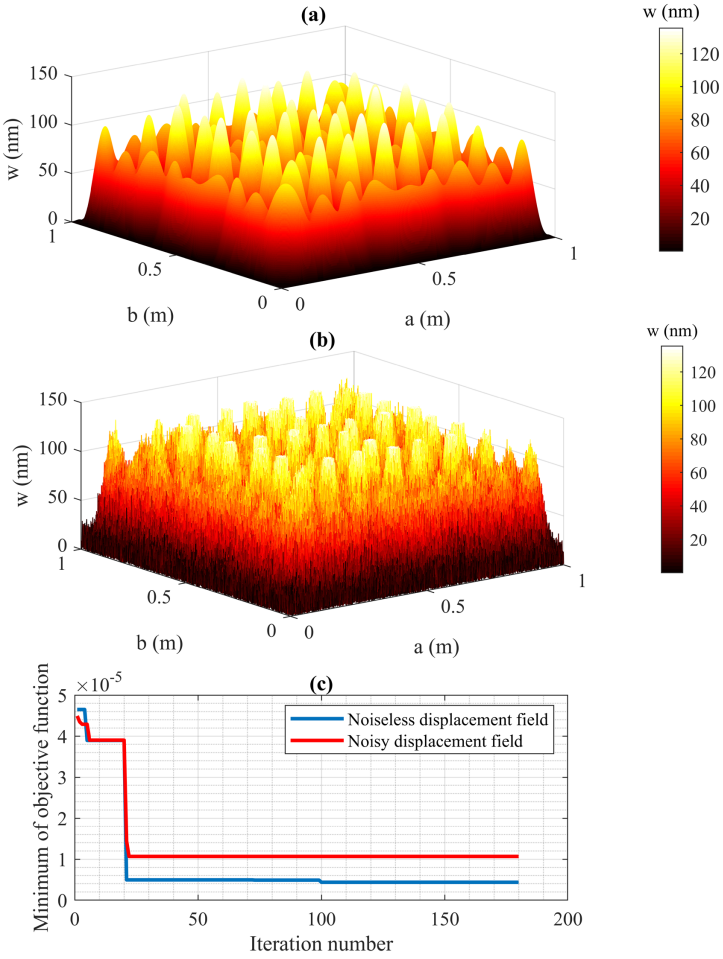


Figure 4-3 – (a) The analytically calculated harmonic response of a simply-supported square plate with known material properties (given in Table 4-1) excited with a harmonic pressure with a magnitude of 10 kPa and frequency of Ω=7.95 kHz. This displacement field was used as the input to our material characterization method and the error of the estimated Young's modulus was 0.01%. (b) The same analytically calculated harmonic response as in Panel (a) after application of white Gaussian noise with a signal to noise ratio of 10 dB. This noisy displacement field was also used as the input to the proposed material characterization method to study the estimation error in presence of the noise. The error of the estimated Young's modulus was 0.68%. (c) The minimum value of the objective function with respect to the number of evaluations of the objective function for material characterization of the simply-supported square plate: using noiseless data shown in panel (a) (blue line) and using noisy data shown in panel (b) (red line). The error remained almost constant after about 20 iterations for both noiseless and noisy data. This shows that the maximum number of iterations used in this chapter (180 iterations) is enough for obtaining convergence.

Table 4-1 – Material properties used in analytical and some of the FEM simulations to validate the proposed holography-based material characterizing method.

Property	**Value**	**Unit**
E	200	GPa
ρ	7850	$\mathrm{Kg/m^3}$
υ	0.3	–
h	0.01	m
a, b	1	m

4.3.1.2 Clamped thin square plate

The clamped boundary condition is important for our future application of the method for hearing diagnosis as the tympanic membrane is clamped around its annulus. In this section, a clamped thin square plate with the geometrical and material properties provided in Table 4-1, was used to further validate the proposed method. The same formulation as for the simply-supported plates (Equations (4-15) and (4-16)) can be used to find the harmonic response [133], while the mode shapes and natural frequencies of a clamped plate must be used in those formulations. The mode shapes of a clamped square plate can be expressed as [165]:

$$W(x,y) = \sum_{m=1}^{p}\sum_{n=1}^{q}\Big\{A_{mn}\Big[cosh\frac{\epsilon_m x}{a} - cos\frac{\epsilon_m x}{a} - \alpha_m\Big(sinh\frac{\epsilon_m x}{a} - sin\frac{\epsilon_m x}{a}\Big)\Big]\ cosh\frac{\epsilon_n y}{a} - cos\frac{\epsilon_n y}{a} - \alpha_n\Big(sinh\frac{\epsilon_n y}{a} - sin\frac{\epsilon_n y}{a}\Big)\Big\} \tag{4-17}$$

where the coefficients A_{mn}, ϵ_m, α_m, ϵ_n and α_n and the natural frequencies of the square plate can be found in [165]. The first 6 mode shapes were used in the present study.

We calculated the magnitude of the displacement field of the clamped plate at four frequencies near the first four natural frequencies of the system (Figure 4-4). The proposed material characterization method was then employed to retrieve the Young's modulus from these vibration patterns. As Table 4-2 shows, the estimated Young's moduli for the resolution of 400×400 had errors of less than 0.18% for all investigated frequencies. The reason that we used a lower grid size here than what was used for the simply-supported plate in the previous section is that calculating the mode shapes in the forward analytical formulations for the clamped plate is computationally more expensive than the simply-supported plate.

Like the simply-supported plate, we added white Gaussian noise (10 dB SNR) to the analytically calculated response to assess the accuracy and robustness of the proposed method (Figure 4-5). The estimated Young's moduli from these noisy displacement fields (Table 4-2) had less than 3.92% error with even quite noisy displacement fields.

4.3.2 Validation using finite-element data

To more rigorously validate the proposed material characterization method by using more complicated plate geometries and to investigate the sensitivity of the method to various experimental errors, we used finite-element analyses to generate complex ground-truth vibration patterns more similar to the data obtained using holographic measurements. In our analyses, we used COMSOL (Version 5.4, MA, USA) and Code_Aster (Version 14.4.0, France) finite-element packages to calculate the steady-state forced harmonic vibration patterns.

4.3.2.1 Elliptical and triangular plates

To further validate the accuracy of the proposed method for plates with more complicated geometries, an elliptical plate and a triangular plate were studied in this section. The mesh convergence was checked for the finite-element calculated displacement fields. Besides, to consider the accuracy of the proposed material characterization method in the presence of noise, white Gaussian noise and non-Gaussian noise were applied to the displacement fields obtained from finite-element calculation.

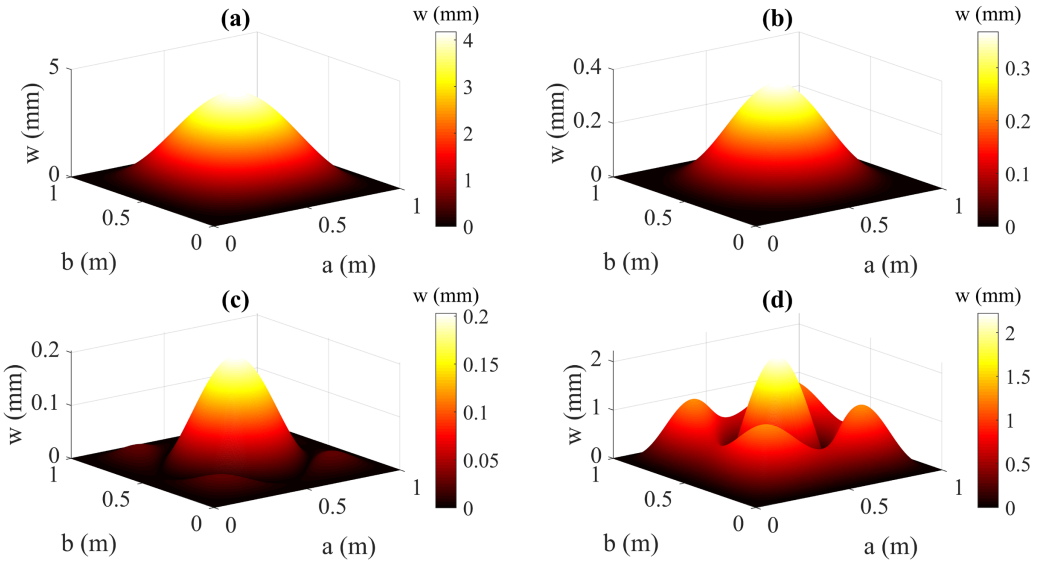


Figure 4-4 – The analytically calculated harmonic response of a clamped plate with known material properties (given in Table 4-1) excited with a harmonic pressure with a magnitude of 10 kPa. Each of these harmonic responses was used as the input to our proposed material characterization method to validate it. The excitation frequencies were: (a) Ω=79.57 Hz; (b) Ω=159.23Hz; (c) Ω=238.85Hz; and (d) Ω=318.30Hz. The results of the estimated Young's modulus are presented in Table 4-2. We observed no specific trends between the estimation errors and the excitation frequencies. The maximum estimation error was 0.18% using the displacement field at Ω=238.85Hz of panel (c).

We considered both domains to be inside a 10 cm×10 cm square. For the elliptical plate, the radii were considered to be 4.52 cm and 1.59 cm and for the triangular plate, two edges were considered to be equal and 8.94 cm long and the other edge was 8.00 cm long. The domains in the field of view outside the elliptical and triangular plates were fixed. The thickness of both plates was assumed to be 100 μm and the stimulus pressures of 1 kPa with various frequencies were uniformly applied on the plates. Besides, both plates were considered to have the material properties listed in Table 4-1 and the resolution was considered to be 1000×1000 for both cases. Figure 4-6 and Figure 4-7 show the displacement magnitude of the finite-element calculated harmonic vibration patterns of the elliptical and triangular plates, respectively. Table 4-3 shows the values of the estimated Young's moduli and estimation errors for both elliptical

and triangular domains for all the cases shown in Figure 4-6 and Figure 4-7. The maximum error of the estimated Young's modulus was 1.49% for the elliptical plate and 0.23% for the triangular plate. Figure 4-8 shows the displacement fields of both plates after adding white Gaussian noise of 10 dB SNR. The maximum error of the estimation was 1.43% for the elliptical and 0.76% for the triangular plates with these noisy displacement fields. Besides, we studied the effects of different values of SNR in the range of 0 to 15 with intervals of 0.5 for both plates and for all 4 frequencies that were discussed before. The maximum error was 3.21% in the estimated Young's modulus even with small values of SNR.

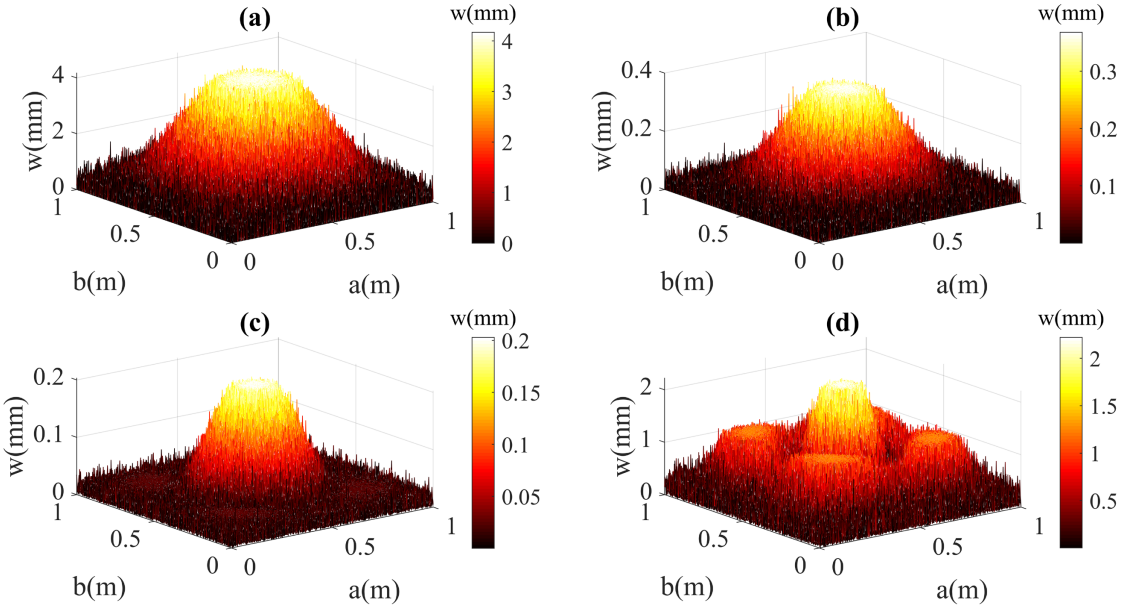


Figure 4-5 – White Gaussian noise with a signal to noise ratio of 10 dB applied to the analytically calculated harmonic response of a clamped plate (Figure 4-4) with known material properties (given in Table 4-1) excited with a harmonic pressure with a magnitude of P=10 kPa. Each of these noisy displacement fields was used as the input to our proposed material characterization method to validate it in the presence of noise. The excitation frequencies were (a) Ω=79.57 Hz; (b) Ω=159.23 Hz; (c) Ω=238.85 Hz; and (d) Ω=318.30 Hz. The results of the estimated Young's modulus are presented in Table 4-2. We observed no specific trends between the errors and the excitation frequencies. The maximum estimation error was 3.92% using the displacement field at Ω=318.30 Hz of panel (d).

Table 4-2 – Results of the proposed material characterization method estimated from noiseless (Figure 4-4) and noisy data (SNR=10 dB, Figure 4-5) of a clamped square plate with the true Young's modulus of 200 GPa.

	Noiseless data		**Noisy data – SNR=10 dB**	
Ω (Hz)	**Estimated Young's Modulus (GPa)**	**Error (%)**	**Estimated Young's Modulus (GPa)**	**Error (%)**
9.57	200.19	0.09	200.11	0.05
159.23	199.69	0.15	201.80	0.9
238.85	200.36	0.18	199.88	0.06
318.3	200.12	0.06	192.15	3.92

4.3.2.2 Non-Gaussian noise

In practice, the experimental data may be contaminated with non-Gaussian noise such as speckle noise and any other probable hardware noise. In order to investigate the robustness of the proposed material characterization method in presence of non-Gaussian noise, the vibration patterns of the elliptical and triangular plates with white Gaussian noise with SNR of 5 dB were converted to non-Gaussian noisy data using the method presented in [167] and [168] with skewness of larger than 1 and kurtosis of larger than 3 [98], [99]. Table 4-4 shows that the estimated Young's modulus with these noisy data had less than 4.2% of error for both plates at all excitation frequencies studied in this section.

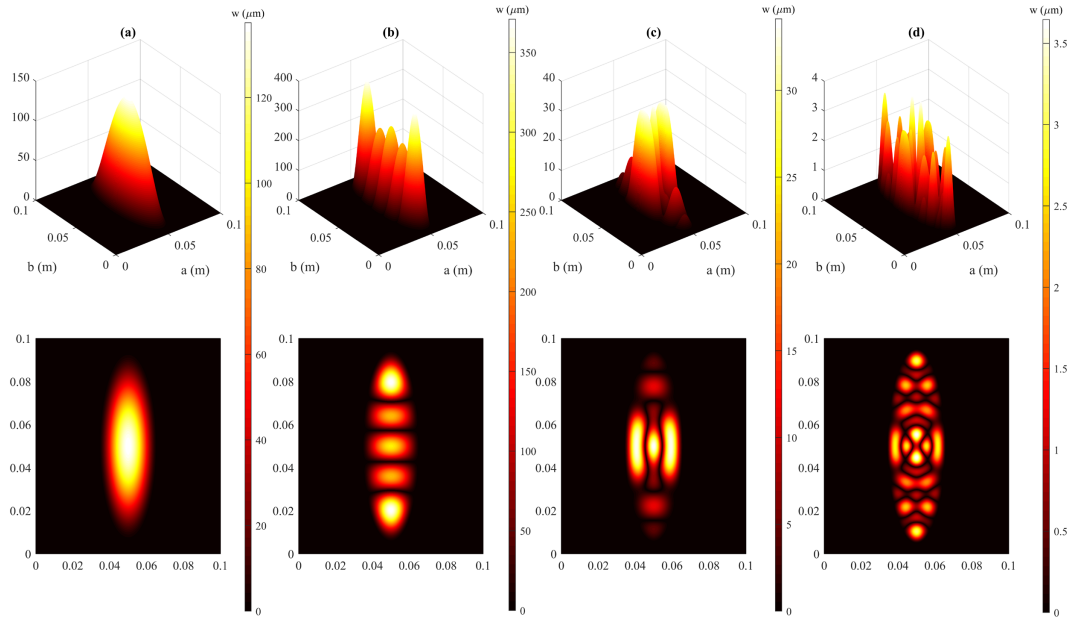


Figure 4-6 – Finite-element calculated harmonic displacement magnitude response of an elliptical plate inside a 10 cm × 10 cm square field of view (top: 3D and bottom: 2D projections). The material properties are given in Table 4-1. These displacement magnitude responses were used to validate the proposed material characterization method. Excitation amplitude was P=1 kPa and the excitation frequencies were: (a) Ω=79.57 Hz; (b) Ω=1.59 kHz; (c) Ω=3.18 kHz; and (d) Ω=7.96 kHz. The results of the estimated Young's modulus are presented in Table 4-3. We observed no specific trends between the errors and the excitation frequencies. The maximum estimation error was 1.49% using the displacement field at Ω=79.57 Hz of Panel (a).

4.3.2.3 Effect of uncertainty in thickness, Poisson's ratio, and boundary conditions

Our proposed material characterization method estimates the Young's modulus assuming no uncertainty in the Poisson's ratio, thickness, and boundary conditions of the plate. In this section, the goal is to determine the effects of uncertainty in these assumptions on the accuracy of the proposed method. We used the finite-element models of elliptical and triangular plates which were benchmarked in previous sections.

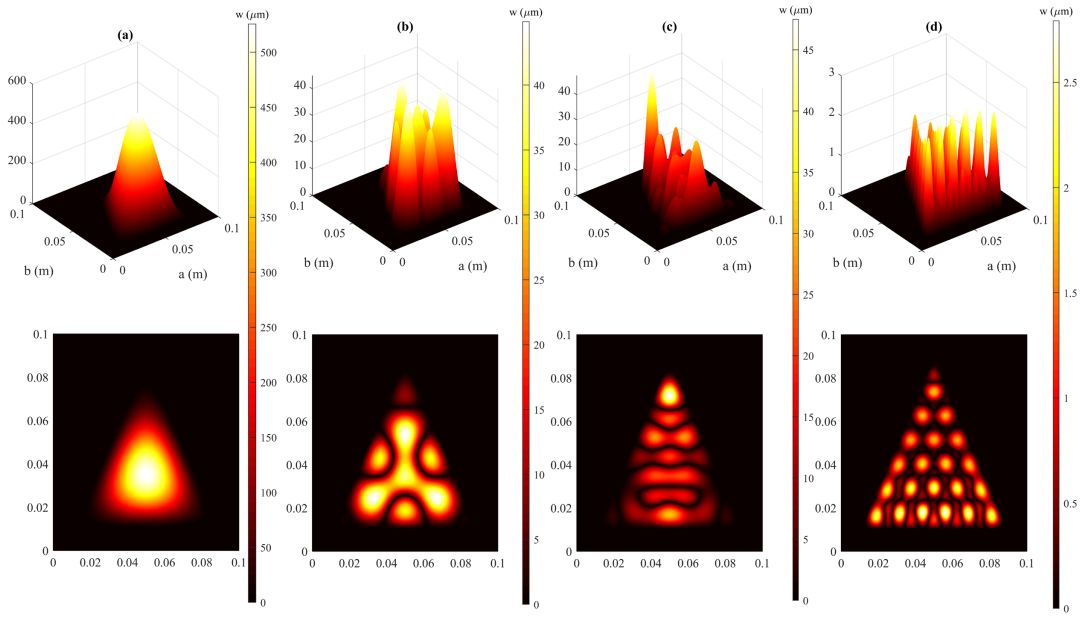


Figure 4-7 – Finite-element calculated harmonic displacement magnitude response of a triangular domain inside a 10 cm × 10 cm square field of view (top: 3D and bottom: 2D projections). The material properties are given in Table 4-1. These displacement magnitude responses were used in the material characterization method to validate it. The excitation amplitude was $P = 1\ kPa$ and excitation frequencies were: (a) Ω=79.57 Hz; (b) Ω=1.59 kHz; (c) Ω=3.18 kHz; and (d) Ω=7.96 kHz. The results of the estimated Young's modulus are presented in Table 4-3. We observed no specific trends between the errors and the excitation frequencies. The maximum estimation error was 0.23% using the displacement field at Ω=3.18 kHz of Panel (c).

Figure 4-9-a shows the error in the estimated Young's moduli due to the error in the thickness assumption for the elliptical domain. These data were obtained by calculating the error in the estimated Young's modulus by varying the thickness from the true value while all other geometrical parameters and the Poisson's ratio and boundary conditions, were kept at the true value in the estimation process. We performed similar investigations on the triangular plate but did not show the results in Figure 4-9 as the results of both domains followed similar trends. In this and all other figures, the dots indicate the evaluation points and the lines indicate regressions for each dataset which was fitted for better visibility. In both domains and for all investigated excitation frequencies, assuming a thickness less than the true value caused

overestimating the Young's modulus because the material characterization method compensates the smaller thickness with higher stiffness to obtain the same displacement field. Although the error is different for each domain and each excitation frequency, the method is more sensitive to errors in the thickness assumption at lower frequencies. This suggests that when uncertainty in the thickness is expected, characterization at higher frequencies can yield more accurate results. In addition, for both domains, at all investigated frequencies, there is an asymmetry for the estimated Young's modulus with respect to the vertical line of zero error in the thickness. Except at the very low frequency (~80 Hz), 3% error in thickness caused 10% or smaller errors in the estimated Young's modulus.

Table 4-3 – Estimated Young's modulus for elliptical and triangular plates with the true Young's moduli of 200 GPa using the noiseless displacement fields shown in Figure 4-6 and Figure 4-7.

	Elliptical plate		**Triangular plate**	
Ω (Hz)	**Estimated Young's Modulus (GPa)**	**Error (%)**	**Estimated Young's Modulus (GPa)**	**Error (%)**
79.57	202.99	1.49	200.17	0.08
1592	200.87	0.43	200.34	0.17
3184	201.07	0.53	200.47	0.23
7961	197.75	1.12	200.16	0.08

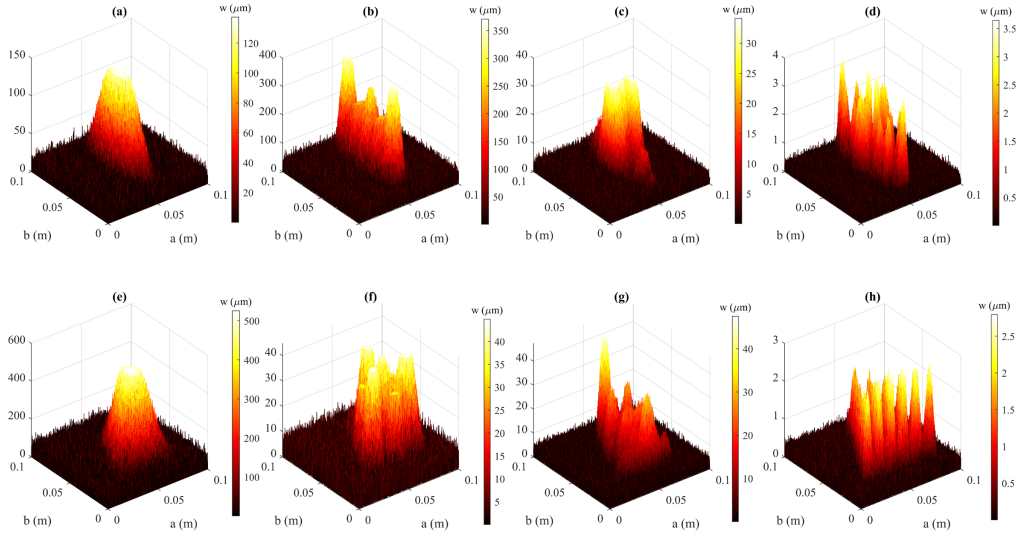


Figure 4-8 – White Gaussian noise with a signal to noise ratio of 10 dB applied to the finite-element calculated harmonic displacement magnitude responses of the elliptical plate of Figure 4-6 and triangular plate of Figure 4-7. These responses were used to validate the material characterization method in the presence of noise. The excitation amplitude was P=1kPa. The excitation frequencies and the error in estimating the Young's modulus for each panel are: (a) Ω=79.57 Hz & error=1.43%; (b) Ω=1.59 kHz & error=0.61%; (c) Ω=3.18 kHz & error=1.20%; (d) Ω=7.96 kHz & error=0.51%; (d) Ω=79.57 Hz & error=0.33%; (e) Ω=1.59 kHz & error=0.14%; (f) Ω=3.18 kHz & error=0.76%; and (g) Ω=7.96 kHz & error=0.03%. The results reveal that there are no specific trends between the errors and the excitation frequencies. The maximum estimation errors for the elliptical and triangular plates were related to the excitation frequencies of Ω=79.57 Hz and 3.18 kHz, respectively.

Figure 4-9-b shows the error in the estimated Young's moduli with respect to the error in the assumed Poisson's ratio for the elliptical plate. These data were obtained by calculating the error in the estimated Young's modulus by varying the Poisson's ratio from the true value while the thickness was kept at the true value in the estimation process. We performed similar investigations on the triangular plate but did not show the results in Figure 4-9 as the results of both domains followed similar trends. The values of Poisson's ratio which are smaller than the true value resulted in a larger estimated Young's modulus and vice versa. For both plates, the general trend of the error in the estimated Young's modulus is almost the same for all

frequencies used in this study. For both domains, 20% error in the Poisson's ratio leads to less than 10% error for all cases. Also, the whole range of 60% error leads to a maximum error of 20% in the estimated Young's modulus.

Table 4-4 – Estimated Young's modulus for elliptical and triangular plates with the true Young's moduli of 200 GPa using displacement fields obtained by applying non-Gaussian noise to the displacement fields shown in Figure 4-6 and Figure 4-7.

	Elliptical plate		**Triangular plate**	
Ω (Hz)	**Estimated Young's Modulus (GPa)**	**Error (%)**	**Estimated Young's Modulus (GPa)**	**Error (%)**
79.57	202.20	0.1	191.63	4.18
1592	200.79	0.39	201.17	0.58
3184	196.07	1.96	202.58	1.29
7961	202.27	1.13	204.46	2.23

4.3.2.4 Non-uniform thickness

In order to investigate the accuracy of the estimation procedure for structures with non-uniform thickness, we studied a circular thin plate with a radius of 3 mm and with an average thickness of 99.20 μm and a standard deviation of 9.18 μm along its radius. The thickness variation of the plate along one radius is shown in Figure 4-9-c and the thickness distribution of the plate was made by revolving this radial thickness distribution. The plate material was chosen to have the following properties: E=60 MPa, υ=0.33 and ρ=1100 kg/m^3 and was excited with a uniform pressure with an amplitude of P=0.7 Pa and frequency of Ω=2900 Hz. The finite-element calculated displacement fields of the plate with non-uniform thickness were used to estimate the Young's modulus. In the proposed material characterization method, however, the average thickness was used. The estimated Young's modulus was found to be 56.27 MPa (6.21% error)

showing that a standard deviation of 10% causes less error in the estimation than the error that a 10% uniform error in the thickness does (Figure 4-9-a).

4.3.2.5 Thick plates

The classical plate theory that was used in the characterization method is valid for thin plates only. In this section, we want to study the errors of the estimated Young's modulus if the method is applied to thick plates. We considered the triangular plate with the same geometry as the plate in Figure 4-7 but with increased thicknesses in the FEM simulations (using 3D solid elements) to obtain the input displacement field. The results for the triangular plate with thicknesses of 5 and 10 mm are presented in Table 4-5. For the plate thicknesses of 5 and 10 mm (50 and 100 times thicker than the plate in Figure 4-7, respectively), the Young's modulus was underestimated with errors of about 17% and 45%, respectively, for all investigated frequencies. These errors are substantially worse than the maximum error of less than 0.25% for all investigated frequencies for the thin plate reported in Table 4-3. These experiments show that the proposed material characterization method can result in large errors if it is used for characterizing thick plates and it should only be used for thin plates as intended in the development of the method.

4.3.2.6 Effects of uncertainty in boundary conditions

We also studied the effects of uncertainty in boundary conditions. In our proposed material characterization method, we assume all boundaries of the plate to be clamped. However, in practice there may be some imperfection in the boundary conditions. To study the effect of error in the boundary condition assumption on the accuracy of the proposed method, we considered the same triangular plate that we studied in Sections 4.3.2.1 and 4.3.2.2 but changed the boundary conditions of the input displacement fields obtained using FEM. We considered three different boundary condition scenarios: (A) one edge of the triangle was simply-supported while the two other edges were clamped, (B) two edges of the triangle were simply-supported while the third edge was clamped, and (C) all edges were simply-supported. In the proposed material characterization method, however, the boundary conditions, were

considered to be clamped for all these scenarios. The results are provided in Table 4-6 at the same four frequencies investigated before for the triangular plate. For all three scenarios, the lowest accuracies are related to the lowest frequency (79.57 Hz) responses and errors of 31.26% to 74.46% with growing errors by increasing the deviation from the true boundary condition from Scenario A to Scenario C. At this frequency when the true boundary condition was assumed in the material characterization method of this triangular plate, the error was 0.08% (Table 4-3). This shows that if the boundary condition is uncertain the proposed method breaks at low frequencies. However, the errors decrease by increasing the excitation frequency so that the errors drop to 8%, 12.45% and 21.48% for Scenarios A, B and C respectively at the highest frequency of 7961 Hz. This suggests since the method is less sensitive to the errors in boundary conditions at high frequencies, when the boundary condition is not certain, high-frequency measurements should be considered. Also Table 4-6 shows that, as it is expected, for each frequency the largest errors are related to Scenario C where the maximum deviation from the true clamped boundary condition exists and all edges of the input displacement field were considered to be simply-supported.

4.3.2.7 Mesh size and runtime

To study the effect of the mesh size used in the characterization method on the estimated Young's modulus, we used finite-element displacement data of the elliptical and triangular plates with an excitation amplitude of P=1 kPa and the excitation frequency of Ω=159.23 Hz with the dimensions and mechanical properties used in previous sections (Table 4-1). The finite-element mesh for calculating the input displacement field was fixed but the characterization mesh size (corresponding to the holographic resolution) was varied.

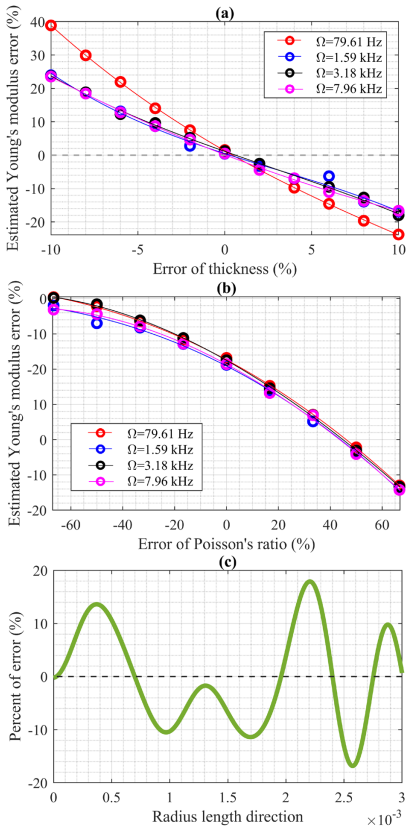


Figure 4-9 – Errors in the assumed value of thickness and Poisson's ratio used in the proposed material characterization method. (a) Effects of errors in the assumed thickness for the elliptical plate of Figure 4-6 on the estimated Young's modulus. The error in the estimation of the Young's modulus increases as the error in accurately specifying the thickness increases. Using a low frequency displacement field causes higher errors in the estimation of the Young's modulus than using higher frequency displacement fields does (e.g., with 10% underestimation of the thickness: 40% error using displacement data at 79.61 Hz vs 24% error using displacement data at 1.59 kHz or higher frequencies).When the thickness is uncertain, measuring the displacement field at higher frequencies can lead to a more accurate estimation of the Young's modulus. (b) Effects of errors in the assumed Poisson's ratio for the elliptical plate of Figure 4-6 on the estimated Young's modulus. The error in the estimation of the Young's modulus increases as the error in accurately specifying the Poisson's ratio increases and the increase is not sensitive to the frequency of excitation. (c) To study the error due to uniform thickness assumption, the effect of variable thickness was studied by revolving this variation of thickness along one radius of the circular plate and calculating the displacement field using the finite element method. Zero error is at the mean thickness. The displacement fields using the variable thickness displacement field were then used in the material characterizing method assuming constant mean thickness to calculate the error in the estimation of the Young's modulus due to the uniform thickness assumption.

Table 4-5 – Estimated Young's modulus for the triangular plate after increasing the original thickness (0.1 mm) of the plate of Figure 4-7 to study the errors of the proposed material characterization method for two thick plates with thicknesses of 5 and 10 mm.

	Thickness= 5 mm		**Thickness= 10 mm**	
Ω (Hz)	**Estimated Young's Modulus (GPa)**	**Error (%)**	**Estimated Young's Modulus (GPa)**	**Error (%)**
79.57	165.68	17.16	108.41	45.80
1592	165.74	17.13	109.87	45.06
3184	166.35	16.83	107.61	46.20
7961	166.90	16.55	109.70	45.15

Table 4-6 – Effects of errors in boundary conditions of the input displacement field on the estimated Young's modulus for the triangular plate. Scenario A: one edge of the triangle was considered to be simply-supported while the other two edges were clamped. Scenario B: two edges of the triangle were considered to be simply-supported while the other edge was clamped. Scenario C: all edges of the triangle were considered to be simply-supported. For all scenarios, the assumed boundary condition in the proposed material characterization method was considered to be clamped for all edges.

	Scenario A		**Scenario B**		**Scenario C**	
Ω (Hz)	**Young's Modulus**	**Error (%)**	**Young's Modulus**	**Error (%)**	**Young's Modulus**	**Error (%)**
79.57	137.48	31.26	85.35	57.33	51.08	74.46
1592	179.61	10.19	141.09	29.45	127.25	36.38
3184	182.87	8.56	161.85	19.08	142.53	28.73
7961	184.01	8.00	175.09	12.45	157.04	21.48

Figure 4-10-a presents the error of the estimated Young's modulus for different mesh sizes for the elliptical plate. The horizontal axis in these figures is the number of nodes considered in each of the edges of the square field of view per centimeter. We performed similar investigations on the triangular plate but did not show the results in Figure 4-10 as the trends of the results for both plates were similar. For a coarse mesh with a size of 2.5×2.5 per cm, errors of more than 70% in both elliptical and triangular plates were obtained. However, upon refining the mesh size, the error rapidly dropped to less than 10% with 10×10 per cm grids for both plates. This figure shows that the method gives less than 2.5% error with 55×55 per cm or finer. For both domains, the errors decreased to less than 1.5% for finer mesh sizes.

Figure 4-10-b shows the runtime with respect to the total number of nodes on the square domain for the elliptical domain. The calculations were performed with one central processing unit (Intel CPU, core i7-8700K, 3.70 GHz). The operating system was Windows 10 and MATLAB R2019a was used for all calculations. We performed the runtime analysis for the triangular plate as well however in Figure 4-10 only the results of the elliptical plate are presented. As this figure shows, increasing the resolution (or the number of calculation nodes), causes an approximately linear increase in the calculation time. A similar linear trend was observed for the triangular plate.

4.3.2.8 Effects of camera angle

Our proposed material characterization method assumes orthogonality of the sensitivity vector of the holography system to the vibrating plane. We investigated the errors that deviations from this assumption may introduce in the estimated Young's modulus by using finite-element calculated displacement fields viewed with an angle α. For this aim, the displacement field was projected on the orthogonal direction for different values of α and the results were used as inputs to the material characterization method.

Figure 4-10-c shows the errors in the estimated Young's modulus with respect to the error in the orthogonality assumption quantified by the angle α for the elliptical plate. We did the same analysis for the triangular plate but only the results of the elliptical plate are presented in

Figure 4-10 as the trend of the errors for both plates were similar. The plates were modeled as described in Section 4.3.2.1 with the same material properties. For both plates, the error in the Young's modulus estimation remains within 3% for up to 45° angle deviation for all frequencies except the lowest frequency investigated. At the lowest frequency, the method is sensitive to errors in the angle as the error in the estimated Young's modulus remains within 3% only for angle errors of less than 10° and the estimation error grows to about 40% for a 45° error in the angle. These results suggest that for non-ideal experimental setups, it is safer to use higher frequencies stimuli to benefit from the insensitivity of the method to angle errors.

4.3.3 Validation using experimental data

In order to assess the accuracy of the proposed method for material characterization of real structures, we measured the harmonic vibration response of a thin circular copper plate using a stroboscopic holography system that is being developed for hearing diagnosis. The diameter and thickness of the plate were 6.25 mm and 0.02 mm, respectively. The tolerance of these measurements was ±2.54 μm. The experimental setup (Figure 4-11-a) consists of a calibrated microphone, a speaker, and an otoscope head which includes a camera and an object illumination component. More details of the experimental setup can be found in [169].

Copper has a low level of damping relative to many other metal and non-metals [170]. The plate was stimulated with a harmonic pressure of 4350 Hz and the displacement field and sound pressure were measured. Figure 4-11-b shows the displacement magnitude field obtained using holography at 13 stroboscopic phases with a resolution of 800×800. The proposed method was used to estimate the Young's modulus using the measured displacement magnitude field assuming the Poisson's ratio and density of 0.34 and 8960 $\frac{\mathrm{Kg}}{\mathrm{m}^3}$, respectively [171], [172]. The estimated Young's modulus using our method was 142.48 GPa which is in the reported range of Young's modulus for copper alloys [171].

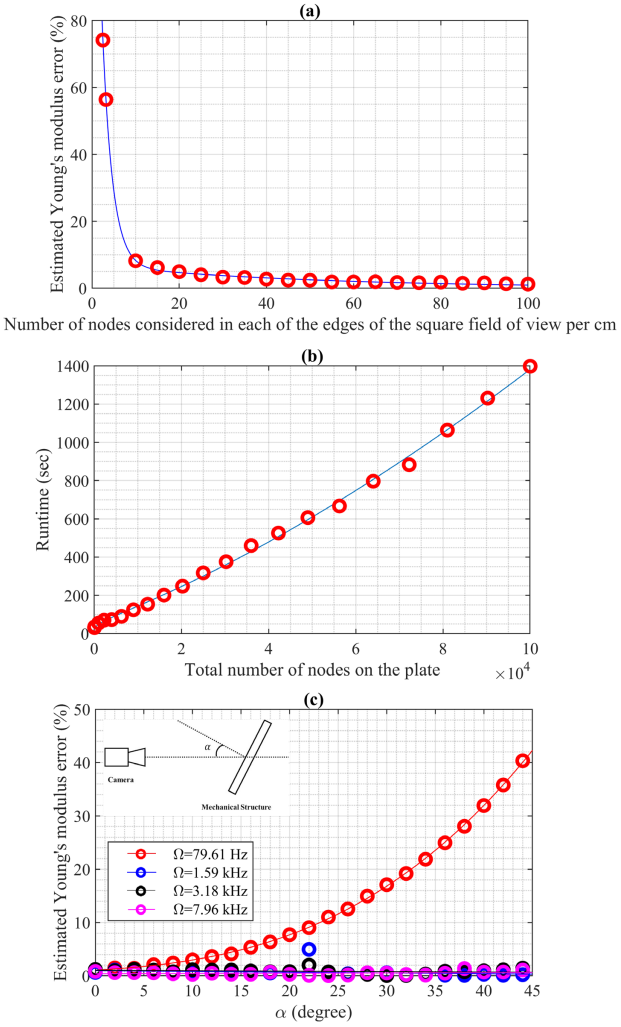


Figure 4-10 – (a) Effect of grid resolution on the estimated Young's modulus for the elliptical plate of Figure 4-6. This study was performed to find the sensitivity of the estimation error to the mesh size. It can be observed that the estimation error is large for coarse meshes (for instance for a mesh with a size of 2.5×2.5 per cm, the estimation error is larger than 70%). However, the error rapidly drops by refining the mesh. (b) Runtime with respect to total number of nodes for the elliptical plate shown in Figure 4-6. Increasing the number of nodes results in an approximately linear increase in the runtime. (c) Error of the estimated Young's modulus with respect to the error in the viewing angle of the camera (α) for the elliptical plate of Figure 4-6. For all frequencies except the lowest frequency, the estimation error remains within 3% for angles errors of up to 45°. However, for the lowest frequency (79.6 Hz), the error is less than 3% for angles up to 10° and increases to about 40% for α =45°. This suggests that low frequency responses are more sensitive to the errors in the viewing angle.

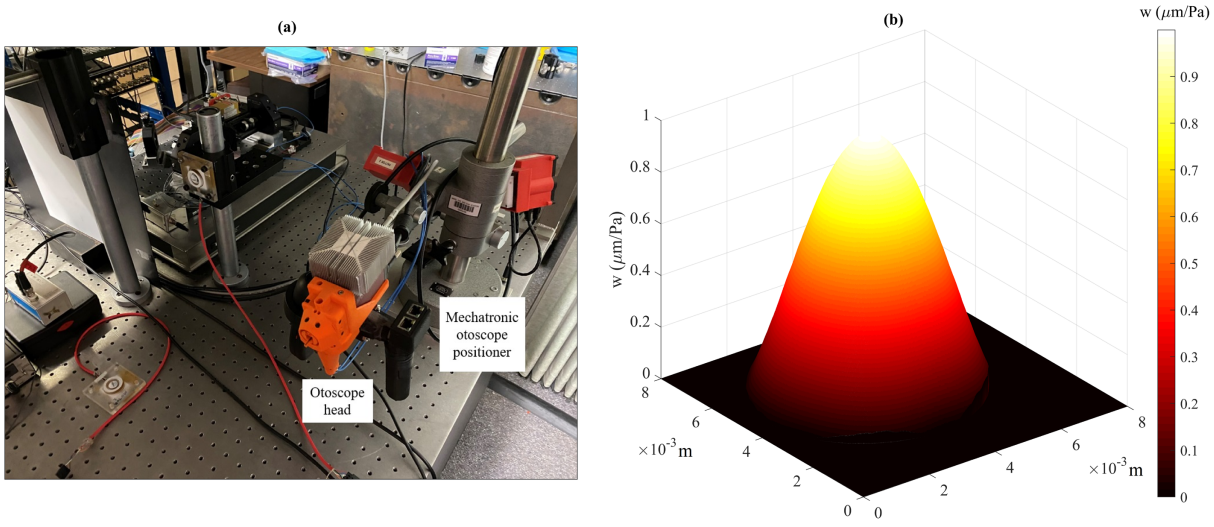


Figure 4-11 – (a) The digital holography system used in this work. The experimental setup consists of a speaker, a microphone, and an otoscope head which includes a camera and an object illumination component. (b) Experimental displacement magnitude normalized by the stimulus sound pressure at 4350 Hz of a thin copper plate obtained using the holography setup. This displacement field was used in the material characterization method and the estimated Young's modulus was in agreement with published material properties of copper [171].

We found that it is crucial that the displacement domain including the entire plate and its non-moving boundary is measured and used as the input to the proposed material characterization method. Failing to provide this domain in its entirety can result in large errors in the material characterization.

4.4 Discussions

As mentioned in Section 4.1, the main aim of this chapter is to use full-field 2D single frequency harmonic vibration data for material characterization where there is no access to high-quality modal data. Our ultimate goal is to develop this method to estimate the Young's modulus of the human tympanic membrane and use it as a diagnostic tool for hearing

pathologies. We used the Bayesian optimization to make this a clinically viable method that can find the global optimum value with the fewest possible number of iterations.

In general, optimization algorithms can be categorized into derivative-based and derivative-free algorithms [173]. The derivative-based methods use derivatives to find the optimal value of the objective function. However, sometimes it is difficult to evaluate the derivative of the objective function and it becomes more challenging when the objective function is noisy [174]. Also, the derivative-based methods are usually considered as local optimization techniques [174]. Derivative-free methods include but not limited to evolutionary algorithms (such as genetic algorithm [175]) pattern search [176], simulated annealing algorithm [176], particle swarm algorithm [176], and Bayesian optimization method.

In order to compare the performance of the Bayesian optimization method with another global optimization technique, we used the genetic algorithm to find the Young's modulus of one of the high-frequency cases with high noise intensity. We chose the elliptical plate with the excitation frequency of 7961 Hz with SNR of 0 dB (presented in Section 4.3.2.1) and used MATLAB genetic algorithm toolbox and considered two evolution scenarios. In Scenario 1, we considered the population of 20 with 9 generations while in Scenario 2, we set the population to be 60 with 3 generations. Both scenarios result in overall 180 times evaluations of the objective function which is the same as the number of evaluations we used with the Bayesian optimization algorithm. The crossover fraction was set to be 0.8. We found that for Scenario 1, the accuracy can be significantly different each time we run the optimization. We repeated the optimization four times for this scenario and the range of error of the estimated Young's modulus was from about 6.6% to 84% while it was 0.63% with our proposed method using Bayesian optimization for this noisy vibration data. This can be due to the differences in the initial populations each time we run the optimization as it is known that in genetic algorithm the accuracy depends on the initial population [177]. We also ran the optimization for Scenario 2 four times and the range of the error of the estimated Young's modulus was from 0.46% to 8.70%. One may be able to get better results by using different parameters in the genetic algorithm making the material characterization process operator dependent [141]. Our

proposed method, on the other hand, is not operator dependent because the Bayesian optimization algorithm does not need parameters to be set by the operator.

Among other derivative-free optimization methods, pattern search methods search in arbitrary directions and modify the motion of the points to get as close as possible to the optimum values. However, these methods may be attracted by local optima [178]. The simulated annealing algorithm is a probabilistic technique that uses a temperature-like variable to control the degree of stochasticity in the random search and finds the optimum value by iteratively going down from a high temperature to a low temperature. In addition to be stochastic, another disadvantage of this method is its slow convergence [177]. The particle swarm method is a derivative-free method that is also highly sensitive to the initial particles chosen [141] and is known to be trapped in local optima [177]. Bayesian optimization method, which is used in the current work, is not affected by the initialization and is known to be able to find the global optimum with a fewer number of iterations in comparison with many other optimization algorithms such as genetic algorithm, particle swarm, and pattern search.

We also presented some unidentifiable cases, conditions under which the method has a poor performance and remedies for such situations. For instance, as mentioned in Section 4.3.2.5, our estimation method does not provide accurate results for thick plates. Also, as discussed in Section 4.3.3, the displacement field of the entire object and its non-moving boundary should be captured in measurements to be able to accurately estimate the Young's modulus. Obtaining such a view, to enable such captures, might be challenging for some measurement scenarios. Moreover, the method was developed based on a negligible damping assumption that can be justified for many low damped engineering structures. However, this limits the application of the method to damped structures. The developments are underway to generalize the method to damped structures.

Chapter 5

Material characterization of human middle ear using machine-learning-based surrogate models

Preface

In this chapter, we generated machine-learning-based surrogate models of the middle ear that can be used for fast computation of the forward mechanics of the middle ear. We apply some modifications to the material characterization method presented in Chapter 4 to make it suitable to be applied to the middle ear. We also used the outcomes of Chapter 3 to focus on the most influential parameters of the middle ear while creating the surrogate models. Our parameter estimation method used full-field vibration patterns of the TM for material characterizations and we verified its accuracy with respect to the FE model for several test samples.

Overview

Finite-element models have been among the most prominent modeling tools for simulating behaviours of the human middle ear. One problem with these models is their high computational costs which makes them unusable for many clinical applications such as real-time estimation of the mechanical properties of the middle-ear structures for diagnostic purposes. This study aims to alleviate this issue in two parts. In the first part, we used machine learning techniques to create surrogate models of the middle ear that can predict its responses with a significantly lower computational cost in comparison to real finite-element models. We used the results of our previous studies on the human middle ear to focus on the model parameters that have the greatest impact on the middle ear vibrations while creating the machine learning models. These parameters include the Young's modulus and thickness of the tympanic membrane and the Young's modulus of the stapedial annular ligament. The eXtreme Gradient Boosting (XGBoost) method was implemented for creating the machine learning models and our investigation results revealed that the created surrogate models can fairly represent the vibrational responses of the umbo, stapes footplate, and vibration patterns of the tympanic membrane at most frequencies. In the second part of the study, we combined the created machine learning models with Bayesian optimization (using the BoTorch library) for fast estimation of the Young's modulus of the tympanic membrane and the Young's modulus of the stapedial annular ligament. Our proposed methods were able to estimate Young's modulus of these two structures separately and simultaneously with values of mean absolute percentage error of less than 7%. The use of surrogate models instead of real finite-element models increases the speed of the parameter estimation remarkably and makes it suitable for future clinical applications (upon further development and validation) where the estimated mechanical properties of the middle-ear structures can be used for diagnostic purposes.

5.1 Introduction

In the area of mechanics of hearing, models of the middle ear have attracted lots of attention in previous years. Researchers have used different modelling techniques including lumped-parameter and finite-element models to simulate middle-ear responses [31], [37], [48], [51], [55], [179]. Oftentimes, the results of experimental measurements performed on human or animal middle ears are used to validate these models [37], [48], [180]. FE models consider the geometrical complexities in the middle ear and also can deal with different material properties and boundary conditions, and as a result, they can give more accurate results in comparison to lumped models. However, due to their high degree of freedom, the computational costs of FE models are usually high, and specific hardware configurations and long runtimes are normally inseparable parts of the FE simulations of the middle ear. This high computational cost of FE models usually makes these models poorly suited for applications in which real-time calculations of model responses are necessary or the applications in which we need to run the model hundreds or thousands of times to solve optimizations problem for different aims such as parameter estimation.

One way to deal with the high computational cost of FE models is to use surrogate models [181]. In order to create these surrogate models, we need to run our FE model a limited number of times and then exploit the results of these simulations to fit a surrogate model that receives the input parameters (i.e., variables in future calculations) and estimates the outputs of interest. Should the surrogate model have our desired accuracy in its predictions, we can use it in lieu of the costly FE models to find the outputs of the system for any new inputs within a few seconds.

Several studies in the literature have already used surrogate models instead of real FE models for fast evaluation of forward mechanics of different biological structures. For instance, Dabiri et al. implemented surrogate models created with machine learning (ML) methods in real-time simulation of left ventricle mechanics [182], [183]. Liu et al. used ML-based surrogate models for fast prediction of failure metrics on the aortic wall [184]. In another study, Halloran et al. investigated the feasibility of ML methods for simulating the mechanical behaviours of the

human liver during the breathing process [185]. In all these studies, FE simulations were used for generating testing and training datasets. In the area of middle-ear mechanics, only very few works in the literature have used surrogate models instead of FE computations. In Chapter 3, we exploited surrogate models generated using the polynomial chaos expansion method for performing a global sensitivity analysis on the middle ear. Aside from using ML models as a replacement of costly FE models, ML models have been also used widely in other applications such as using medical images of ears or different parts of the body for diagnostic purposes [186]–[190].

The mechanical properties of tissues can be considered as a diagnostic index for various diseases [191]. In fact, diseases cause alterations in the microstructures of the tissues and the mechanical properties of the tissues are remarkably controlled by their microstructures [11]. Traditional mechanical methods for estimating the material properties cannot be used in situ and also most of the time these methods are destructive [11]. Therefore, computational methods can be suitable choices for the estimation of the mechanical properties of biological structures [11]. FE method is one of the computational methods that can be used in combination with optimization techniques and clinical measurements for non-destructive estimation of the material properties of biological structures. However, as mentioned earlier, usually FE models have high computational costs. Using ML models drastically decrease the computational costs of FE models for estimating these mechanical properties and makes the parameter inference methods suitable for future possible clinical applications. Several researchers utilized surrogate models for the evaluation of forward biomechanical responses of different biological structures for the purpose of fast parameter inference. For instance, Cai et al. used ML-based surrogate models for the estimation of passive parameters of the left ventricular myocardium [192]. Davies et al. also proposed a parameter inference method for estimating myocardial properties from surrogate models created using local Gaussian and low rank Gaussian processes [193]. In another study, Noé et al. used multivariate output Gaussian process to infer constitutive parameters of the left ventricle [194].

This chapter consists of two parts. In the first part, we will propose creating ML-based surrogate models for fast simulation of middle-ear dynamics with a wide range of variability for input parameters that can account for both normal and pathological ears. We will show that the created ML models are able to predict the amplitude and phase of the umbo (the most inferior part of the malleus that is attached to the central part of the TM) and stapes footplate (the part of the stapes that is connected to the cochlea through the oval window) and the full-field vibration patterns of the TM with outstanding accuracies (with respect to the FE results). These ML models of the middle ear can be used for different purposes such as developing real-time surgical simulators [116], [117].

In the second part of this chapter, we will use the created ML models of the full-field vibration pattern of the TM for estimating the Young's modulus of TM and SAL. This part of the current chapter is an extension to our previous study on developing parameter estimation methods as a diagnostic tool for middle ear disorders (Chapter 4). In that study, we proposed a method for estimating the Young's modulus of 2D thin planar structures using the harmonic full-field vibration patterns of the structure. Here, we apply some changes to our proposed method, making it suitable to be applied to the TM vibration patterns to estimate the mechanical properties of some of the most influential structures in the middle ear.

5.2 Methods

5.2.1 Finite-element model

The FE model of the human middle ear used in this study was created based on the segmentation of μCT images dataset of a 73-year-old male cadaver temporal bone. The details of segmentation and mesh generation processes can be found in Chapter 2. Our model includes TM, ossicles, AML, LML, IMJ, ISJ, SML, SAL, PIL, and manubrial fold.

The model was excited by applying a uniform pressure (with an amplitude of 1 Pa) to the lateral surface of the TM. The material properties of the baseline model and the boundary conditions are the same as the ones in Chapter 2. The TM annulus was fully clamped and the AML, LML, PIL, SML, and SAL were considered to be fixed at their distal end where they

are connected to the middle-ear cavity wall The cochlear load was represented by four dashpots attached to the stapes footplate. All computations were carried out using Code_Aster (version 14.4.0) open-source FE package. We used the dynamic transient solver of Code_Aster for constructing the frequency response functions of the umbo and stapes footplate and for these simulations, a step function was considered for the excitation of the model (pressure). We implemented the implicit Newmark-β scheme into the model, and to have an unconditionally stable solution, the values of β and γ in the Newmark-β scheme were chosen to be 0.25 and 0.5, respectively [37], [88]. The displacement frequency response functions of the umbo and stapes footplate were created by differentiating the step response with respect to time and then using the fast Fourier transform. For these transient simulations, the value of the time span was considered to be 25 ms and the value of the time step was 10 μs. Applying the aforementioned values of the time step and time span in the simulations results in 405 equally spaced frequencies in the frequency range of 100 Hz to 10 kHz. In Chapter 2, we checked the dependency of the model results on the changes in these two values. Moreover, the values of baseline model parameters were chosen to be exactly the same as the values we used in Chapter 2. For all full-field vibration patterns of the TM in this chapter, we used harmonic vibration analysis of Code_Aster.

Our initial mesh consisted of 7,656 seven-node second-order triangular shell elements (TRIA7) for TM and 195,820 ten-node second-order tetrahedral elements (TETRA10) for all other structures. We refined this mesh using the Homard utility of Code_Aster to check mesh convergence. We increased the number of the triangular elements and tetrahedral elements by factors of four and eight, respectively. We compared the results of the refined mesh and the original mesh in 24 equally spaced frequencies in the frequency range of 100 Hz to 10 kHz. We observed a maximum difference of less than 0.90 dB for the displacement amplitude of the umbo and less than 1.44 dB for the amplitude of the stapes footplate. As a trade-off between the accuracy and computational cost, we considered our initial mesh for all simulations in this chapter.

5.2.2 Uncertain model parameters and design of experiments

The middle ear consists of multiple structures and even if we consider linear isotropic material property (which is the simplest assumption) for each of them, we will end up having tens of parameters in our model and we need to know the values of all these parameters to be able to create an FE model. For creating the ML model, it is very helpful if we can reduce the number of these parameters as it will be hard to create accurate ML models with so many parameters, especially if the variations of each of these parameters are large. Additionally, based on our findings in Chapter 3 and also based on other the studies conducted on the human middle-ear model, the effects of variations of some of these parameters on the vibrations of the middle ear are negligible [10], [37], [55], [101]. In Chapter 3, we performed a global sensitivity analysis on the middle-ear model and found the parameters that have the most significant impacts on the outputs. Our results suggested that the mechanical parameters that have the most considerable impacts on the amplitude of the umbo and stapes footplate in the frequency range of 100 Hz to 10 kHz are the Young's modulus of the TM (E_{TM}) and SAL (E_{SAL}). Our global sensitivity analysis results also suggested that the thickness of the TM has considerable effects on the variations of the amplitude of the umbo and stapes footplate at many frequencies. Hence, in this chapter, we considered the Young's modulus of the TM and SAL and the thickness of the TM as the input parameters for creating our ML models.

As mentioned before, one of our main purposes of training ML models and parameter estimations is to use them as a diagnostic index for hearing pathologies. Therefore, we need to consider a significant variation for each of these parameters. For this aim, the values of coefficient of variation of the Young's modulus of the TM and SAL were considered to be 50% and the range of the TM thickness values was chosen based on the reported ranges in the literature [87]. The ranges of these three parameters are reported in Table 5-1 and we assumed a uniform distribution for these three parameters. The mean values of the input parameters are 12 MPa, 1.4 MPa, and 74 μm for the Young's modulus of the TM, the Young's modulus of the SAL, and the thickness of the TM, respectively. Random input parameters of the ML models were created using the Latin Hypercube sampling method [105].

Table 5-1 – Range of parameters considered in creating ML models.

Parameter	Min value	Max value
Thickness of TM	30 µm	150 µm
E_{TM}	1.61 MPa	22.39 MPa
E_{SAL}	0.19 MPa	2.61 MPa

5.2.3 Machine-learning model

The ML models in our study were constructed using eXtreme Gradient Boosting (XGBoost)[5] [195] which can be used for both classification and regression [196]. XGBoost is an efficient implementation of the gradient-boosting decision tree framework [197], [198]. In several applications, XGBoost has been shown to have a better performance in comparison to many common approaches for creating ML models such as multi-layer perceptron and support vector machines [192], [196], [199].

Considering a dataset $D = \{(x_i, y_i): i = 1, .., q,\ x_i \epsilon \mathbb{R}^p\}$, where we have p features and q samples [200], each tree ensemble model uses G additive functions for output prediction and can be represented as [195]:

$$\hat{y}_i = \sum_{g=1}^{G} f_g(x_i)\ , f_g \in F \tag{5-1}$$

where $\hat{y}_i$ is the predicted output, F is the space of regression trees also known as classification and regression tree (CART) and f_g is a function in the functional space F [192]. In order to create the ML model, XGBoost minimizes the following loss functions [195]:

$$\mathcal{L}(\phi) = \sum_{t} l(\hat{y}_i, y_i) + \sum_{g} \Omega(f_g) \tag{5-2}$$

[5] https://xgboost.ai/

$$\Omega(f\ ) = \gamma T\ \ + \frac{1}{2}\lambda\|\omega\ \ \|^2$$

where T is the number of leaves and l is a distance function that measures the difference between the target value (y_i) and the predicted value ($\hat{y}_i$). Also, λ and γ are parameters for controlling degrees of regularization and ω is the weight score of leaves. More details regarding the XGBoost framework can be found in [195], [201].

One crucial aspect that should be considered in training any ML model is hyperparameter tuning. The values of hyperparameters can significantly affect the performance of the ML model [202]. We used Scikit-learn library[6] [203] to implement a grid-search method with five-fold cross-validation for the hyperparameter tuning. The size of the training and testing datasets were 950 and 100, respectively. The values of hyperparameters considered in the grid search are as follows[7]: learning_rate was considered to be 0.05,0.075, and 0.1; max_depth was considered to be 6,8, and 10 and n_estimators was considered to be 2000 and 5000. A separate ML model was created for each frequency.

In order to measure the accuracy of the created ML models with respect to the FE results, we used two different measures; coefficient of determination (R^2) for the values of amplitude and mean cosine difference (MCD) for the values of phase. These two measures are defined as follows [192], [204]:

$$R^2 = 1 - \frac{\sum_{i=1}^{m}(y_i - \hat{y}_i)^2}{(y_i - \bar{y}^2)^2} \quad , \quad \bar{y} = \frac{1}{m}\sum_{i=1}^{m} y_i \tag{5-3}$$

$$MCD = \frac{1}{m}\sum_{i=1}^{m} cos\left(\theta_i - \hat{\theta}_i\right) \tag{5-4}$$

where y_i and θ_i *(i=1,2,..., m)* are true values, $\hat{y}_i$ and $\hat{\theta}_i$ *(i=1,2,..., m)* are predicted values, and m is the size of the testing dataset. The closer these two measures are to unity, the better the ML model's performance.

[6] https://scikit-learn.org/stable/
[7] https://xgboost.readthedocs.io/en/stable/

We are interested in the motions (amplitude and phase) of the umbo, stapes footplate, and TM vibration pattern. So, at each frequency, we created two ML models for umbo (real and imaginary parts of responses), two ML models for stapes footplate (real and imaginary parts of responses), and three models for each of the nodes of the TM (real, imaginary, and magnitude of responses). The reason why we created separate models for the magnitude of the TM nodes (in addition to the real and imaginary parts) will be elaborated shortly. Also, for creating the ML models of nodes on the TM at each frequency, we put them in a vector form. The details about the number of nodes on the TM considered for creating ML models will be presented shortly.

The results for the amplitude and phase of the umbo amplitude and phase of the stapes footplate, and full-field TM phase patterns were then calculated based on ML models of real and imaginary parts of the responses at each frequency. The full-field TM amplitude patterns were not calculated using the real and imaginary parts and we directly used the ML models that we had created for the magnitude of TM nodes. The logic behind this was to reduce the runtime of the parameter estimation. In the parameter estimation method, which will be discussed in Section 5.2.4, we use the amplitude of different nodes on the TM. Therefore, in each optimization iteration, we need to find the amplitude of those nodes and compare them with the true values. If we use ML models of real and imaginary parts, we need to first estimate the real and imaginary parts of the response from respective ML models (for real and imaginary parts) and then we need to compute that magnitude value in another step, whereas, if we use the ML models of magnitude, all these steps will be integrated into a single one. Therefore, having ML models that can directly calculate these amplitude values, increases the parameter estimation speed in comparison to the case we want to predict real and imaginary parts in each optimization iteration and then find the amplitude from that.

We should also note that our original mesh consisted of 15,455 nodes on the TM. In order to reduce the computational costs of creating ML models, we only considered 1009 nodes across the TM for creating ML models. When choosing these nodes, we paid attention to the distribution of the nodes to keep them the same in all regions of the TM. The density of the

nodes in the manubrium area was higher than other regions of the TM. The reason for this was that the original mesh was finer in that region in comparison to the other regions of the TM. The distribution of the nodes on the TM will be provided later in Section 5.3.2.

We should note that in all parts, umbo and TM vibration patterns are reported in the direction normal to the manubrium at the umbo and the stapes footplate motion is reported in the stapes piston-like direction.

5.2.4 Parameter estimation

We used Bayesian optimization for the estimation of the Young's moduli of TM and SAL. Bayesian optimization uses a computationally inexpensive surrogate model to approximate the real objective function [140]. This method is shown to have very good performance even with noisy measurement data [79], [205]. In Chapter 4, we used Bayesian optimization for material characterization of thin planar structures measure with stroboscopic holography and observed that this method has several privileges over other common optimization techniques. More details about the Bayesian optimization as well as a review of some of its applications can be found in [140].

In the current study, we used the vibration amplitude pattern of the TM for parameter estimation. We know that the impacts of variations of the Young's modulus of the SAL on the variations of the umbo and stapes footplate are more considerable at low frequencies (Chapter 3). Also, the effects of variations of the Young's modulus of the TM on the variations of the umbo and stapes footplate responses are significant at most frequencies above 1 kHz (Chapter 3). Therefore, we considered the vibration patterns at frequencies of 100 Hz and 5 kHz for the estimation of the Young's modulus of the SAL and TM, respectively. The following two objective functions were defined for the estimation of these two Young's moduli:

$$obj(E_{SAL}) = \left(\frac{\sqrt{\sum_{j=1}^{n} \left(d_j^c - d_j^m \right)^2}}{n} \right)^{-1} \quad @f = 100\ Hz \tag{5-5}$$

$$obj(E_{TM}) = \left(\frac{\sqrt{\sum_{j=1}^{n} \left(d_j^c - d_j^m\right)^2}}{n} \right)^{-1} \quad @f = 5\ kHz \tag{5-6}$$

where d_j^c represents the calculated displacement of node j and d_j^m is the true displacement of node j. Also, n is the total number of nodes on the TM used in the optimization process.

As mentioned in Section 5.2.3, in our ML model, we considered a total number of 1009 nodes on the TM. We conducted two scenarios for the estimation of the Young's moduli of the TM and SAL. These scenarios were created based on the values feature importance of the nodes. In fact, each node of the TM has three features that are the Young's modulus of SAL, Young's modulus of TM, and thickness of the TM. Using the feature importance, we are able to determine which features have the most effects on the predicted values of motions of each of the TM nodes. We used the built-in feature importance of XGBoost to determine the most influential features for each node. The feature importances were calculated using the gain algorithm [8] that calculates the contribution of each tree to the improvement of model performance [206], [207].

As mentioned earlier, we considered two scenarios for estimation of the Young's moduli of the TM and SAL: one with all nodes on the TM (n = 1009) and the other one with considering only nodes of the TM that have values of feature importance of greater than 0.5 (n < 1009). The sum of values of feature importance for each output is 1 and in fact, a feature importance of greater than 0.5 shows that the desired feature, had a contribution of greater than 50% on the estimated output. More details about the two scenarios considered for parameter estimation will be provided in Section 5.3.2.

For simultaneous estimation of the Young's modulus of the TM and SAL, we suggest using an objective function which is a combination of equations (5-5) and (5-6)):

$$obj(E_{TM}, E_{SAL}) = \frac{1}{\alpha}\ obj(E_{TM}) + obj(E_{Sal}) \tag{5-7}$$

[8] https://xgboost.readthedocs.io/en/stable/

As the functions $obj(E_{TM})$ and $obj(E_{SAL})$ are defined at two different frequencies, and as the number of nodes we considered on the TM for each of them is different (see Section 5.2.4), the orders of their magnitude can be different from each other. Therefore, we needed to define a parameter α to tune the contribution of the two objective functions in our estimation. We manually found the value of this parameter by running the optimization process for a few cases and ended up with the value of 3.2. Our observations suggest that the value of this parameter can have significant effects on the parameter estimation accuracy and one may need to retune it for measurements at other frequencies or with a different number of nodes.

We employed BoTorch open-source Bayesian optimization for parameter estimation [208]. The acquisition function used in all our simulations was the Expected Improvement function [158]. The values of parameters num_restarts and raw_samples were chosen to be 20 and 512, respectively. Also, the number of initial random guesses was set to be 5 and the number of model evaluations in the Bayesian optimization process was set to be 200. Also, in order to measure the accuracy of the estimated values, we used mean absolute percentage error (MAPE) which is defined as:

$$MAPE = \frac{1}{m}\sum_{t=1}^{m}\left|\frac{A_t - E_t}{A_t}\right| \times 100 \tag{5-8}$$

where A_t and E_t represent the true and estimated values of sample *t*, respectively. Figure 5-1 illustrates the workflow of the creation of ML models as well as the parameter estimation.

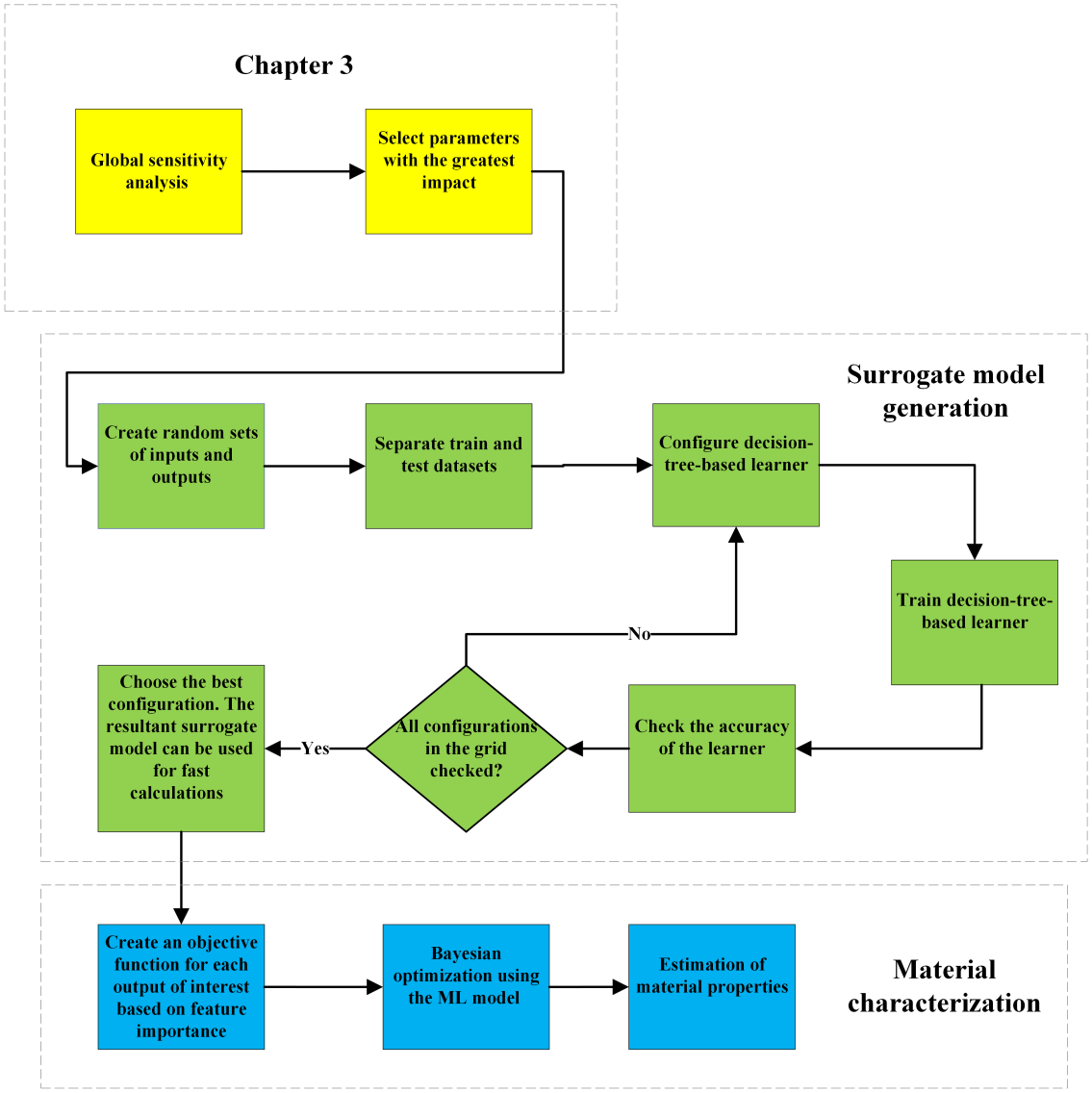


Figure 5-1 – Workflow of the creation of ML models and parameter estimation. In the first step, we used the global sensitivity analysis results from Chapter 3 to find the most important parameters in the middle-ear model. We then created some random sets of inputs for these parameters using the mean values equal to respective values in the baseline model and the ranges reported in Table 5-1 (with uniform distribution). In total, we had 1050 FE simulations and the size of our training and testing datasets were set to be 950 and 100, respectively. Afterward, the ML models were trained. The grid search method was used to find the hyperparameters of the ML model that resulted in the most accurate predictions with respect to the FE results. In the next step, we defined objective functions for each output of interest and used these objective functions for parameter estimation.

5.3 Results

5.3.1 Predictions of machine-learning models

In this section, we present the results of created ML models and their accuracy (with respect to the FE results) in predicting the response of the umbo, stapes footplate, and TM vibration patterns. Figure 5-2 shows the results of predictions of the ML models for the amplitude and phase of the umbo. As mentioned previously, we had 100 simulations in our testing dataset. Here we showed the true and predicted values of the umbo displacement amplitude and phase for 5 random sets of parameters in the testing dataset. Based on the results presented in this figure, the ML model calculates the amplitude and phase of the umbo very accurately (with respect to the FE results) at almost all frequencies in the range of 100 Hz to 10 kHz. The difference between the true displacement amplitude of the umbo and the predicted values in these 5 samples is less than 2 dB at more than 90% of frequencies. The values of cosine difference are greater than 0.97 at all frequencies and for all these samples.

Figure 5-3 shows the results of predictions of the ML models for the amplitude and phase of the stapes footplate. Similar to Figure 5-2, it presents the true and predicted vibration patterns for 5 random sets of parameters chosen from our testing dataset. For all samples, the difference between the predicted and true amplitude of the stapes footplate is less than 2 dB at more than 91 % of frequencies and the cosine difference between the predicted and true phase values is more than 0.99 at all frequencies.

Figure 5-2 and Figure 5-3 show the response of the ML models for the umbo and stapes footplate for several random sample parameter sets chosen from the testing dataset. To provide a more comprehensive analysis of the performance of the ML models, we reported the values of R^2 (for the displacement amplitude of the umbo and stapes footplate) and MCD (for the displacement phase of umbo and stapes footplate) in Figure 5-4. The results presented in this figure are calculated based on the ML predictions of all 100 samples of the testing dataset. For both amplitudes of the umbo and stapes footplate, the value of R^2 is very close to 1 at low frequencies (below 200 Hz) and high frequencies (above 6 kHz). The minimum value of R^2

for the amplitude of the umbo happens near the frequency of about 600 Hz (R^2 of about 0.93) and the minimum value of R^2 for the amplitude of the stapes footplate occurs near the frequency of about 900 Hz (R^2 of about 0.92). Moreover, the MCD results of the displacement phase of the umbo and stapes footplate presented in Figure 5-4 indicate that the phase values obtained using ML models are very accurate (with respect to the FE results) at frequencies below 500 Hz for both umbo and stapes footplate (MCD of very close to unity). The minimum value of MCD for the displacement phase of the umbo occurs at the frequency of about 1.8 kHz (MCD of 0.95) and the minimum value of MCD for the phase of the stapes footplate is obtained at 4.0 kHz (MCD of 0.96).

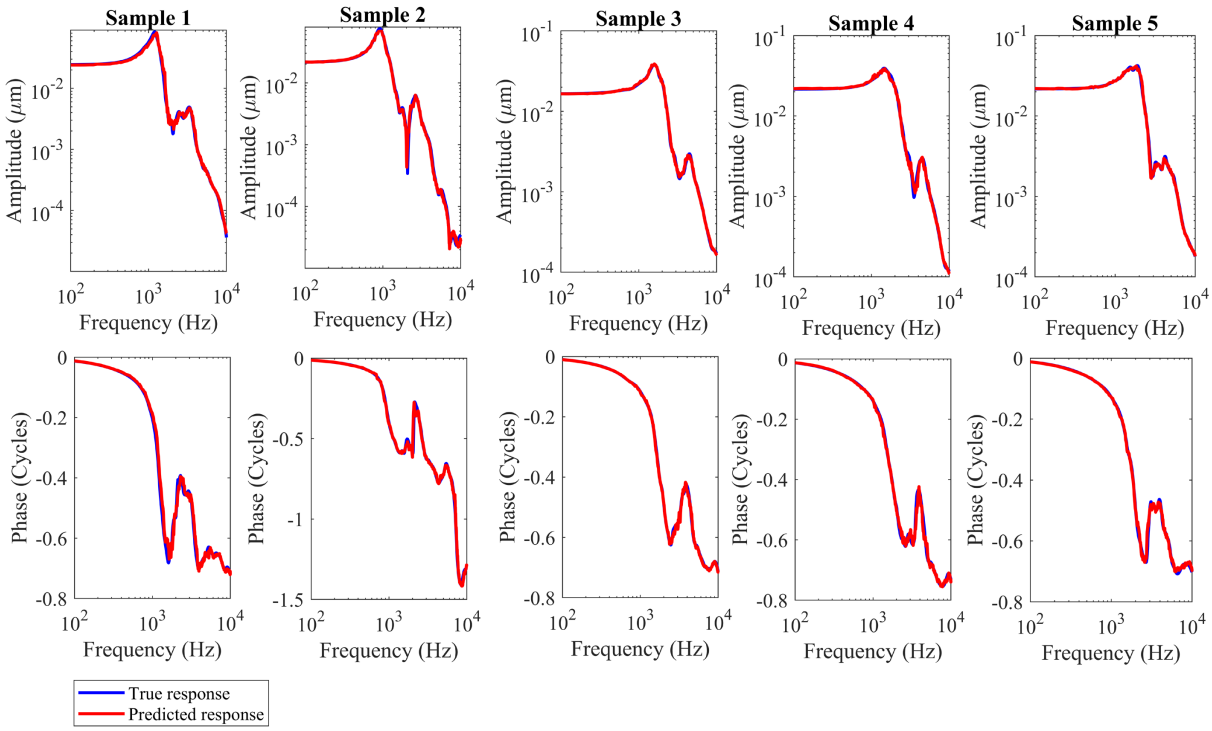


Figure 5-2 – Results of predictions of created ML models for the amplitude and phase of umbo. Results of five random samples from the testing dataset are presented here. The ML models can fairly represent the amplitude and phase of the umbo at almost all frequencies. The difference between the predicted and true values of the displacement amplitude of the umbo in these 5 samples is less than 2 dB at more than 90% of frequencies. Also, for all samples shown in this figure, the cosine difference between the true and predicted phase values is greater than 0.97 at all frequencies.

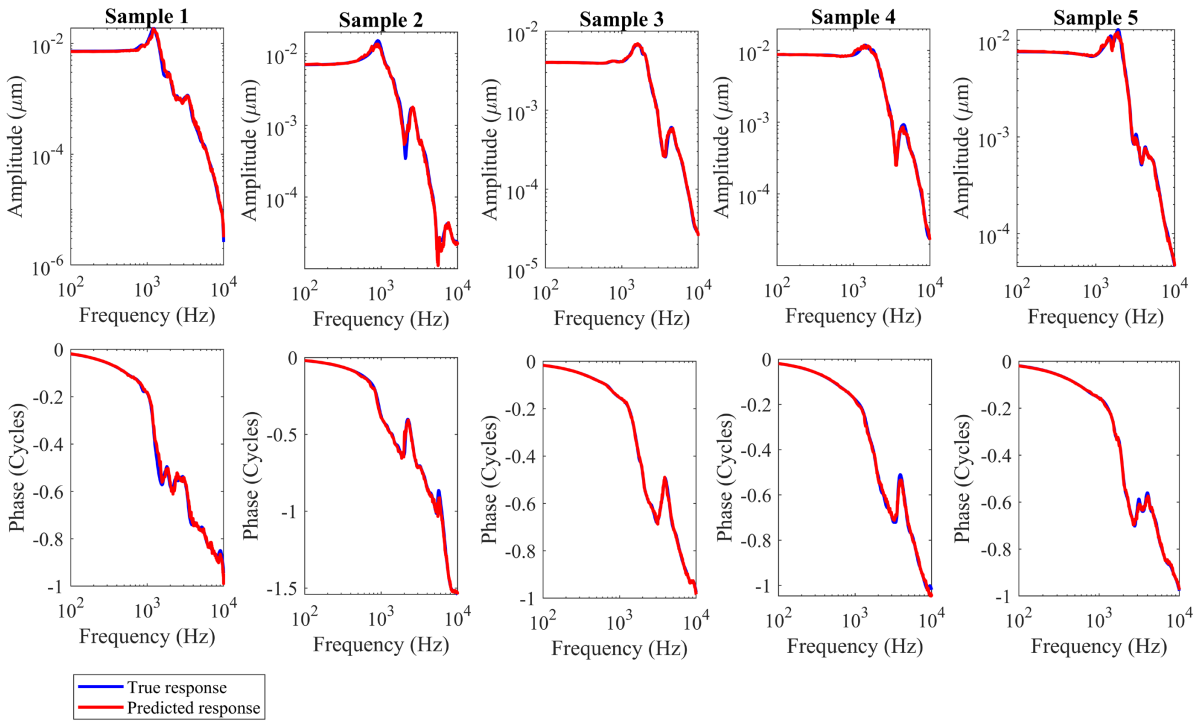


Figure 5-3 – Results of predictions of created ML models for the amplitude and phase of the stapes footplate. Results of five random samples from the testing dataset are presented here. The ML models can fairly represent the amplitude and phase of the stapes footplate at almost all frequencies. The difference between the predicted and true values of the displacement amplitude of the stapes footplate in these 5 samples is less than 2 dB at more than 91% of frequencies. Also, for all samples shown in this figure, the cosine difference between the true and predicted phase values is greater than 0.99 at all frequencies.

One of the main components we should always consider in training ML models is the size of the training dataset. Due to the relatively high computational cost of the FE models of the middle ear, it can be quite beneficial to have an idea about the effects of the size of the training dataset on the accuracy of predictions of ML models with respect to the FE results. To investigate these effects, Figure 5-5 presents the R^2 value of the displacement amplitude of the umbo and stapes footplate at three different frequencies: 100 Hz (low), 5 kHz (middle), and 10 kHz (high) with respect to the size of the training dataset. For each size of the training dataset, the size of the testing dataset was considered to be equal to $\left[\frac{\text{size of test dataset}}{10}\right] + 1$. As

expected, increasing the size of the training dataset results in increasing the value of R^2. For both amplitudes of the umbo and stapes footplate, an R^2 of about or greater than 0.95 is attainable when we have more than 400 model simulations in our testing dataset.

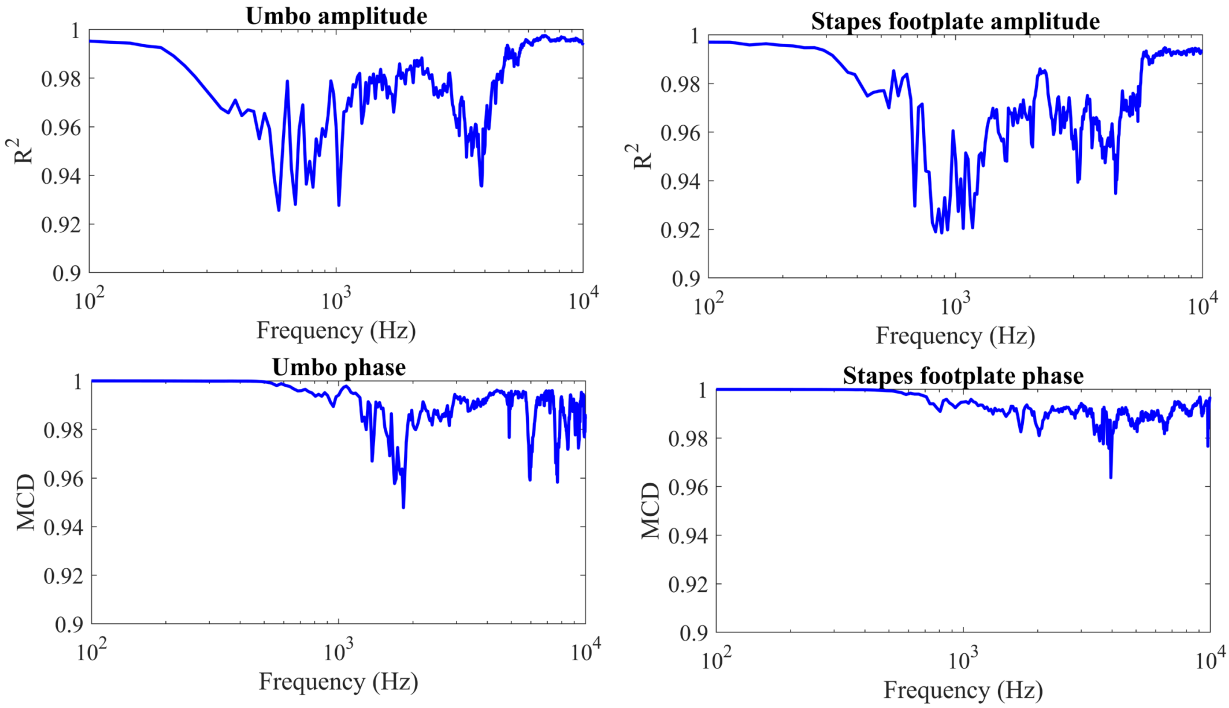


Figure 5-4 – Values of R^2 (for the amplitude) and MCD (for the phase) of the umbo and stapes footplate in the frequency range of 100 Hz to 10 kHz. The values of R^2 and MCD are calculated based on the predictions of the ML models for the whole testing dataset (with the size of 100). For both amplitudes of the umbo and stapes footplate amplitudes, the value of R^2 is very close to 1 at very frequencies below 200 Hz and frequencies above 6 kHz. The minimum values of R^2 for the amplitude of the umbo and stapes footplate are about 0.93 (at 600 Hz) and 0.92 (at 900 Hz), respectively. Also, for both umbo and stapes footplate, the values of MCD of the phase are greater than 0.94 at all frequencies.

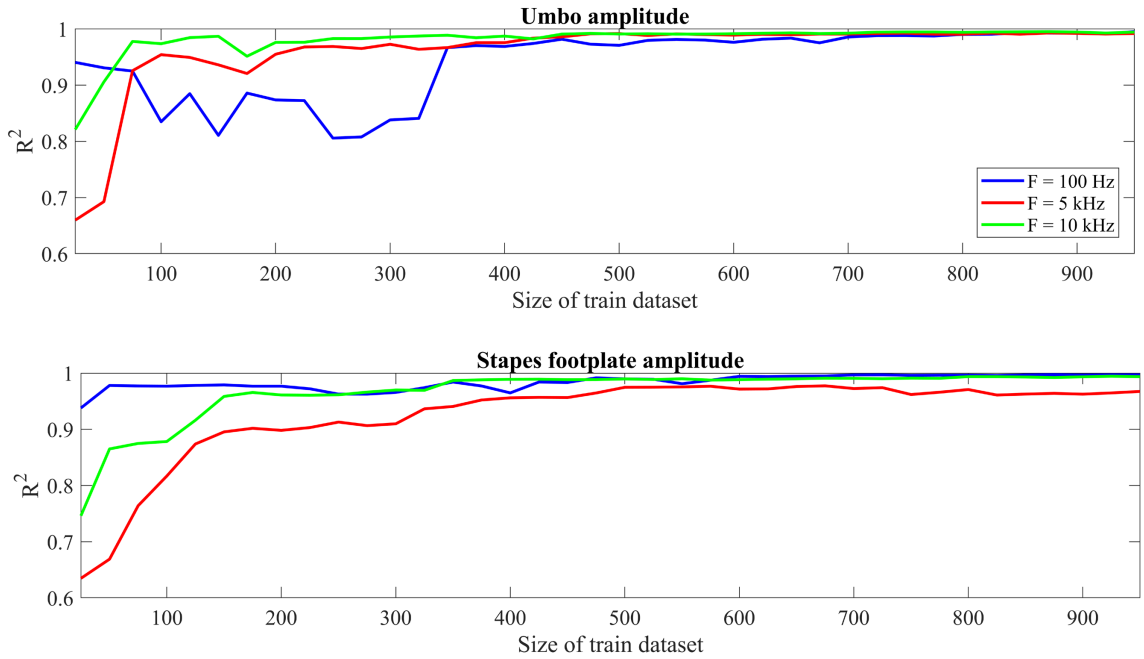


Figure 5-5 – The values of R^2 with respect to the size of the training dataset at three different frequencies: 100 Hz (low), 5 kHz (middle), and 10 kHz (high). For both amplitudes of the umbo and stapes footplate, an R^2 of about or greater than 0.95 is attainable when we have more than 400 model simulations in our testing dataset.

The ability of ML models to predict the vibrations patterns of the TM is another factor of interest in the current study. Figure 5-6 illustrates the ML model results for calculating the displacement amplitude vibration patterns of the TM. The results are depicted at three frequencies: 100 Hz (low), 5 kHz (middle), and 10 kHz (high). The left and middle columns of Figure 5-6 present the true and predicted vibration patterns, respectively, for a random sample obtained from the testing dataset. They show that the true and predicted patterns are very similar at all three frequencies. For the sample test shown here, the differences between the predicted and true values are less than 2 dB at more than 94 % of nodes across the TM for the three frequencies discussed here. Also, to provide a more detailed insight into the accuracy of the ML models with respect to the FE results, the R^2 values calculated using 100 samples in the testing dataset are provided in the rightmost column of Figure 5-6. At all three frequencies,

the values of R^2 are greater than 0.9 in more than 90% of the nodes across the TM. The minimum values of R^2 at the excitation frequencies of 100 Hz, 5 kHz, and 10 kHz are 0.96, 0.71, and 0.66, respectively.

The ML model results for calculating displacement phase patterns are shown in Figure 5-7. The results are shown at the same frequencies considered for the amplitude patterns of the TM (Figure 5-6). Similarly, the left and middle columns show the true and predicted values of phase patterns, respectively, for a random sample obtained from the test case. For all three frequencies, the true and predicted phase patterns are very similar to each other. For all of them, the cosine difference is greater than 0.9 at more than 97% of the nodes on the TM. Also, to evaluate the accuracy of the ML models (with respect to the FE results) in predicting vibration phase patterns, the rightmost column of Figure 5-7 illustrates the values of MCD calculated based on the whole testing dataset with 100 samples. Similar to what we observed for the vibration amplitude patterns in Figure 5-6, here also the predicted phase values are very similar to the true phase values obtained from the FE model for most of the nodes across the TM (at all three frequencies, the MCD value of more than 99% of nodes is greater than 0.9 except for a few nodes in the annular region. The minimum values of MCD at the frequencies of 100 Hz, 5 kHz, and 10 kHz are 0.98, 0.88, and 0.92, respectively.

5.3.2 Parameter estimation using combination of machine-learning models and Bayesian optimization

In this section, we present the results of the parameter estimation which was done by combining the obtained ML models introduced in Sections 5.2.3 and 5.3.1 with the Bayesian optimization discussed in Section 5.2.4.

In the first step, we focused on the estimation of the Young's modulus of the SAL. We used the objective function in Equation (5-5) for estimating this parameter from the full-field vibration pattern of the TM (at frequency of 100 Hz) using two different scenarios: the first scenario was to use all nodes on the TM for parameter estimation and the second scenario was to exploit only the nodes with feature importance values of greater than 0.5 for this parameter.

The aim was to compare the parameter estimation results of the two scenarios to find the best way for estimating the Young's modulus of the SAL. The nodes on the TM that have values of feature importance of greater than 0.5 are shown in red color on the left panel of the Figure 5-8. Based on the results presented in this figure, these nodes lay on the manubrium.

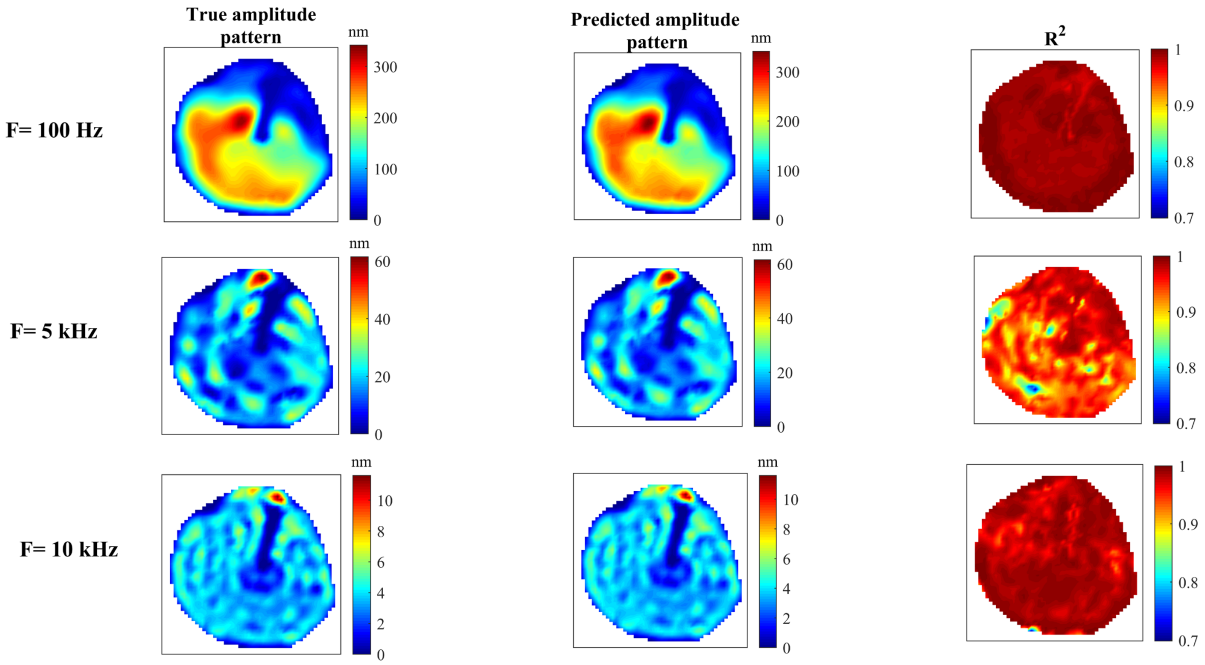


Figure 5-6 – ML model prediction results of the TM amplitude vibration pattern. The results are presented at three frequencies: 100 Hz (low), 5 kHz (middle), and 10 kHz (high). The left and middle columns show the true and predicted vibration amplitude patterns for one of the random test sets, respectively. At all these three frequencies, the predicted amplitude pattern is very close to the true pattern. The rightmost column represents the values of R^2 at these frequencies. The values of R^2 presented in this column are calculated based on the predictions of the model for the whole testing dataset (with the size of 100).

The results of the parameter estimation are presented in Table 5-2. Due to space limitation, only the results of 10 random samples from the testing dataset are included in this table. However, the MAPE and maximum error values reported in this table, are calculated based on the parameter estimation results obtained from all 100 samples in the testing dataset. Based on the results presented in Table 5-2, the MAPE is 25.36% when we use all nodes on the TM for

our parameter estimation and is 3.24 when we use only nodes on the manubrium (i.e., the nodes with high feature importance shown in red in Figure 5-8 (left)). This shows that using the nodes on the manubrium leads to a more accurate estimation of the values of the Young's modulus of the SAL (with respect to the FE model). The values of maximum error also confirm this; the maximum error is 579.29% when we used all nodes on the TM for parameter estimation and the maximum error among all 100 samples in the testing dataset is equal to 22.60% when we used only the nodes with high feature importance for estimating the Young's modulus of the SAL.

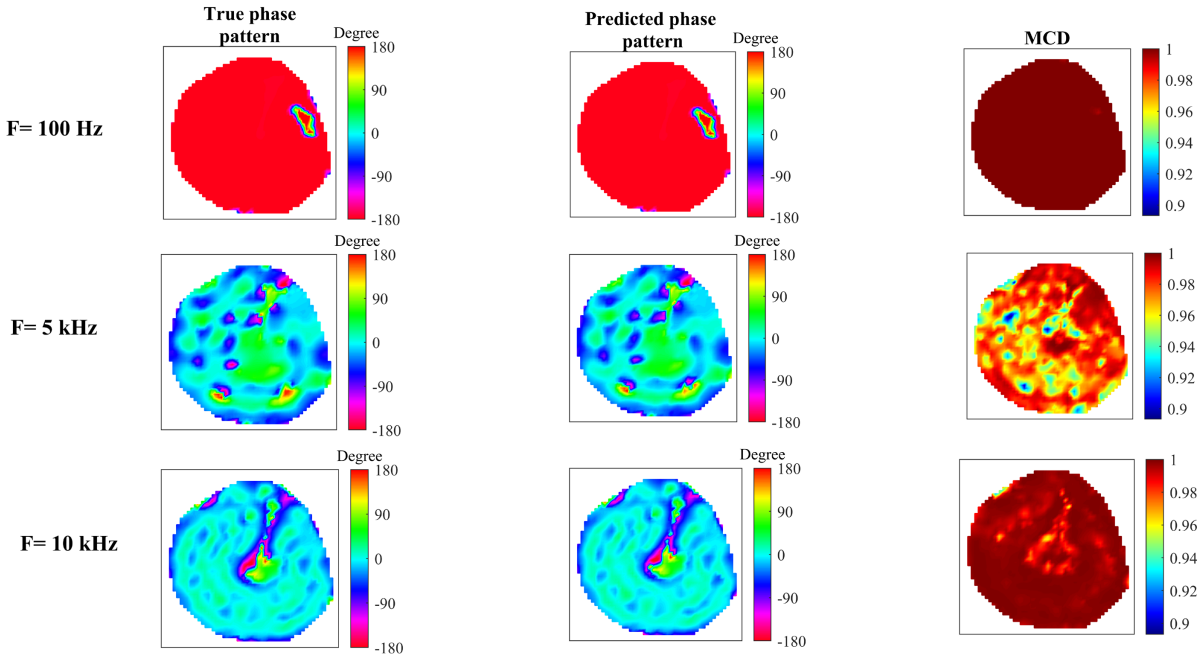


Figure 5-7 – ML model prediction results of the TM phase vibration pattern. The results are presented at three frequencies: 100 Hz (low), 5 kHz (middle), and 10 kHz (high). The left and middle columns show the true and predicted vibration phase patterns for one of the random test sets. The results show that at all these three frequencies, the predicted phase pattern is very close to the true pattern. The rightmost column represents the values of MCD at these frequencies. The values of MCD presented in this column are calculated based on the predictions of the model for the whole testing dataset (with the size of 100).

To estimate the Young's modulus of the TM, we employed the objective function provided in Equation (5-6), which uses the vibration data at the frequency of 5 kHz, with two different scenarios. Similar to what we had for the estimation of the Young's modulus of the SAL, in the first scenario for the estimation of the Young's modulus of the TM, the model considered all nodes on the TM, and in the second scenario, the model took only the nodes that had a feature importance of greater than 0.5 (for the Young's modulus of the TM). The nodes with high feature importance are shown in red in the right panel of Figure 5-8. Based on the results illustrated this figure, most of the nodes with high feature importance lay on the manubrium and there are a few nodes in other regions of the TM.

The results of the parameter estimation of the Young's modulus of the TM are exhibited in Table 5-3. Here also, the results of only 10 random samples from the testing dataset are presented. However, the values of MAPE and maximum error were calculated using all 100 samples of the testing dataset. Based on the results presented in Table 5-3, the value of MAPE is 2.00% when our model encompasses all nodes on the TM for estimating its Young's modulus and this value is 2.84% when the model takes only nodes with high feature importance for parameter estimation. Also, the maximum error is 9.71% if the model uses all nodes and is 41.36% if it includes only the nodes with high feature importance. These results reveal that, unlike the Young's modulus of the SAL, using all nodes on the TM leads to a more accurate estimation of its Young's modulus (with respect to the FE model).

Table 5-2 – True and estimated values and estimation error of E_{SAL}. The objective function in the Equation (5-5) was used for estimating values in this table. We considered two different scenarios: 1. Using all nodes of the TM for parameter estimation and 2. Using nodes on the TM that have a feature importance of greater than 0.5 for E_{SAL} (Figure 5-8).

	True value (MPa)	**Estimated value – All nodes (MPa)**	**Error (%)**	**Estimated value – Node with feature importance greater than 0.5 (MPa)**	**Error (%)**
	1.27	0.78	38.88	1.23	3.06
	1.24	1.87	50.86	1.28	3.64
	2.20	2.21	0.41	2.22	0.64
	0.94	0.98	3.53	0.97	2.32
	1.17	1.31	11.62	1.12	4.33
	2.50	2.48	0.61	2.60	4.22
	0.27	0.26	4.47	0.28	3.58
	2.52	1.89	25.02	2.56	1.77
	0.58	0.46	19.64	0.55	3.67
	1.69	1.25	26.19	1.61	5.07
MAPE all 100 samples.			25.36		3.24
Max error among all 100 samples.			579.29		22.60

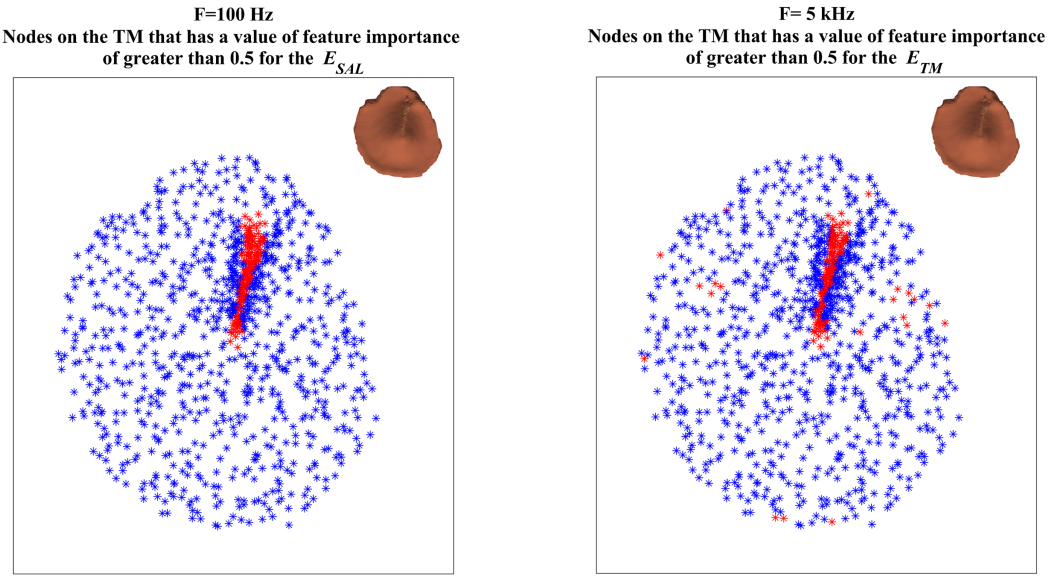


Figure 5-8 – Left: all sample nodes on the TM with the nodes that have values of feature importance of greater than 0.5 for the Young's modulus of SAL at 100 Hz shown in red (187 nodes). Right: all sample nodes on the TM with the nodes that have values of feature importance of greater than 0.5 for the Young's modulus of TM at 5 kHz shown in red (173 nodes).

So far, we demonstrated the results of estimations of the Young's modulus of the TM and SAL separately. Now we want to study the accuracy of the proposed material characterization method (with respect to the FE model) when estimating both of these parameters simultaneously. We used the objective function presented in Equation (5-7) for the simultaneous estimation of the Young's moduli of the TM (at 5 kHz) and SAL (at 100 Hz). Previously in this section, we reported that for the Young's modulus of the SAL, the estimation results are more accurate (with respect to the FE model) if we only consider the nodes on the manubrium and for the Young's modulus of the TM, the estimation results are more accurate (with respect to the FE model) if we consider all nodes on the TM for parameter estimation. Therefore, in the objective function presented in Equation (5-7), we used the displacement amplitude of all nodes of the TM for the first term and used only the displacement data of nodes on the manubrium for the second term.

Table 5-3 – True and estimated values and estimation error of E_{TM}. The objective function in the Equation (5-6) was used for estimating values in this table. We considered two different scenarios:1. Using all nodes of the TM for parameter estimation and 2. Using nodes on the TM that have feature importance of greater than 0.5 for E_{TM} (Figure 5-8).

	True value (MPa)	**Estimated value – All nodes (MPa)**	**Error (%)**	**Estimated value – Nodes with feature importance greater than 0.5 (MPa)**	**Error (%)**
	9.38	9.31	0.76	9.69	3.20
	3.37	3.44	2.22	3.29	2.40
	13.27	13.13	1.08	13.01	2.01
	11.53	11.46	0.59	11.30	1.98
	17.75	17.41	1.93	17.45	1.69
	18.00	18.33	1.85	18.26	1.45
	14.92	14.61	2.12	14.77	1.01
	2.10	2.24	7.04	2.31	10.10
	2.76	2.67	3.00	1.62	41.36
	7.50	7.34	2.14	7.43	0.93
MAPE for all 100 samples.			2.00		2.84
Max error among all 100 samples.			9.71		41.36

The results of the simultaneous estimation of the Young's modulus of the TM and SAL are presented in Table 5-4. Similar to Table 5-2 and Table 5-3, here also only 10 samples from the dataset are exhibited and the MAPE and maximum errors reported are related to all 100 samples of the testing dataset. Based on the results, the proposed parameter estimation leads to a very low MAPE; the value of MAPE is 6.70% for the Young's modulus of the TM and is 3.49% for the Young's modulus of the SAL. Also, the maximum errors of the parameter estimation are 26.52% and 23.05% for the Young's moduli of the TM and SAL, respectively.

Also, in order to analyze the convergence of the Bayesian optimization, Figure 5-9 illustrates the best-observed values of the different objective functions discussed previously (Equations (5-5)(5-7)) with respect to the number of iterations in the Bayesian optimization process. For the results presented in this figure, all nodes on the TM were considered for Equation (5-6) and the first term in Equation (5-7), and only the nodes on the manubrium (high feature importance) were considered for Equation (5-5) and second term of Equation (5-7). For the estimation of the Young's modulus of the SAL using Equation 5 and the TM using Equation 6 around 35 and 15 iterations were required, respectively. Also, the combined estimation of both parameters using Equation 7 converged after about 130 iterations.

5.4 Discussions

In this chapter, we created surrogate models of the middle ear using ML methods and exploited these methods for estimation of the Young's modulus of the SAL and the TM.

Since the middle ear is made up of several structures, we need tens of input parameters when creating FE models of the middle ear. Considering all these parameters makes creating the surrogate models arduous. Also, we know that the size of training data exponentially increases by increasing the model parameters [209]. On the other hand, as the FE models of the middle ear usually bear high computational costs, we have limitations in collecting training dataset. These limitations can be even more severe for experimental measurements due to the complexities of the measurements of the middle-ear responses.

Table 5-4 – True and estimated values and estimation error of the E_{TM} and E_{SAL}. The objective function in the Equation (5-7) was used for estimating values in this table and the values of E_{TM} and E_{SAL} were found simultaneously.

	True value of E_{TM} (MPa)	**Estimated value of E_{TM} (MPa)**	**Error (%)**	**Estimated value of E_{SAL} (MPa)**	**Estimated value of E_{SAL} (MPa)**	**Error (%)**
	9.38	8.34	11.14	1.27	1.24	2.08
	3.37	3.35	0.33	1.24	1.24	0.41
	13.27	13.08	1.42	2.20	2.20	0.10
	11.53	11.35	1.56	0.94	0.97	2.43
	17.75	17.37	2.17	1.17	1.22	4.38
	18.00	19.48	8.19	2.50	2.44	2.16
	14.92	14.23	4.61	0.27	0.28	1.86
	2.10	2.39	14.17	2.52	2.60	3.43
	2.76	2.31	16.31	0.58	0.62	7.71
	7.50	6.86	8.57	1.69	1.79	5.69
MAPE for all 100 samples.			6.70			3.49
Max error among all 100 samples.			26.52			23.05

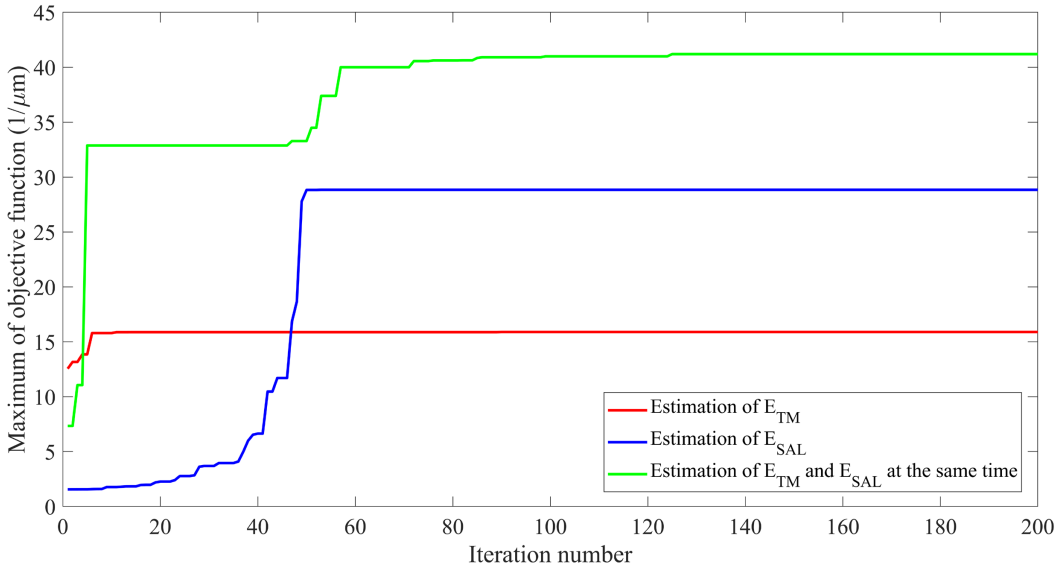


Figure 5-9 – Best observed values of objective functions for the estimation the Young's modulus of the TM, Young's modulus of the SAL, and simultaneous estimation of the Young's modulus of TM and SAL with respect to the iteration number in the Bayesian optimization process. For the Young's modulus of the TM and SAL, the Bayesian optimization converges after about 15 and 35 iterations, respectively, while for the simultaneous estimation of these two parameters, the Bayesian optimization converges almost after 130 iterations.

In order to reduce the number of parameters for creating the ML models, we used our previous global sensitivity analysis results presented in Chapter 3 and focused on the parameters that have the greatest impacts on the displacement amplitudes of the umbo and stapes footplate (i.e., the thickness and the Young's modulus of the TM, and the Young's of the SAL). Although in this chapter we only focused on these parameters as the most influential parameters in the middle ear, future ML models can also include some of the other parameters that have some effects on the middle ear vibrations at different frequencies (e.g., the Young's modulus of the ossicles and the damping of the SAL).

In Chapter 2 and Chapter 3, we had considered normal distribution for all model parameters with a maximum CV of 20%. This chapter was conducted with a uniform distribution for all parameters and the values of CV were 50% for the Young's modulus of the TM and SAL. This

difference is due to the different scopes of the two studies. The main focus of our previous studies (Chapter 2 and Chapter 3) was on the normal middle ears but this work is the basis for future developments of material characterization methods of the human middle ear for diagnostics [79]. Unfortunately, we do not have accurate estimations of the ranges of variabilities of the Young's modulus of the TM and SAL in presence of different middle-ear pathologies. Such measurements seem necessary to make diagnostic methods, such as the one proposed in this chapter, as accurate as possible.

In Section 5.3.1, we demonstrated the ML model results. We observed that the proposed ML models can fairly represent both the amplitude and phase of the displacements of the umbo and stapes footplate as well as the TM vibration patterns at most frequencies in the range of 100 Hz to 10 kHz. These ML models can be used as a reliable replacement for the costly FE models to predict middle ear responses.

In Section 5.3.2, we presented the parameter estimation results. We demonstrated that the values of the Young's modulus of the TM and SAL can be estimated using the full-field vibration pattern of the TM. In experimental measurements, these high-resolution vibration patterns can be obtained using stroboscopic holography measurements [74], [79], [123].

We used the Bayesian optimization method in this chapter. One reason for choosing Bayesian optimization is its ability to solve global optimization problems with fewer model evaluations needed in comparison to many common optimization methods such as genetic algorithm, pattern search, and particle swarm [138], [141]. Additionally, in Chapter 4, we observed that Bayesian optimization can deal with high values of signal-to-noise ratio and is not operator dependent in comparison to some of the most common optimization methods. Based on the previous observations, and the results presented in this chapter, Bayesian optimization can be a good choice for fast parameter estimation of middle-ear structures for future possible clinical applications.

As mentioned previously, based on our previous global sensitivity analysis results, we considered the thickness of the TM, Young's modulus of the TM, and the Young's modulus

of SAL in our ML models. However, in our proposed parameter estimation method, we only considered the Young's modulus of the TM and SAL. Our previous results presented in the Chapter 2 and Chapter 3 showed strong interactions between the Young's modulus and the thickness of the TM at most frequencies. Therefore, considering both of these parameters in the material characterization process can be challenging and it can also result in decreasing the accuracy of the optimizations. In addition to that, there are currently some methods to measure the full-field thickness of the TM in real-time in vivo [210], [211]. These methods can be used in combination with the parameter estimation method proposed in this chapter to measure the thickness of the TM and to estimate material properties of the middle-ear structures at the same time.

For both Young's moduli of the TM and SAL, we monitored the feature importance of the nodes of the TM and based on them implemented different scenarios for the parameter estimation. We observed that at low frequencies (100 Hz), the nodes that are placed on the manubrium have high feature importance (greater than 0.5) for the Young's modulus of the SAL. We also observed that for the Young's modulus of the TM at middle frequencies (5 kHz), the nodes with high feature importance (greater than 0.5) are mostly placed on the manubrium and there are very few nodes in other regions of the TM. In addition to the implications of these observations in the parameter estimation procedure that were discussed before in Section 5.3.2, these observations can suggest that, at the frequencies discussed here, the nodes on the manubrium are more sensitive to the changes in the material properties of the TM and SAL than other regions of the TM.

Previous studies have shown that the two parameters considered in this study for parameter estimation (Young's modulus of the TM and SAL) can undergo significant changes in the presence of middle ear pathologies. For instance, otosclerosis results in changes in the stiffness of the SAL and TM [56], [61], [179], [212]. Study of further effects of different types of middle-ear pathologies on the stiffness of the TM and SAL is an important research objective that needs further investigation.

Chapter 6

Mechanical effects of medical device attachment to human tympanic membrane: A finite-element analysis

Preface

There are several treatment methods for hearing pathologies that rely on attaching a medical device to the TM. In this chapter, we studied the mechanical effects of these devices (resulted from mass and stiffness of the device) on sound conduction in the middle ear. We used our open-cavity model that was first presented in Chapter 2 and attach different devices with various material and geometrical properties to different locations on the TM to study the effects of variations of size, location, and material properties of the medical device on the vibrations in the middle ear.

Overview

Several treatment methods for hearing disorders rely on attaching medical devices to the tympanic membrane. These treatment methods include but are not limited to the tympanostomy tube insertion and attachment of tympanic membrane driving transducers. In this study, we systematically analyzed the effects of variations of the material and geometrical properties and location of the medical devices attached to the tympanic membrane on the vibrations in the middle ear. We created a finite-element model of the human middle ear using μCT images and validated our model with existing experimental measurements in the literature. We then attached cylindrical medical devices to the tympanic membrane in our finite element model and studied their effects on sound conduction in the middle ear. In terms of variations of material properties, we chose three materials for the medical devices: PDMS, Teflon, and stainless steel. It was observed that for all three materials, the addition of the device results in the magnification of the effects of anti-resonances of the middle ear. Additionally, the variations of the material properties led to significant changes in the middle-ear resonance frequency. We also observed that the impacts of changing the material properties of the device on the umbo and stapes footplate motions are negligible at high frequencies (above 5 kHz). Furthermore, we compared the results of the middle-ear model including the complete structure of the medical device with the results of a middle-ear model in which the medical device was represented as a point mass. We found significant differences between the results of these two simulations and concluded that point-mass models cannot accurately represent the behaviour of the middle ear in the presence of the device. We also juxtaposed the results of models with deformable and rigid medical devices and discussed the differences. In terms of geometrical properties, we studied the effects of variations of base diameter and height of the devices on the middle-ear vibration outputs. Our results suggest that the variations of the diameter and height have negligible effects on the middle-ear vibrations at very low frequencies (below 200 Hz) but can have considerable impacts at higher frequencies. Moreover, for Teflon and stainless steel, the effects of changing the device height were negligible at very high frequencies (above 5 kHz). Furthermore, we discussed the effects of medical device attachment

on the vibration patterns of the tympanic membrane as well as the impacts of the variations of the location of the device on the stapes footplate responses. The findings of our study enable optimizing new and existing treatment methods to have the least adverse effects on human hearing.

6.1 Introduction

Implantable middle ear hearing devices can be used as an effective solution to help people with different kinds of hearing impairments. An example of an existing application is the tympanostomy tube insertion. These tubes are inserted into the TM through a surgery, which is usually performed under general anesthesia [213]. Tympanostomy tube insertion itself is one of the most common ambulatory surgeries performed in children in the United States [214]. Also, the attachment of TM driving transducers [215]–[218] and placement of different kinds of transducers on the ossicles [219], [220] are other examples of treatment methods that rely on attaching medical devices to middle-ear structures.

By implanting the devices into the middle ear, the mechanical characteristics of the hearing system are changed. Analysis of these changes is beneficial to help minimize the adverse effects of the addition of the device on human hearing. One way to systematically study these changes is by implementing middle-ear models as they have shown promising accuracy in the prediction of the middle-ear performance. These models can be used for several purposes such as understanding the mechanics of the middle ear, improving diagnostic tests, and developing surgical simulators [37].

Early middle-ear models were lumped-parameter models. The main advantage of these models is their low computational costs. However, they do not account for the complexities in the middle-ear structures and this can affect the accuracy of the model predictions [100]. To overcome this issue, the work of Funnell et al. in 1978 paved the way for developing Finite Element models of the middle ear [21]. FE models of the middle ear were used for different purposes, including estimation of the material properties of the middle-ear structures [54],

prediction of the middle-ear response in the presence of different hearing diseases and disorders such as TM perforation [60], and elucidation of the effects of interindividual variability of the mechanical and geometrical parameters on the middle-ear responses (Chapter 2).

Some researchers have also studied the effects of attaching medical devices to different parts of the ossicles using FE models [4]–[6]. Gan et al. worked on the functional characterization of a totally implantable hearing system which was aimed to help people with sensorineural hearing loss [4]. They exploited FE modelling along with laser Doppler vibrometry measurements of cadaver temporal bones to analyze the mass loading effects of the placement of two different models of transducers on the ossicles. They investigated the efficiency of the electromagnetic coupling of their proposed implantable system as well. In another study, Wang et al. placed a floating mass transducer and a magnet of a contactless electromagnetic transducer at different positions on the ossicles and used FE modelling to study the mass loading effects of these transducers [5]. They investigated the performance of the transducers by changing their location, the crimping connection, and the damping of the crimping mechanism. Also, Zhang and Gan provided a comprehensive FE model to study the efficiency of forward and reverse mechanical driving in the presence of middle-ear implantable hearing devices [6]. They simulated the forward mechanical driving by affixing a floating mass transducer to the ossicles and the reverse mechanical driving by attaching the transducer to the round window membrane. They also studied the effects of cochlear implants on the passive vibration of the basilar membrane.

In this study, we aim to concentrate on the middle-ear implantable hearing devices that are designed to be attached to the TM. The attachment of medical devices to the TM has been investigated by some researchers using FE models, experimental measurements, or a combination of both [215]–[217], [221]. Hamanishi et al. proposed a non-invasive electromagnetic hearing aid that consisted of several parts, including a vibrator coil that was designed to be attached to the central part of the TM [217]. They used FE modelling along with experimental measurements of an artificial middle ear to find the optimal shape, mass,

and position of the vibrator coil attached to the TM that led to sufficient performance of their proposed hearing-aid device. Liu et al. analyzed the effects of attachment of three different types of middle-ear implants on the hearing compensation performance [216]. FE modelling was used in their study, and they validated their baseline FE model with the existing experimental data in the literature. The three types of middle-ear implants that they investigated in their work include TM driving transducer (attached to the central part of the TM), floating mass transducer (attached to the long process of incus), and incus body driving transducer (attached to the body of incus with a driving rod). They observed that the mass loading can significantly affect the performance of the TM driving transducer and floating mass transducer at some frequencies. They also showed that among all three types of these transducers, the TM driving transducer is the optimal one if the mass of the transducer is too small. Also, in another study, Nishihara et al. performed an experimental investigation on the effects of change of the mass of several middle-ear structures on the middle-ear responses [221]. To this end, they placed modelling clay spheres with different masses and diameters on various locations on the TM and explored how they affect the motions of the umbo and stapes footplate using laser Doppler vibrometry. They observed that the attachment of these spheres can either increase or decrease the amplitude of the umbo and stapes footplate at some frequencies.

Despite the above-mentioned studies on medical device attachments to the TM, a systematic understanding of how the medical device contributes to the changes in the mechanical characteristics of the middle ear is still lacking. Therefore, in this chapter, we take advantage of a validated FE model to perform a detailed systematic investigation on the influence of various parameters of the devices placed on the TM (such as their material properties, geometrical properties, and location) on the sound conduction in the middle ear. The findings of this study can contribute to optimizing the design of new or current devices that rely on attaching medical devices to the TM.

6.2 Methods

6.2.1 Baseline model

The middle-ear model used in this study was created by the segmentation of μCT images obtained from a 73-year-old male cadaver temporal bone and all simulations were conducted with Code_Aster. The details of the segmentation process and mesh generation can be found in Chapter 2. In all parts of this chapter, by the baseline model, we mean the model of the middle ear without any medical devices that consists of TM, ossicles, AML, LML, IMJ, ISJ, SML, SAL, PIL, and manubrial fold. The model does not include the middle-ear cavity and ear canal. We performed all computations using harmonic vibration analysis of Code_Aster (version 14.4.0) open-source FE package. Previous studies have shown that the linear assumption is a valid assumption for regular hearing tasks (at least up to 120 dB SPL [68], [222]). Therefore, we assumed all materials to be linear elastic and chose the material properties for the baseline model same as the values reported in Table 2-1.

The initial mesh consisted of 7,656 seven-node second-order triangular shell elements (TRIA7) for the TM and 195,820 ten-node second-order tetrahedral elements (TETRA10) for all other structures. In order to check the mesh convergence, we used Homard utility of Code_Aster to make this mesh finer [89]. We increased the number of tetrahedral elements by a factor of 8 and the number of triangular elements by a factor of 4 and compared the results of this refined mesh with the results of our initial mesh at 24 equally spaced frequencies in the range of 100 Hz to 10 kHz. The maximum difference between the results of the refined mesh and the initial mesh was 1.44 dB for the amplitude of the stapes footplate and 0.90 dB for the amplitude of the umbo. As a trade-off between the accuracy and computational cost, we chose the initial mesh for all structures of the model except the TM for which we chose the refined mesh. The logic behind choosing the finer elements for the TM was that it made us able to have more accuracy in the construction of the conformal meshing of the medical device which will be discussed in Section 6.2.2 in detail. Altogether, our baseline model had 31,114 triangular elements for the TM and 196,907 tetrahedral elements for all other structures of the middle ear. Figure 6-1-a presents the baseline model of the middle ear. The boundary conditions of

the model were considered to be the same as the boundary conditions we had considered in Chapter 2; the parts of the LML, AML, SAL, PIL, and SML that are connected to the cavity wall were considered to be fixed and the TM annulus was fully clamped. Also, the excitation of the model was considered to be a uniform pressure (with a magnitude of 1 Pa) applied to the lateral surface of the TM and the outer surface of the medical device. In order to construct the frequency response function, we excited the model with 413 equally spaced frequencies in the range of 100 Hz to 10 kHz.

6.2.2 Medical-device model

The mesh of the medical device was added to the model after the segmentation and mesh generation of the baseline model. The medical devices attached to the TM were all considered to have almost cylindrical shapes. We should note that due to the curvatures of the TM, it was not possible to have exact and in-plane circles at the base of these cylindrical devices in our model.

Here are the steps we followed for creating the meshes of the medical devices. First, we chose the central point of the base of the cylindrical device. This point was located on the surface of the TM. Second, we determined the desired radius of the base of the device and found all nodes on the TM mesh that laid within a circle with the considered radius and the center we had chosen in the first step. Thus, we had a highlighted circular array of nodes on the TM mesh. We then chose the triangular elements of the TM mesh that included all these highlighted nodes, which formed the base surface of our medical device. Third, we extruded the base surface in the normal direction to the plane of the tympanic annulus. We did this by considering multiple extrusion steps and each step led to a new layer of elements until the desired height of the cylinder device was attained. For all of the medical devices investigated in this chapter, the height of each extrusion step was 100 μm unless specified otherwise. It is worth mentioning that for assuring the model accuracy and mesh convergence of the extruded elements, we checked whether decreasing the height of each extrusion step changes the results, and we observed that decreasing this value to half does not have any significant effects on the results of our simulations as follows. Decreasing the height of the extrusion step to half (from 100 μm

to 50 μm) for a device made of Polydimethylsiloxane (PDMS) with a diameter and height of 1 mm, resulted in less than 0.1 dB difference in the stapes footplate amplitude at 98% of frequencies in the range of 100 Hz to 10 kHz with a maximum difference of 0.41 dB.

The meshes of the medical devices consisted of second-order triangular prism elements (PENTA15). To give an estimation of the number of elements of the device, we should say that a device with a diameter of 1 mm, a height of 1 mm, and an extrusion step height of 100 μm had 1,840 triangular prism elements.

The aforementioned post-processing procedures of the baseline mesh and (i.e., adding the mesh of the medical device to the middle-ear model) were done using the mesh module of the Salome software (www.salome-platform.org, version 9.3.0). The steps of creating the mesh of the medical device are illustrated in Figure 6-1-b. The device shown in this figure is attached to the anterior inferior quadrant of the TM with a diameter of 2 mm and a height of 1 mm. We considered different material (i.e., Young's modulus, density, and Poisson's ratio) and geometrical (i.e., height and base diameter) properties for the medical device to discuss the effects of their variations on the vibrations of the middle-ear structures. Moreover, we placed the medical devices at different locations on the TM to find out how the location of the device affects these vibrations.

We considered three different materials for the medical device: Polydimethylsiloxane (PDMS), Teflon - Polytetrafluoroethylene (PTFE), and stainless steel. PDMS was chosen due to its vast applications in recent developments of medical devices [223] and the fact that it can be a potential material for future middle-ear implants. Also, Teflon and stainless steel were chosen as they are common materials for manufacturing tympanostomy tubes [224], and therefore they can also be appropriate materials for future devices. Additionally, PDMS is a flexible and light material, stainless steel is a stiff and heavy material, and Teflon is moderate in flexibility and density in comparison to PDMS and steel. Therefore, by choosing these three materials, we covered a wide range of materials in terms of flexibility and density. The results of this study can also be beneficial for designing and optimizing current/future medical devices

with other similar materials. We adopted linear elastic models for all these materials using the reported material properties in the literature (Table 6-1) [225]–[228].

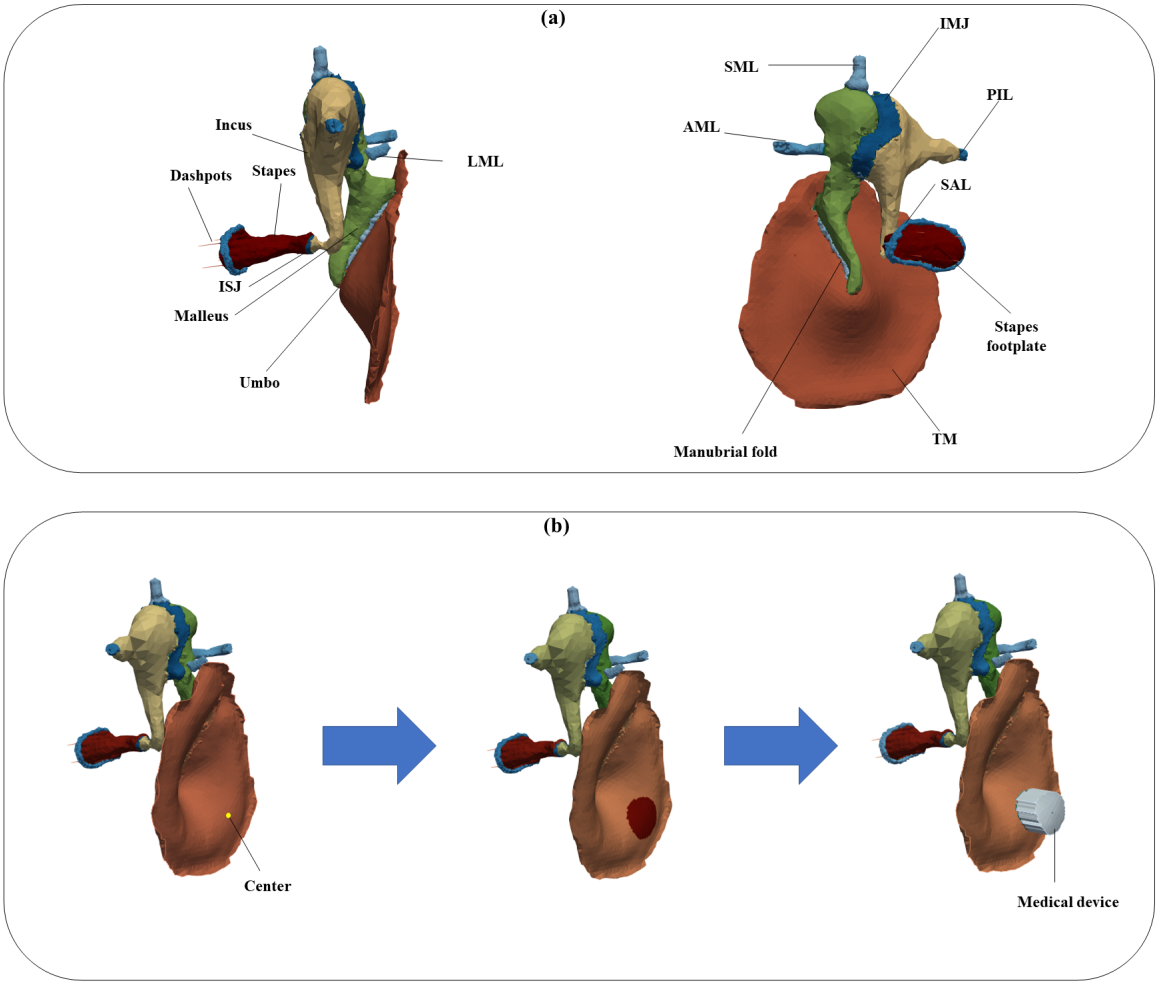


Figure 6-1 – (a) Schematic of the baseline model (the middle-ear model without any medical devices attached to the TM). (b) Steps of creating the mesh of the medical device. In the first step, we chose the location of the base of the device on the mesh of the TM. The device shown here is located on the anterior inferior quadrant of the TM. In the second step, a circular array of elements around this point with a specific diameter (e.g., 2 mm for the illustrated case) was highlighted. In the third step, the highlighted area was extruded in the direction of the normal to the plane of the tympanic annulus. The height of the device was set to be 1 mm in the models shown here.

Table 6-1 – Material properties of PDMS, Teflon, and stainless steel.

Material	Young's modulus (MPa)	Poisson's ratio	Density (kg/m^3)
PDMS	0.75 [225]	0.49 [225]	920 [225]
Teflon	653.2 [226]	0.46 [226]	2200 [227]
Stainless steel	193000 [228]	0.31 [228]	7750 [228]

In different sections of this chapter, we needed to analyze the response of the model accounting for the TM with the medical device attached to it compared to the response of the baseline model. We, therefore, defined the two measures below for calculating the difference in the amplitude and phase of the responses:

$$\text{Amplitude ratio (dB)} = 20log_{10}\left(\frac{A_{MD}}{A_B}\right) \quad (6\text{-}1)$$

$$\text{Phase difference (cycles)} = (\emptyset_{MD} - \emptyset_B) \quad (6\text{-}2)$$

where A_{MD} represents the amplitude of the model with the medical device attached to the TM and A_B represents the amplitude of the baseline model. Also, $\emptyset_{MD}$ and $\emptyset_B$ are the phase of the model with the medical device attached to the TM and the phase of the baseline model, respectively. Also, all phase difference values were wrapped to [-π,π] to make the interpretation easier.

6.3 Results

6.3.1 Baseline model results and comparison with experimental data

In all results reported in this section, the response of the umbo is reported in the direction of the normal to the manubrium at the umbo and the motion of the stapes footplate is reported in the stapes piston-like direction. Figure 6-2 illustrates the results of our baseline model representing the umbo and stapes footplate displacements normalized by the excitation pressure in the frequency range of 100 Hz to 10 kHz. In this figure and all other figures of this

chapter, the response of the umbo is reported in the direction of the normal to the manubrium at the umbo and the motion of the stapes footplate is reported in the stapes piston-like direction. that the middle-ear resonance frequency happens at 1.4 kHz in the baseline model. Below this frequency, the normalized amplitudes of the umbo and stapes footplate displacement are 0.020 and 0.007 μm/Pa, respectively. The maximum displacement amplitudes are 0.047 μm/Pa for the umbo and 0.012 μm/Pa for the stapes, and both happen at the middle-ear resonance frequency. Above the middle-ear resonance frequency, the displacement amplitudes of both umbo and stapes footplate decrease until the frequency of 2.7 kHz. Above this frequency, the displacement amplitudes of the umbo and stapes footplate increase slightly until 4 kHz. Figure 6-2 shows that increasing the frequency beyond this value results in decreasing the umbo and stapes footplate displacement amplitudes with slopes of about 25 dB/octave and 24 dB/octave, respectively. Also, the phase values shown in Figure 6-2 illustrate that the umbo and stapes footplate motions are in phase until the frequency of about 2.5 kHz and then a minor disparity happens in their phase at higher frequencies. The maximum phase difference between the umbo and stapes footplate displacement is about 0.29 cycles at 10 kHz.

To validate the modelling results, we also presented the results of open-cavity laser Doppler vibrometry measurements of stapes footplate displacement of Voss et al. in Figure 6-2 [68]. The measurements performed by Voss et al. were in terms of velocity and we converted them to displacement. Also, Voss et al. did not apply the effects of viewing angle to their results. Although the exact viewing angle of their measurements was not exactly known, they reported a range of 20°−50° degrees for it. Here we corrected their results by considering a viewing angle of 35°. Based on the results presented in Figure 6-2, the corrected results of the stapes footplate measurements of Voss et al. are in good agreement with the results of the stapes footplate displacement amplitude and phase obtained from our model. Below the middle-ear resonance frequency, the maximum difference between the results of the model and the corrected results of Voss et al. was less than 1.6 dB. Additionally, the middle-ear resonance frequency in our model and experimental measurements are very close to each other (both at

about 1.4 kHz). Also, for the frequencies higher than the middle-ear resonance frequency, the mean difference between our model and the experimental data from Voss et al. is about 7 dB.

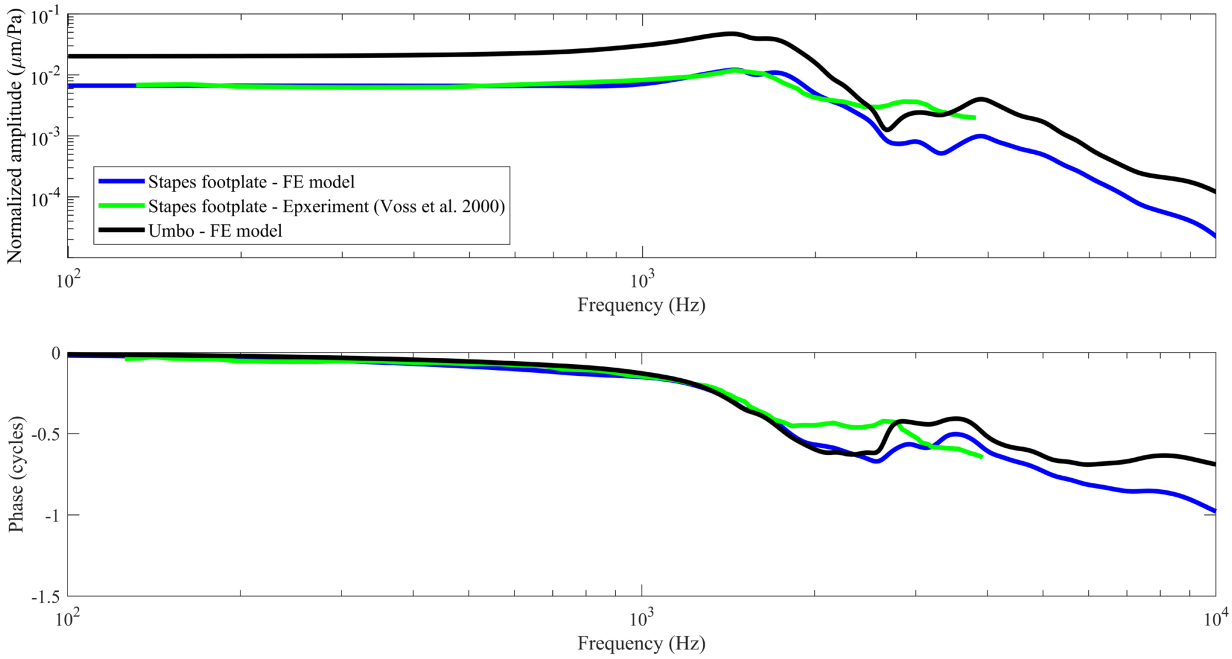


Figure 6-2 – The displacement amplitude and phase of the umbo and stapes footplate from the baseline model (the middle-ear model without any medical devices attached to the TM). The FE modelling results are compared with the corrected open-cavity results of Voss et al. which were obtained experimentally (measurements of Bone 25 in their work) [68]. *The middle-ear resonance frequency in both FE model results and experimental results of Voss et al. is about 1.4 kHz.*

6.3.2 Effects of material properties of attached device

In this section, we attached a cylindrical medical device to the anterior inferior quadrant of the tympanic membrane to study the effects of the variations of material properties of the device on the umbo and stapes footplate responses. For all simulations in this section, the device diameter and height were 2 mm and 1 mm, respectively. As explained in Section 6.2.2, we chose three different materials for the device: PDMS, Teflon, and stainless steel.

The frequency response function of the umbo displacement is presented in Figure 6-3-a&c. The results suggest that attaching the device decreases the middle-ear resonance frequency.

The resonance of the baseline model occurs at 1.4 kHz, however, after attachment of the devices, the resonance happens at the frequencies of 411 Hz, 745 Hz, and 960 Hz for stainless steel, Teflon, and PDMS, respectively. Also, Figure 6-3 indicates that the attachment of the medical device magnifies the effects of several anti-resonances of the baseline model. These anti-resonances can be detected in both the amplitude (Figure 6-3-a) and phase (Figure 6-3-c). The baseline model shows a slight anti-resonance at a frequency a little higher than the middle-ear resonance frequency (i.e., at about 1.6 kHz). This anti-resonance is magnified when the devices are attached to the TM and happens at frequencies of 435, 817, 1 kHz for stainless steel, Teflon and, PDMS, respectively. When the devices are attached to the TM, a new anti-resonance occurs at about 625 Hz, 1.2 kHz, and 1.4 kHz for stainless steel, Teflon, and PDMS, respectively, which does not exist in the baseline model. Also, the results show another anti-resonance happens in the baseline model at frequency of about 2.5 kHz that does not disappear by attaching any of the devices. Moreover, based on Figure 6-3-a, for all three devices, the slope of decrease of the umbo amplitude at frequencies above 4 kHz is calculated to be about 28 dB/octave, which is very close to the respective slope of the baseline model (25 dB/octave).

The amplitude ratio and phase difference of the umbo displacement results are presented in Figure 6-3-b&d. For all three materials, at frequencies below the middle-ear resonance frequency, the amplitude ratio and phase difference values are very close to zero, suggesting that the addition of the device does not have any significant effects at these frequencies. Additionally, for all three devices, the amplitude is considerably amplified at the middle-ear resonance frequency; 14.01 dB for stainless steel at 411 Hz, 9.24 dB for Teflon at 745 Hz, and 5.71 dB for PDMS at 960 Hz. For all three devices, immediately after the resonance frequency, the device attenuates the motion up to 5.24 dB (at 435 Hz), 7.36 dB (at 817 Hz), and 2.57 dB (at 1 kHz) for stainless steel, Teflon, and PDMS, respectively. The phase difference values around the middle-ear resonance frequency are also considerable; -0.34 cycles for stainless steel at 434 Hz, -0.28 for Teflon at 769 Hz, and -0.18 for PDMS at 984 Hz. All these phase difference values are negative, indicating that at these frequencies, the motion of the umbo in the model with the medical device lags behind the response of the umbo in the baseline model.

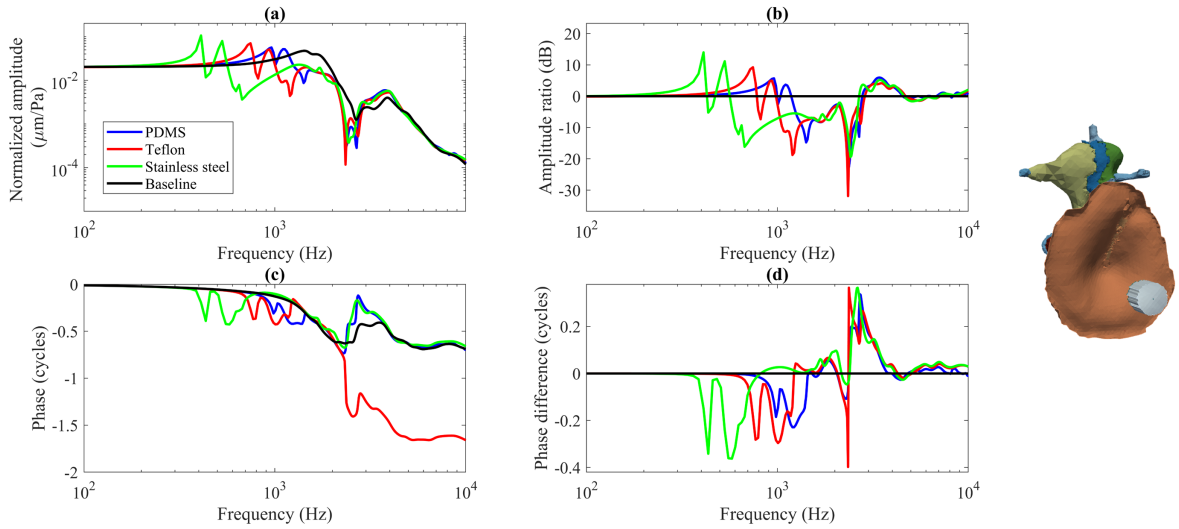


Figure 6-3 – Umbo displacement frequency response function of the model with medical devices attached to the TM. The medical device was placed on the anterior inferior quadrant of the TM. The diameter of the device was 2 mm and its height was 1 mm. We considered three different material properties for the device: PDMS, Teflon, and stainless steel. (a,c): Normalized amplitude and phase of the baseline model and the models with medical devices. It can be perceived that the addition of the device results in a decrease in the middle-ear resonance frequency. The most significant decrease is related to stainless steel. PDMS causes the smallest shift in the resonance frequency. (b,d): The amplitude ratio and phase difference of the model responses. We can observe that although all three devices cause considerable changes in the umbo vibrations at some frequencies, the effects of variation of the material properties are negligible at frequencies above 5 kHz.

For all three devices, at most frequencies between the middle-ear resonance frequency and the frequency of about 3 kHz, the amplitude ratio is negative, which shows attachment of the medical device attenuates the amplitude in this range. Also, the most significant attenuation of the amplitude happens at the same frequency range; 19.42 dB for stainless steel, 31.90 dB for Teflon, and 22.66 dB for PDMS, and this maximum attenuation occurs at a frequency of about 2.4 kHz for all of them.

From the frequency of 3 kHz to 5 kHz, the amplitude is amplified for all devices and the phase difference is also positive at most frequencies. Above 5 kHz, the values of amplitude ratio and phase difference of all devices are small; the amplitude ratio is less than 2.07 dB and the phase difference is less than 0.03 cycles for all of them, suggesting that the variations of the material properties of the device do not have significant effects on the motions of the umbo at these frequencies.

The frequency response functions of the normalized amplitude and phase of the stapes footplate are presented in Figure 6-4-a&c. Here also we can see the shift in the resonance frequency that we observed in Figure 6-3-a&c. The middle-ear resonance frequency of the baseline model happens at about 1.4 kHz while the resonance frequencies of the models with devices occur at 411 Hz, 721 Hz, and 960 Hz for stainless steel, Teflon, and PDMS, respectively. Also, similar to the umbo response, the attachment of the medical devices results in the magnification of the effects of the anti-resonances of the baseline model. These anti-resonances can be detected in both amplitude (Figure 6-3-a) and phase (Figure 6-3-c) plots. For all three devices, similar to what we observed for the umbo in Figure 6-3, the first anti-resonance happens immediately after the middle-ear resonance frequency; these frequencies are 435 Hz, 793 Hz, and 1 kHz for stainless steel, Teflon, and PDMS, respectively. The baseline model results also show a slight anti-resonance after the middle-ear resonance frequency at 1.6 kHz. The models with stainless steel, Teflon, and PDMS devices also experience another anti-resonance at 625 Hz, 1.2 kHz, and 1.4 kHz, respectively. Moreover, the stapes footplate responses of all three devices as well as the baseline model show an anti-resonance near the frequency of 2.8 kHz. Furthermore, we can observe that the slope of the decrease of the amplitude at frequencies higher than 3.9 kHz is about 26 dB/octave, which is close to the slope of the baseline model (24 dB/octave).

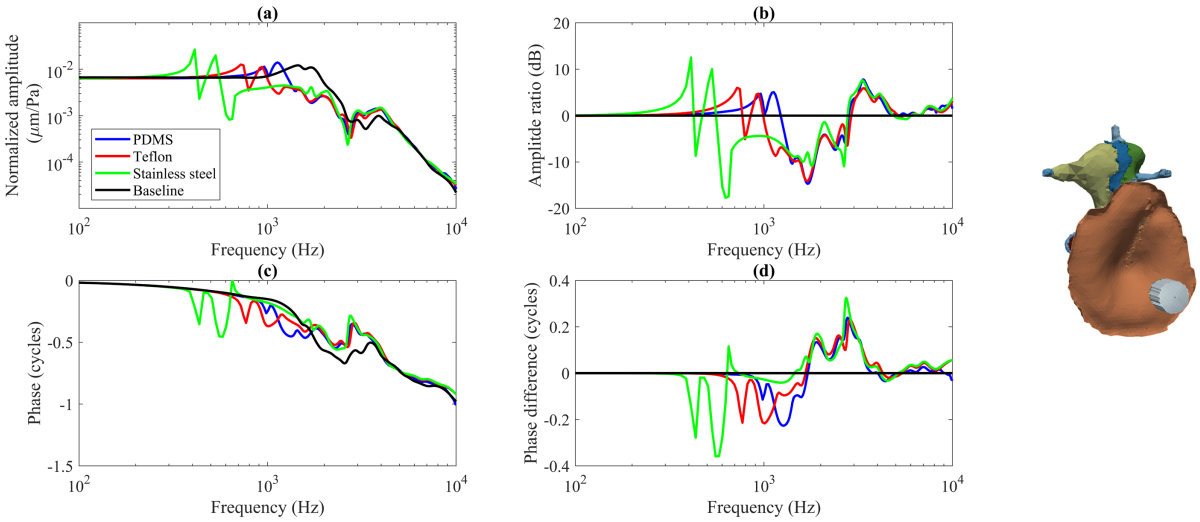


Figure 6-4 – Stapes footplate displacement frequency response function of the model with medical devices attached to the TM. The medical device was placed on the anterior inferior quadrant of the TM. The diameter of the device was 2 mm and its height was 1 mm. We considered three different material properties for the device: Silicone rubber, Teflon, and stainless steel. (a,c): Normalized amplitude and phase of the baseline model and the models with medical devices. It can be perceived that the addition of the device results in a decrease in the middle-ear resonance frequency. The most significant decrease is related to stainless steel. PDMS causes the smallest shift in resonance frequency. (b,d): The amplitude ratio and phase difference of the model responses. The results show that although all three devices cause considerable changes in the umbo vibrations at some frequencies, the effects of variation of the material properties are negligible at frequencies above 5 kHz.

The amplitude ratio and phase difference results of the stapes footplate are also presented in Figure 6-4-b&d. Similar to the umbo response, we can see that the amplitude ratio and phase difference are very close to zero at frequencies below the middle-ear resonance frequency and a considerable amplification of the amplitude takes place at the middle-ear resonance frequency; 12.54 dB for stainless steel at 411 Hz, 6.01 dB for Teflon at 721 Hz, and 4.73 dB for PDMS at 960 Hz. Moreover, the values of the phase difference around the middle-ear resonance frequency are negative for all three materials, showing that the stapes footplate motion in the model with the medical device lags behind the baseline model at these frequencies; -0.28 cycles for stainless steel at 435 Hz, -0.21 cycles for Teflon at 769 Hz, and -

0.11 cycles for PDMS at 984 Hz. Furthermore, analogous to the umbo responses, at most frequencies above the middle-ear resonance frequency and below 3 kHz, we can observe considerable attenuation of the amplitude and significant values of phase difference. The greatest loss at this frequency range is 10.93 dB for stainless steel at 2.7 kHz, 14.09 dB for Teflon at 1.7 kHz, and 14.69 dB for PDMS at 1.7 kHz. Between frequencies of 3 kHz to 5 kHz, the amplitude is amplified for all three devices. The values of phase difference are negative between the middle-ear resonance frequency and frequency of about 1.7 kHz, and are positive for frequencies between 1.7 kHz and 5 kHz. The greatest phase difference in this frequency range (1.7 kHz to 5 kHz) is 0.32 cycles for stainless steel at 2.7 kHz, 0.23 cycles for Teflon at 2.8 kHz, and 0.24 cycles for PDMS at 2.8 kHz. Based on Figure 6-4-b&d, analogous with the umbo response, the difference in the material properties of the medical device does not have significant effects on the stapes footplate amplitude and phase at frequencies greater than 5 kHz. For all three materials, the values of the amplitude ratio and phase difference are small at frequencies greater than 5 kHz. The greatest amplitude ratio in this frequency range (5 kHz to 10 kHz) is 3.75 dB for stainless steel, 3.16 dB for Teflon, and 2.58 dB for PDMS. Also, the greatest absolute value of the phase difference is 0.06 cycles for stainless steel and Teflon, and 0.03 cycles for PDMS.

In order to determine whether the observed changes were solely due to the mass loading of the TM or the stiffness of the device also had some contributions, we considered three rigid devices with the densities of PDMS, Teflon, and stainless steel. Figure 6-5 shows the results of the stapes footplate displacement obtained using these rigid models compared to the results of the models with deformable devices as previously presented in Figure 6-4. The amplitude and phase results shown in this figure reveal that the rigid-body assumption is pretty accurate (with respect to the FE results of the deformable devices) for Teflon and stainless steel at all frequencies except frequencies near the middle-ear resonance frequency. The mean absolute value of the difference between the amplitude results of the rigid device model and deformable device model among all frequencies in the range of 100 Hz to 10 kHz are 0.25, 0.23, and 1.13 dB for stainless steel, Teflon, and PDMS, respectively. On the other hand, the mean absolute

value of the difference in the stapes displacement for PDMS is almost 5 times greater than the respective values for stainless steel and Teflon. For PDMS, in addition to significant differences near the middle-ear resonance frequency, Figure 6-5 shows remarkable differences between the results of the rigid and deformable models at some other frequencies. For instance, there is a difference of 7.2 dB between the results obtained from deformable and rigid devices for PDMS at 2.9 kHz.

In this section, we also compare the results of the model with the full cylindrical device attached to it against the results of a model in which the medical device is represented as a point mass. In order to make this comparison, we first attached a medical device with a diameter of 2 mm and height of 1 mm to the anterior inferior quadrants of the TM and ran our simulations with this device. We then replaced this device with a point mass which was located at the center of the base of the full device and had exactly the same mass as the full device (2.35 mg for PDMS, 5.63 mg for Teflon, and 19.84 mg for stainless steel). Figure 6-6 shows the stapes footplate amplitude and phase responses for these simulations.

For all three materials, we can observe a significant difference in the middle-ear resonance frequency between the results of the full-device model and the results of the point-mass model. This difference is about 400 Hz for PDMS and Teflon, and about 200 Hz for stainless steel; the resonance frequency of the model with the full medical device is always greater than the resonance frequency of the model with the point-mass device. Additionally, for all three materials, the full-device model results and the point-mass model results are significantly different from each other at most frequencies. The mean absolute value of the difference between the amplitude results of the point-mass model and the results of the full-device model among all frequencies in the range of 100 Hz to 10 kHz is 2.44 dB for PDMS, 2.50 dB for Teflon, and 2.72 dB for stainless steel. Also, the maximum absolute values of the differences between the amplitude results of the two models, which occur near the frequency of 2.7 kHz, are 12.80 dB for PDMS, 12.48 dB for Teflon, and 16.62 dB for stainless steel.

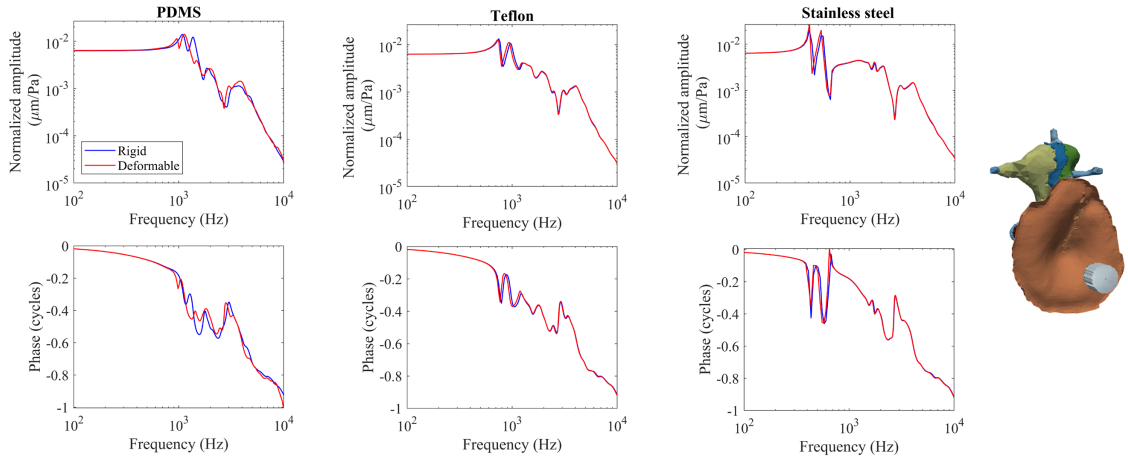


Figure 6-5 – Comparison of the stapes footplate displacement results of the models with the rigid medical devices with the results of the models with deformable medical devices. The devices were attached to the anterior inferior quadrant of the TM. The diameter of the devices was 2 mm and their height was 1 mm. For all three materials we considered in this study, the maximum difference between the results of the rigid and deformable devices happens near the resonance frequency. At most frequencies, the rigid assumption is pretty accurate for Teflon and stainless steel (with respect to the FE results of the deformable devices).

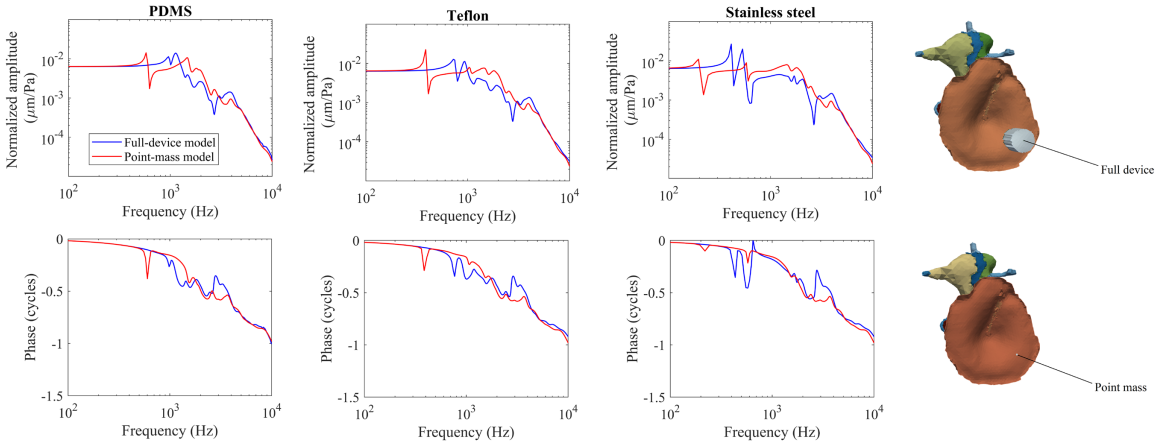


Figure 6-6 – Comparison of the stapes footplate displacement results of the model with the full medical device attached to the anterior inferior quadrant of the TM with the results of the model in which the medical device is represented as a point mass. The point mass was located at the center of the base of the device. The diameter and height of the device were 2 mm and 1 mm, respectively. The results show that the point-mass model cannot accurately calculate the response of the middle ear in the presence of the medical device (with respect to the FE results of the full-device model).

6.3.3 Effects of geometrical properties of attached device

In this section, we study the effects of variations in the diameter and height of the cylindrical medical device on the motions of the stapes footplate. We placed our medical device on the anterior inferior quadrant of the TM and varied its geometrical parameters.

Figure 6-7 illustrates the effects of the variations of the device diameter from 1 mm to 3mm on the motions of the stapes footplate with a constant height of 1 mm. Based on the results, at very low frequencies (below 200 Hz), for all three materials (PDMS, Teflon, and stainless steel), variations of the device diameter do not have considerable effects on the variations of the amplitude and phase of the stapes footplate. Additionally, based on Figure 6-7, we cannot detect any specific relations between the device diameter and amplitude ratio or phase difference. For PDMS, the most significant attenuation of the amplitude happens when the diameter of the device is 3 mm, and this happens at the frequency of 1.7 kHz (15.37 dB). This maximum value decreases by decreasing the diameter. When the diameter is 1 mm, the highest decrease in the amplitude, which is 13.07 dB happens at the frequency of 2.5 kHz. The most significant value of the phase difference for PDMS occurs when the diameter is 1 mm, which is 0.29 cycles at 2.6 kHz.

For Teflon also, the most significant attenuation of the amplitude of the stapes footplate happens when the diameter is 3 mm. For this diameter, the maximum attenuation is at the frequency of 1.7 kHz (15.18 dB). Moreover, the maximum absolute value of phase difference occurs when the diameter is 3 mm, which is 0.32 cycles at 840 Hz. No specific trend exists between the diameter and amplitude ratio or phase difference. For instance, the maximum attenuation of the amplitude for the diameters of 1 mm, 1.5 mm, 2 mm, and 2.5 mm are 14.69 dB, 14.00 dB, 14.09 dB, and 14.66 dB, respectively.

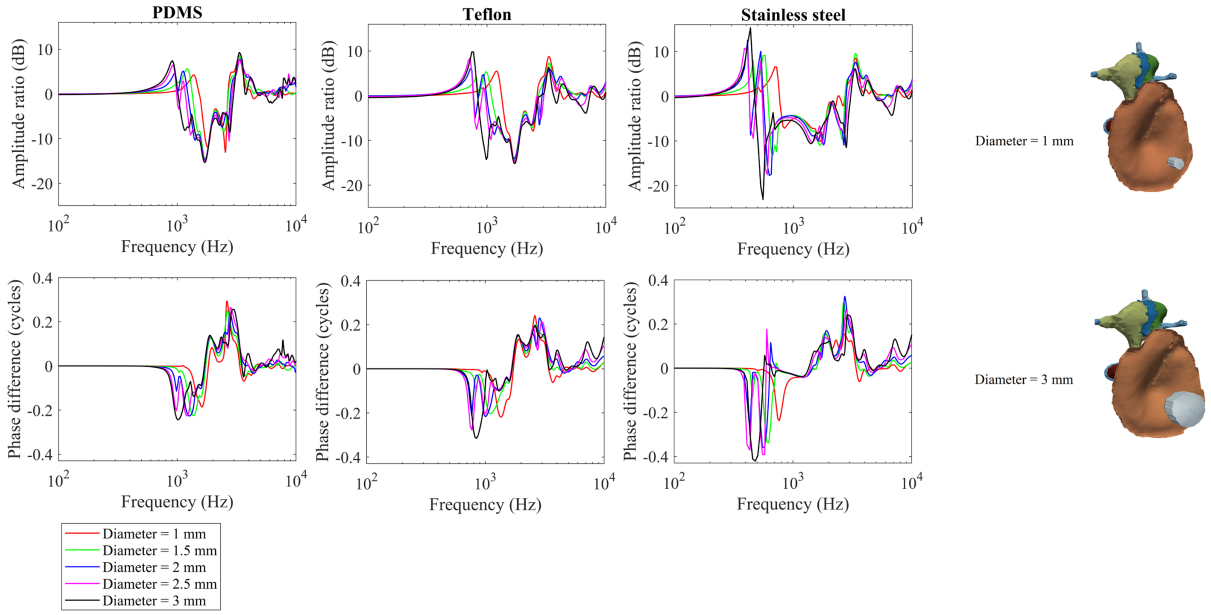


Figure 6-7 – Effects of changing the diameter of the device on the stapes footplate displacement amplitude and phase. The device was attached to the anterior inferior quadrant of the TM and its height was set to be 1 mm. The variations of the diameter do not have considerable effects on the motions of the stapes footplate at very low frequencies (below 200 Hz) but can have significant effects at higher frequencies.

For stainless steel, the maximum attenuation of the stapes footplate amplitude and the greatest absolute value of phase difference happens when the diameter of the device is 3 mm. They both occur near the frequency of 500 Hz, where we can see 23.12 dB loss in the stapes footplate amplitude and an absolute value of phase difference of 0.42 cycles. Here also, cannot detect a specific relation between the diameter and amplitude ratio or phase difference.

Figure 6-8 presents the amplitude ratio and phase difference of the stapes footplate while changing the height of the device from 0.5 mm to 2 mm with a constant diameter of 2 mm. Analogous to the device diameter (Figure 6-7), the change in the height does not have a remarkable influence on the stapes footplate amplitude and phase at very low frequencies

(below 200 Hz). Also, for Teflon and PDMS, the effects of height are negligible at frequencies above 5 kHz.

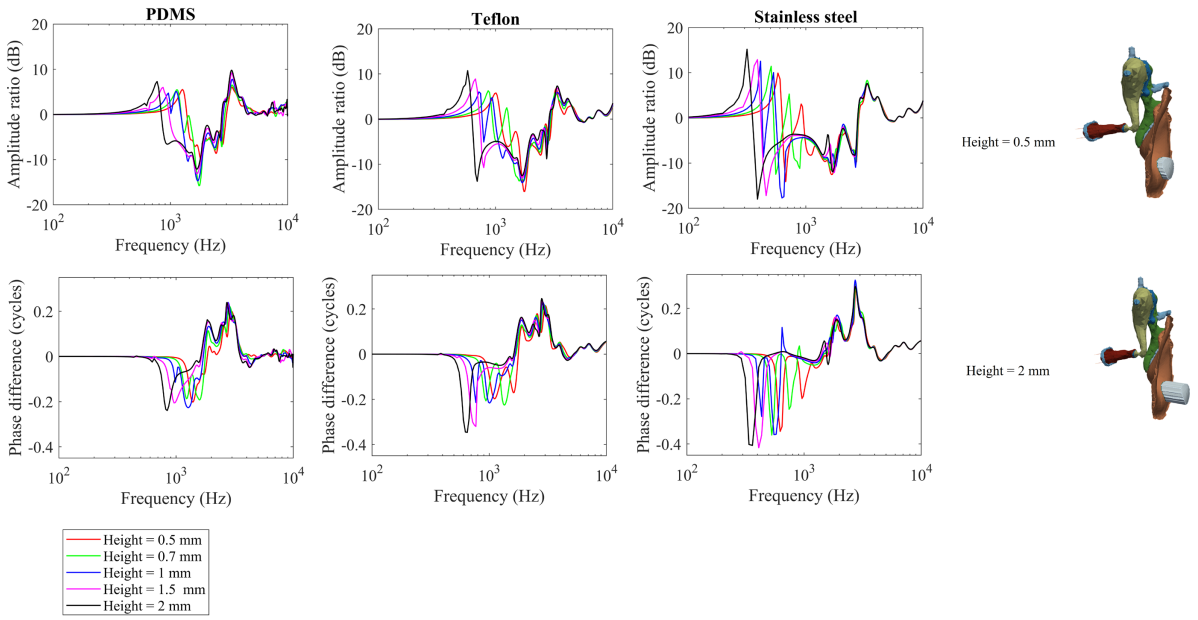


Figure 6-8 – Effects of changing the height of the device on the stapes footplate displacement amplitude and phase. The device was attached to the anterior inferior quadrant of the TM and its diameter was set to be 2 mm. The variations of the height of the device have negligible effects on the motions of the stapes footplate at very low frequencies (below 200 Hz). Also, for Teflon and stainless steel, the effects of variations of height are negligible at frequencies above 5 kHz.

For all three devices, increasing the height results in decreasing the natural frequency of the system and as a result, we can see a shift in the peaks of the responses. In other words, greater height results in smaller middle-ear resonance frequency. For PDMS, the values of resonance frequency for the heights of 0.5, 0.7, 1, 1.5, and 2 are 1.3 kHz, 1.1 kHz, 960 Hz, 865 Hz, and 770 Hz, respectively. For Teflon, the values of resonance frequency for the heights of 0.5, 0.7, 1, 1.5, and 2 are 1 kHz, 865 Hz, 721 Hz, 674 Hz, and 578 Hz, respectively. For stainless steel, the values of resonance frequency for the heights of 0.5, 0.7, 1, 1.5, and 2 are 578 Hz, 506 Hz, 411 Hz, 387 Hz, and 315 Hz, respectively. Other than this trend between the height and

resonance frequency, we could not detect any specific trends between the height and the amplitude ratio or phase difference of the stapes footplate. For PDMS, the most significant attenuation of the amplitude of the stapes footplate (15.78 dB) happens when the height is 0.7 mm, and this occurs near the frequency of 1.7 kHz. The maximum phase difference values are very close to each other for the height values of 2 mm, 1.5 mm, and 1 mm, which is 0.24 cycles appearing at 2.7 kHz. Also, for Teflon, the most significant attenuation of the amplitude of the stapes footplate takes place near the frequency of 1.7 kHz (16.05 dB) when the height is 0.5 mm. The greatest absolute value of the phase difference occurs when the height is 2 mm, which is 0.35 cycles at 650 Hz. Also, for stainless steel, the maximum attenuation of the amplitude (about 17 dB) is almost the same when height is 1 mm, 1.5 mm, and 2 mm; however, for these height values, the maximum loss appears in different frequencies; 626 Hz for a height of 1 mm, 458 Hz for a height of 1.5 mm, and 387 Hz for a height of 2 mm. Moreover, the maximum absolute value of phase difference comes up with heights of 2 mm and 1.5 mm (about 0.41 cycles and near the frequency of 400 Hz for both of them).

In order to provide a more detailed analysis of the effects of the geometrical parameters of the device, we considered two devices with the same volume but different aspect ratios; defined as the device height divided by its diameter. The results of this comparison are provided in Figure 6-9. The first aspect ratio was 1 (with a diameter and a height of 1 mm) while the second aspect ratio was 0.29 (with a diameter of 1.5 mm and a height of 0.44 mm). The height of each extrusion step for the devices with the aspect ratios of 1 and 0.29 was 50 μm and 49.15 μm, respectively.

As mentioned in Section 6.2.2, because of the curvatures of the base of the device (which is located on the TM surface), the devices are not exactly cylindrical. Therefore, to create the two models with the same volume, we modified the diameter and height of both devices manually and monitored their volume until the dimensions ended up with the same volumes, which is 0.55 mm^3 for both aspect ratios.

For all three devices, a significant disparity exists between the results of the two models at most frequencies. Moreover, we cannot find any specific trends between the amplitude ratio

or phase difference and the aspect ratio of the model. For PDMS, the most significant attenuation of the amplitude is almost the same for both aspect ratios (about 13 dB at 2.6 kHz) and the most considerable phase difference for the aspect ratios of 1 and 0.29 are 0.29 cycles at 2.6 kHz and 0.18 cycles at 2.7 kHz, respectively. Also, for Teflon, the most significant attenuation of the amplitude is14.68 dB at 1.7 kHz for the aspect ratio of 1 and 11.66 dB at 2.5 kHz for the aspect ratio of 0.29. Additionally, its maximum phase difference for both aspect ratios of 1 and 0.29 occurs at 2.6 kHz with the value of 0.23 cycles. Also, for stainless steel, the maximum attenuations of amplitudes of devices with aspect ratios of 1 and 0.29 are 10.09 dB and 13.30 dB, respectively and they both happen at 1.7 kHz. Furthermore, the maximum absolute value of phase difference for stainless steel is 0.24 cycles at 769 Hz for the aspect ratio of 1 and 0.27 cycles at 2.7 kHz for the aspect ratio of 0.29.

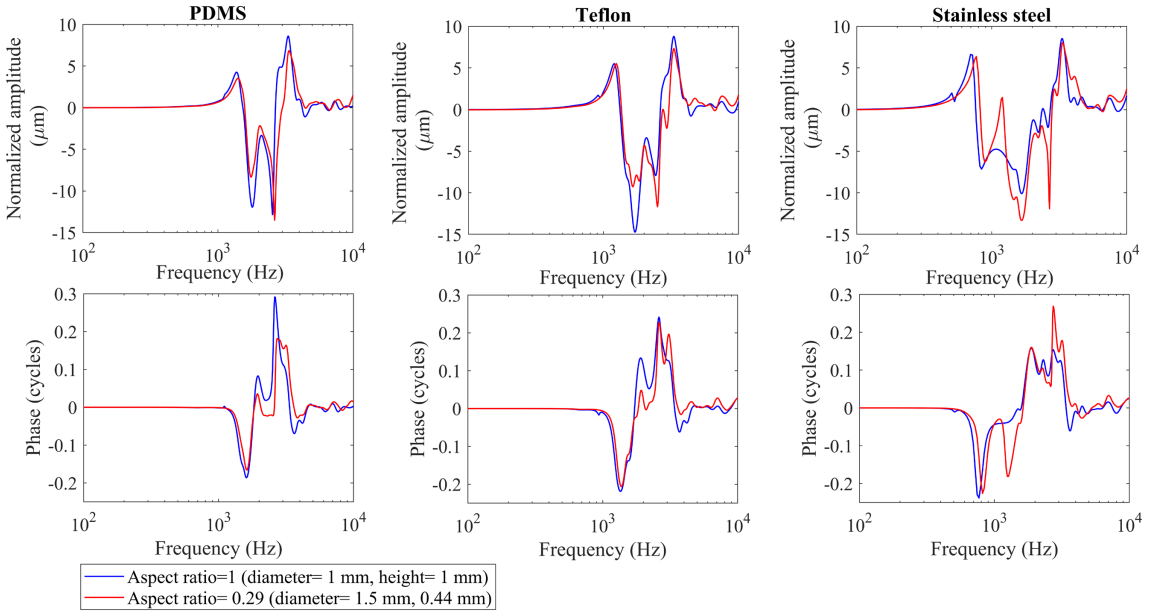


Figure 6-9 – Comparison of the results of the stapes footplate displacement of two devices with the same volume but different aspect ratios. The first device had an aspect ratio of unity (both diameter and height of 1 mm), while the second device had an aspect ratio of 0.29 (diameter of 1.5 mm and a height of 0.44 mm). For PDMS, the maximum attenuation of the stapes footplate amplitude is almost the same for both aspect ratios. For Teflon, the larger aspect ratio results in a greater loss in the stapes footplate amplitude and greater phase difference. On the other hand, for stainless steel, the loss in the spates footplate amplitude is greater for the device with the smaller aspect ratio.

6.3.4 Effects of location of device

To shed light on the effects of variations of the location of the device on the sound conduction in the middle ear, we placed a medical device on all quadrants of the TM as shown in Figure 6-10, and compared the results. The device diameter and height were adopted to be 2 mm and 1mm, respectively. However, due to the considerations we had in creating the models of the device (Section 6.2.2), it was not possible to make the base area and volumes of the medical devices on different quadrants exactly the same as each other. In Table 6-2, we have reported the base area and volume of the medical devices in Figure 6-10. Based on the values presented in this table, the variations in the base area and volume are very small. The coefficient of variation is about 0.45 % for the base area and about 1.14 % for the volume.

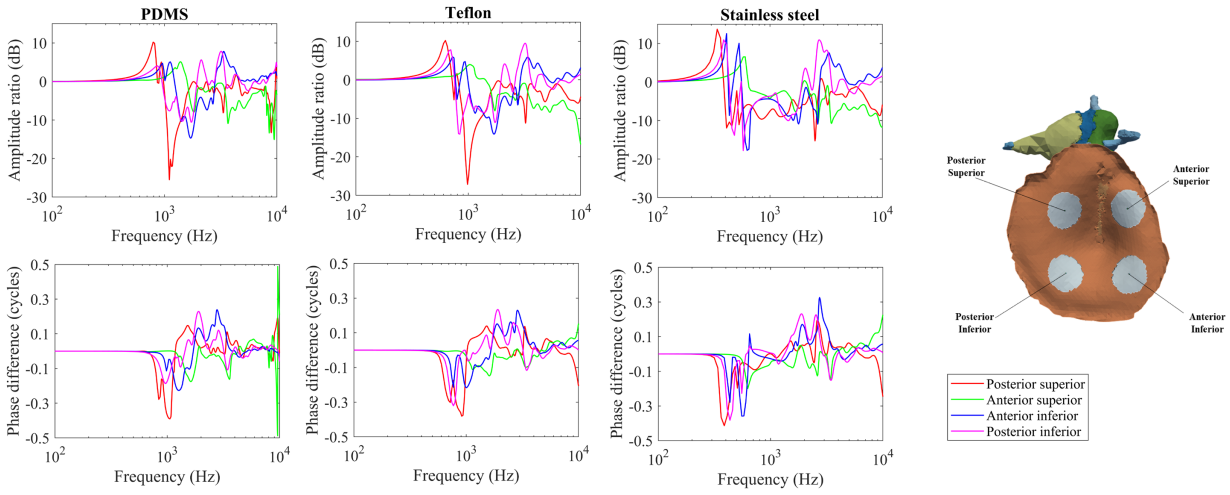


Figure 6-10 – Effects of variations of the location of the medical device on the stapes footplate displacement amplitude and phase. The diameter and height of all devices were 2 mm and 1 mm, respectively. The exact base area and volume of the devices are reported in Table 6-2. For PDMS and Teflon, the greatest loss in the amplitude happens when the device is located on the posterior superior quadrant of the TM, while for stainless steel, the greatest loss in the amplitude occurs when the device is attached to the anterior inferior and posterior inferior quadrants of the TM.

Table 6-2 – Base area and volume of the medical devices used for results reported in Figure 6-10.

Location on the TM	Base area (mm^2)	Volume (mm^3)
Posterior Superior	2.85	2.62
Anterior Superior	2.88	2.61
Anterior Inferior	2.86	2.56
Posterior Inferior	2.87	2.57

Based on the results of Figure 6-10, for PDMS, the maximum attenuation of the stapes footplate amplitude (25.50 dB at 1.1 kHz) appears when the device is placed on the posterior superior quadrant. Moreover, the maximum phase difference (about 0.5 cycles) happens at very high frequencies (about 9.7 kHz) when the device is placed on the anterior superior quadrant. Also, when the device is attached to the anterior superior quadrant, the maximum attenuation of the amplitude (15.07 dB) occurs at very high frequencies (about 9.5 kHz). The other location is the anterior inferior quadrant of the TM in which the maximum attenuation of amplitude is about 14.69 dB at 1.7 kHz and the maximum phase difference is about 0.24 cycles at 2.8 kHz. Furthermore, attaching the device to the posterior inferior quadrant results in a maximum attenuation of 10.57 dB at 1.7 kHz in the amplitude and a maximum phase difference of 0.23 cycles at 1.9 kHz between the results of the baseline model and the results of the model with the medical device attached to the TM.

Based on Figure 6-10, for Teflon, the maximum attenuation of the amplitude of the stapes footplate (27.14 dB at 984 Hz) and the maximum absolute value of the phase difference (0.38 cycles at 937 Hz) happens when the device is attached to the posterior superior quadrant of the TM. If the device is attached to the anterior superior quadrant, we observe a maximum attenuation of 16.80 dB and a maximum phase difference of about 0.15 cycles both at 10 kHz. Moreover, attaching the device to the anterior inferior quadrant of the TM results in the

maximum attenuation of the amplitude and maximum phase difference of 14.09 dB at 1.7 kHz and 0.23 cycles at 2.8 kHz, respectively. Also, when the device is located on the posterior inferior quadrant, the maximum loss in the amplitude and the maximum absolute values of the phase difference are about 14.10 dB at 841 Hz and 0.32 cycles at 769 Hz, respectively.

For stainless steel, the maximum attenuation of the amplitude and the absolute value of the phase difference are almost the same for the circumstances in which we place the device on the posterior inferior and anterior inferior quadrants (about 18 dB and 0.37 cycles). Based on the results of Figure 6-10, attaching the stainless steel device to the anterior superior quadrant of the TM leads to the maximum attenuation of 11.77 dB in the amplitude and the maximum phase difference of 0.23 cycles and both of these values occur at very high frequencies (about 10 kHz). Furthermore, attaching the stainless steel device to the posterior superior quadrant of the TM results in a maximum attenuation of the 15.28 dB at 2.5 kHz in amplitude and a maximum absolute value of phase difference of 0.41 cycles at 387 Hz.

The means of the absolute values of the amplitude ratio among all frequencies in the range of 100 Hz to 10 kHz are also provided in Table 6-3, which represents that for all three materials, the greatest mean value is related to the posterior superior and anterior superior quadrants of the TM.

Table 6-3 – Mean of the absolute values of the amplitude ratio among all frequencies in the range of 100 Hz to 10 kHz.

Location on the TM	**PDMS (dB)**	**Teflon (dB)**	**Stainless steel (dB)**
Posterior superior	3.45	4.18	4.99
Anterior superior	4.37	6.01	6.36
Anterior inferior	2.64	2.73	3.13
Posterior inferior	2.15	2.38	2.71

6.3.5 Effects of device attachment on vibration patterns of TM

In this section, we study the vibration patterns of the TM in the presence of medical devices at low frequencies (200 Hz), mid frequencies (5 kHz), and high frequencies (10 kHz). The vibration patterns are presented in the direction of normal to the manubrium at the umbo and the results of the amplitude and phase are presented in Figure 6-11 and Figure 6-12, respectively. In all cases, a device with a diameter of 1 mm and a height of 2 mm was attached to the anterior inferior quadrant of the TM and the vibration patterns of the model with this device are compared to the vibration patterns of the baseline model. For the amplitude, as shown in Figure 6-11, we can observe that at the frequency of 200 Hz, the addition of the device does not change the vibration patterns, and the patterns of all three devices and the baseline are very similar to each other. However, at frequencies of 5 kHz and 10 kHz, the effects of attachment of the medical device are more significant. At these frequencies, for all three materials, the region in which the device is attached has a lower amplitude in comparison to the baseline model. Additionally, some regions on the anterior and inferior sides of the medical device have higher displacement amplitudes in comparison to the baseline model. Similarly, for the phase patterns, as represented in Figure 6-12, the attachment of the device does not have any effects on the phase at 200 Hz. All nodes on the TM are almost in phase at this frequency; no matter whether any devices are attached or not. At frequencies of 5 kHz and 10 kHz, the phase patterns of the superior section of the TM remain almost unchanged. However, in the inferior region, some changes occur in the phase pattern, which are maximum in the region where the device is attached.

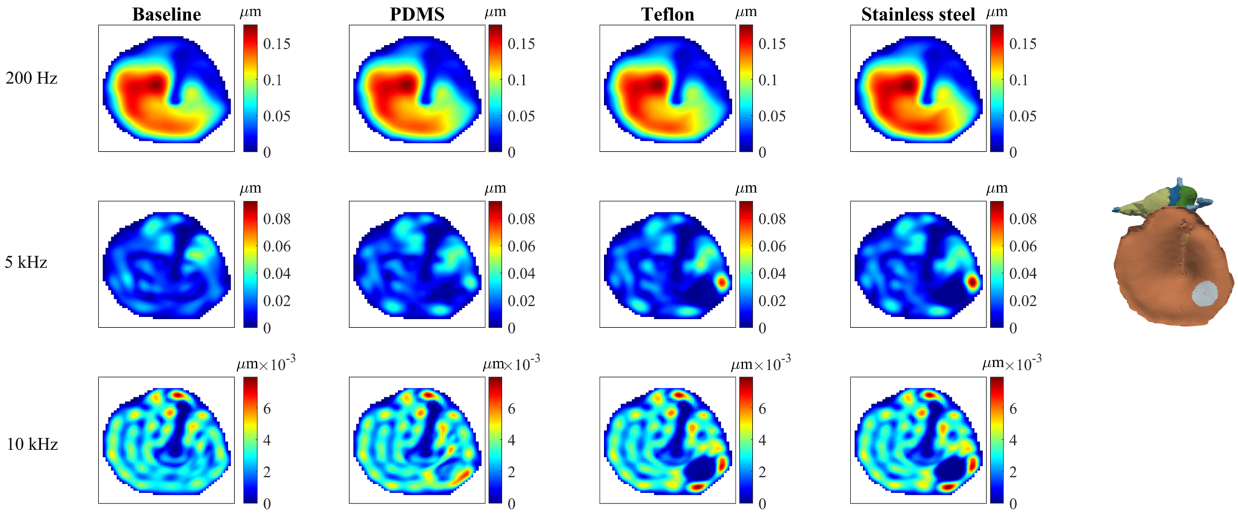


Figure 6-11 – Vibration patterns of the TM displacement amplitude without any medical devices attached to it (baseline) and with medical devices with different material properties attached to the anterior inferior quadrant. The diameter and height of the device were considered to be 2 mm and 1 mm, respectively. The attachment of the medical device does not change the vibration pattern at 200 Hz. However, at higher frequencies (5 kHz and 10 kHz), some differences exist between the vibration patterns of the models with medical devices and the baseline model. The most considerable differences occur around the region where the device is located.

6.4 Discussions

In Section 6.3.1 we reported the behaviours of the baseline model (Figure 6-2) at different frequencies. We also showed that the results of our simulation are very close to the results of the measurements of Voss et al. [68] at frequencies below the middle-ear resonance frequency. However, some differences appear between the experimental results of Voss et al. and the results of our simulations at frequencies above the middle-ear resonance frequency. One of the main sources of these discrepancies is the presence of uncertainties in the material and geometrical properties of the model. These uncertainties include epistemic and aleatory uncertainties. In Chapter 2, we added the effects of aleatory uncertainties to our baseline model and observed that these uncertainties can have significant effects on the middle-ear model predictions at several frequencies.

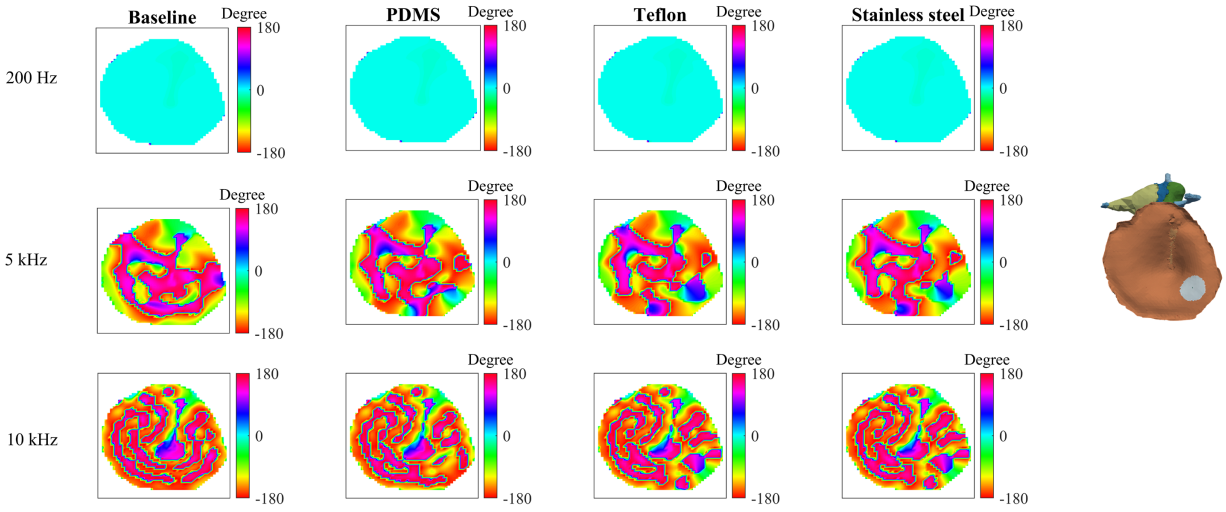


Figure 6-12 – Phase patterns of the TM displacement without any medical devices attached to it (baseline) and with medical devices with different material properties attached to the anterior inferior quadrant. The diameter and height of the device were considered to be 2 mm and 1 mm, respectively. At 200 Hz, the attachment of the medical device does not have any specific impacts on the phase. At frequencies of 5 kHz and 10 kHz, for all three materials, the most considerable phase difference between the models with the device and the baseline model occurs in the region where the device is attached.

Additionally, in this study, we did not include the middle-ear cavity in the model. The first reason is simply that the inclusion of the middle-ear cavity adds to the complexity of the model and leads to a high computational cost. Moreover, we only focused on the mechanical effects of the medical device attached to the TM that can be studied using a model without middle-ear cavity (which is similar to the open-cavity condition in experimental measurements). In some special cases, the medical device can have remarkable acoustical effects on the middle ear as well. For instance, if the we need to create perforations on the TM (such as what happens in the tympanostomy tube insertion), there will be significant changes in the acoustical behaviours of the middle ear as a result of the attachment of the device.

The other rationale behind ignoring the middle-ear cavity in our modelling is that for normal ears, the inclusion of the middle-ear cavity would be anticipated to have a negligible effect on the stapes footplate responses, at least at frequencies up to 4 kHz [10], [68]. Moreover, in most parts of this chapter, we have compared the results of the model containing the medical device attached to the TM with the results of the baseline model. Because both of these models do not include the middle-ear cavity, the inclusion of the middle-ear cavity would not likely impact the outcomes of our current study.

Furthermore, we did not model the ear canal and we assumed that the pressure applied to the outer surface of the device was identical to the pressure applied to the TM. Based on the results reported in [44], the variations of the pressure distribution are negligible near the TM. Therefore, our assumption is a reasonable one. It is also worth noting that the greatest device height that we considered in this study was about 2 mm which is not remarkable in comparison to the ear canal length which is almost 25 mm as reported by Zemplenyi et al. [229].

In Section 6.3.2, we presented the effects of the variations of the material properties of the device on the umbo and stapes footplate responses. Figure 6-3 and Figure 6-4 showed that the placement of the device shifts the middle-ear resonance frequency to lower frequencies and the effects of the medical device attachment are negligible at very low frequencies (below the middle-ear resonance frequency in the presence of the device). These behaviours can also be detected in the results of other studies in the literature. The shift in the resonance frequency (as a result of the attachment of the medical device to the TM) can be discerned from the results of [216], [217] and the robustness of the middle-ear responses to the attachment of the device to the TM at low frequencies can be perceived from the results of [215]–[217]. Furthermore, we observed that at some frequencies, the attachment of the device can increase/decrease the umbo and stapes footplate amplitude. A significant increase in the amplitude was observed near the middle-ear resonance frequency (after the attachment of the device) and this is mainly due to the shift in the resonance frequency. Around the resonance frequency, for a constant geometry and location, the device made of stainless steel (that was the heaviest material we considered) had the greatest increase in the amplitude of the umbo and stapes footplate. Similar

trends were observed in the results of studies performed by Liu et al. and Hamanishi et al. as well [216], [217]. These studies investigated the effects of changing the mass of a device attached to the center of the TM. Their results show an increase in the stapes footplate displacement and intracochlear sound pressure at the frequencies near the resonance frequency. Similar to our findings, their results also show that the heavier the device, the greater the increase in the amplitude of the motion. We also observed that affixing the medical device to the TM results in the magnification of the effects of anti-resonances of the middle ear. The results of simulations of Hamanishi et al. also represent a similar behaviour [217]. Having all this said, the trends observed by Liu et al. and Hamanishi et al. at higher frequencies are not identical with the findings of our study. Several factors such as the difference in the location of the device, its geometry, its material properties, and the type of excitation between their model and the model in our study can contribute to these disparities between the results at high frequencies.

Based on the results provided in Section 6.3.2, the variations of the material properties of the device do not have considerable effects on the umbo and stapes motions at frequencies higher than 5 kHz. The greatest loss in the amplitude for all three devices happened between the middle-ear resonance frequency and 5 kHz. Therefore, due to the fact that PDMS results in the least shift in the resonance frequency, we can conclude that among all three devices we studied here, PDMS is the most appropriate choice. This is because when we use PDMS, the range of frequencies between the resonance frequency and frequency of 5 kHz is smaller than the respective range for Teflon and stainless steel, and as a result, losses in the amplitude of the motion of the stapes footplate and umbo occur at fewer frequencies in comparison to Teflon and stainless steel.

Additionally, in Section 6.3.2, we studied the effects of considering rigid medical devices instead of deformable devices. Rigid body assumption can reduce the computational cost which can be beneficial in design procedures that need running too many simulations for optimization purposes. Figure 6-5 showed that for stainless steel and Teflon, the rigid body assumption can fairly represent the behaviours of the devices at all frequencies except

frequencies near the middle-ear resonance frequency. This suggests that for these two materials (and other similar materials), the most important material property that should be considered in the design procedure of the medical devices is density. Conversely, the rigid body assumption was not accurate enough for PDMS (with respect to the FE results of the deformable device). We varied the Young's modulus of PDMS in our model to see its effects on the mean absolute value of the difference between the amplitudes of the rigid and deformable models. The results (not presented here) showed that, as expected, the difference decreases by increasing the Young's modulus and a mean absolute value of the difference of below 0.2 dB is attainable when the Young's modulus is greater than 375 MPa, which is 500 times greater than the Young's modulus of PDMS.

In Section 6.3.2, we also compared the response of the full-device model with the response of the point-mass device model. The significant discrepancy between their results concludes that the point-mass model cannot accurately reflect the effects of the medical device attached to the TM (with respect to the FE results of the full-device model). In fact, the results of the two models suggest that in addition to the effects of changes in the mass of the middle ear as a result of the attachment of the device, other impacts of the device on the model (such as changes in the stiffness of the middle ear as a result of the attachment of the device) are important, and should be carefully considered in the design of the medical devices. For instance, the middle-ear resonance frequencies of the point-mass models are always smaller than the respective frequencies of the full-device model, which is due to the fact that the points-mass models do not change the stiffness of the baseline model.

In Section 6.3.3, we studied the effects of variations of geometrical parameters of the device on the stapes footplate responses. For all three devices, the variations of the diameter and height do not have any significant effects at very low frequencies (below 200 Hz). We also observed that the variations of the height have negligible effects on the stapes motions at frequencies greater than 5 kHz for Teflon and stainless steel. However, no specific trends were detected between the changes in diameter/height and the amplitude ratio/phase difference at other frequencies. Moreover, we considered two devices with the same volume but different aspect

ratios and compared the results. The responses of the two models were different from each other at most frequencies (except low frequencies) for all three materials. This shows that in addition to the volume and material properties, the shape of the device also contributes to the changes in the stapes footplate vibrations.

Current medical devices are usually placed at a specific location on the TM. For instance, tympanostomy tubes are usually placed on the anterior inferior quadrant [230]. The location of the device is one of the important aspects that should be considered in designing medical devices. Based on the application of the device, we may or may not be able to consider different locations on the TM for the placement of the device. In the circumstances where we have the option of choosing the exact location of the device, it is beneficial to select an area that leads to the least adverse effects on the middle-ear vibrations. In Section 6.3.4, we placed the device on different quadrants of the TM and studied its effects on the stapes footplate amplitude and phase. For PDMS and Teflon, the maximum loss in the amplitude of the stapes footplate occurs when the device is located on the posterior superior quadrant of the TM, and for stainless steel, the most significant losses in the amplitude and most considerable phase differences are almost the same for three quadrants; i.e., posterior superior, posterior inferior, and anterior inferior quadrants. We also calculated the mean absolute value of the amplitude ratio for all three devices among all frequencies in the range of 100 Hz to 10 kHz. Based on those results, the best locations for placing the device are the anterior inferior and posterior inferior quadrants of the TM (inferior section of the TM) as they result in the smaller values of the mean absolute value of the amplitude ratio in comparison to the posterior superior and anterior superior quadrans.

In Section 6.3.5, we studied the vibration patterns of the middle ear with the medical device attached to it. We observed that affixing the medical device to the TM does not have any effects at low frequencies. However, at higher frequencies, it changes the vibration/phase pattern of the region in which the device is attached and some adjacent regions. The least change in the vibration pattern is obtained when the material of the device is PDMS.

The current study provided a comprehensive analysis of the mechanical effects of medical devices attached to the TM and our findings can be used for optimizing and developing current or future middle-ear medical devices. Future studies can employ models that include the middle-ear cavity and ear canal to analyze the combination of acoustical and mechanical effects of attachment of medical devices in the treatment methods that require us to create a perforation on the TM in addition to the attachment of the device (such as tympanostomy tube insertion).

Chapter 7

Acoustical effects of medical device attachment to human tympanic membrane: A finite-element analysis

Preface

In Chapter 6, we studied the mechanical effects of medical devices attached to the TM. In some surgical procedures (such as tympanostomy tube insertion), we need to create holes on the TM in addition to attaching a medical device to it. In this chapter, we studied the effects of attachment of these medical devices on sound conduction in the middle ear. To be able to model TM perforations, we added the middle-ear cavity and a part of the ear canal to our previous model which was first presented in Chapter 2. We then studied the effects of perforation with different sizes and on different locations of the TM and compared the results obtained from our model with experimental results in the literature. Afterward, we investigated the effects of having both acoustical effects of perforations and mechanical effects of attaching a medical device to the TM on vibrations in the middle ear.

Overview

There are several therapeutic approaches for the treatment of hearing disorders that rely on the attachment of medical devices to the tympanic membrane. Attachment of these devices can change the mechanical and acoustical characteristics of the middle ear and these changes can affect the middle-ear vibrations. The changes in the mechanical characteristics can result from the mass, stiffness, and geometry of the attached device. Along with these changes, sometimes the medical device attachment process involves creating perforations on the tympanic membrane (such as what happens during tympanostomy tube insertion). In these cases, we have changes in both the mechanical and acoustical characteristics of the middle ear. This study aims to investigate the acoustical effects of medical devices attached to the tympanic membrane and the combination of these acoustical effects with the mechanical effects of the attached devices. We used the finite-element method to create a model of the middle ear including the middle ear cavity and systematically studied the effects of size and the location of the tympanic membrane perforations on the middle-ear vibration outputs. Experimental measurement results in the literature were used to validate our model at different steps. We then used this validated model to investigate the combination of the mechanical and acoustical effects of medical devices on the middle-ear vibration outputs. The results reveal that when we have both the mechanical effects of the device (due to its mass, stiffness, etc,.) and the acoustical effects of it (due to perforations), the hearing loss resulted from the acoustical effects are more significant at low frequencies (below about 1 kHz). Whereas, at higher frequencies, the mechanical effects of the device are dominant. The findings of this study can give insights into the optimal design of the shape, location, and other characteristics of current and future medical devices.

7.1 Introduction

Middle-ear implants have been shown to be appropriate choices for the treatment of various types of hearing impairments [3]. Some of these implantable devices are designed to be attached to the TM. An example of these devices is TM driving transducers that mechanically vibrate the TM and ossicles [215]–[218]. Tympanostomy tubes are another example of medical devices designed to be attached to the TM [231]. The attachment of these devices to the TM can alter the middle-ear vibration characteristics. Analyzing these changes helps us to increase the design efficacy of these devices in a way that their attachment results in the least adverse effects on sound conduction in the middle ear.

The changes in the vibration responses of the middle ear, post-attachment of the device, originate from the changes in mechanical and acoustical characteristics of the middle ear as a result of affixing the medical device. The medical device has its own mass, stiffness, and geometrical properties and its attachment to the TM changes the mechanical characteristics of the middle ear. In Chapter 6, we investigated the mechanical effects of medical devices attached to the TM. In addition to these changes in the mechanical characteristics of the middle ear, some treatment procedures require us to make perforations on the TM (e.g., tympanostomy tube insertion). These perforations can significantly affect the acoustical behaviours of the middle ear and in situations where we have a device attached to the perforated TM, we have changes in both acoustical and mechanical characteristics of the middle ear at the same time. The current study aims to investigate the acoustical effects of having perforations with different sizes on different locations of the TM as well as the combinations of acoustical and mechanical effects of medical devices such as tympanostomy tubes. The outcomes of this study can facilitate the optimization of current/future medical devices to have the least adverse effects on sound conduction in the middle ear.

The effects of perforations on middle-ear vibrations have been addressed by several studies in the literature. In a series of studies, Voss et al. Investigated the effects of different parameters of TM perforations including the size and location of the perforations on the sound transmission in the human middle ear [77], [232]–[234]. They experimentally measured

different outputs of the middle ear including the stapes footplate velocity and the middle-ear cavity pressure. They also used their experimental results to develop a circuit model to simulate the middle-ear responses with perforated TM. In another study, Gan et al. created a finite-element model to simulate the middle-ear responses in the presence of TM perforations [60]. They created two perforations on the inferior section of the TM in both their FE model and human cadaver temporal bones and compared the model results with the experimental measurement results to validate their model. They also studied the effects of having multiple perforations on the TM using their FE model. Recently, Bevis et al. implemented both experimental measurements and FE modelling to investigate the effects of the size and location of the TM perforations on sound transmission in the middle ear [235]. In addition to the investigations on the effects of TM perforations, some studies have explored the effects of attaching different medical devices to the TM. A review of these studies can be found in Chapter 6.

Although the studies mentioned previously in this section provided a substantive understanding of some aspects of TM perforations and their effects on middle-ear vibrations, there are some unanswered questions about the effects of TM perforations on middle-ear responses. For instance, the effects of TM perforations on the vibration patterns of the TM are still unknown. In this chapter, we developed an FE model, which was validated with experimental measurement results in the literature, to predict the middle-ear responses in the presence of TM perforations. We used this model to systematically investigate the effects of TM perforations on vibrations of different structures in the middle ear. We then employed our model to conduct a comprehensive analysis of the mechanical and acoustical effects of implantable hearing devices attached to the TM and the combination of these effects on the sound conduction in the middle ear for the first time.

7.2 Methods

7.2.1 Geometry and mesh

The whole segmentation process was performed using Slicer software (version 4.11.20.200930) [85]. The geometry of all middle ear structures except the middle-ear cavity was created by segmentation of μCT images obtained from a 73-year-old male cadaver temporal bone. In previous chapters, we used this reconstructed geometry to develop FE models of the middle ear for open-cavity simulations. The μCT images dataset we used for those works does not include the complete structure of the middle-ear cavity. Therefore, it was not possible to segment the middle ear cavity volume using that dataset. In order to reconstruct the middle-ear cavity, we used the 3D model of one of the datasets provided in the OpenEar library [236]. This library consists of 3D models of eight adult cadaver temporal bones. The data provided in the OpenEar library (https://doi.org/10.5281/zenodo.1473724) is available under the Creative Commons Attribution 4.0 License (https://creativecommons.org/licenses/by/4.0). We compared the structures in our middle-ear model with the ones in these eight models and found that model "Theta" in the OpenEar dataset has the most similarity to our previously reconstructed model. Figure 7-1-a represents the segmented geometries of malleus, incus, and stapes from our previous model and from model "Theta" in the OpenEar dataset. As Figure 7-1-a illustrates, the morphological features of these three structures are very close to each other in both models. Due to the similarity of our previous model with the model "Theta" in the OpenEar dataset, we decided to keep our previous model structures and only add the middle ear cavity volume and cavity wall from the segmentation provided for model "Theta" in the OpenEar dataset. We should note that due to the smoothing and mesh generation process, and also due to the difference between the resolution of our dataset and the resolution of the "theta" dataset in the OpenEar library, there might be some differences between our final reconstructed geometry of the middle-ear cavity and the original geometry presented in the "Theta" dataset of the OpenEar library.

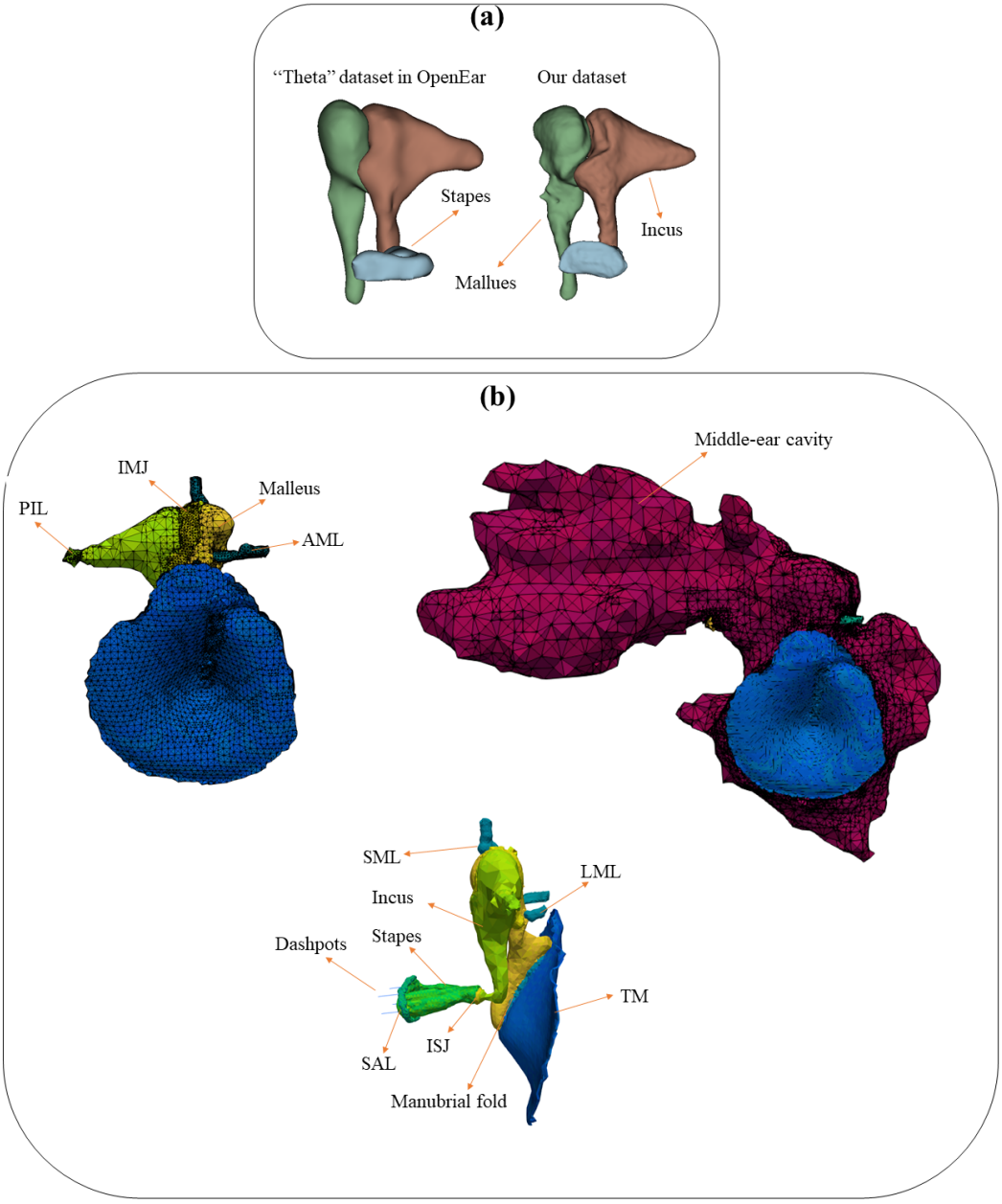


Figure 7-1 – (a) Reconstructed 3D models of the malleus, incus, and stapes from the "Theta" dataset in OpenEar library (left) and from our dataset (right). The size and morphological features obtained using both datasets are very similar to each other. The models of structures in the middle ear were created from segmentation of our dataset and the middle-ear cavity model was created by segmentations provided in the "Theta" dataset of OpenEar library. (b) The created meshes of the middle-ear structures and middle-ear cavity. The partial ear canal model is not shown in this figure.

After segmenting all parts, we created meshes for all structures using Cleaver2 meshing tool through the Segmentmetsher toolbox of the Slicer. To create coarse elements in the regions where deformations are smaller (such as ossicles) and fine elements in other parts, a sizing field was manually created and the mesh was generated based on that. The mesh generation process was done on the gra-vdi nodes of the Graham cluster of Digital Research Alliance of Canada.

The way we created the final mesh of the TM and ear canal was different from other structures. In fact, in the meshes generated from Slicer, all other structures in our model had volumetric mesh. Segmenting and meshing a very thin layer such as TM is very challenging and generating a volumetric mesh for the TM can result in nonrealistic thickness values in different regions of it. Therefore, we decided to generate a surface mesh for the TM in the first step (the mesh that was generated using Slicer). This surface mesh of the TM was then converted to a volumetric mesh by extruding it in the mesh module of Salome software (version 9.3.0). We considered a uniform thickness of 74 μm for the TM (Chapter 2) and 5 extrusion steps were used for creating the volumetric mesh of the TM. Regarding the ear canal, due to technical limitations, our reconstrued model and initial mesh (generated from Slicer) did not contain the ear canal. However, to be able to study the effects of perforations, it was necessary to include the ear canal in the model. For this aim, in a similar way we used for creating the volumetric mesh for the TM, the lateral surface of the TM was extruded in the direction of normal to the tympanic annulus for 2 mm. This partial ear canal (that had a length smaller than the actual length of the ear canal) was used for all simulations. We considered 20 extrusion steps for generating the mesh of the partial ear canal.

Our final mesh includes the TM, ossicles, AML, LML, IMJ, ISJ, SML, SAL, PIL, and partial ear canal. The tympanic cavity, aditus ad antrum, and a part of the antrum are also included in the model [68]. Mastoid air cells are not included in the model and the Eustachian tube was considered to be blocked [60]. Figure 7-1-b presents the reconstructed geometry and mesh of the middle-ear structures and middle-ear cavity. The volume of the air in the middle ear cavity

in our final model is 992 mm^3. Also, in some simulations, we added the mesh of the medical device to the model as will be explained in Section 7.2.1.2.

The model consisted of 169,283 quadratic tetrahedral elements (TETRA10 3D) for the air inside the middle-ear cavity, 219,351 quadratic tetrahedral elements (TETRA10 3D) for the ossicles, ligaments, joints inside the middle ear, 32,155 quadratic pentahedral elements (PENTA15) for the TM, and 128,620 quadratic pentahedral elements (PENTA15) for the ear canal. In order to check the accuracy of the created mesh, we refined this mesh and compared the results obtained using the original and refined meshes together. We used the Homard utility of Code_Aster to refine the mesh of the middle-ear structures and middle-ear cavity [89]. The meshes of the air elements, ossicles, ligaments, and joints were refined by multiplying them by a factor of 8 (that resulted in 3,109,072 quadratic tetrahedral elements in total). The mesh of the base surface of the TM was multiplied by a factor of 4. Also, the extrusion steps for the mesh of the TM and ear canal were increased to 8 and 40 (from 5 and 20), respectively. The refined mesh had 205,792 quadratic pentahedral elements of the TM and 1,028,960 quadratic pentahedral elements for the ear canal. We compared the results of the original and refined mesh at ten frequencies in the frequency range of 500 Hz to 9.5 kHz with frequency intervals of 1 kHz. The difference between the displacement amplitude of the umbo in the results obtained from the original and refined meshes was less than 1 dB in 9 of the frequencies (out of 10) and the maximum difference was 1.12 dB. Also, the difference between the amplitude of the stapes footplate in the results obtained from the original and refined meshes was less than 1 dB in 7 of the frequencies (out of 10) and the maximum difference was 1.82 dB. As a trade-off between the accuracy and computational cost, the original mesh was chosen for all calculations in this chapter.

7.2.1.1 Perforations in the model

The segmented geometry of the TM and the original mesh did not have any perforations on the TM. The holes were added to the TM by post-processing the mesh in the Salome software. In this section, we briefly explain how we created different holes on the TM mesh.

We first considered a node on the TM as the center of the hole we want to create. This node could be located on any quadrant of the TM. Next, we determined the desired diameter of the hole and highlighted all nodes that laid inside a circle with the center of the chosen node and desired diameter. We call this desired diameter D_{des}. After that, we highlighted the elements on the TM surface that contained all nodes selected in the second step. The highlighted elements were then manually modified to avoid sharp edges and irregularities on the hole boundaries. Due to the triangular shape of the elements, the created holes did not have exact circular shapes.

We considered eight different models of holes in our simulations. Four holes named "Hole 1", "Hole 2", "Hole 3", and "Hole 4" were created on the anterior inferior quadrant of the TM. The values of D_{des} considered for creating these holes were 0.8 mm, 1.2 mm, 2 mm, and 3.3 mm, respectively. These diameters were chosen based on the existing experimental measurements of Voss et al. on the perforation sizes (measurements on Bone 24L in their work) [233], [237]. We also had four other nodes named "Hole A", "Hole B", "Hole C", and "Hole D". These holes were located on the posterior-superior, anterior-superior, anterior-inferior, and posterior-inferior quadrants of the TM, respectively. The value of D_{des} for all these four holes was 1 mm.

The exact values of the surface area of all eight holes we considered in this study are reported in Table 7-1 and the shape and exact location of these holes will be presented in the figures presented in Section 7.3.

7.2.1.2 Model of the medical device

In Section 7.3.5, we study the effects of having both the acoustical effects of perforations and the mechanical effects of medical devices attached to the TM. We should note that the mesh of the device was created in the same way we created the mesh of the ear canal. We highlighted the base of the medical device on the lateral TM surface and extruded it in the direction of normal to the tympanic annulus. The height of each extrusion step was the same as the value we had considered for the extrusion of the ear canal.

Table 7-1 – Surface area of the holes on the TM. PS, AS, AI, and PI stand for posterior-superior, anterior-superior, anterior-inferior, and posterior-inferior quadrants of the TM, respectively.

Location on TM	AI				PS	AS	AI	PI
Hole ID	Hole 1	Hole 2	Hole 3	Hole 4	Hole A	Hole B	Hole C	Hold D
Surface area (mm^2)	0.51	1.05	3.03	9.22	0.78	0.76	0.77	0.75

For the simulations in Section 7.3.5, we considered Hole 2 to represent the acoustical effects of the device, and for the mechanical effects of the device, we build up a volumetric mesh of the device around Hole 2 with a total length of 1 mm. The outer desired diameter (D_{des}) of the base of this device was 2.2 mm. The values of the length of the device and its inner and outer desired diameters were chosen to be in the ranges reported for the tympanostomy tubes [238].

We considered three different material properties for the device: PDMS, Teflon, and stainless steel. We used linear elastic models for the device and used the material properties reported in the literature (Table 6-1).

7.2.2 Finite-element model

We used Code_Aster open-source FE code (version 14.4.0) for all FE simulations in this chapter. All results were computed using harmonic vibration analysis. The material properties of the middle-ear structures were exactly the same as the ones used in previous chapters. The air in the middle-ear cavity and ear canal was assumed to be inviscid and the values of density and speed of sound within it were considered to be 1.2 $\frac{kg}{m^3}$ and 340 $\frac{m}{s}$, respectively [51].

The boundary conditions of the model are as follows: the TM annulus and the parts of the SAL, AML, LML, PIL, and SML connected to the middle-ear cavity wall were considered to be fixed. Additionally, the value of acoustic impedance for the middle-ear cavity wall and the ear-canal wall was considered to be equal to 7.8×10^6 rayls which is reported to be the acoustic impedance of bone [239]. Moreover, the contact region between the middle-ear structures and air in the middle-ear cavity or ear canal was defined as the fluid-solid interaction (FSI) surface. TM had two FSIs on its lateral and medial surfaces. Also, for the simulations with perforations on the TM, the thin contact surface between the TM structure and the air inside the perforated region was defined as FSI surface. Moreover, for the simulations with medical devices attached to the TM, the contact surface between the device and the air in the ear canal was defined as FSI surface.

The excitation of the model was considered to be a harmonic velocity source that was applied normal to the lateral surface of the ear canal [51], [235]. The excitation amplitude was constant at all frequencies and had a value of 56 μm/s. This particular value was chosen for the excitation amplitude as it generates a pressure amplitude of about 1 Pa (~ 94 dB SPL) at the umbo at the excitation frequency of 200 Hz.

In different parts of the current chapter, we use two terms P_{TM} and P_{cav} to express the pressure at the TM and inside the cavity. P_{TM} represents the pressure of the umbo in our model and P_{cav} represents the pressure of one of the nodes on the neck of the stapes as a representative of the pressure inside the cavity.

The frequency response curves were plotted at the frequency range of 100 Hz to 10 kHz with a resolution of 50 Hz. All FE computations were performed on the Niagara cluster of Digital Research Alliance of Canada. For the model with the original mesh (including the middle-ear cavity and partial ear canal), we allocated 30 GB of memory for computations at each frequency allowing 6 parallel simulations on one node of Niagara and each simulation took about 35 minutes to complete.

We should also add two other notes: the first note is that in all sections of this chapter, by the baseline model, we mean the model of the middle ear with intact TM and closed cavity. The second note is that in some sections of this chapter, we needed to compare the response of the baseline model with the response of the model with medical-devices/perforations. We, therefore, defined a measure called amplitude ratio for calculating the difference in the amplitude of the responses:

$$\text{Amplitude ratio (dB)} = 20log_{10}\left(\frac{A_{MD/P}}{A_B}\right) \tag{7-1}$$

where $A_{MD/P}$ represents the amplitude of the model with the medical device attached to the TM or in the presence of TM perforations (or both) and A_B represents the amplitude of the baseline model. In all results, the values of $A_{MD/P}$ and A_B used in the calculation of the amplitude ratio were normalized with respect to P_{TM}.

7.3 Results

7.3.1 Baseline model results

In this section, we present the baseline model results and results of simulations of the open-cavity model and compare them with experimental measurement results in the literature. We should note that, in our simulations, the only difference between the closed-cavity (baseline) and open-cavity models was the inclusion of the middle-ear cavity; the ear canal geometry and excitation mechanism were exactly the same for both open and closed cavity models.

Figure 7-2 presents the open and closed cavity frequency response curves of the umbo displacement. It should be noted that in this figure, the umbo response is reported in the direction of the normal to the manubrium at the umbo. Also, the amplitude and phase values of the umbo are normalized with respect to P_{TM}. We can observe that below the middle-ear resonance frequency (about 1.6 kHz for the open-cavity model) the umbo normalized amplitude in the closed-cavity model is smaller than the amplitude obtained from the open-cavity model. The difference between the amplitude values of the two models is about 2.48 dB at 100 Hz. At frequencies above resonance frequency, the open and closed cavity results are

very close to each other except near the frequency of 4.6 kHz, where an anti-resonance appears in the closed-cavity results.

The phase results presented in Figure 7-2 also indicate that the responses of open and closed cavity models are almost in phase at frequencies below middle-ear resonance frequency. Near the resonance frequency (about 1.6 kHz), there is a phase difference of about 0.06 cycles (at 1.8 kHz) between the results of the two models. At higher frequencies also, the results are almost in phase except near the frequency of 4.7 kHz where we can detect a sudden phase change of about 0.29 cycles in the closed-cavity model results due to the anti-resonance we detected in the amplitude plot.

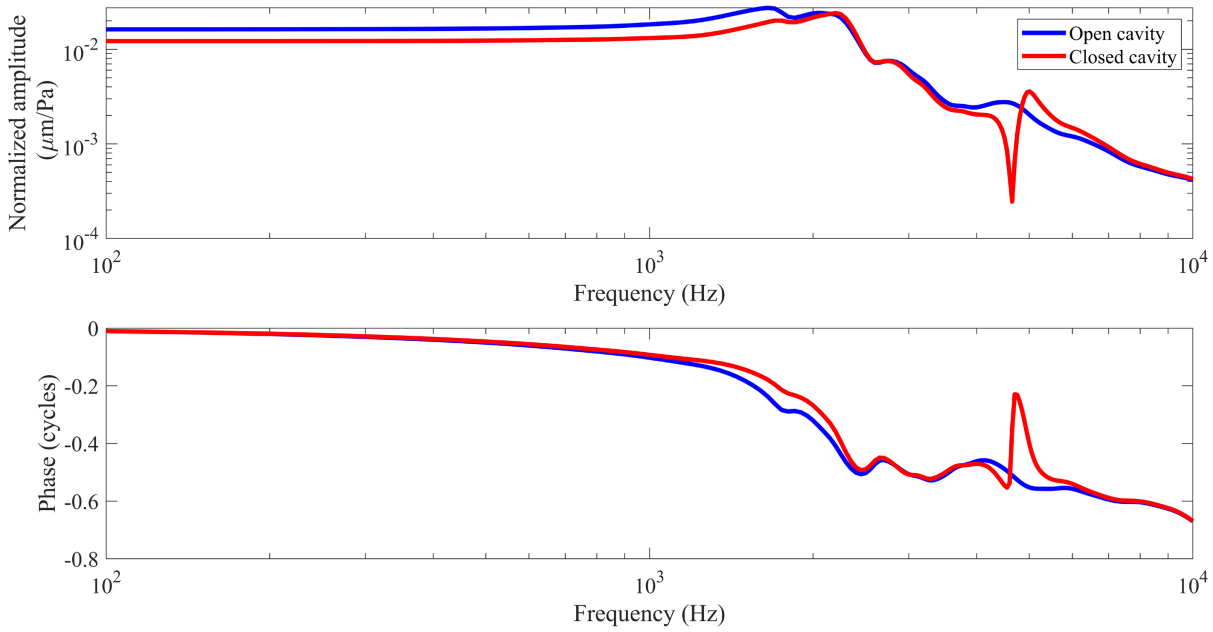


Figure 7-2 – Frequency response curve of the umbo displacement normalized with respect to P_{TM}. At frequencies below the middle-ear resonance frequency, the umbo displacement amplitude in the closed-cavity model is smaller than in the open-cavity model (difference of about 2.48 dB at 100 Hz). The responses of both models are in phase at these frequencies. Near the middle-ear resonance frequency, there is a phase difference of about 0.06 cycles (at 1.8 kHz) between the results. At higher frequencies, the amplitude and phase values obtained from both models are very close to each other except near the frequency of about 4.6 kHz where we can detect an anti-resonance in the closed-cavity model results.

Figure 7-3 illustrates the frequency response of the stapes footplate displacement obtained from the open and closed cavity models (normalized with respect to P_{TM}). We should note that the stapes footplate results presented in this figure are reported in the piston-like direction of the stapes. To compare our model results with experimental measurements, the open and closed cavity measurement results of Voss et al. (on Bone 25 in their work) are also presented in this figure [68]. The measurement results of Voss et al. were in terms of velocity and we converted them to displacement. Also, they did not apply any angle corrections to their laser Doppler vibrometry measurement results, however, they reported a range of 20°-50° between the laser beam and stapes piston-like motion. We used the average value of this range (35°) to correct their measurement results. Similar to the umbo response (Figure 7-2), here also the amplitude of the closed-cavity model is smaller than the amplitude of the open-cavity model at low frequencies. The difference between amplitudes at low frequencies is about 2.33 dB (at 100 Hz). We can see a similar trend in the experimental measurement results of Voss et al. as well and in their measurements, the difference between open-cavity and closed-cavity amplitudes at low frequencies is about 2.63 dB (at 126 Hz). Our model results show that, similar to what we observed for the umbo (Figure 7-2), at frequencies higher than the middle-ear resonance frequency, the stapes footplate amplitudes obtained from the open and closed cavity models are very close to each other except near the frequency of 4.6 kHz where we can detect an anti-resonance in the closed-cavity model results. Similar to what we observed in our model results, the stapes footplate amplitude in the open and closed cavity measurements of Voss et al. are also very similar to each other at frequencies higher than the middle-ear resonance frequency up to 4 kHz.

Figure 7-3 also illustrates that the open and closed cavity model results are almost in phase at frequencies below the middle-ear resonance frequency (about 1.6 kHz). Near the middle-ear resonance frequency, there is a difference of about 0.06 cycles (at about 1.8 kHz) between the open and closed cavity phase results. At higher frequencies, the open and closed cavity model results are almost in phase except near the frequency of 4.6 kHz where we can detect the effects of the anti-resonance we had observed in the amplitude plot and also in Figure 7-2; there is a

sudden difference of about 0.31 cycles near this frequency (at 4.7 kHz) between the phases of the open and closed cavity models. The open and closed cavity measurement results of Voss et al. are also in phase at frequencies below the middle-ear resonance frequency and at frequencies higher than that. Near the middle-ear resonance frequency, there is a difference of about 0.06 cycles (at about 1.8 kHz) between open and closed cavity results in their measurements.

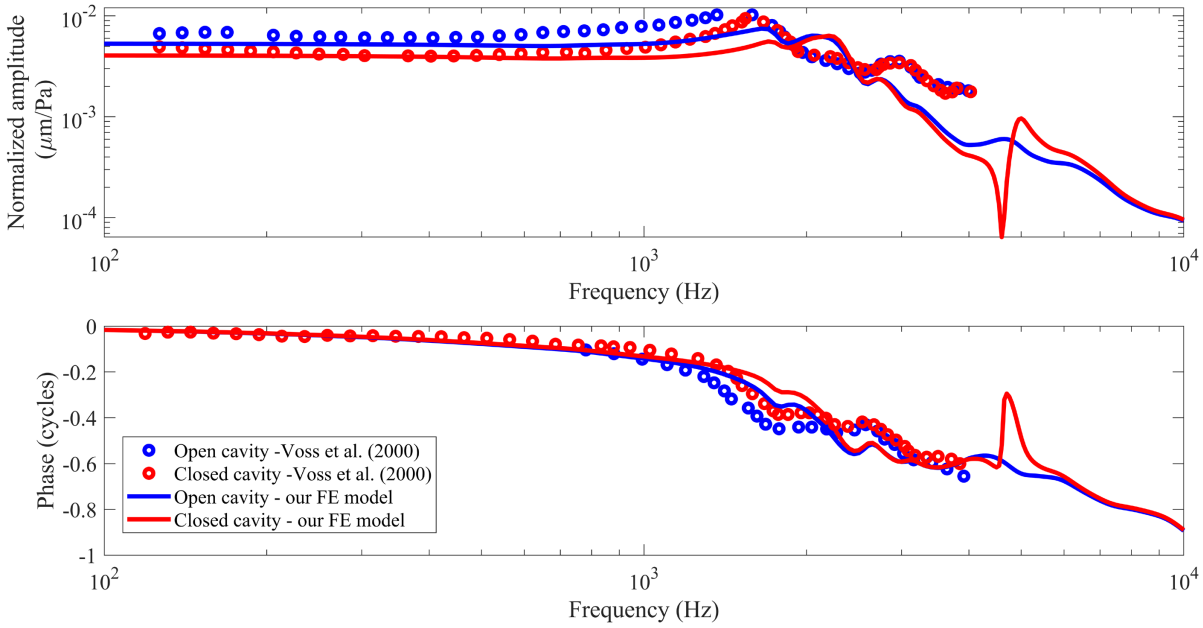


Figure 7-3 – Frequency response curve of the stapes footplate displacement normalized with respect to P_{TM}. At frequencies below the middle-ear resonance frequency, the stapes footplate displacement amplitude in the closed-cavity model is smaller than in the open-cavity model (difference of about 2.33 dB at 100 Hz). The responses of both models are in phase at these frequencies. Near the middle-ear resonance frequency, there is a phase difference of about 0.06 cycles (at about 1.8 kHz) between the results. At higher frequencies, the amplitude and phase values obtained from both models are very close to each other except near the frequency of about 4.6 kHz where we can detect an anti-resonance in the closed-cavity model results. The open and closed-cavity measurement results of Voss et al. are also presented in this figure [68]. *The measurement results of Voss et al. were converted to displacement and corrected by a viewing angle of 35°. The difference between the amplitude of the stapes footplate in experimental measurements is about 2.63 dB (at 126 Hz) and the phase difference between open and closed cavity measurements near the middle-ear resonance frequency in the experimental measurements is about 0.06 cycles (at about 1.8 kHz).*

In order to provide a deeper understanding of the acoustical behaviours of the middle ear, Figure 7-4 presents the pressure distribution inside the middle-ear cavity. In this figure, the amplitude values of the nodes inside the middle-ear cavity are normalized with respect to P_{TM} at each frequency. We studied the pressure distribution inside the middle-ear cavity at three frequencies: 500 Hz (in the low-frequency range), 4.2 kHz (in the mid-frequency range, and also near the frequency of anti-resonances observed in the closed-cavity model results in Figure 7-2 and Figure 7-3), and 8 kHz (in the high-frequency range).

Figure 7-4 illustrates that at low frequencies (500 Hz) the maximum and minimum pressure inside the middle-ear cavity occur at the antrum and anterior-inferior side of the middle-ear cavity, respectively. At 4.2 kHz, the maximum pressure occurs at both the antrum area and the anterior-inferior side of the middle-ear cavity and the minimum pressure occurs near the aditus ad antrum. At 8 kHz, the anterior-inferior side of the middle-ear cavity is where the maximum pressure occurs and the minimum pressure happens near the antrum.

Although only the values of pressure at three frequencies are presented here, we studied the pressure distribution in the middle-ear cavity at other frequencies in our study as well. The results of other frequencies are not presented in this chapter. Based on the results of other frequencies, at frequencies below about 4 kHz, the maximum pressure occurs at the antrum and the minimum pressure happens at the anterior-inferior section of the middle-ear cavity (similar to the pressure distribution at 500 Hz in Figure 7-4). Then, near 4 kHz, the distribution of the pressure inside the middle-ear cavity changes and we have areas with maximum pressure at both anterior-inferior and posterior-superior sections of the middle-ear cavity (similar to what we observed in Figure 7-4 for the frequency of 4.2 kHz). At higher frequencies (until 10 kHz), the pressure distribution will be very similar to the distribution at 8 kHz in Figure 7-4; the maximum pressure occurs at the anterior section of the middle-ear cavity and the minimum pressure near the antrum.

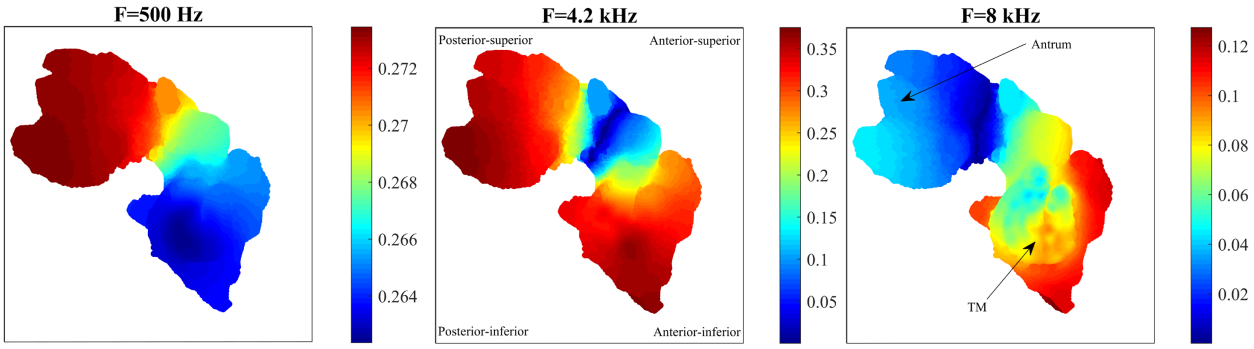


Figure 7-4 – The pressure distribution inside the middle-ear cavity. The values of pressure are normalized with respect to P_{TM}. At low frequencies (500 Hz), the maximum pressure happens at the antrum and the minimum pressure area is the anterior-inferior side of the middle-ear cavity. At the frequency of 4.2 kHz (which is close to the frequency at which an anti-resonance in the closed-cavity model results was observed in Figure 7-2 and Figure 7-3), the regions with maximum pressure are the posterior side of the antrum and anterior-inferior side of the middle-ear cavity and the region around aditus ad antrum is the low-pressure area (appears as a dark nodal line). At high frequencies, (8 kHz), the minimum and maximum pressure occur near the antrum and the anterior-inferior side of the middle-ear cavity, respectively.

7.3.2 Effects of varying the size of perforations

In this section, we study the effects of varying the size of the perforation on the middle-ear responses. The amplitude ratio of the stapes footplate of the models with Hole 1, Hole 2, Hole 3, and Hole 4 are presented in this Figure 7-5. The results of the measurements of Voss et al. are also presented in this figure [233], [237].

Based on both experimental and modelling results in Figure 7-5, perforations have significant effects on the motions of the stapes footplate, especially at very low frequencies. Our model results show that at very low frequencies, the amplitude ratio is about -20 dB for all four perforation sizes. Increasing the frequency results in an anti-resonance in our model results. The frequency at which this anti-resonance happens is directly related to the perforation size and increasing the perforation size increases the frequency at which this anti-resonance occurs; this anti-resonance occurs at 400 Hz, 500 Hz, 650 Hz, and 850 Hz for Hole 1, Hole 2, Hole 3, and Hole 4, respectively. Our model results illustrate that, for all perforation sizes, the amplitude of the stapes footplate starts to increase at frequencies higher than the frequency of

this anti-resonance up to about 1.1 kHz, 1.3 kHz, 1.6 kHz, and 1.2 kHz for Hole 1, Hole 2, Hole 3, and Hole 4, respectively. In this frequency range, the larger the perforation size, the smaller the stapes footplate amplitude The same behaviour can also be detected in the experimental measurement results of Voss et al.; their experimental measurement results also show that at low frequencies, increasing the frequency results in an increase in the amplitude of the stapes footplate of the perforated ears. In both our model results and the experimental results of Voss et al. at some frequencies (above 900 Hz) the amplitude of the perforated ear exceeds the amplitude of the baseline model (normal ear). At frequencies around 3 kHz, the experimental results of Voss et al. show another decrease in the amplitude of the perforated ears in comparison to the amplitude of the baseline model. Their results show that around this frequency, the higher the perforation size, the greater the loss in amplitude. A similar trend can be detected in our model results at higher frequencies (around 5 kHz). At frequencies higher than that, our model results show that the amplitude of the stapes footplate of the perforated ear again starts to increase and gets larger than the baseline model amplitude at very high frequencies (around 9 kHz).

After analyzing the effects of the size of the perforation on the normalized stapes footplate amplitude, we study the effects of perforations with different sizes on the pressure in the middle-ear cavity and ear canal. Figure 7-6 presents the pressure ratio $\left(\frac{P_{cav}}{P_{TM}}\right)$ of our FE model and the experimental measurements of Voss et al. (one Bone 24L in their work) [234, p.]. We should note that in the measurements of Voss et al., the P_{cav} value was measured near the oval window. Also, they stated that P_{TM} in their measurements is the pressure within the ear canal adjacent to TM. As we mentioned in Section 7.2.2 our P_{TM} represents the pressure of the ear canal at the umbo in our model and P_{cav} represents the pressure of one of the nodes on the neck of the stapes. Although the regions we chose to measure pressure values are very close to the regions stated by Voss et al., there may be some differences in the results due to differences in the exact location of measurements.

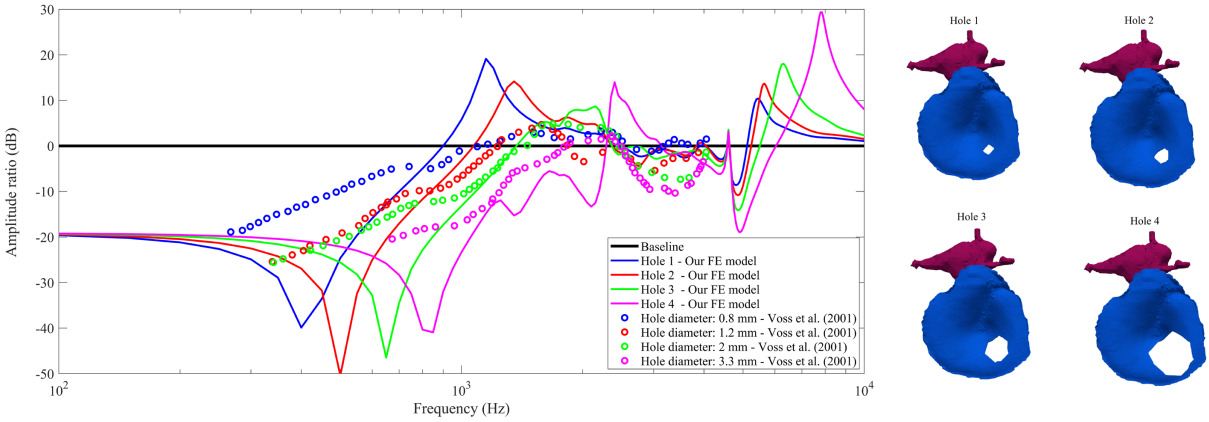


Figure 7-5 – Effects of variations of perforation size on the stapes footplate responses. We considered four different perforations (Hole 1, Hole 2, Hole 3, and Hole 4) in our model. All perforations were located on the anterior-inferior quadrant of the TM. The exact surface area of each hole is presented in Table 7-1. The amplitude ratio values of the normalized stapes footplate displacement for all 4 perforation sizes in our model are presented in this figure. Also, the experimental measurement results of Voss et al. (on Bone 24L in their work) for different perforation sizes are illustrated in this figure [233], [237]. *Both experimental results and Voss et al. and our model results assert that the most considerable losses in the presence of TM perforations happen at low frequencies.*

Our FE model results, as well as the experimental measurement results of Voss et al. presented in Figure 6, illustrates that when there are no perforations on the TM, the pressure ratio is significantly smaller than 1 at low frequencies. The pressure ratio of our model and experimental measurement results of Voss et al. at low frequencies are about 0.26 and 0.34, respectively. In the experimental measurement results of Voss et al., this pressure ratio starts to decrease at frequencies around 900 Hz until the frequency of about 2.3 kHz. Then, there is an increase in the pressure ratio until the frequency of about 3.3 kHz and after that, again we can see a decrease in the pressure ratio. In our baseline model, a decrease in the pressure ratio starts at a frequency of about 1.7 kHz and continues until the frequency of about 2.9 kHz. After that, we can observe an increase in the pressure ratio (up to the frequency of about 5 kHz) followed by a decrease at higher frequencies.

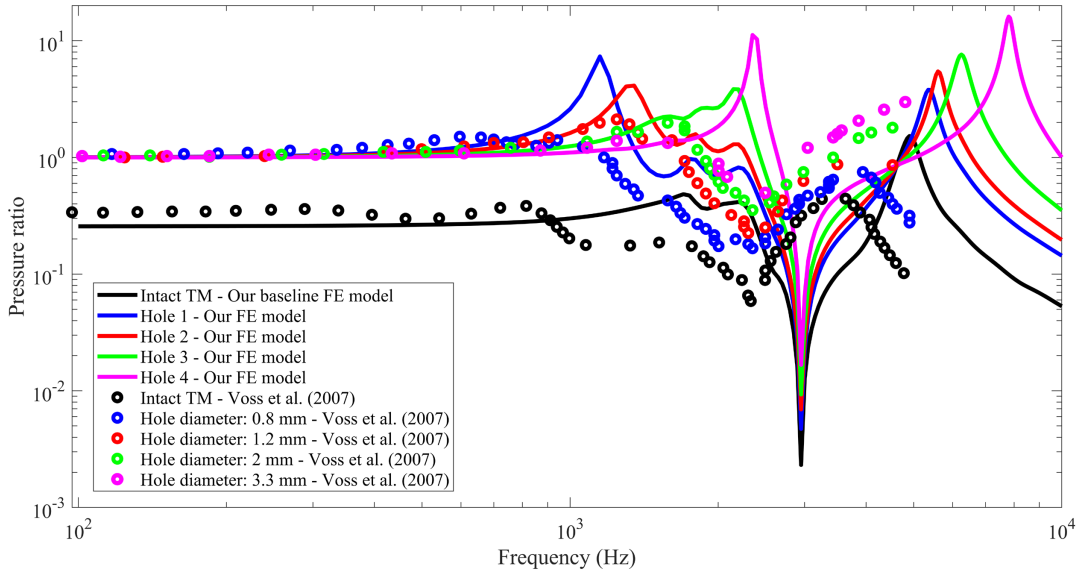


Figure 7-6 – Pressure ratio $\left(\frac{P_{cav}}{P_{TM}}\right)$ *of the baseline model (intact TM) and models with perforations of different sizes (Hole 1, Hole 2, Hole 3, and Hole 4). The experimental measurement results of Voss et al. (on Bone 24L in their work) are also presented in this figure* [234]. *Both our model results and the experimental measurement results of Voss et al. show that when there are no perforations on the TM, the pressure inside the middle-ear cavity is much smaller than the pressure of the ear canal (near TM) at low frequencies. The presence of perforations leads to pressure ratio values of very close to 1 at low frequencies.*

Our model results and experimental results of perforated ears presented in Figure 7-6 show that when there is a perforation on the TM, the value of P_{cav} is almost the same as the value of P_{TM} at low frequencies no matter how big or small the perforation is; for all perforation sizes, the amplitude ratio obtained using both our FE model and the experimental measurements are very close to 1 at low frequencies. The experimental measurement results of three holes (1.2 mm, 2 mm, and 3.3 mm) show a slight increase in the pressure ratio at the frequency range of about 900 Hz followed by a decrease in the pressure ratio values obtained for all four holes. This decrease in the pressure ratio continues until the frequency of about 2.3 kHz and after that, there is a slight increase in the pressure ratio values until the frequency of about 3.4 kHz. Beyond this frequency, the experimentally calculated values of the pressure ratio of two holes

(2 mm and 3.3 mm) continue to increase. Our model results show that increasing frequency from very low frequencies (where the pressure ratio was 1) results in an increase for all four perforation sizes at frequencies higher than 800 Hz. The larger the size of the hole, the larger the frequency in which this increase starts (about 400 Hz, 500 Hz, 650 Hz, and 950 Hz for Hole 1, Hole 2, Hole 3, and Hole 4, respectively). The results of all four holes obtained using our model show a significant decrease in the pressure ratio near the frequency of about 2.9 kHz. Then similar to what we observed in the pressure ratio of the baseline model, there is an increase in the pressure ratio of all four models (up to 5.3 kHz, 5.6 kHz, 6.2 kHz, and 7.8 kHz for Hole 1, Hole 2, Hole 3, and Hole 4, respectively) followed by a decrease at higher frequencies.

7.3.3 Effects of varying the location of perforations

In this section, we study the effects of variations in the location of the perforations on the stapes footplate motions. Figure 7-7 presents the results of simulations of models with Hole A (posterior-superior), Hole B (anterior-superior), Hole C (anterior-inferior), and Hole D (posterior-inferior) on the TM. The results presented in this figure reveal that the variations of the location of the device have very little effect on the vibrations of the stapes footplate. The maximum difference between the results of different holes is related to the anti-resonance at low frequencies (at 450 Hz) where the model with Hole A has a slightly smaller larger amplitude ratio than the results of the other three models with Holes B, C, and D; amplitude ratio of Hole A at this frequency is 8.61 dB larger than amplitude ratio values of other holes. At higher frequencies, the maximum difference in the value of amplitude ratio obtained from the models with Holes A, B, C, and D is less than 7 dB.

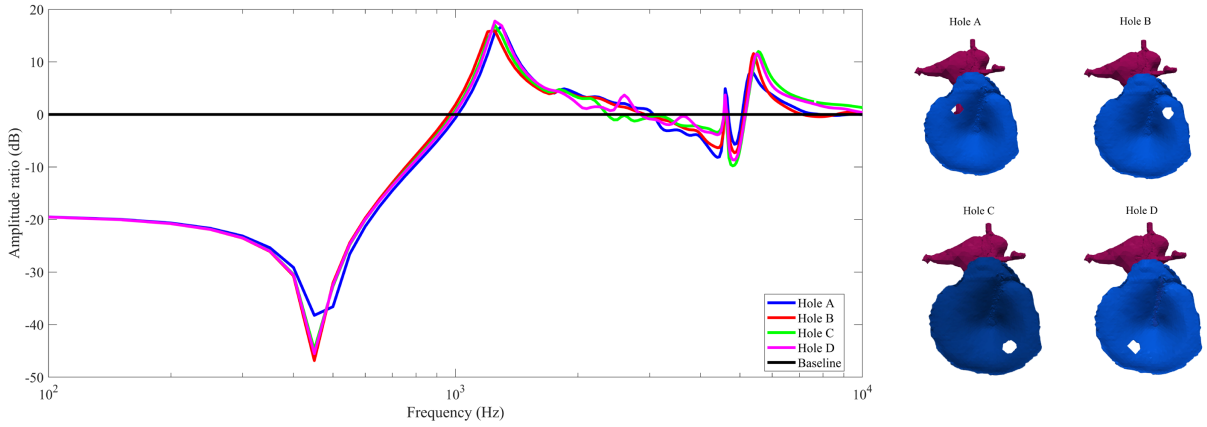


Figure 7-7 – Effects of variations of the location of the perforations on the stapes footplate responses. The results of models with Hole A (posterior-superior quadrant), Hole B (anterior-superior quadrant), Hole C (anterior-inferior quadrant), and Hole D (posterior-inferior quadrant) are presented in this figure. The results show that varying the location of the perforations does not have remarkable effects on hearing loss at most frequencies.

7.3.4 Vibrations patterns of the TM

In this section, we study the vibration patterns on the TM in the presence of the perforations and compare them with the vibration patterns of the baseline model. We should note that the vibration patterns presented in this section are reported in the direction of the normal to the manubrium at the umbo and are normalized with respect to the P_{TM}. To simulate the perforated TM, the model with Hole 3 was used in this section.

Figure 7-8 illustrates the vibration amplitude patterns of the TM in the baseline model and model with Hole 3 at three different frequencies of 500 Hz, 4.2 kHz, and 8 kHz. Based on the results presented in this figure, at low frequencies (500 Hz), TM perforations result in a significant decrease in the amplitude of almost all nodes on the TM. The mean values of the normalized amplitude of all nodes on the TM in the baseline and perforated model at this frequency are 0.028 µm/Pa and 0.001 µm/Pa, respectively. At 4.2 kHz, the amplitude values of most nodes on the TM in the model with a perforated ear are smaller than the amplitude of the same nodes in the baseline model except in some sections of the posterior-superior quadrant of the TM. The mean values of the normalized amplitude of all nodes on the TM in the baseline

and perforated model at this frequency are 0.011 μm/Pa and 0.006 μm/Pa, respectively. At 8 kHz, the amplitudes of most areas on the TM in the perforated ear results are greater than the respective amplitudes of the baseline model. The mean of the amplitude of all nodes on the TM in the baseline and perforated model at this frequency are 0.004 μm/Pa and 0.008 μm/Pa, respectively.

The phase patterns of the TM in the baseline model and the model with Hole 3 are presented in Figure 7-9. At 500 Hz, the inclusion of perforation results in a phase difference of about 180°in almost all regions of the TM. Based on the results presented in Figure 7-9, at 4.2 kHz and 8 kHz the phase of most regions on the TM in the baseline model and the model with Hole 3 are very close to each other except for the region around the perforated area. The values of the circular mean of all nodes on the TM also confirm these observations [93]. For the baseline model, the circular mean of all nodes across the TM at frequencies of 500 Hz, 4.2 kHz, and 8 kHz are 5.91°, 123.16°, and 150.94° respectively. Also, the values of the circular mean of all nodes on the TM in the results of the model with perforated TM at frequencies of 500 Hz, 4.2 kHz, and 8 kHz are 172.82°, 118.98°, and 147.36°, respectively.

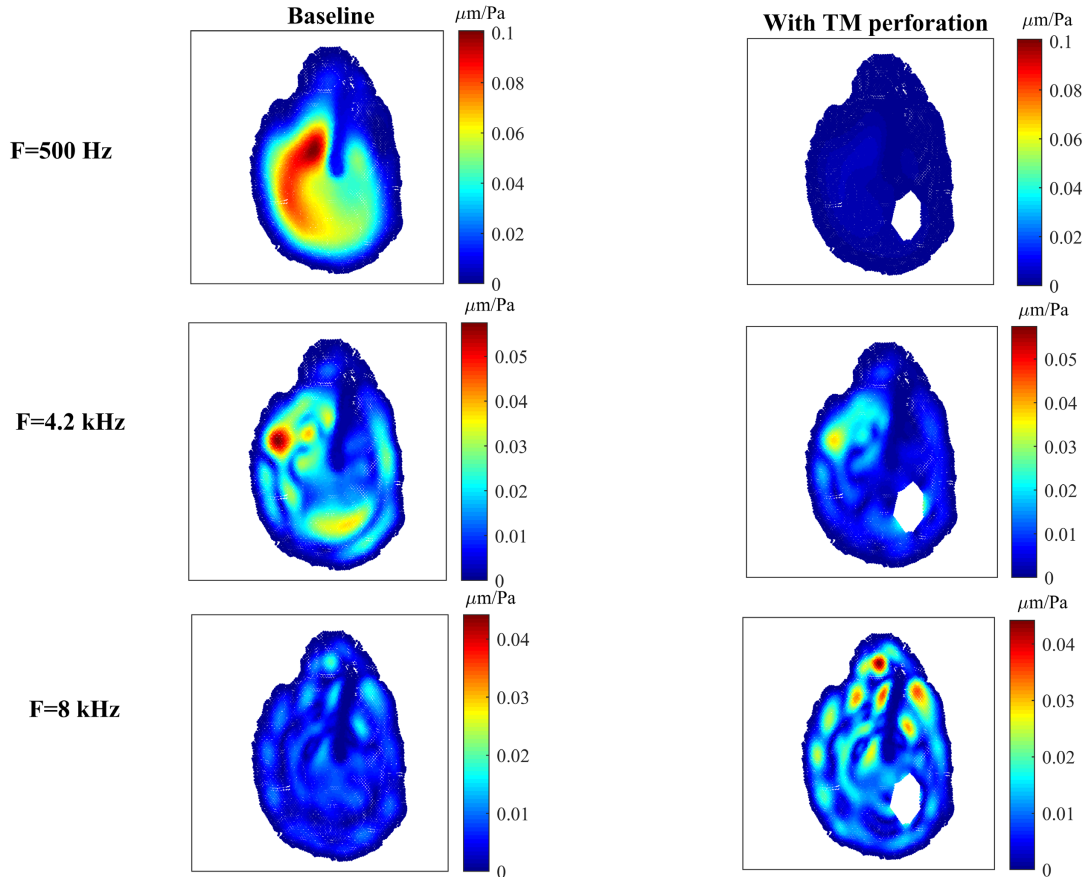


Figure 7-8 – Effects of TM perforations on the full-field vibration amplitude pattern of the TM. The results are normalized with respect to P_{TM}. The model with Hole 3 was used to simulate the effects of perforations here. At 500 Hz, having a perforation on the TM results in significant decreases in the amplitude in almost all regions across the TM. At 4.2 kHz, the inclusion of the perforation results in a decrease in the amplitude of several nodes on the TM, except in the posterior-superior quadrant. At 8 kHz, the amplitude values of most of the nodes across the TM in the perforated ear are greater than the amplitude of the same nodes in the baseline model.

7.3.5 Simultaneous mechanical and acoustical effects of medical devices

In this section, we study the effects of having both the mechanical effects of a medical device attached to the TM and the acoustical effects of TM perforations. As explained in Section 7.2.1.2, Hole 2 was used to add the acoustical effects of perforations. Also, to model the mechanical effects of the device, cylindrical geometry with a hole on it (Hole 2) was attached to the TM. Figure 7-10 shows the model of the device as well as the results of our simulations.

For the models with the devices, the results of all three different material properties stated in Section 7.2.1.2 are provided. We aimed to provide a detailed analysis of the mechanical effects of medical devices and the acoustical effects of perforations separately and also in combination with each other. To this end, for each material type, the values of amplitude ratio for three different scenarios are reported: the ear model with perforation on the TM and without any devices (only acoustical effects); the ear model with a medical device attached to the TM and without any perforations (only mechanical effects of the device), and the middle-ear model with both perforation and medical device on the TM (both acoustical and mechanical effects).

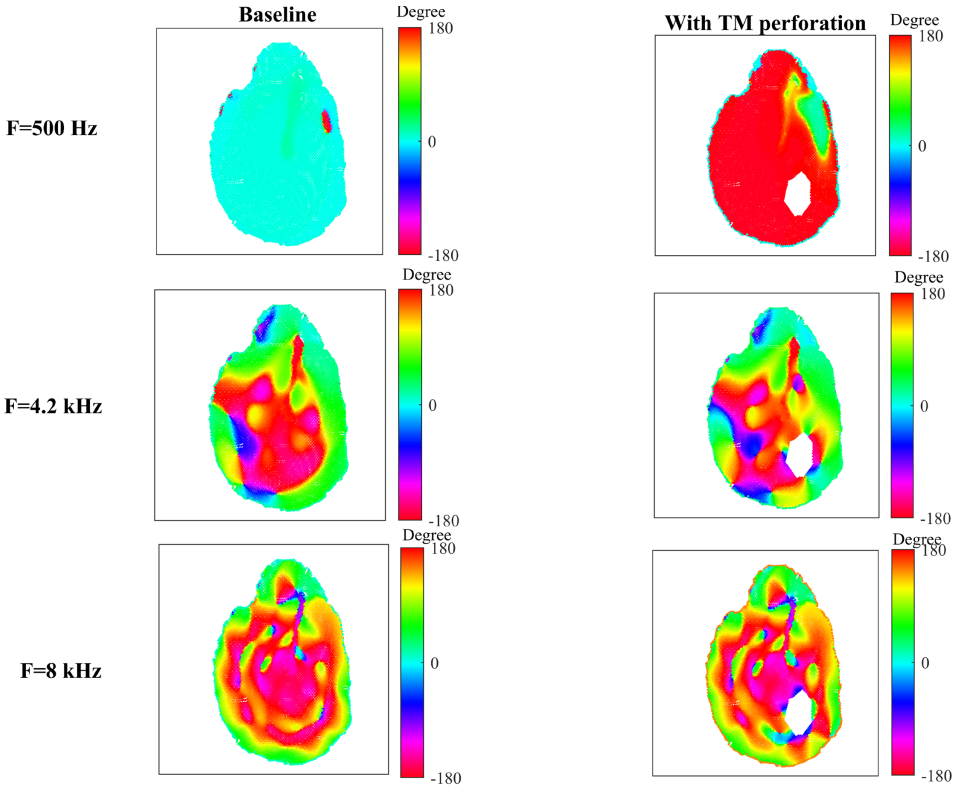


Figure 7-9 – Effects of TM perforations on the full-field vibration phase pattern of the TM. The results are normalized with respect to P_{TM}. The model with Hole 3 was used to simulate the effects of perforations here. At 500 Hz, the inclusion of the perforation results in a phase difference of about 180° between the results of the perforated and baseline models in most areas across the TM. At 4.2 kHz and 8 kHz, the inclusion of the perforations does not have significant effects on the phase of patterns of the TM except in the regions around the perforated area.

The results presented in Figure 7-10 illustrate that the addition of the device itself does not have any specific effects on the amplitude at very low frequencies (up to 800 Hz, 600 Hz, and 300 Hz for PDMS, Teflon, and stainless steel, respectively) and for all three material types, the values of amplitude ratio when the device is attached on the TM, without perforating it, is very close to zero at low frequencies. Similar to what we observed in Chapter 6, the attachment of the medical device shifts the middle-ear resonance frequency to lower frequencies. Based on the frequency response functions of the models with devices attached to them (not shown here), we concluded that the maximum shift is related to the stainless steel device (about 1 kHz) and the minimum shift is related to the PDMS device (about 250 Hz).

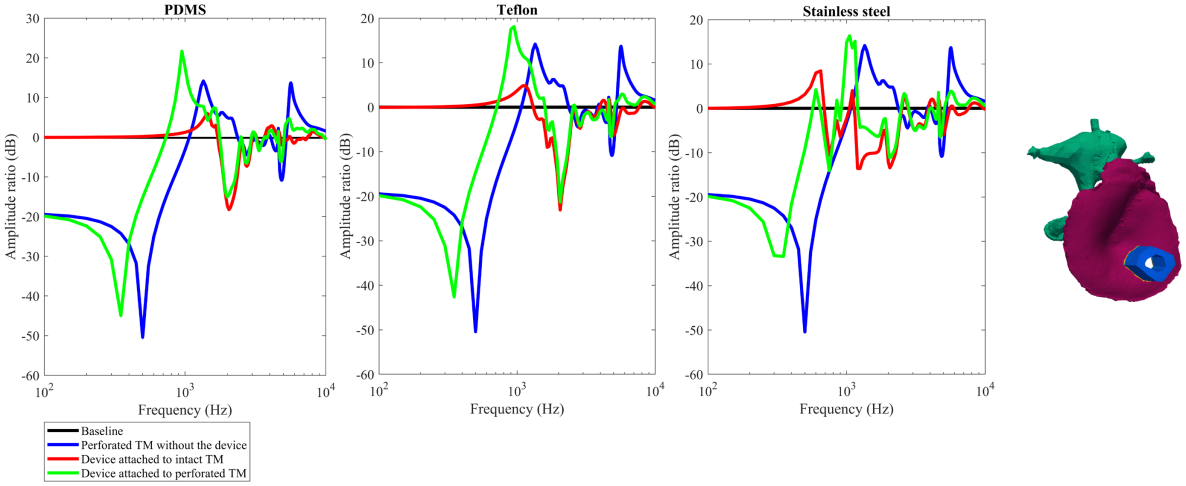


Figure 7-10 – Amplitude ratio of the stapes footplate in the presence of the medical device and perforations. We considered three different material properties for the medical devices. For each material property, we presented the results of three scenarios: having perforation on the TM without any medical devices attached to it (only acoustical effects); having a device attached to the intact TM (only mechanical effects); having a device attached to the perforated TM (both mechanical and acoustical effects). The results show when we have both mechanical and acoustical effects of the medical device, the acoustical effects of the device are more considerable at low frequencies (below about 1 kHz) whereas the mechanical effects of the device are dominant at higher frequencies.

As we observed in previous sections, having perforations on the TM results in significant decreases in the stapes footplate amplitude at low frequencies. We also observed an anti-

resonance in the stapes footplate responses when TM was perforated. We can observe that, for all three material types of the device considered in this chapter, when we have both the mechanical effects of the medical device and acoustical effects of perforations together, the frequency of this anti-resonance is shifted to lower frequencies. For all three material types, the inclusion of the device changes the frequency of this anti-resonance from 500 Hz to 350 Hz. In previous sections (7.3.2 and 7.3.3) we observed that the stapes footplate amplitude starts to increase at frequencies higher than the frequency of this anti-resonance. This increase in the amplitude with increasing the frequency happens when we attach the device to the perforated TM, however, because the addition of the device shifts the anti-resonance frequency to lower frequencies, this increase in the amplitude starts at lower frequencies in comparison to the situation in which there are no devices attached to the perforated TM. At higher frequencies (above about 1 kHz), the mechanical effects of the device overcome the acoustical effects of perforations, and then for all three material types, the amplitude ratio of the model with the medical device attached to the perforated TM is very similar to the amplitude ratio of the model with the medical device attached to the intact TM at those frequencies. We calculated the mean of absolute value of the difference between the results of the model with the medical device attached to perforated TM and the results of two other models (model with the medical device attached to intact TM and model with perforated TM without any medical devices). The mean absolute values of the difference between the results of the model with the device attached to the perforated TM and the model with the device attached to the intact TM at frequencies above 1 kHz are 1.96 dB, 2.15 dB, 2.27 dB for PDMS, Teflon, and stainless steel, respectively. Also, the mean of absolute values of the difference between the results of the model with the device attached to perforated TM and the model with perforated TM without any devices are 3.61 dB, 3.90 dB, 4.28 dB for the PDMS, Teflon, and stainless steel, respectively. Based on these results, for all three materials, at frequencies above 1 kHz, the mean differences between the results of the model with both acoustical and mechanical effects and the model with just mechanical effects are smaller than the difference between the model with both acoustical and mechanical effects and the model with only acoustical effects.

7.4 Discussions

This study is an extension to Chapter 6 in which we analyzed the mechanical effects of medical devices attached to the TM. In the current study, we addressed the effects of the medical device attachment in the treatment procedures in which we need to create perforations on the TM, in addition to the attachment of the device. These treatment procedures include but are not limited to tympanostomy tube insertion, which is a common treatment of otitis media. The current study aims to provide a deep insight into the acoustical effects of the perforations and the combination of these acoustical effects with the mechanical effects of the medical devices attached to the TM. The outcomes of this study can lead to optimizing the existing/future medical devices to minimize hearing losses as a result of the attachment of these devices to the TM.

In the first step of the current study, we added the middle-ear cavity and a partial ear canal to our previous model of the middle ear as explained in Section 7.2. We then compared the open/closed cavity results obtained using our model with open/closed cavity measurement results of Voss et al. as explained in Section 7.3.1 [68]. The trends we observed in the open vs. closed cavity responses obtained using our model are very similar to the trends in open vs. closed cavity measurement results of Voss et al.; at low frequencies, the inclusion of the middle-ear cavity adds to the stiffness of the system and low-frequency responses of the closed-cavity model are stiffer than the open-cavity model results. In addition to the experimental measurement results of Voss et al., other studies in the literature also confirm that the inclusion of the middle ear cavity results in increasing the stiffness of the model at low frequencies [71]. Also, in both the experimental measurement results of Voss et al. and our model results, the open and closed cavity model responses are very similar at most frequencies higher than the middle-ear resonance frequency. Near 4.6 kHz, our closed cavity model results show an anti-resonance that does not exist in the open-cavity results obtained from our model. In order to provide a deeper analysis of the sources of this anti-resonance and to provide a detailed understanding of the acoustical behavious of our closed-cavity middle-ear model, we presented the pressure distribution inside the middle-ear cavity in Section 7.3.1. Based on the

pressure distribution results, the middle-ear cavity resonance happens around the frequency of 4.6 kHz. This can be detected from the specific pattern of the pressure distribution inside the middle-ear cavity around 4.2 kHz. We monitored the pressure distribution at all frequencies (in the range of 10 Hz to 10 kHz) in our study and observed that this pattern in the pressure distribution (two areas with maximum pressure at the posterior-superior and anterior-inferior regions of the middle-ear cavity) only occurs around the frequency of the anti-resonances observed in closed-cavity results of umbo and stapes footplate in Figure 7-2 and Figure 7-3. In fact, as the middle-ear cavity resonance is happening at these frequencies, most of the energy of the model goes to the cavity and we can see its effect on the anti-resonances in the umbo and stapes footplate responses. Similar observations about the presence of anti-resonances at the middle-ear cavity resonance frequency have been previously reported in the literature as well [51].

In Section 7.3.2 we studied the effects of varying the perforation size on the stapes footplate displacement and on the pressure inside the ear. We compared our model results with the experimental measurement results of Voss et al. [233], [237]. We observed that perforations can have significant effects on the stapes footplate displacement specifically at low frequencies where the stapes footplate amplitude of the perforated ear is considerably smaller than the stapes footplate amplitude of the ear with intact TM. The results of our perforated TM models show an anti-resonance at very low frequencies. These anti-resonances have been also observed in some other studies in the literature. For instance, similar anti-resonances have been observed at the low-frequency response of the stapes footplate of the mouse middle ear when the pars flaccids is removed (which is similar to having perforations on the TM) [240]. At frequencies higher than the frequency of this anti-resonance, the stapes footplate amplitude in our model starts to increase. This increase can be observed in the experimental measurement results of Voss et al. and other experimental and other modelling results with perforated TM in the literature [60], [233], [235], [240]. At these frequencies, similar to what was observed in other experimental works, the larger the perforation size, the smaller the stapes footplate amplitude [60], [233], [235], [237].

In Section 7.3.3, we studied the effects of variations of the location of the perforation on the stapes footplate amplitude by placing four holes with the almost same surface area on different quadrants of the TM and comparing the results. Our model results show that the variations of the location of the TM perforations have negligible effects on the motions of the stapes footplate. This observation is also consistent with the observations and measurement results of Voss et al. [234], [241].

In Section 7.3.4, we studied the vibration patterns of the TM in the presence of the perforations and compared them with the vibration patterns of the baseline model. Our results suggested that, at low frequencies (500 Hz), the amplitudes of all nodes on the TM in the perforated ear are significantly smaller than the amplitude of the same nodes in the baseline model and for most nodes across the TM, we observed a uniform phase difference of 0.5 cycles between the results of the baseline model and the results obtained from the perforated ear model. At 4.2 kHz, the amplitudes of most regions in the perforated ear model (except some regions in the posterior-superior quadrant) were smaller than the amplitude of the same regions in the baseline model. At higher frequencies (8 kHz), the amplitudes of most regions on the TM in the perforated model were greater than the amplitude of the same regions in the baseline model. Also, at 4.2 kHz and 8 kHz, the phase difference between the baseline and perforated models was insignificant in most regions except in the regions around the perforated area. These observations show that the perforations can have considerable effects on the vibration patterns of the TM at most frequencies.

In Section 7.3.5 we studied the effects of changing acoustical and mechanical characteristics of the middle ear by attaching medical devices made of different materials to the perforated and intact TM. We considered three different scenarios to study these effects and their combinations: the device attached to the intact TM (only mechanical effects); the perforation on TM without any devices (only acoustical effects), and the device attached to the perforated TM (both acoustical and mechanical effects). The results show that when we have both the acoustical effects of perforations and mechanical effects of the device, at low frequencies (below about 1 kHz), the hearing loss as a result of perforations is significantly greater than

the hearing loss as a result of the attachment of the device. These observations are consistent with existing experimental results in the literature. In the study performed by Nishihara et al., the effects of attachment of tympanostomy tubes to the TM as well as the effects of attaching different masses to the TM were investigated [221]. From their results, it can be interpreted that at low frequencies, the hearing losses as a result of the attachment of tympanostomy tubes are more considerable than the hearing loss resulting from the attachment of the device itself. Our results show that at higher frequencies, on the other hand, the mechanical effects of the medical device are dominant. In fact, for all three material studies here, the high-frequency responses of the model with devices attached to perforated TM are very similar to the results of the model in which the device is attached to intact TM. It is generally known that the low-frequency responses of the middle ear are stiffness dominant and high-frequency responses are mass dominant [118]. The results of our simulation presented in Section 7.3.5 suggest that in fact the effects of changes in the acoustical characteristics of the middle ear as a result of the perforations appear as the changes in the stiffness of the middle ear at low frequencies and the changes in the mechanical characteristics of the middle ear as the result of the attachment of the device mostly appear as the changes in the mass of the middle ear at high frequencies.

Chapter 8
Conclusions and future work

8.1 Summary

In this thesis, some unknown aspects of the biomechanics of the human middle ear have been studied. FE Models of the middle ear have been created and validated using experimental measurements data in the literature and were used in combination with stochastic modelling methods to provide a clear understating of the effects of inter-individual variabilities on the middle-ear vibrations. Moreover, a comprehensive global sensitivity analysis was performed on the middle ear to identify the parameters with the greatest impact and also to find the most significant interactions among parameters at a wide range of excitation frequencies. Additionally, a systematic investigation was undertaken to elucidate the mechanical and acoustical effects of the attachment of medical devices to the tympanic membrane on sound conduction in the middle ear.

Also, a non-invasive method for fast estimation of the mechanical properties of middle-ear structures was proposed that can be further developed to be eventually used for diagnostic purposes. As an initial step, a method was proposed for the estimation of the Young's modulus of 2D thin planar structures using its full-field harmonic vibration data. This method was then modified and combined with machine-learning techniques for fast estimation of the most influential mechanical parameters of the middle ear.

8.2 Original contributions

1. In Chapter 2, we used a stochastic FE model of the middle ear to study the effects of inter-individual variabilities in the mechanical properties of all structures of the middle ear as well as the thickness of the TM on sound conduction in the middle ear. The major outcomes are:

    a) The uncertainties in the model parameters can be magnified by more than three times in the umbo and stapes footplate responses at frequencies above 2 kHz.

b) The middle-ear model is biased and we observed distortions in the output distributions of the stochastic FE model.

c) By increasing the frequency, the highly-uncertain regions spatially spread out on the tympanic membrane surface.

2. In Chapter 3, we performed a global sensitivity analysis on the middle ear. The major findings are:

   a) The created PCE-based surrogate models of the amplitudes of the umbo and stapes footplate and the phase of the stapes footplate can accurately represent the behaviours of the stochastic FE model at most frequencies.

   b) Although the importance of each parameter varies with frequency, the most influential parameters are the Young's modulus of the tympanic membrane and stapedial annular ligament, the damping of the stapedial annular ligament, the Young's modulus of ossicles, and the thickness of the tympanic membrane.

   c) The most significant interactions happen between the Young's modulus and thickness of the TM.

3. In Chapter 4, a novel method was introduced for estimation of the Young's modulus of 2D thin structures using harmonic vibration data from holography measurements, it was found that [79]:

   a) For all noise-free benchmark vibration data, and also for the data with Gaussian and non-Gaussian noise high-intensity noise, the highest value of the error of the estimated values of Young's modulus was less than 5%.

   b) For each case study, estimations at different frequencies revealed that when uncertainties in the geometrical and material parameters are negligible, the effects of the excitation frequency are not considerable on the estimation outcome.

c) The accuracy of our proposed method can be compromised if the boundary condition is incorrectly specified.

d) Error in the viewing angle of the experimental holography setup results in estimation errors of less than 3% for camera angle errors of up to 10° for all frequencies.

e) When uncertainty in the thickness of the object exists or an ideal perpendicular viewing angle is hard to obtain in the experimental setup, material characterization at higher frequencies is recommended.

f) The method is promising especially for material characterization applications in which access to high-quality free vibration or modal data is limited.

4. In Chapter 5, we used machine-learning-based surrogate models for fast material characterization of the middle-ear structures. The outcomes are:

    a) ML-based surrogate models created using eXterme gradient boosting method can fairly represent the amplitude and phase of the umbo and stapes footplate and vibration patterns of the TM at most frequencies even with a wide range of variations for model parameters.

    b) The parameter estimation method that works based on the combination of ML-based surrogate models with Bayesian optimization can accurately estimate the Young's modulus of the TM and SAL (with respect to the FE model) at the same time and separately.

5. In Chapter 6, we investigated the mechanical effects of medical devices attached to the TM, the major findings are:

    a) The variations of the material properties of the medical device lead to significant changes in the middle-ear resonance frequency.

    b) The effects of changing the material properties of the device on the umbo and stapes footplate motions are negligible at frequencies above 5 kHz.

c) Point-mass models cannot accurately represent behaviours of middle ear (with respect to the FE results of the full-device models) in the presence of the medical device.

d) The variations of diameter/height of the medical device can have considerable impacts on the middle-ear vibrations at several frequencies.

e) Implanting the medical device to the TM does not have significant effects on the TM vibration patterns at low frequencies. However, it changes the amplitude/phase pattern of the region in which the device is attached and some adjacent regions at higher frequencies.

6. In Chapter 7, we investigated the acoustical effects of medical devices attached to the TM. The major outcomes are:

   a) TM perforations can have significant effects on the displacement of the umbo, stapes footplate, and the vibration patterns of the TM at different frequencies.

   b) The location of the perforations on the TM does not have remarkable effects on middle-ear vibration outputs.

   c) The size of perforation has considerable effects on sound conduction in the middle ear.

   d) When we have both the acoustical effects (as a result of TM perforations) and the mechanical effects of the device (as a result of its mass and stiffness), the acoustical effects are dominant at low frequencies (below about 1 kHz). However, at frequencies above 1 kHz, the behvaiours of the middle ear are significantly affected by the mechanical effects of the device.

8.3 Future work

In this section, a few suggestions are made for future modelling and experimental works.

The stochastic FE model presented in Chapter 2 considers uncertainty in the mechanical parameters of all structures of the middle ear as well as the thickness of the TM. To increase

the generalizability of the findings, it is necessary to add variations in the morphological features to the stochastic model as well. As changing the scale of each of the structures of the middle-ear results in applying some changes to the mesh, finding a systematic approach to study the variations of the geometrical parameters can be challenging. These variations in the morphological features can then can be fed into the global sensitivity analysis procedure introduced in Chapter 3 to rank the importance of the shape/geometry of different structures in the middle ear. Additionally, one other suggestion is to perform further experimental and modelling investigations on large populations of ears to determine the distribution of each of the model parameters.

The method proposed in Chapter 4 for estimation of the Young's modulus of thin planar structures does not consider the damping of the structures. The addition of the damping can increase the applicability of the proposed estimation method specifically for biological structures. Also, as the method needs the complete boundary of the vibrating domain to apply the finite-difference equations, in cases where the displacement field of the entire object and its non-moving boundary is not measurable, some user-interactive techniques can be implemented in the model. Using these techniques the user can specify the exact boundary of the object so that the parameter estimation method can apply the mechanical equations of motion to the whole domain and then only use the nodes on the domain for which we have experimental measurements for the calculation of the objective function in the optimization process.

The proposed material characterization method in Chapter 5 is able to estimate the Young's modulus of the TM and SAL with high accuracies. As observed in the global sensitivity analysis results provided in Chapter 3, there are some other mechanical parameters in the middle ear model, such as the damping of the SAL, that have remarkable effects on the vibration responses of some of the structures of the middle ear at some frequencies. Characterizing the mechanical properties of these structures can add to the generalizability of the proposed parameter estimation method. Additionally, in order to increase the usability of the diagnostic tools such as the method proposed in Chapter 5, it is necessary to perform further

experimental and modelling studies on the effects of different middle-ear pathologies on the mechanical properties of middle-ear structures.

In Chapter 6 and Chapter 7 we studied the mechanical and acoustical effects of medical devices attached to the TM on the sound conduction in the middle ear in silico. Future studies can address the same problems using experimental measurements and in a systematic way with medical devices accurately manufactured with different sizes, geometries, and material properties.

References

[1] W. James, “Development of the ear and hearing,” *Journal of perinatology*, vol. 20, no. 1, pp. S12–S20, 2000.

[2] R. P. Venekamp, R. A. M. J. Damoiseaux, and A. G. M. Schilder, “Acute otitis media in children,” *BMJ Clin Evid*, vol. 2014, Sep. 2014, Accessed: Jan. 03, 2020. [Online]. Available: https://www.ncbi.nlm.nih.gov/pmc/articles/PMC4166866/

[3] S. Puria, “Middle ear hearing devices,” in *The Middle Ear*, Springer, 2013, pp. 273–308.

[4] R. Z. Gan, C. Dai, X. Wang, D. Nakmali, and M. W. Wood, “A totally implantable hearing system – Design and function characterization in 3D computational model and temporal bones,” *Hearing Research*, vol. 263, no. 1–2, pp. 138–144, May 2010, doi: 10.1016/j.heares.2009.09.003.

[5] X. Wang, Y. Hu, Z. Wang, and H. Shi, “Finite element analysis of the coupling between ossicular chain and mass loading for evaluation of implantable hearing device,” *Hearing Research*, vol. 280, no. 1–2, pp. 48–57, Oct. 2011, doi: 10.1016/j.heares.2011.04.012.

[6] Xiangming Zhang and R. Z. Gan, “A Comprehensive Model of Human Ear for Analysis of Implantable Hearing Devices,” *IEEE Trans. Biomed. Eng.*, vol. 58, no. 10, pp. 3024–3027, Oct. 2011, doi: 10.1109/TBME.2011.2159714.

[7] Y.-L. Song and C.-F. Lee, “Computer-aided modeling of sound transmission of the human middle ear and its otological applications using finite element analysis,” *Tzu Chi Medical Journal*, vol. 24, no. 4, pp. 178–180, Dec. 2012, doi: 10.1016/j.tcmj.2012.08.004.

[8] K. R. Whittemore, S. N. Merchant, B. B. Poon, and J. J. Rosowski, “A normative study of tympanic membrane motion in humans using a laser Doppler vibrometer (LDV),” *Hearing Research*, vol. 187, no. 1, pp. 85–104, Jan. 2004, doi: 10.1016/S0378-5955(03)00332-0.

[9] R. Aibara, J. T. Welsh, S. Puria, and R. L. Goode, “Human middle-ear sound transfer function and cochlear input impedance,” *Hearing Research*, vol. 152, no. 1–2, pp. 100–109, Feb. 2001, doi: 10.1016/S0378-5955(00)00240-9.

[10] K. N. O’Connor, H. Cai, and S. Puria, “The effects of varying tympanic-membrane material properties on human middle-ear sound transmission in a three-dimensional finite-element model,” *The Journal of the Acoustical Society of America*, vol. 142, no. 5, pp. 2836–2853, Nov. 2017, doi: 10.1121/1.5008741.

[11] B. Alekya, S. Rao, and H. J. Pandya, “Engineering approaches for characterizing soft tissue mechanical properties: A review,” *Clinical Biomechanics*, vol. 69, pp. 127–140, 2019.

[12] M. John S. Oghalai and P. William E. Brownell, “Chapter 44. Anatomy & Physiology of the Ear,” in *CURRENT Diagnosis & Treatment in Otolaryngology—Head & Neck Surgery, 3e*, A. K. Lalwani, Ed. New York, NY: The McGraw-Hill Companies, 2012. [Online]. Available: accessmedicine.mhmedical.com/content.aspx?aid=55770441

[13] Blausen.com staff, “Medical gallery of Blausen medical 2014,” *WikiJournal of Medicine*, vol. 1, no. 2, pp. 1–79, 2014, doi: 10.15347/wjm/2014.010.
[14] Y. Onchi, “A study of the mechanism of the middle ear,” *The Journal of the Acoustical Society of America*, vol. 21, no. 4, pp. 404–410, 1949.
[15] J. Zwislocki, “Analysis of the middle-ear function. Part I: Input impedance,” *J. Acoust. Soc. Am.*, vol. 34, no. 9B, pp. 1514–1523, 1962, doi: 10.1121/1.1918382.
[16] H. Hudde and C. Weistenhofer, “Circuit models of middle ear function,” in *Rosowski, J. J., Mercahnt. S. N. (Eds.) The function and mechanics of normal, diseased and reconstructed middle ears*, Kugler Publications, 2000, pp. 39–58.
[17] P. Parent and J. B. Allen, “Wave model of the cat tympanic membrane,” *The Journal of the Acoustical Society of America*, vol. 122, no. 2, pp. 918–931, Aug. 2007, doi: 10.1121/1.2747156.
[18] J. Aernouts, “Mechanical properties of the tympanic membrane: Measurement and modeling,” PhD Thesis, University of Antwerp, 2012.
[19] J. Fish and T. Belytschko, *A first course in finite elements*, vol. 1. John Wiley & Sons New York, 2007.
[20] T. Belytschko, W. K. Liu, B. Moran, and K. Elkhodary, *Nonlinear finite elements for continua and structures*. John wiley & sons, 2014.
[21] W. R. Funnell and C. A. Laszlo, “Modeling of the cat eardrum as a thin shell using the finite-element method,” *J. Acoust. Soc. Am.*, vol. 63, no. 5, pp. 1461–1467, May 1978, doi: 10.1121/1.381892.
[22] W. R. Funnell, “On the undamped natural frequencies and mode shapes of a finite-element model of the cat eardrum,” *J. Acoust. Soc. Am.*, vol. 73, no. 5, pp. 1657–1661, May 1983, doi: 10.1121/1.389386.
[23] W. R. Funnell, W. F. Decraemer, and S. M. Khanna, “On the damped frequency response of a finite-element model of the cat eardrum,” *J. Acoust. Soc. Am.*, vol. 81, no. 6, pp. 1851–1859, Jun. 1987, doi: 10.1121/1.394749.
[24] K. Williams and T. Lesser, “A finite element analysis of the natural frequencies of vibration of the human tympanic membrane. Part I,” *British journal of audiology*, vol. 24, no. 5, pp. 319–327, 1990.
[25] T. H. J. Lesser, K. R. Williams, and A. W. Blayney, “Mechanics and materials in middle ear reconstruction,” *Clinical Otolaryngology & Allied Sciences*, vol. 16, no. 1, pp. 29–32, 1991, doi: 10.1111/j.1365-2273.1991.tb01938.x.
[26] N. Maftoon, “Experimental and Modelling Study of Gerbil Middle Ear,” McGill University Libraries, 2014.
[27] H. Wada, T. Metoki, and T. Kobayashi, “Analysis of dynamic behavior of human middle ear using a finite-element method,” *The Journal of the Acoustical Society of America*, vol. 92, no. 6, pp. 3157–3168, Dec. 1992, doi: 10.1121/1.404211.
[28] H. M. Ladak and W. R. J. Funnell, “Finite-element modeling of the normal and surgically repaired cat middle ear,” *The Journal of the Acoustical Society of America*, vol. 100, no. 2, pp. 933–944, Aug. 1996, doi: 10.1121/1.416205.

[29] J. Dirckx, W. Decraemer, and G. Dielis, “Phase shift method based on object translation for full field automatic 3-D surface reconstruction from moire topograms,” *Applied Optics*, vol. 27, no. 6, pp. 1164–1169, 1988.
[30] W. R. J. Funnell and W. F. Decraemer, “On the incorporation of moiré shape measurements in finite-element models of the cat eardrum,” *The Journal of the Acoustical Society of America*, vol. 100, no. 2, pp. 925–932, Aug. 1996, doi: 10.1121/1.416252.
[31] W. R. J. Funnell, N. Maftoon, and W. F. Decraemer, “Modeling of Middle Ear Mechanics,” in *The Middle Ear: Science, Otosurgery, and Technology*, S. Puria, R. R. Fay, and A. N. Popper, Eds. New York, NY: Springer, 2013, pp. 171–210. doi: 10.1007/978-1-4614-6591-1_7.
[32] S. J. Daniel, W. R. Funnell, A. G. Zeitouni, M. D. Schloss, and J. Rappaport, “Clinical applications of a finite-element model of the human middle ear,” *J Otolaryngol*, vol. 30, no. 6, pp. 340–346, Dec. 2001, doi: 10.2310/7070.2001.19393.
[33] E. L. Ritman, “Micro-computed tomography—current status and developments,” *Annu. Rev. Biomed. Eng.*, vol. 6, pp. 185–208, 2004.
[34] D. J. Kelly, P. J. Prendergast, and A. W. Blayney, “The effect of prosthesis design on vibration of the reconstructed ossicular chain: a comparative finite element analysis of four prostheses,” *Otol. Neurotol.*, vol. 24, no. 1, pp. 11–19, Jan. 2003, doi: 10.1097/00129492-200301000-00004.
[35] C. S. Mikhael, W. R. J. Funnell, and M. Bance, “Middle-ear Finite-Element Modelling with Realistic Geometry and a Priori Material-Property Estimates,” *CMBES Proceedings*, vol. 28, Dec. 2005, Accessed: Feb. 05, 2020. [Online]. Available: https://proceedings.cmbes.ca/index.php/proceedings/article/view/464
[36] N. Elkhouri, H. Liu, and W. R. J. Funnell, “Low-frequency finite-element modeling of the gerbil middle ear,” *Journal of the Association for Research in Otolaryngology*, vol. 7, no. 4, pp. 399–411, 2006.
[37] N. Maftoon, W. R. J. Funnell, S. J. Daniel, and W. F. Decraemer, “Finite-Element Modelling of the Response of the Gerbil Middle Ear to Sound,” *JARO*, vol. 16, no. 5, pp. 547–567, Oct. 2015, doi: 10.1007/s10162-015-0531-y.
[38] H. M. Ladak, W. R. J. Funnell, W. F. Decraemer, and J. J. J. Dirckx, “A geometrically nonlinear finite-element model of the cat eardrum,” *The Journal of the Acoustical Society of America*, vol. 119, no. 5, pp. 2859–2868, Apr. 2006, doi: 10.1121/1.2188370.
[39] X. Wang, T. Cheng, and R. Z. Gan, “Finite-element analysis of middle-ear pressure effects on static and dynamic behavior of human ear,” *J. Acoust. Soc. Am.*, vol. 122, no. 2, pp. 906–917, Aug. 2007, doi: 10.1121/1.2749417.
[40] L. Qi, H. Liu, J. Lutfy, W. R. J. Funnell, and S. J. Daniel, “A nonlinear finite-element model of the newborn ear canal,” *J. Acoust. Soc. Am.*, vol. 120, no. 6, pp. 3789–3798, Dec. 2006, doi: 10.1121/1.2363944.
[41] S. Ihrle, M. Lauxmann, A. Eiber, and P. Eberhard, “Nonlinear modelling of the middle ear as an elastic multibody system—applying model order reduction to acousto-structural coupled systems,” *Journal of Computational and Applied Mathematics*, vol. 246, pp. 18–26, 2013.

[42] H. Motallebzadeh, M. Charlebois, and W. R. J. Funnell, "A non-linear viscoelastic model for the tympanic membrane," *The Journal of the Acoustical Society of America*, vol. 134, no. 6, pp. 4427–4434, 2013.
[43] M. Charlebois, H. Motallebzadeh, and W. R. J. Funnell, "Visco-hyperelastic law for finite deformations: a frequency analysis," *Biomechanics and modeling in mechanobiology*, vol. 12, no. 4, pp. 705–715, 2013.
[44] R. Z. Gan, Q. Sun, B. Feng, and M. W. Wood, "Acoustic–structural coupled finite element analysis for sound transmission in human ear—Pressure distributions," *Medical Engineering & Physics*, vol. 28, no. 5, pp. 395–404, Jun. 2006, doi: 10.1016/j.medengphy.2005.07.018.
[45] J. P. Fay, S. Puria, and C. R. Steele, "The discordant eardrum," *PNAS*, vol. 103, no. 52, pp. 19743–19748, Dec. 2006, doi: 10.1073/pnas.0603898104.
[46] J. P. Tuck-Lee, P. M. Pinsky, C. R. Steele, and S. Puria, "Finite element modeling of acousto-mechanical coupling in the cat middle ear," *The Journal of the Acoustical Society of America*, vol. 124, no. 1, pp. 348–362, Jul. 2008, doi: 10.1121/1.2912438.
[47] T. Koike, H. Wada, and T. Kobayashi, "Modeling of the human middle ear using the finite-element method," *The Journal of the Acoustical Society of America*, vol. 111, no. 3, pp. 1306–1317, Feb. 2002, doi: 10.1121/1.1451073.
[48] R. Z. Gan, B. Feng, and Q. Sun, "Three-Dimensional Finite Element Modeling of Human Ear for Sound Transmission," *Annals of Biomedical Engineering*, vol. 32, no. 6, pp. 847–859, Jun. 2004.
[49] R. Z. Gan, B. P. Reeves, and X. Wang, "Modeling of Sound Transmission from Ear Canal to Cochlea," *Ann Biomed Eng*, vol. 35, no. 12, pp. 2180–2195, Dec. 2007, doi: 10.1007/s10439-007-9366-y.
[50] P. J. Prendergast, P. Ferris, H. J. Rice, and A. W. Blayney, "Vibro-acoustic modelling of the outer and middle ear using the finite-element method," *Audiol. Neurootol.*, vol. 4, no. 3–4, pp. 185–191, Aug. 1999, doi: 10.1159/000013839.
[51] H. Motallebzadeh, N. Maftoon, J. Pitaro, W. R. J. Funnell, and S. J. Daniel, "Fluid-structure finite-element modelling and clinical measurement of the wideband acoustic input admittance of the newborn ear canal and middle ear," *Journal of the Association for Research in Otolaryngology*, vol. 18, no. 5, pp. 671–686, 2017.
[52] J. Aernouts and J. J. J. Dirckx, "Elastic characterization of the gerbil pars flaccida from in situ inflation experiments," *Biomech Model Mechanobiol*, vol. 10, no. 5, pp. 727–741, Oct. 2011, doi: 10.1007/s10237-010-0269-8.
[53] J. Aernouts, J. R. M. Aerts, and J. J. J. Dirckx, "Mechanical properties of human tympanic membrane in the quasi-static regime from in situ point indentation measurements," *Hearing Research*, vol. 290, no. 1, pp. 45–54, Aug. 2012, doi: 10.1016/j.heares.2012.05.001.
[54] D. De Greef *et al.*, "Viscoelastic properties of the human tympanic membrane studied with stroboscopic holography and finite element modeling," *Hearing Research*, vol. 312, pp. 69–80, Jun. 2014, doi: 10.1016/j.heares.2014.03.002.
[55] H. Motallebzadeh, N. Maftoon, J. Pitaro, W. R. J. Funnell, and S. J. Daniel, "Finite-Element Modelling of the Acoustic Input Admittance of the Newborn Ear Canal and

Middle Ear," *Journal of the Association for Research in Otolaryngology*, vol. 18, no. 1, pp. 25–48, Feb. 2017, doi: 10.1007/s10162-016-0587-3.
[56] A. Huber, T. Koike, H. Wada, V. Nandapalan, and U. Fisch, "Fixation of the anterior mallear ligament: diagnosis and consequences for hearing results in stapes surgery," *Ann. Otol. Rhinol. Laryngol.*, vol. 112, no. 4, pp. 348–355, Apr. 2003, doi: 10.1177/000348940311200409.
[57] C. Dai, T. Cheng, M. W. Wood, and R. Z. Gan, "Fixation and detachment of superior and anterior malleolar ligaments in human middle ear: Experiment and modeling," *Hear Res*, vol. 230, no. 1–2, pp. 24–33, Aug. 2007, doi: 10.1016/j.heares.2007.03.006.
[58] R. Z. Gan and X. Wang, "Multifield coupled finite element analysis for sound transmission in otitis media with effusion," *J. Acoust. Soc. Am.*, vol. 122, no. 6, pp. 3527–3538, Dec. 2007, doi: 10.1121/1.2793699.
[59] C. F. Lee, J. H. Chen, Y. F. Chou, L. P. Hsu, P. R. Chen, and T. C. Liu, "Optimal graft thickness for different sizes of tympanic membrane perforation in cartilage myringoplasty: a finite element analysis," *Laryngoscope*, vol. 117, no. 4, pp. 725–730, Apr. 2007, doi: 10.1097/mlg.0b013e318031f0e7.
[60] R. Z. Gan, T. Cheng, C. Dai, F. Yang, and M. W. Wood, "Finite element modeling of sound transmission with perforations of tympanic membrane," *J. Acoust. Soc. Am.*, vol. 126, no. 1, pp. 243–253, Jul. 2009, doi: 10.1121/1.3129129.
[61] B. Sackmann, P. Eberhard, and M. Lauxmann, "Parameter identification from normal and pathological middle ears using a tailored parameter identification algorithm," *Journal of biomechanical engineering*, vol. 144, no. 3, 2022.
[62] G. Volandri, F. Di Puccio, P. Forte, and C. Carmignani, "Biomechanics of the tympanic membrane," *Journal of Biomechanics*, vol. 44, no. 7, pp. 1219–1236, Apr. 2011, doi: 10.1016/j.jbiomech.2010.12.023.
[63] G. von Békésy, *Über die Messung der Schwingungsamplitude der Gehörknöcheln mittels einer kapazitiven Sonde*. 1941.
[64] S. M. Khanna and J. Tonndorf, "Tympanic Membrane Vibrations in Cats Studied by Time-Averaged Holography," *The Journal of the Acoustical Society of America*, vol. 51, no. 6B, pp. 1904–1920, Jun. 1972, doi: 10.1121/1.1913050.
[65] O. Løkberg, K. Hagmoen, and T. Gundersen, "Vibration measurement of the human tympanic membrane-in vivo," *Acta Oto-Laryngologica*, vol. 89, no. 1–2, pp. 37–42, 1980.
[66] T. Buunen and M. Vlaming, "Laser–Doppler velocity meter applied to tympanic membrane vibrations in cat," *The Journal of the Acoustical Society of America*, vol. 69, no. 3, pp. 744–750, 1981.
[67] J. J. Rosowski, M. E. Ravicz, S. W. Teoh, and D. Flandermeyer, "Measurements of Middle-Ear Function in the Mongolian Gerbil, a Specialized Mammalian Ear," *AUD*, vol. 4, no. 3–4, pp. 129–136, 1999, doi: 10.1159/000013831.
[68] S. E. Voss, J. J. Rosowski, S. N. Merchant, and W. T. Peake, "Acoustic responses of the human middle ear," *Hearing Research*, vol. 150, no. 1–2, pp. 43–69, Dec. 2000, doi: 10.1016/S0378-5955(00)00177-5.

[69] J. J. Rosowski and C. Y. Lee, “The effect of immobilizing the gerbil’s pars flaccida on the middle-ear’s response to static pressure,” *Hear. Res.*, vol. 174, no. 1–2, pp. 183–195, Dec. 2002, doi: 10.1016/s0378-5955(02)00655-x.
[70] N. Maftoon, W. R. J. Funnell, S. J. Daniel, and W. F. Decraemer, “Experimental Study of Vibrations of Gerbil Tympanic Membrane with Closed Middle Ear Cavity,” *J Assoc Res Otolaryngol*, vol. 14, no. 4, pp. 467–481, Aug. 2013, doi: 10.1007/s10162-013-0389-9.
[71] N. Maftoon, W. R. J. Funnell, S. J. Daniel, and W. F. Decraemer, “Effect of opening middle-ear cavity on vibrations of gerbil tympanic membrane,” *J. Assoc. Res. Otolaryngol.*, vol. 15, no. 3, pp. 319–334, Jun. 2014, doi: 10.1007/s10162-014-0442-3.
[72] J. M. Flores-Moreno *et al.*, “Holographic otoscope for nanodisplacement measurements of surfaces under dynamic excitation,” *Scanning*, vol. 33, no. 5, pp. 342–352, 2011, doi: 10.1002/sca.20283.
[73] M. Khaleghi, C. Furlong, M. Ravicz, J. T. Cheng, and J. J. Rosowski, “Three-dimensional vibrometry of the human eardrum with stroboscopic lensless digital holography,” *J Biomed Opt*, vol. 20, no. 5, p. 051028, May 2015, doi: 10.1117/1.JBO.20.5.051028.
[74] J. T. Cheng, N. Maftoon, J. Guignard, M. E. Ravicz, and J. Rosowski, “Tympanic membrane surface motions in forward and reverse middle ear transmissions,” *The Journal of the Acoustical Society of America*, vol. 145, no. 1, pp. 272–291, Jan. 2019, doi: 10.1121/1.5087134.
[75] C. Bergevin and E. S. Olson, “External and middle ear sound pressure distribution and acoustic coupling to the tympanic membrane,” *The Journal of the Acoustical Society of America*, vol. 135, no. 3, pp. 1294–1312, 2014.
[76] O. de La Rochefoucauld and E. S. Olson, “A sum of simple and complex motions on the eardrum and manubrium in gerbil,” *Hearing research*, vol. 263, no. 1–2, pp. 9–15, 2010.
[77] S. E. Voss, J. J. Rosowski, S. N. Merchant, and W. T. Peake, “Middle-ear function with tympanic-membrane perforations. II. A simple model,” *The Journal of the Acoustical Society of America*, vol. 110, no. 3, pp. 1445–1452, 2001, doi: 10.1121/1.1394196.
[78] S. M. Hesabgar, H. Marshall, S. K. Agrawal, A. Samani, and H. M. Ladak, “Measuring the quasi-static Young’s modulus of the eardrum using an indentation technique,” *Hearing Research*, vol. 263, no. 1, pp. 168–176, May 2010, doi: 10.1016/j.heares.2010.02.005.
[79] A. Ebrahimian, H. Tang, C. Furlong, J. T. Cheng, and N. Maftoon, “Material characterization of thin planar structures using full-field harmonic vibration response measured with stroboscopic holography,” *International Journal of Mechanical Sciences*, vol. 198, p. 106390, May 2021, doi: 10.1016/j.ijmecsci.2021.106390.
[80] X. Zhang and R. Z. Gan, “Dynamic Properties of Human Stapedial Annular Ligament Measured With Frequency–Temperature Superposition,” *J Biomech Eng*, vol. 136, no. 8, pp. 0810041–0810047, Aug. 2014, doi: 10.1115/1.4027668.
[81] T. Cheng and R. Z. Gan, “Mechanical properties of anterior malleolar ligament from experimental measurement and material modeling analysis,” *Biomech Model Mechanobiol*, vol. 7, no. 5, pp. 387–394, Oct. 2008, doi: 10.1007/s10237-007-0094-x.

[82] S. A. Rohani, S. Ghomashchi, S. K. Agrawal, and H. M. Ladak, "Estimation of the Young's modulus of the human pars tensa using in-situ pressurization and inverse finite-element analysis," *Hearing Research*, vol. 345, pp. 69–78, 2017.
[83] N. Ghadarghadar, S. K. Agrawal, A. Samani, and H. M. Ladak, "Estimation of the quasi-static Young's modulus of the eardrum using a pressurization technique," *Computer methods and programs in biomedicine*, vol. 110, no. 3, pp. 231–239, 2013.
[84] C. J. Roy and W. L. Oberkampf, "A comprehensive framework for verification, validation, and uncertainty quantification in scientific computing," *Computer Methods in Applied Mechanics and Engineering*, vol. 200, no. 25–28, pp. 2131–2144, Jun. 2011, doi: 10.1016/j.cma.2011.03.016.
[85] A. Fedorov *et al.*, "3D Slicer as an image computing platform for the Quantitative Imaging Network," *Magnetic resonance imaging*, vol. 30, no. 9, pp. 1323–1341, 2012.
[86] K. Homma, Y. Shimizu, N. Kim, Y. Du, and S. Puria, "Effects of ear-canal pressurization on middle-ear bone- and air-conduction responses," *Hear Res*, vol. 263, no. 0, pp. 204–215, May 2010, doi: 10.1016/j.heares.2009.11.013.
[87] S. Van der Jeught, J. J. J. Dirckx, J. R. M. Aerts, A. Bradu, A. G. H. Podoleanu, and J. A. N. Buytaert, "Full-field thickness distribution of human tympanic membrane obtained with optical coherence tomography," *J. Assoc. Res. Otolaryngol.*, vol. 14, no. 4, pp. 483–494, Aug. 2013, doi: 10.1007/s10162-013-0394-z.
[88] N. M. Newmark, "A Method of Computation for Structural Dynamics," *Journal of the Engineering Mechanics Division*, vol. 85, no. 3, pp. 67–94, 1959.
[89] G. Nicolas and T. Fouquet, "Adaptive mesh refinement for conformal hexahedralmeshes," *Finite Elements in Analysis and Design*, vol. 67, pp. 1–12, May 2013, doi: 10.1016/j.finel.2012.11.008.
[90] W. Edeling *et al.*, "The impact of uncertainty on predictions of the CovidSim epidemiological code," *Nat Comput Sci*, vol. 1, no. 2, pp. 128–135, Feb. 2021, doi: 10.1038/s43588-021-00028-9.
[91] S. Marelli and B. Sudret, "UQLab: A Framework for Uncertainty Quantification in Matlab," in *Vulnerability, Uncertainty, and Risk*, Liverpool, UK, Jun. 2014, pp. 2554–2563. doi: 10.1061/9780784413609.257.
[92] G. L. Pearce and D. D. Frisbie, "Statistical evaluation of biomedical studies," *Osteoarthritis and Cartilage*, vol. 18, pp. S117–S122, Oct. 2010, doi: 10.1016/j.joca.2010.04.014.
[93] P. Berens, "CircStat: A MATLAB Toolbox for Circular Statistics," *Journal of Statistical Software*, vol. 31, no. 1, Art. no. 1, Sep. 2009, doi: 10.18637/jss.v031.i10.
[94] A. Pewsey, "The large-sample joint distribution of key circular statistics," *Metrika*, vol. 60, no. 1, pp. 25–32, Jul. 2004, doi: 10.1007/s001840300294.
[95] N. I. Fisher, *Statistical Analysis of Circular Data*. Cambridge university press, 1995.
[96] J. L. Hintze and R. D. Nelson, "Violin Plots: A Box Plot-Density Trace Synergism," *The American Statistician*, vol. 52, no. 2, p. 181, May 1998, doi: 10.2307/2685478.
[97] C. Forbes, M. Evans, N. Hastings, and B. Peacock, *Statistical distributions*, vol. 4. Wiley New York, 2011.

[98] L. T. DeCarlo, “On the meaning and use of kurtosis,” *Psychological Methods*, vol. 2, no. 3, pp. 292–307, 1997, doi: 10.1037/1082-989X.2.3.292.
[99] D. P. Doane and L. E. Seward, “Measuring Skewness: A Forgotten Statistic?,” *Journal of Statistics Education*, vol. 19, no. 2, Jul. 2011, doi: 10.1080/10691898.2011.11889611.
[100] F. Zhao, T. Koike, J. Wang, H. Sienz, and R. Meredith, “Finite element analysis of the middle ear transfer functions and related pathologies,” *Medical Engineering & Physics*, vol. 31, no. 8, pp. 907–916, Oct. 2009, doi: 10.1016/j.medengphy.2009.06.009.
[101] D. De Greef, F. Pires, and J. J. Dirckx, “Effects of model definitions and parameter values in finite element modeling of human middle ear mechanics,” *Hearing research*, vol. 344, pp. 195–206, 2017.
[102] H. Osnes and J. Sundnes, “Uncertainty analysis of ventricular mechanics using the probabilistic collocation method,” *IEEE transactions on biomedical engineering*, vol. 59, no. 8, pp. 2171–2179, 2012.
[103] L. C. Lobato, S. Paul, and J. A. Cordioli, “Statistical analysis of the human middle ear mechanical properties,” *The Journal of the Acoustical Society of America*, vol. 151, no. 3, pp. 2043–2054, 2022.
[104] R. L. Goode, M. Killion, K. Nakamura, and S. Nishihara, “New knowledge about the function of the human middle ear: development of an improved analog model.,” *The American journal of otology*, vol. 15, no. 2, pp. 145–154, 1994.
[105] A. Sobester, A. Forrester, and A. Keane, *Engineering design via surrogate modelling: a practical guide*. John Wiley & Sons, 2008.
[106] B. Iooss and P. Lemaître, “A Review on Global Sensitivity Analysis Methods,” in *Uncertainty Management in Simulation-Optimization of Complex Systems: Algorithms and Applications*, G. Dellino and C. Meloni, Eds. Boston, MA: Springer US, 2015, pp. 101–122. doi: 10.1007/978-1-4899-7547-8_5.
[107] I. M. Sobol′, “Global sensitivity indices for nonlinear mathematical models and their Monte Carlo estimates,” *Mathematics and Computers in Simulation*, vol. 55, no. 1–3, pp. 271–280, Feb. 2001, doi: 10.1016/S0378-4754(00)00270-6.
[108] S. Marelli, C. Lamas, and B. Sudret, *UQLab user manual - Sensitivity analysis*. 2015. doi: 10.13140/RG.2.1.1419.4404.
[109] A. Saltelli, “Making best use of model evaluations to compute sensitivity indices,” *Computer physics communications*, vol. 145, no. 2, pp. 280–297, 2002.
[110] A. Saltelli, P. Annoni, I. Azzini, F. Campolongo, M. Ratto, and S. Tarantola, “Variance based sensitivity analysis of model output. Design and estimator for the total sensitivity index,” *Computer physics communications*, vol. 181, no. 2, pp. 259–270, 2010.
[111] B. Sudret, “Global sensitivity analysis using polynomial chaos expansions,” *Reliability Engineering & System Safety*, vol. 93, no. 7, pp. 964–979, Jul. 2008, doi: 10.1016/j.ress.2007.04.002.
[112] N. Fajraoui, M. Fahs, A. Younes, and B. Sudret, “Analyzing natural convection in porous enclosure with polynomial chaos expansions: Effect of thermal dispersion, anisotropic permeability and heterogeneity,” *International Journal of Heat and Mass Transfer*, vol. 115, pp. 205–224, Dec. 2017, doi: 10.1016/j.ijheatmasstransfer.2017.07.003.

[113] S. Marelli and B. Sudret, “UQLab user manual - Polynomial chaos expansions,” 2015, doi: 10.13140/RG.2.1.3778.7366.
[114] B. Efron, T. Hastie, I. Johnstone, and R. Tibshirani, “Least angle regression,” *Ann. Statist.*, vol. 32, no. 2, pp. 407–499, Apr. 2004, doi: 10.1214/009053604000000067.
[115] G. Blatman and B. Sudret, “An adaptive algorithm to build up sparse polynomial chaos expansions for stochastic finite element analysis,” *Probabilistic Engineering Mechanics*, vol. 25, no. 2, pp. 183–197, Apr. 2010, doi: 10.1016/j.probengmech.2009.10.003.
[116] G. Kazmitcheff *et al.*, “Validation method of a middle ear mechanical model to develop a surgical simulator,” *Audiology and Neurotology*, vol. 19, no. 2, pp. 73–84, 2014.
[117] G. Kazmitcheff *et al.*, “Registration of a validated mechanical atlas of middle ear for surgical simulation,” in *International Conference on Medical Image Computing and Computer-Assisted Intervention*, 2013, pp. 331–338.
[118] M. E. Ravicz, J. J. Rosowski, and S. N. Merchant, “Mechanisms of hearing loss resulting from middle-ear fluid,” *Hearing research*, vol. 195, no. 1–2, pp. 103–130, 2004.
[119] J. Caillet, F. Marrot, Y. Unia, and P.-A. Aubourg, “Comprehensive approach for noise reduction in helicopter cabins,” *Aerospace Science and Technology*, vol. 23, no. 1, pp. 17–25, Dec. 2012, doi: 10.1016/j.ast.2012.03.004.
[120] J.-C. Pascal, X. Carniel, V. Chalvidan, and P. Smigielski, “Determination of phase and magnitude of vibration for energy flow measurements in a plate using holographic interferometry,” *Optics and Lasers in Engineering*, vol. 25, no. 4, pp. 343–360, Oct. 1996, doi: 10.1016/0143-8166(95)00080-1.
[121] C. Trillo *et al.*, “Measurement of the complex amplitude of transient surface acoustic waves using double-pulsed TV holography and a two-stage spatial Fourier transform method,” *Meas. Sci. Technol.*, vol. 14, no. 12, pp. 2127–2134, Oct. 2003, doi: 10.1088/0957-0233/14/12/012.
[122] O. A. Sapozhnikov, A. V. Morozov, and D. Cathignol, “Piezoelectric transducer surface vibration characterization using acoustic holography and laser vibrometry,” in *IEEE Ultrasonics Symposium, 2004*, Aug. 2004, vol. 1, pp. 161-164 Vol.1. doi: 10.1109/ULTSYM.2004.1417693.
[123] H. Tang *et al.*, “High-Speed Holographic Shape and Full-Field Displacement Measurements of the Tympanic Membrane in Normal and Experimentally Simulated Pathological Ears,” *Applied Sciences*, vol. 9, no. 14, p. 2809, Jan. 2019, doi: 10.3390/app9142809.
[124] P. Razavi, M. E. Ravicz, I. Dobrev, J. T. Cheng, C. Furlong, and J. J. Rosowski, “Response of the human tympanic membrane to transient acoustic and mechanical stimuli: Preliminary results,” *Hear Res*, vol. 340, pp. 15–24, Oct. 2016, doi: 10.1016/j.heares.2016.01.019.
[125] H. Tang, P. Razavi, N. Maftoon, J. J. Rosowski, C. Furlong, and J. T. Cheng, “Comparative Modal Analysis of the Tympanic Membrane Mechanics Between Normal and Experimentally Simulated Pathological Ears,” in *Mechanics of Biological Systems and Materials & Micro-and Nanomechanics, Volume 4*, Cham, 2020, pp. 63–71. doi: 10.1007/978-3-030-30013-5_11.

[126] J. Caillet, J. C. Carmona, and D. Mazzoni, “Estimation of plate elastic moduli through vibration testing,” *Applied Acoustics*, vol. 68, no. 3, pp. 334–349, Mar. 2007, doi: 10.1016/j.apacoust.2006.01.011.
[127] M. Alfano and L. Pagnotta, “Determining the elastic constants of isotropic materials by modal vibration testing of rectangular thin plates,” *Journal of Sound and Vibration*, vol. 293, no. 1–2, pp. 426–439, May 2006, doi: 10.1016/j.jsv.2005.10.021.
[128] A. Davis *et al.*, “Visual Vibrometry: Estimating Material Properties from Small Motions in Video,” *IEEE Transactions on Pattern Analysis and Machine Intelligence*, vol. 39, no. 4, pp. 732–745, Apr. 2017, doi: 10.1109/TPAMI.2016.2622271.
[129] N. Hasheminejad, C. Vuye, A. Margaritis, W. Van den bergh, J. Dirckx, and S. Vanlanduit, “Characterizing the Complex Modulus of Asphalt Concrete Using a Scanning Laser Doppler Vibrometer,” *Materials*, vol. 12, no. 21, Art. no. 21, Jan. 2019, doi: 10.3390/ma12213542.
[130] S. Sehgal and H. Kumar, “Structural Dynamic Model Updating Techniques: A State of the Art Review,” *Arch Computat Methods Eng*, vol. 23, no. 3, pp. 515–533, Sep. 2016, doi: 10.1007/s11831-015-9150-3.
[131] L. Pagnotta, “Recent progress in identification methods for the elastic characterization of materials,” *International Journal of Mechanics*, vol. 2, no. 4, 2008.
[132] M. Alfano and L. Pagnotta, “Recent Developments and Selected Patents on Vibration Based Methods for the Elastic Characterization of Isotropic Materials,” *Recent Patents on Mechanical Engineering*, vol. 2, pp. 130–143, Jan. 2010, doi: 10.2174/1874477X10902020130.
[133] S. S. Rao, *Vibration of Continuous Systems*. John Wiley & Sons, 2019.
[134] M. Bonnet and A. Constantinescu, “Inverse problems in elasticity,” *Inverse Problems*, vol. 21, pp. R1–R50, 2005, doi: 10.1088/0266-5611/21/2/R01.
[135] G. Aksu and R. Ali, “Free vibration analysis of stiffened plates using finite difference method,” *Journal of Sound and Vibration*, vol. 48, no. 1, pp. 15–25, Sep. 1976, doi: 10.1016/0022-460X(76)90367-9.
[136] T. Asakura, T. Ishizuka, T. Miyajima, and M. Toyoda, “Finite-difference time-domain analysis of the vibration characteristics of a beam-plate structure using a dimension-reduced model,” *Applied Acoustics*, vol. 92, pp. 75–85, May 2015, doi: 10.1016/j.apacoust.2014.12.011.
[137] X.-D. Yang, W. Zhang, L.-Q. Chen, and M.-H. Yao, “Dynamical analysis of axially moving plate by finite difference method,” *Nonlinear Dynamics*, vol. 67, no. 2, pp. 997–1006, Jan. 2012, doi: 10.1007/s11071-011-0042-2.
[138] Y. Zhang, D. W. Apley, and W. Chen, “Bayesian Optimization for Materials Design with Mixed Quantitative and Qualitative Variables,” *Sci Rep*, vol. 10, no. 1, p. 4924, Dec. 2020, doi: 10.1038/s41598-020-60652-9.
[139] R. Lam, K. Willcox, and D. H. Wolpert, “Bayesian optimization with a finite budget: An approximate dynamic programming approach,” in *Advances in Neural Information Processing Systems*, 2016, pp. 883–891.

[140] B. Shahriari, K. Swersky, Z. Wang, R. P. Adams, and N. de Freitas, "Taking the Human Out of the Loop: A Review of Bayesian Optimization," *Proceedings of the IEEE*, vol. 104, no. 1, pp. 148–175, Jan. 2016, doi: 10.1109/JPROC.2015.2494218.
[141] Z.-L. Wang, T. Ogawa, and Y. Adachi, "Influence of Algorithm Parameters of Bayesian Optimization, Genetic Algorithm, and Particle Swarm Optimization on Their Optimization Performance," *Advanced Theory and Simulations*, vol. 2, no. 10, p. 1900110, 2019, doi: 10.1002/adts.201900110.
[142] T. Marwala, Ed., "Finite-element-model Updating Using a Bayesian Approach," in *Finite-element-model Updating Using Computional Intelligence Techniques: Applications to Structural Dynamics*, London: Springer London, 2010, pp. 183–201. doi: 10.1007/978-1-84996-323-7_10.
[143] K.-V. Yuen and L. S. Katafygiotis, "Bayesian time–domain approach for modal updating using ambient data," *Probabilistic Engineering Mechanics*, vol. 16, no. 3, pp. 219–231, Jul. 2001, doi: 10.1016/S0266-8920(01)00004-2.
[144] H. Moravej, T. H. Chan, K.-D. Nguyen, and A. Jesus, "Vibration-based Bayesian model updating of civil engineering structures applying Gaussian process metamodel," *Advances in Structural Engineering*, vol. 22, no. 16, pp. 3487–3502, Dec. 2019, doi: 10.1177/1369433219858723.
[145] J. N. Reddy, *Theory and Analysis of Elastic Plates and Shells*. CRC Press, 2006. doi: 10.1201/9780849384165.
[146] J. Ezeh, O. Ibearugbulem, and C. Onyechere, "Pure bending analysis of thin rectangular flat plates using ordinary finite difference method," *International Journal of Emerging Technology and Advanced Engineering*, vol. 3, no. 3, pp. 20–23, 2013.
[147] R. Chartrand, "Numerical Differentiation of Noisy, Nonsmooth Data," *ISRN Applied Mathematics*, vol. 2011, pp. 1–11, 2011, doi: 10.5402/2011/164564.
[148] G. A. Wood, "DATA SMOOTHING AND DIFFERENTIATION PROCEDURES IN BIOMECHANICS," *Exercise and Sport Sciences Reviews*, vol. 10, no. 1, pp. 308–362, Jan. 1982.
[149] M. Brunot, "Comparison of Numerical Differentiation Techniques for Aircraft Identification," *J. Aerosp. Eng.*, vol. 32, no. 5, p. 06019002, Sep. 2019, doi: 10.1061/(ASCE)AS.1943-5525.0001003.
[150] N. Srinivas, A. Krause, S. M. Kakade, and M. Seeger, "Gaussian Process Optimization in the Bandit Setting: No Regret and Experimental Design," *IEEE Trans. Inform. Theory*, vol. 58, no. 5, pp. 3250–3265, May 2012, doi: 10.1109/TIT.2011.2182033.
[151] C. E. Rasmussen and C. K. I. Williams, *Gaussian processes for machine learning*. Cambridge, Mass: MIT Press, 2006.
[152] D. Barac, M. D. Multerer, and D. Iber, "Global optimization using Gaussian processes to estimate biological parameters from image data," *Journal of Theoretical Biology*, vol. 481, pp. 233–248, Nov. 2019, doi: 10.1016/j.jtbi.2018.12.002.
[153] K. Swersky, "Improving Bayesian Optimization for Machine Learning using Expert Priors," Ph.D. thesis, University of Toronto, 2017.
[154] J. Snoek, H. Larochelle, and R. P. Adams, "Practical Bayesian Optimization of Machine Learning Algorithms," in *Advances in Neural Information Processing Systems*

25, F. Pereira, C. J. C. Burges, L. Bottou, and K. Q. Weinberger, Eds. Curran Associates, Inc., 2012, pp. 2951–2959. Accessed: Jan. 27, 2020. [Online]. Available: http://papers.nips.cc/paper/4522-practical-bayesian-optimization-of-machine-learning-algorithms.pdf

[155] T. Howison, J. Hughes, and F. Iida, "Morphologically programming the interactions of V-shaped falling papers," *Artificial Life Conference Proceedings*, vol. 32, pp. 359–366, Jul. 2020, doi: 10.1162/isal_a_00306.

[156] E. Brochu, V. M. Cora, and N. de Freitas, "A Tutorial on Bayesian Optimization of Expensive Cost Functions, with Application to Active User Modeling and Hierarchical Reinforcement Learning," *arXiv:1012.2599 [cs]*, Dec. 2010, Accessed: Jun. 04, 2019. [Online]. Available: http://arxiv.org/abs/1012.2599

[157] E. C. Garrido-Merchán and D. Hernández-Lobato, "Dealing with Integer-valued Variables in Bayesian Optimization with Gaussian Processes," *arXiv:1706.03673 [stat]*, Jun. 2017, Accessed: Jul. 10, 2019. [Online]. Available: http://arxiv.org/abs/1706.03673

[158] D. R. Jones, M. Schonlau, and W. J. Welch, "Efficient Global Optimization of Expensive Black-Box Functions," *Journal of Global Optimization*, vol. 13, no. 4, pp. 455–492, Dec. 1998, doi: 10.1023/A:1008306431147.

[159] A. D. Bull, "Convergence Rates of Efficient Global Optimization Algorithms," *Journal of Machine Learning Research*, vol. 12, no. 10, p. 26, 2011.

[160] J. Lancaster, R. Lorenz, R. Leech, and J. H. Cole, "Bayesian Optimization for Neuroimaging Pre-processing in Brain Age Classification and Prediction," *Front Aging Neurosci*, vol. 10, Feb. 2018, doi: 10.3389/fnagi.2018.00028.

[161] S. Gregori, M. Tur, A. Pedrosa, and F. J. Fuenmayor, "The Use of Bayesian Optimisation Techniques for the Pantograph-Catenary Dynamic Interaction Stochastic Problem," in *EngOpt 2018 Proceedings of the 6th International Conference on Engineering Optimization*, Cham, 2019, pp. 997–1008. doi: 10.1007/978-3-319-97773-7_86.

[162] R. Lorenz *et al.*, "The Automatic Neuroscientist: A framework for optimizing experimental design with closed-loop real-time fMRI," *Neuroimage*, vol. 129, pp. 320–334, Apr. 2016, doi: 10.1016/j.neuroimage.2016.01.032.

[163] A. Agarwalla, A. K. Jain, K. V. Manohar, and A. T. Saxena, "Bayesian optimisation with prior reuse for motion planning in robot soccer," presented at the ACM International Conference Proceeding Series, 2018, pp. 88–97. doi: 10.1145/3152494.3152502.

[164] R. Martinez-Cantin, "Funneled Bayesian Optimization for Design, Tuning and Control of Autonomous Systems," *IEEE Transactions on Cybernetics*, vol. 49, no. 4, pp. 1489–1500, Apr. 2019, doi: 10.1109/TCYB.2018.2805695.

[165] A. W. Leissa, "Vibration of plates," Jan. 1969. Accessed: May 24, 2019. [Online]. Available: https://ntrs.nasa.gov/search.jsp?R=19700009156

[166] P. Hagedorn and A. DasGupta, *Vibrations and Waves in Continuous Mechanical Systems*. John Wiley & Sons, 2007.

[167] V. Denoël, "Application des méthodes d'analyse stochastique à l'étude des effets du vent sur les structures du génie civil," University of Liège, 2005. Accessed: Jul. 27, 2019. [Online]. Available: https://orbi.uliege.be/handle/2268/13962

[168] K. R. Gurley, M. A. Tognarelli, and A. Kareem, "Analysis and simulation tools for wind engineering," *Probabilistic Engineering Mechanics*, vol. 12, no. 1, pp. 9–31, Jan. 1997, doi: 10.1016/S0266-8920(96)00010-0.

[169] I. Dobrev, C. Furlong, J. T. Cheng, and J. J. Rosowski, "Optimization of a lensless digital holographic otoscope system for transient measurements of the human tympanic membrane," *Exp Mech*, vol. 55, no. 2, pp. 459–470, Feb. 2015, doi: 10.1007/s11340-014-9945-4.

[170] J. Zhang, R. J. Perez, and E. J. Lavernia, "Documentation of damping capacity of metallic, ceramic and metal-matrix composite materials," *J Mater Sci*, vol. 28, no. 9, pp. 2395–2404, 1993, doi: 10.1007/BF01151671.

[171] W. Soboyejo, *Mechanical Properties of Engineered Materials*. CRC Press, 2002. doi: 10.1201/9780203910399.

[172] D. R. Lide, *CRC Handbook of Chemistry and Physics*, vol. 85. CRC Press, 2004.

[173] J. Larson, M. Menickelly, and S. M. Wild, "Derivative-free optimization methods," *Acta Numerica*, vol. 28, pp. 287–404, May 2019, doi: 10.1017/S0962492919000060.

[174] G. Venter, "Review of Optimization Techniques," in *Encyclopedia of Aerospace Engineering*, American Cancer Society, 2010. doi: 10.1002/9780470686652.eae495.

[175] K. Deb, "An introduction to genetic algorithms," *Sadhana*, vol. 24, no. 4, pp. 293–315, Aug. 1999, doi: 10.1007/BF02823145.

[176] M. J. Kochenderfer and T. A. Wheeler, *Algorithms for optimization*. Cambridge, Massachusetts: The MIT Press, 2019.

[177] L. Yang, X. Yang, Y. Wu, and X. Liu, "Applied Research on Distributed Generation Optimal Allocation Based on Improved Estimation of Distribution Algorithm," *Energies*, vol. 11, no. 9, Art. no. 9, Sep. 2018, doi: 10.3390/en11092363.

[178] E. Baeyens, A. Herreros, and J. R. Perán, "A Direct Search Algorithm for Global Optimization," *Algorithms*, vol. 9, no. 2, Art. no. 2, Jun. 2016, doi: 10.3390/a9020040.

[179] B. Feng and R. Z. Gan, "Lumped parametric model of the human ear for sound transmission," *Biomechanics and modeling in mechanobiology*, vol. 3, no. 1, pp. 33–47, 2004.

[180] R. Z. Gan, Q. Sun, R. K. Dyer, K.-H. Chang, and K. J. Dormer, "Three-dimensional modeling of middle ear biomechanics and its applications," *Otol. Neurotol.*, vol. 23, no. 3, pp. 271–280, May 2002, doi: 10.1097/00129492-200205000-00008.

[181] J. Kudela and R. Matousek, "Recent advances and applications of surrogate models for finite element method computations: a review," *Soft Computing*, pp. 1–25, 2022.

[182] Y. Dabiri, A. Van der Velden, K. L. Sack, J. S. Choy, G. S. Kassab, and J. M. Guccione, "Prediction of left ventricular mechanics using machine learning," *Frontiers in physics*, vol. 7, p. 117, 2019.

[183] Y. Dabiri, A. Van der Velden, K. L. Sack, J. S. Choy, J. M. Guccione, and G. S. Kassab, "Application of feed forward and recurrent neural networks in simulation of left ventricular mechanics," *Scientific Reports*, vol. 10, no. 1, pp. 1–11, 2020.

[184] M. Liu *et al.*, "Computation of a probabilistic and anisotropic failure metric on the aortic wall using a machine learning-based surrogate model," *Computers in Biology and Medicine*, vol. 137, p. 104794, 2021.

[185] D. Lorente *et al.*, "A framework for modelling the biomechanical behaviour of the human liver during breathing in real time using machine learning," *Expert Systems with Applications*, vol. 71, pp. 342–357, 2017.
[186] A. Ebrahimian, H. Mohammadi, M. Babaie, N. Maftoon, and H. R. Tizhoosh, "Class-Aware Image Search for Interpretable Cancer Identification," *IEEE Access*, vol. 8, pp. 197352–197362, 2020, doi: 10.1109/ACCESS.2020.3033492.
[187] M. Viscaino, J. C. Maass, P. H. Delano, M. Torrente, C. Stott, and F. Auat Cheein, "Computer-aided diagnosis of external and middle ear conditions: A machine learning approach," *PLoS One*, vol. 15, no. 3, p. e0229226, 2020.
[188] H. Byun *et al.*, "An assistive role of a machine learning network in diagnosis of middle ear diseases," *Journal of Clinical Medicine*, vol. 10, no. 15, p. 3198, 2021.
[189] M. G. Crowson *et al.*, "Machine learning for accurate intraoperative pediatric middle ear effusion diagnosis," *Pediatrics*, vol. 147, no. 4, 2021.
[190] B. J. Erickson, P. Korfiatis, Z. Akkus, and T. L. Kline, "Machine learning for medical imaging," *Radiographics*, vol. 37, no. 2, p. 505, 2017.
[191] C. F. Guimarães, L. Gasperini, A. P. Marques, and R. L. Reis, "The stiffness of living tissues and its implications for tissue engineering," *Nature Reviews Materials*, vol. 5, no. 5, pp. 351–370, 2020.
[192] L. Cai, L. Ren, Y. Wang, W. Xie, G. Zhu, and H. Gao, "Surrogate models based on machine learning methods for parameter estimation of left ventricular myocardium," *R. Soc. open sci.*, vol. 8, no. 1, p. 201121, Jan. 2021, doi: 10.1098/rsos.201121.
[193] V. Davies *et al.*, "Fast parameter inference in a biomechanical model of the left ventricle by using statistical emulation," *Journal of the Royal Statistical Society. Series C, Applied Statistics*, vol. 68, no. 5, p. 1555, 2019.
[194] U. Noè *et al.*, "Gaussian process emulation to accelerate parameter estimation in a mechanical model of the left ventricle: a critical step towards clinical end-user relevance," *Journal of the Royal Society Interface*, vol. 16, no. 156, p. 20190114, 2019.
[195] T. Chen and C. Guestrin, "XGBoost: A Scalable Tree Boosting System," in *Proceedings of the 22nd ACM SIGKDD International Conference on Knowledge Discovery and Data Mining*, San Francisco California USA, Aug. 2016, pp. 785–794. doi: 10.1145/2939672.2939785.
[196] R. Agata and I. G. N. M. Jaya, "A comparison of extreme gradient boosting, SARIMA, exponential smoothing, and neural network models for forecasting rainfall data," *J. Phys.: Conf. Ser.*, vol. 1397, no. 1, p. 012073, Dec. 2019, doi: 10.1088/1742-6596/1397/1/012073.
[197] J. H. Friedman, "Greedy function approximation: A gradient boosting machine.," *Ann. Statist.*, vol. 29, no. 5, Oct. 2001, doi: 10.1214/aos/1013203451.
[198] J. H. Friedman, "Stochastic gradient boosting," *Computational Statistics & Data Analysis*, vol. 38, no. 4, pp. 367–378, Feb. 2002, doi: 10.1016/S0167-9473(01)00065-2.
[199] W. Chang *et al.*, "A Machine-Learning-Based Prediction Method for Hypertension Outcomes Based on Medical Data," *Diagnostics*, vol. 9, no. 4, p. 178, Nov. 2019, doi: 10.3390/diagnostics9040178.

[200] M. Chen, Q. Liu, S. Chen, Y. Liu, C.-H. Zhang, and R. Liu, "XGBoost-based algorithm interpretation and application on post-fault transient stability status prediction of power system," *IEEE Access*, vol. 7, pp. 13149–13158, 2019.
[201] Z. Que and Z. Xu, "A data-driven health prognostics approach for steam turbines based on XGBoost and DTW," *IEEE Access*, vol. 7, pp. 93131–93138, 2019.
[202] J. Hao, "Supervised Machine Learning," in *Computational Psychometrics: New Methodologies for a New Generation of Digital Learning and Assessment*, A. A. von Davier, R. J. Mislevy, and J. Hao, Eds. Cham: Springer International Publishing, 2021, pp. 159–171. doi: 10.1007/978-3-030-74394-9_9.
[203] F. Pedregosa *et al.*, "Scikit-learn: Machine Learning in Python," *MACHINE LEARNING IN PYTHON*, p. 6.
[204] D. Modlin, M. Fuentes, and B. Reich, "Circular conditional autoregressive modeling of vector fields," *Environmetrics*, vol. 23, no. 1, pp. 46–53, Feb. 2012, doi: 10.1002/env.1133.
[205] S. Diwale, M. K. Eisner, C. Carpenter, W. Sun, G. C. Rutledge, and R. D. Braatz, "Bayesian optimization for material discovery processes with noise," *Mol. Syst. Des. Eng.*, vol. 7, no. 6, pp. 622–636, 2022, doi: 10.1039/D1ME00154J.
[206] H. Dai, G. Huang, H. Zeng, and F. Yang, "PM2. 5 Concentration Prediction Based on Spatiotemporal Feature Selection Using XGBoost-MSCNN-GA-LSTM," *Sustainability*, vol. 13, no. 21, p. 12071, 2021.
[207] H. Fathipour-Azar, "Data-driven estimation of joint roughness coefficient," *Journal of Rock Mechanics and Geotechnical Engineering*, vol. 13, no. 6, pp. 1428–1437, 2021.
[208] M. Balandat *et al.*, "BoTorch: A Framework for Efficient Monte-Carlo Bayesian Optimization." arXiv, Dec. 08, 2020. Accessed: Jun. 14, 2022. [Online]. Available: http://arxiv.org/abs/1910.06403
[209] L. Meng *et al.*, "Machine learning in additive manufacturing: a review," *Jom*, vol. 72, no. 6, pp. 2363–2377, 2020.
[210] Z. Hubler, N. D. Shemonski, R. L. Shelton, G. L. Monroy, R. M. Nolan, and S. A. Boppart, "Real-time automated thickness measurement of the in vivo human tympanic membrane using optical coherence tomography," *Quantitative imaging in medicine and surgery*, vol. 5, no. 1, p. 69, 2015.
[211] R. Dsouza *et al.*, "In vivo detection of nanometer-scale structural changes of the human tympanic membrane in otitis media," *Scientific reports*, vol. 8, no. 1, pp. 1–13, 2018.
[212] A. Karuppannan and A. Barman, "Wideband absorbance tympanometry: a novel method in identifying otosclerosis," *European Archives of Oto-Rhino-Laryngology*, vol. 278, no. 11, pp. 4305–4314, 2021.
[213] S. Cofer *et al.*, "Tympanostomy Tube Placement in Children Using a Single-Pass Tool with Moderate Sedation," *Otolaryngol Head Neck Surg*, vol. 157, no. 3, pp. 533–535, Sep. 2017, doi: 10.1177/0194599817707178.
[214] R. M. Rosenfeld, "Tympanostomy Tube Controversies and Issues: State-of-the-Art Review," *Ear Nose Throat J*, vol. 99, no. 1_suppl, pp. 15S-21S, Nov. 2020, doi: 10.1177/0145561320919656.

[215] R. Perkins, “Earlens tympanic contact transducer: A new method of sound transduction to the human ear,” *Otolaryngology - Head and Neck Surgery*, vol. 114, no. 6, pp. 720–728, Jun. 1996, doi: 10.1016/S0194-5998(96)70092-X.
[216] H. Liu, S. Ge, G. Cheng, J. Yang, Z. Rao, and X. Huang, “Transducer Type and Design Influence on the Hearing Loss Compensation Behaviour of the Electromagnetic Middle Ear Implant in a Finite Element Analysis,” *Advances in Mechanical Engineering*, vol. 6, p. 867108, Jan. 2014, doi: 10.1155/2014/867108.
[217] S. Hamanishi, T. Koike, H. Matsuki, and H. Wada, “A new electromagnetic hearing aid using lightweight coils to vibrate the ossicles,” *IEEE transactions on magnetics*, vol. 40, no. 5, pp. 3387–3393, 2004.
[218] Y.-L. Song *et al.*, “The development of a non-surgical direct drive hearing device with a wireless actuator coupled to the tympanic membrane,” *Applied acoustics*, vol. 74, no. 12, pp. 1511–1518, 2013.
[219] E.-P. Hong, M.-K. Kim, I.-Y. Park, S. -h. Lee, Y. Roh, and J.-H. Cho, “Vibration Modeling and Design of Piezoelectric Floating Mass Transducer for Implantable Middle Ear Hearing Devices,” *IEICE Transactions on Fundamentals of Electronics, Communications and Computer Sciences*, vol. E90-A, no. 8, pp. 1620–1627, Aug. 2007, doi: 10.1093/ietfec/e90-a.8.1620.
[220] A. Pegan, “Active Middle Ear Vibrant Soundbridge Sound Implant,” *ACC*, 2019, doi: 10.20471/acc.2019.58.02.20.
[221] S. Nishihara, H. Aritomo, and R. L. Goode, “Effect of Changes in Mass on Middle Ear Function,” *Otolaryngol Head Neck Surg*, vol. 109, no. 5, pp. 899–910, Nov. 1993, doi: 10.1177/019459989310900520.
[222] M. Vlaming and L. Feenstra, “Studies on the mechanics of the normal human middle ear,” *Clinical Otolaryngology & Allied Sciences*, vol. 11, no. 5, pp. 353–363, 1986.
[223] A. Victor, J. Ribeiro, and F. F. Araújo, “Study of PDMS characterization and its applications in biomedicine: A review,” *JMEB*, vol. 4, no. 1, pp. 1–9, Aug. 2019, doi: 10.24243/JMEB/4.1.163.
[224] H. Sandra and D. J. Kay, “Tympanostomy Tube Selection: A Review of the Evidence,” *International Journal of Head and Neck Surgery*, vol. 7, no. 1, pp. 17–22, Mar. 2016, doi: 10.5005/jp-journals-10001-1259.
[225] D. Armani, C. Liu, and N. Aluru, “Re-configurable fluid circuits by PDMS elastomer micromachining,” in *Technical Digest. IEEE International MEMS 99 Conference. Twelfth IEEE International Conference on Micro Electro Mechanical Systems (Cat. No.99CH36291)*, Orlando, FL, USA, 1999, pp. 222–227. doi: 10.1109/MEMSYS.1999.746817.
[226] Z. Bi and D. W. Mueller, “Friction predication on pin-to-plate interface of PTFE material and steel,” *Friction*, vol. 7, no. 3, pp. 268–281, Jun. 2019, doi: 10.1007/s40544-018-0224-8.
[227] C. B. Ruchti and L. Niemeyer, “Ablation Controlled Arcs,” *IEEE Trans. Plasma Sci.*, vol. 14, no. 4, pp. 423–434, 1986, doi: 10.1109/TPS.1986.4316570.
[228] R. Trochimczuk, “Analysis of Parallelogram Mechanism used to Preserve Remote Center of Motion for Surgical Telemanipulator,” *International Journal of Applied*

Mechanics and Engineering, vol. 22, no. 1, pp. 229–240, Feb. 2017, doi: 10.1515/ijame-2017-0013.

[229] J. Zemplenyi, S. Gilman, and D. Dirks, "Optical method for measurement of ear canal length," *The Journal of the Acoustical Society of America*, vol. 78, no. 6, pp. 2146–2148, Dec. 1985, doi: 10.1121/1.392676.

[230] I. Kivekäs and D. Poe, "Is there an optimal location for tympanostomy tube placement?," *The Laryngoscope*, vol. 125, no. 7, pp. 1513–1514, 2015, doi: 10.1002/lary.25127.

[231] M. S. Morris, "Tympanostomy tubes: types, indications, techniques, and complications," *Otolaryngologic Clinics of North America*, vol. 32, no. 3, pp. 385–390, 1999.

[232] S. E. Voss, J. J. Rosowski, S. N. Merchant, and W. T. Peake, "Middle-ear function with tympanic-membrane perforations. I. Measurements and mechanisms," *The Journal of the Acoustical Society of America*, vol. 110, no. 3, pp. 1432–1444, 2001, doi: 10.1121/1.1394195.

[233] Susan E. Voss, John J. Rosowski, Sa, "How do Tympanic-membrane Perforations Affect Human Middle-ear Sound Transmission?," *Acta Oto-Laryngologica*, vol. 121, no. 2, pp. 169–173, Jan. 2001, doi: 10.1080/000164801300043343.

[234] S. E. Voss, J. J. Rosowski, S. N. Merchant, and W. T. Peake, "Non-ossicular signal transmission in human middle ears: experimental assessment of the 'acoustic route' with perforated tympanic membranes," *The Journal of the Acoustical Society of America*, vol. 122, no. 4, pp. 2135–2153, 2007.

[235] N. Bevis, B. Sackmann, T. Effertz, M. Lauxmann, and D. Beutner, "The impact of tympanic membrane perforations on middle ear transfer function," *European Archives of Oto-Rhino-Laryngology*, vol. 279, no. 7, pp. 3399–3406, 2022.

[236] D. Sieber *et al.*, "The OpenEar library of 3D models of the human temporal bone based on computed tomography and micro-slicing," *Scientific data*, vol. 6, no. 1, pp. 1–9, 2019.

[237] S. E. Voss, "Effects of tympanic-membrane perforations on middle-ear sound transmission: measurements, mechanisms, and models," PhD Thesis, Massachusetts Institute of Technology, 1998.

[238] P. Filip, A. Govindan, and M. Cosetti, "In-office myringotomy and tympanostomy tube insertion," *Operative Techniques in Otolaryngology-Head and Neck Surgery*, vol. 32, no. 2, pp. 104–110, 2021.

[239] E. Stolz, "Cerebral veins and sinuses," *Handbook on neurovascular ultrasound*, vol. 21, pp. 182–193, 2006.

[240] H. Motallebzadeh and S. Puria, "Mouse middle-ear forward and reverse acoustics," *The Journal of the Acoustical Society of America*, vol. 149, no. 4, pp. 2711–2731, 2021.

[241] R. P. Mehta, J. J. Rosowski, S. E. Voss, E. O'Neil, and S. N. Merchant, "Determinants of hearing loss in perforations of the tympanic membrane," *Otology & neurotology: official publication of the American Otological Society, American Neurotology Society [and] European Academy of Otology and Neurotology*, vol. 27, no. 2, p. 136, 2006.

[242] M. Asai, A. M. Huber, and R. L. Goode, “Analysis of the best site on the stapes footplate for ossicular chain reconstruction,” *Acta oto-laryngologica*, vol. 119, no. 3, pp. 356–361, 1999.
[243] H. Kurokawa and R. L. Goode, “Sound pressure gain produced by the human middle ear,” *Otolaryngology—Head and Neck Surgery*, vol. 113, no. 4, pp. 349–355, 1995.
[244] A. Needham, D. Jiang, A. Bibas, G. Jeronimidis, and A. F. O’Connor, “The effects of mass loading the ossicles with a floating mass transducer on middle ear transfer function,” *Otology & Neurotology*, vol. 26, no. 2, pp. 218–224, 2005.

Appendices

Appendix A

Range of model parameters for Chapter 2

Table A – Range of the uncertain parameters used in stochastic FE model.

Parameter	**Range for CV of 10% [min,max]**	**Range for CV of 20% [min,max]**	**Parameter**	**Range for CV of 10% [min,max]**	**Range for CV of 20% [min,max]**
Poisson's ratio of TM	[0.31,0.49]	[0.14,0.49]	Young's modulus of AML (MPa)	[1.26,2.90]	[0.51,3.80]
Poisson's ratio of ossicles	[0.21,0.41]	[0.11,0.48]	Young's modulus of LML (MPa)	[1.35,2.62]	[0.69,3.24]
Poisson's ratio of IMJ	[0.28,0.49]	[0.07,0.49]	Young's modulus of manubrial fold (MPa)	[0.81,1.64]	[0.42,2.08]
Poisson's ratio of ISJ	[0.30,0.49]	[0.11,0.49]	Young's modulus of SML (MPa)	[3.04,6.45]	[1.18,7.99]
Poisson's ratio of SAL	[0.32,0.49]	[0.15,0.49]	Thickness of TM (μm)	[50.99,98.68]	[27.98,123.35]
Poisson's ratio of PIL	[0.32,0.49]	[0.16,0.49]	Cochlear load (N.s/m)	[0.16,0.36]	[0.08,0.44]
Poisson's ratio of AML	[0.34,0.49]	[0.19,0.49]	Damping (α_2 coefficient) of TM (s)	[24.98,54.05]$\times 10^{-7}$	[9.97,68.09] $\times 10^{-7}$
Poisson's ratio of LML	[0.30,0.49]	[0.12,0.49]	Damping (α_2 coefficient) of ossicles (s)	[2.57,5.72]$\times 10^{-7}$	[1.15,7.44]$\times 10^{-7}$
Poisson's ratio of manubrial fold	[0.26,0.49]	[0.02,0.49]	Damping (α_2 coefficient) of IMJ (s)	[8.56,17.16] $\times 10^{-5}$	[4.12,21.31] $\times 10^{-5}$

Parameter	Range for CV of 10% [min,max]	Range for CV of 20% [min,max]	Parameter	Range for CV of 10% [min,max]	Range for CV of 20% [min,max]
Poisson's ratio of SML	[0.28,0.49]	[0.08,0.49]	Damping (α_2 coefficient) of ISJ (s)	[8.82,17.07] $\times 10^{-5}$	[4.64,21.14] $\times 10^{-5}$
Young's modulus of TM (MPa)	[8.19,16.61]	[4.39,21.23]	Damping (α_2 coefficient) of SAL (s)	[9.24,16.86] $\times 10^{-5}$	[5.48,20.71] $\times 10^{-5}$
Young's modulus of ossicles (MPa)	[9565.60,18522.78]	[5131.20,23045.55]	Damping (α_2 coefficient) of PIL (s)	[8.93,17.13] $\times 10^{-5}$	[4.87,21.25] $\times 10^{-5}$
Young's modulus of IMJ (MPa)	[21.19,39.97]	[12.37,49.94]	Damping (α_2 coefficient) of AML (s)	[8.72,17.68] $\times 10^{-5}$	[4.45,22.36] $\times 10^{-5}$
Young's modulus of ISJ (MPa)	[19.32,39.76]	[8.65,49.51]	Damping (α_2 coefficient) of LML (s)	[8.81,16.79] $\times 10^{-5}$	[4.61,20.58] $\times 10^{-5}$
Young's modulus of SAL (MPa)	[0.94,1.88]	[0.49,2.36]	Damping (α_2 coefficient) of manubrial fold (s)	[24.19,53.50] $\times 10^{-7}$	[8.37,67.00] $\times 10^{-7}$
Young's modulus of PIL	[1.28,2.60]	[0.56,3.20]	Damping (α_2 coefficient) of SML (s)	[8.60,17.56] $\times 10^{-5}$	[4.21,22.11] $\times 10^{-5}$

Appendix B

Comparison of the stochastic FE model results with several experimental results in the literature for Chapter 2

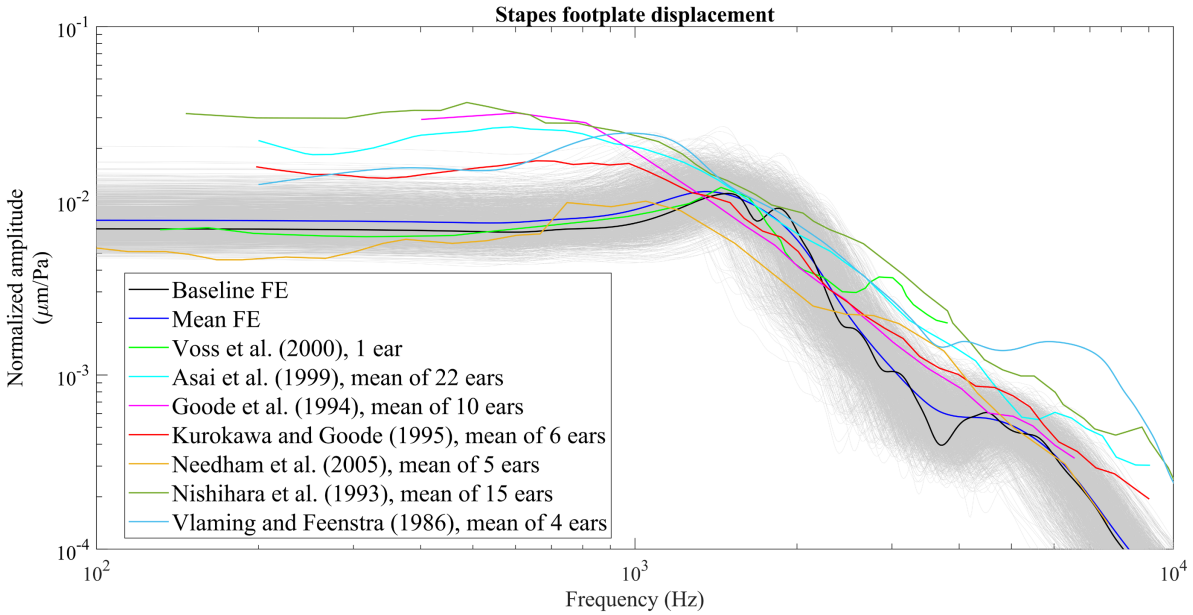


Figure B – Comparison of the stochastic FE model results of the stapes footplate with several experimental results in the literature[68], [104], [221], [222], [242]–[244]. *The gray thin lines represent the stochastic FE model results of the stapes footplate with CV of 20% for model parameters. All experimental measurement results are reported in the piston-like direction of the stapes footplate. For the works that did not report a value of the measurement angle between the laser beam and the piston-like motion of the stapes, we assumed an angle of 35°. Also, for the works that reported a range for measurement angle between the laser beam and piston-like direction, the mean value of the reported range was used. The experimental results presented in this figure reveal that the variations of the experimental measurements are higher than the maximum variation we considered in our model (CV of 20% for model parameters). The high variation of the experimental results can be due to the morphological variability as well.*

Appendix C

Range of model parameters for Chapter 3

Table C – Range of variation of model parameters and the values used for generating results in column (b) of Figure 3-4.

Structure	**E (MPa) – [min,max]**	**E (MPa) for Figure 3-4-b**	**Poisson's ratio - [min,max]**	**Poisson's ratio for Figure 3-4-b**	**α_2 (s) - [min,max]**	**α_2 (s) for Figure 3-4-b**
TM	[4.39,21.23]	9.60	[0.14,0.49]	0.39	[9.97,68.09]×10^{-7}	3.20×10^{-6}
Malleus	[5131.20,23045.55]	11200	[0.11,0.48]	0.24	[1.15,7.44]×10^{-7}	3.20×10^{-7}
Incus	[5131.20,23045.55]	11200	[0.11,0.48]	0.24	[1.15,7.44]×10^{-7}	3.20×10^{-7}
Stapes	[5131.20,23045.55]	11200	[0.11,0.48]	0.24	[1.15,7.44]×10^{-7}	3.20×10^{-7}
IMJ	[12.37,49.94]	24	[0.07,0.49]	0.39	[4.12,21.31]×10^{-5}	1.04×10^{-4}
ISJ	[8.65,49.51]	24	[0.11,0.49]	0.39	[4.64,21.14]×10^{-5}	1.04×10^{-4}
SAL	[0.49,2.36]	1.12	[0.15,0.49]	0.39	[5.48,20.71]×10^{-5}	1.04×10^{-4}

Structure	E (MPa) – [min,max]	E (MPa) for Figure 3-4-b	Poisson's ratio - [min,max]	Poisson's ratio for Figure 3-4-b	α_2 (s) - [min,max]	α_2 (s) for Figure 3-4-b
PIL	[0.56,3.20]	1.6	[0.16,0.49]	0.39	$[4.87,21.25]\times 10^{-5}$	1.04×10^{-4}
LML	[0.69,3.24]	1.6	[0.12,0.49]	0.39	$[4.61,20.58]\times 10^{-5}$	1.04×10^{-4}
Manubrial fold	[0.42,2.08]	0.96	[0.02,0.49]	0.39	$[8.37,67.00]\times 10^{-7}$	3.20×10^{-6}
SML	[1.18,7.99]	3.92	[0.08,0.49]	0.39	$[4.21,22.11]\times 10^{-5}$	1.04×10^{-4}
AML	[0.51,3.80]	1.6	[0.19,0.49]	0.39	$[4.45,22.36]\times 10^{-5}$	1.04×10^{-4}
TM thickness (μm) – [min,max]		[27.98,123.35]		TM thickness (μm) for Figure 3-4-b		59.20
Cochlear load (N.s/m) – [min,max]		[0.08,0.44]		Cochlear load (N.s/m) for Figure 3-4-b		0.21